LBNL-42161

ERNEST ORLANDO LAWRENCE
BERKELEY NATIONAL LABORATORY

Solid State Nuclear Magnetic Resonance Studies of Prion Peptides and Proteins

Jonathan Heller

Materials Sciences Division

August 1997

Ph.D. Thesis

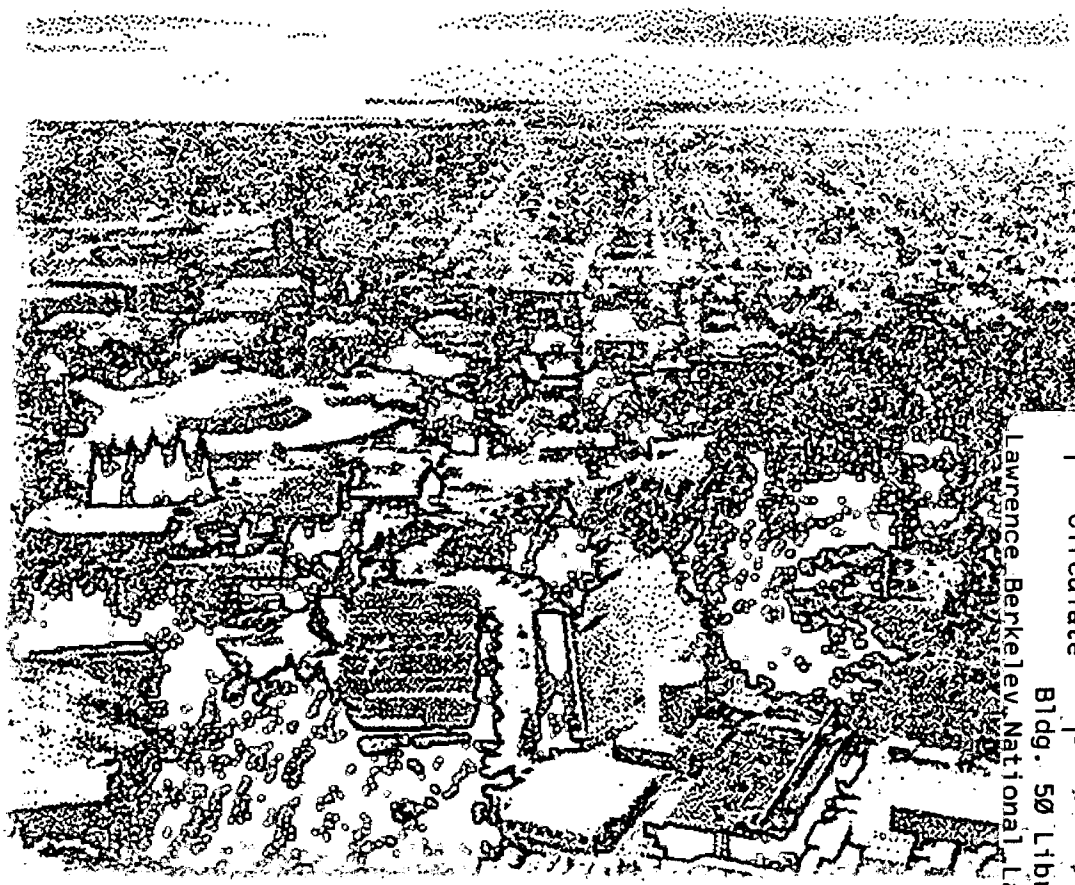

DISCLAIMER

LBNL-42161

Solid State Nuclear Magnetic Resonance Studies of Prion Peptides and Proteins

Jonathan Heller
Ph.D. Thesis

Department of Biophysics
University of California, Berkeley

and

Materials Sciences Division
Ernest Orlando Lawrence Berkeley National Laboratory
University of California
Berkeley, CA 94720

August 1997

This work was supported by the Director, Office of Energy Research, Office of Basic Energy Sciences, Materials Sciences Division, and the Howard Hughes Medical Institute through the U.S. Department of Energy under Contract No. DE-AC03-76SF00098.

Solid State Nuclear Magnetic Resonance Studies of Prion Peptides and Proteins

by

Jonathan Heller

B.A. (Harvard University) 1989

a dissertation submitted in partial satisfaction of the

requirements for the degree of

Doctor of Philosophy

in

Biophysics

in the

GRADUATE DIVISION

of the

UNIVERSITY of CALIFORNIA, BERKELEY

Committee in charge:

Professor David E. Wemmer, Chair
Professor Yeon-Kyun Shin
Professor Alexander Pines

FALL 1997

Solid State Nuclear Magnetic Resonance Studies of Prion Peptides and Proteins

by

Jonathan Heller

Abstract

Solid State Nuclear Magnetic Resonance Studies of Prion Peptides and Proteins

by

Jonathan Heller

Doctor of Philosophy in Biophysics

University of California, Berkeley

Professor David E. Wemmer, Chair

High-resolution structural studies using x-ray diffraction and solution nuclear magnetic resonance (NMR) are not feasible for proteins of low solubility and high tendency to aggregate. Solid state NMR (SSNMR) is in principle capable of providing structural information in such systems, however to do this efficiently and accurately, further SSNMR tools must be developed This dissertation describes the development of three new methods and their application to a biological system of interest, the prion protein (PrP).

First, a protocol is presented for the determination of internuclear distances, and errors associated with these measurements, using rotational-resonance magnetization-exchange NMR in systems with inhomogeneously broadened lines. Then, a simple method for the determination of backbone dihedral angles in peptides is presented. This method compares experimentally measured chemical-shift anisotropies (CSA) with *ab initio* chemical-shielding calculations to predict dihedral angles for alanine residues. Lastly, the unsuccessful attempts to measure longer distances, between a localized free radical and a spin one-half nucleus, are described.

The application of these techniques to PrP is discussed. Conformation-dependent chemical-shift measurements, rotational-resonance distance measurements, and dihedral angle measurements have been carried out to analyze the conformation of solid-state peptides lacking long-range three-dimensional order, corresponding to a region of PrP designated H1. Conformational changes in PrP seem to be responsible for prion diseases and the H1 region is predicted to play a key role in the secondary structure transformation that generates the infectious protein. SSNMR data show that the conformation of this peptide is dependent on the solvent from which it is lyophilized. The peptide can take an extended, β-sheet-like conformation, or an α-helical conformation.

Dedicated to Connie and to all my family

Table of Contents

List of Figures

List of Tables

Acknowledgments

First, I have to thank Connie. Without a doubt, she is my best friend. Without her support and companionship, graduate school would have been much more difficult. It has been a fun few years, mostly because of her. I have learned a lot more than biophysics. And, of course, I have to thank her for graduating before me so that I could enjoy Thistle for my last year.

When I was growing up, I swore that I would not follow in my parents footsteps and become a scientist. Things (meaning me) change. Each year, to the horror of the child that I was, I become more like my parents. Since I am turning into them, I guess its good that I like and respect them so much. Their friendship and their advice (yes, I'm even admitting that!) have helped me through graduate school. My debt to them will never be repaid in full.

My brother is the original reason for my move to California. (It was here or Texas.) Since I started here, he has gotten married and had three kids. Much more productive than I. He, Karen, Rebecca, Boaz, and Jonah are a huge part of my life, and I am glad to have them around me. Again, graduate school would have been very different without all of them.

I have also gained many new family members. Helen and Juan and all the rest have given me a big family to be a part of. All the meals and discussions and events have been a fun and necessary distraction.

I have been lucky enough to have two advisors. Dave has taught me a lot and has been a pleasure to work with. He has always made time for my numerous interruptions and has kept me moving forward. Alex, I have to thank for his Vision. He has been inspirational, always throwing around new ideas and dreams. The two of them together have helped me understand a lot about Science.

Since I have had two advisors, I have had twice the number of people to interact. I have worked most closely with people on the prion project. Russell Larsen, Andrew Kolbert and Matthias Ernst taught me almost all I know about NMR. Their mentoring and collaboration was one of the most important aspects of my graduate career. Since the start they gave me, I have worked with Dave Laws, Hans Bitter, Kai Liu and Seth Bush. It was a pleasure to work with them all and to have had many positive collaborations.

Others in the labs have contributed to my education and my fun. I would like to thank those who are gone (Bernhard, Patty, Mike, Brian, Andrew, Fred, Rafa, Tim, Werner, Pete, Nat, Andrea, Ray from the Wemmer lab and Holly, Marcia, Young, Rebecca, Lucy, Jay, Gerry, Geoff, Jonathan, Stefano, Mei, Klaus, Tanja, Angelo from the Pines lab) and those who are still around (Steph, Cheryl, Corey, Ho, Christian, John, Chino, Peter, Peter, Qing, Doro, Jeff in the Wemmer lab and Boyd, Marco, Yung-Ya, Susan, Tomas, Thomas, Roberto, David, Dave, Fred, Eike, Jeff, Matt, Dihn, Lana, Annjoe, Yi-Qiao, Shuan-Hu in the Pines lab).

There are still more who have contributed to both my science and my enjoyment. Dione has kept the Pines lab running and helped make my life easier (even though she harasses me). Dave King and his peptide synthesizer have made my graduate career much shorter. It has been a pleasure working with him. Our collaborators in the Prusiner lab have also been helpful, mainly Mike Baldwin and Darlene Groth. And many people in Calvin Lab, including Jim Bartholomew and Alex Grantz, have made working there fun.

Lastly, I would like to thank the HHMI for financial support.

SECTION I:

INTRODUCTION

Chapter 1

Prion Diseases

Prion diseases are neurodegenerative disorders that occur in animals and humans. Symptoms include spongiform degeneration, amyloid plaque formation, vacuolation, ataxia and dementia. The disorders are novel in that they appear to be transmitted by proteinaceous agents devoid of nucleic acids and that they are manifest in inherited, sporadic, or infectious illnesses.

Evidence suggests that a protein, named the prion protein (PrP), causes prion diseases. No nucleic acids have been found to be associated with infectivity and the gene encoding for PrP is not part of the infectious particle. The only known component of the infectious particle is PrP and the prion protein is the primary component of the amyloid plaques formed in the diseased state. PrP is also found in healthy animals, but it has a different tertiary structure in its "normal" form than in its infectious form.

In order to elucidate the structure of PrP in its infectious state, it is necessary to use new spectroscopic techniques because the protein is not soluble and the plaques, which contain the interesting conformation of PrP, have no long range order. Solid-state nuclear magnetic resonance is a promising technique for doing high-resolution structural studies of proteins in solid, non-crystalline states, but tools must first be developed in order to achieve this goal. The development of such tools and their application to peptides derived from the prion protein are the subjects of this thesis.

1.1 Prion Diseases in Animals

Scrapie was the first prion disease to be characterized. By 1938, it was known that the disease could be transferred between sheep. In 1948, 1,500 of 18,000 sheep, vaccinated two years earlier against looping ill virus with formalin treated extracts of ovine lymphoid tissue, died of scrapie[1]. Since then, prion diseases have been recognized in a number of different animals, including cows, cats, goats, mule deer, elk, mink and nyala (see table 1.1).

More recently, prion diseases have become a major concern in Britain and the rest of the world. In 1985, the first cases of Bovine Spongiform Encephalopathy (BSE), more commonly known as mad cow disease, were observed in Britain. Since then over 150,000 cattle with the disorder have died or been slaughtered. Evidence suggests that the cause of the outbreak was the use of scrapie contaminated sheep offal as feed. Between 1978 and 1980, feed plants in England changed the way feed was processed. The use of hydrocarbon solvents was eliminated, removing the delipidation step of the processing. It is speculated that the delipidation step made the infectious particle more susceptible to inactivation. As a result, the British government banned the practice of feeding cattle sheep offal. In the years between the change in processing and the appearance of BSE, the disease had to jump the species barrier and incubate in infected cattle.

In 1996, it was reported that the occurrence of human Creutzfeld Jakob Disease (CJD) in young people (mean age of 26 years), who had shown very limited susceptibility to the disease, had increased in Britain[2]. Ten cases were reported, including two cases in which onset occurred in the late teens. It is suspected that these new cases are due to the ingestion of BSE infected beef. Several other cases were reported elsewhere in Europe in the year after these

Table 1.1: Prion diseases in animals and humans

Animal Disease:	host:
scrapie	sheep/goats
bovine spongiform encephalopathy (BSE) (mad cow disease)	cattle
transmissible mink encephalopathy	mink
chronic wasting disease	mule deer/elk
feline spongiform encephalopathy	cats
exotic ungulate encephalopathy	nyala
Human Disease	mode of propagation
kuru	infectious
Creutzfeldt-Jakob Disease (CJD)	sporadic, inherited, infectious
Gerstmann-Straussler-Scheinker Syndrome (GSS)	inherited
Fatal Familial Insomnia (FFI)	inherited

initial cases were publicized. This caused an international scare, leading to the ban of British beef in much of the world, and to the slaughter of much of the British cattle herd.

1.2 Prion Diseases in Humans

Prion diseases also occur in humans, but only between 1 and 10 people in 100 million suffer from prion diseases[3]. In the 1960's, Gajdusek and coworkers first characterized kuru as a prion disease. Kuru was once the most common cause of death among people of the Fore tribe in the Highlands of

Papua New Guinea. The disease was transmitted by ritualistic cannibalism and it has disappeared with the end of these practices. In 1966, Gajdusek and coworkers showed that kuru could be transferred to chimpanzees by injecting them with diseased brain tissue from humans with kuru[4].

Prion diseases are unique in that they can be sporadic, inherited or infectious. CJD can be caused by inherited mutations in the genome[3], particularly in the gene that encodes for the prion protein (PrP), or it can occur very late in life as a sporadic event[5], or it can be transferred from one human to another via the injection of components of brain tissue[6]. Gerstmann-Straussler-Scheinker disease (GSS) and Fatal Familial Insomnia (FFI) are inherited human prion diseases. The diseases generally affect people between 40 and 70 years of age[3].

1.3 The Protein-Only Hypothesis

The search for a virus that causes prion diseases has to date yielded no positive results. The viral life cycle (figure 1.1) includes nucleic acids, either DNA or RNA, as a necessary part of transmission. Although nucleic acids necessary for prion disease transmission have been sought for many years, none have been found. Infectivity is resistant to nuclease digestion by micrococcal nuclease, nuclease P, deoxyribonucleases I and II, ribonucleases A, H, III and T_1, and phoshodiesterases I and II. Infectivity is not subject to UV inactivation, divalent cation hydrolysis, and psoralen photoreaction, all of which inactivate most viruses. Several studies have shown that the infectious particle is at most 50 kDa, much smaller than would be expected if it were viral or if it consisted of DNA coding for protein[7].

Many hypotheses have been proposed to explain the disorders,

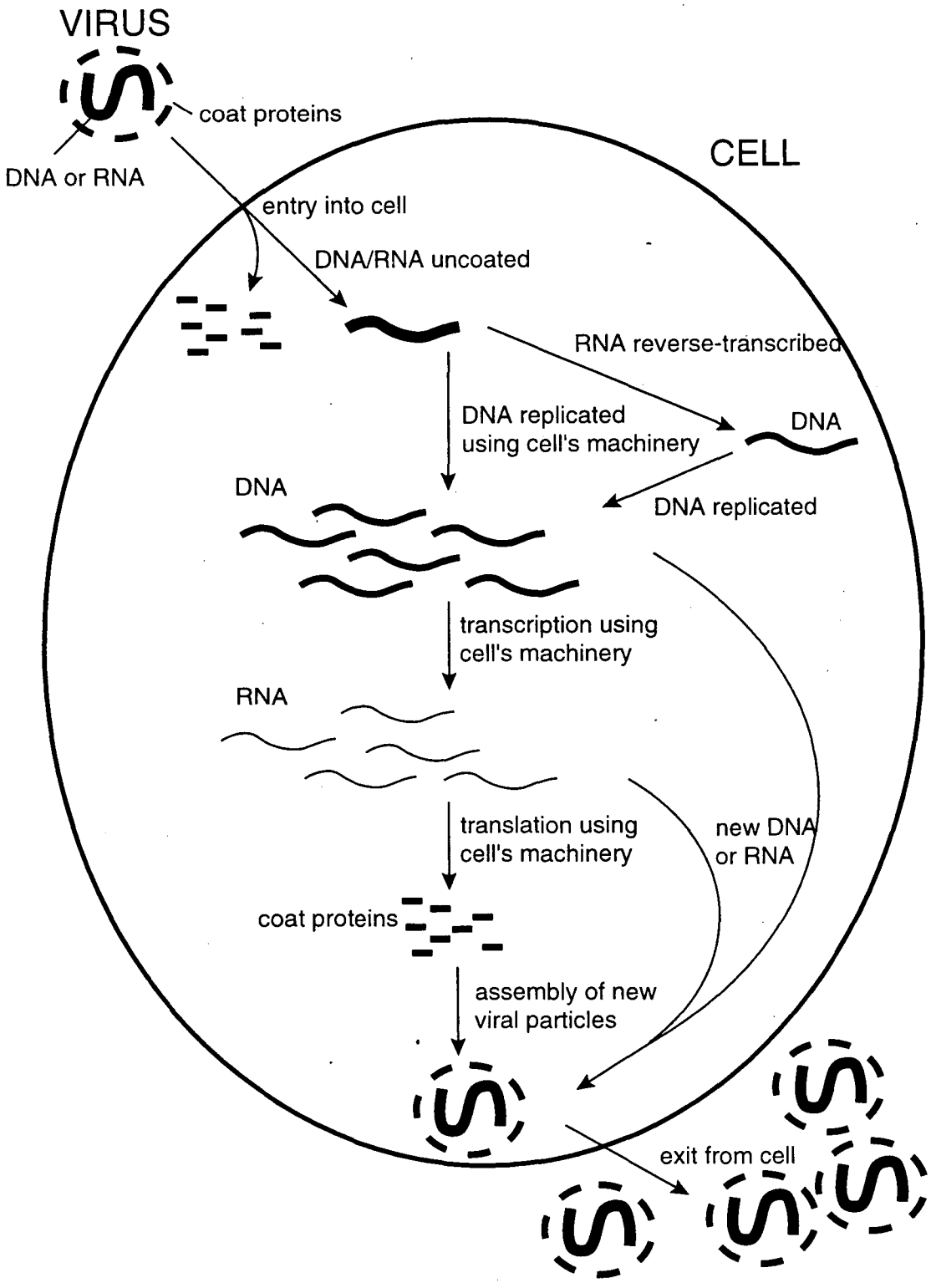

Figure 1.1: The life cycle of a virus. Either DNA or RNA is necessary for viral replication.

including that the cause is a parasite[8], a filterable virus[9], a replicating abnormal polysaccharide[10], a naked nucleic acid[11], an unconventional virus[12], a nucleoprotein complex[13], a nucleic acid surrounded by a polysaccharide coat[14], a membrane bound DNA[15], and a replicating protein[16]. Of these theories, only the last, the replicating protein hypothesis, has evidence supporting it. Because prion diseases are the first group of diseases for which there is evidence supporting a protein-only hypothesis, and because such a hypothesis seems contrary to the central dogma of modern biology (i.e. that DNA is used to make RNA which is used to make proteins; proteins can not make other proteins), the theory was very controversial and was met with great skepticism.

The infective agent in prion diseases is subject to inactivation by all of the following: urea, phenol, SDS, chaotropic salts, and diethyl pyrocarbonate[7]. These agents act on proteins, and this evidence was the first to suggest that a protein was responsible for the disorders. In 1982 the term "prion" was introduced to denote a "small *pro*teinaceous *in*fectious particle" that was thought to be the cause of disease[7]. Since these initial experiments, much data in support of a protein-only hypothesis has been collected.

Prusiner and coworkers isolated a protease-resistant protein, PrP27-30 (27-30 kDa prion protein), associated with scrapie infectivity[17]. It was found that PrP27-30 formed rods in the presence of detergents, which were ultra-structurally indistinguishable from amyloid rods found in infected brain. A 33-35 kDa form of the protein, PrP^{Sc} (Scrapie prion protein), was then isolated. mRNA levels encoding PrP were found to be the same in infected and normal brain, and a normal, protease-sensitive form of the protein, PrP^{C} (cellular prion protein), was isolated[18].

Evidence has been compiled suggesting that PrP causes prion diseases. No nucleic acids have been found to be associated with infectivity and the gene encoding for PrP is not part of the infectious particle. Prion diseases do not create immunogenic responses, suggesting that no foreign proteins are involved. The only known component of the infectious particle is PrP^{Sc}.

1.4 The Prion Protein

PrP has 254 residues in Syrian golden hamsters (see figure 1.2), and is found mostly in the central nervous system. (The numbering used in this thesis will be that of the protein found in Syrian golden hamster.) The N-terminal 22 residues are cleaved off in the rough endoplasmic reticulum[19,20]. PrP also has a 23 residue C-terminal signal sequence that is cleaved off after a glycosyl phosphatidylinositol (GPI) moiety is added at position ^{231}Ser[21]. The GPI anchors the protein to the cell surface. Asparagine-linked oligosaccharides are found at positions 181 and 197 [18,22]. A disulfide bond occurs between ^{179}Cys and ^{214}Cys[20]. The N-terminal 67 residues of the mature protein (residues 23-90) contain several Gly-Pro rich octarepeats having a consensus sequence GGWGQPHG. The number of octarepeats is species dependent.

PrP is very highly conserved among mammals[23,24] (see figure 1.3). Human and hamster PrP are 90% identical and primates and humans have between 92.9% and 99.6% identity. Most differences are found in the N-terminal signal peptide and most are conservative mutations. It is believed that some mutations are significant in preventing or delaying infection of one species by the PrP^{Sc} of another species, a phenomenon known as the species barrier.

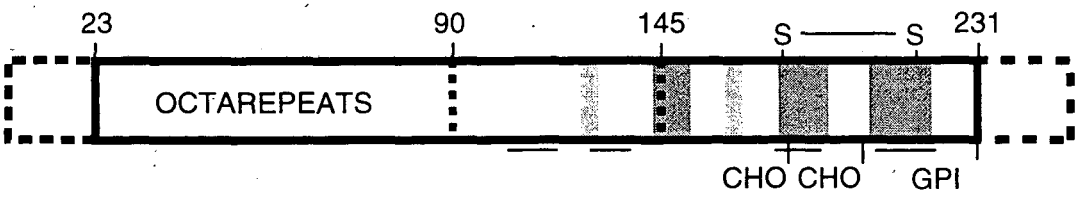

Figure 1.2: A schematic diagram of the prion protein. The N- and C-termini are cleaved after the protein is glycosylated at residues 181 and 197 and after the GPI anchor is attached to residue 231. A disulfide bond links residue 179 to 214. Several octarepeats occur between residues 23 and 90. Residues predicted to be helical (H1 - H4) have a bar underneath them. Residues found to be helical in the NMR structure are in dark gray, while those found to be in the β-sheet are in light gray.

The function of PrP is unknown. The strong sequence conservation would suggest that the protein has an important function which depends highly on its primary structure. However, transgenic (Tg) mice in which the gene has been disrupted appear normal[25], suggesting that the protein is not essential or that mice developing without PrP can compensate for its absence. It was reported that hippocampal slices from these PrP-null mice have weakened γ-aminobutyric acid type A receptor-mediated fast inhibition and impaired long-term potentiation[26]. Whether PrP^C function is related to these observations, and whether loss of these functions is related to disease, is still under investigation.

Edman sequencing and mass spectroscopy data suggest that PrP^C and PrP^{Sc} have identical primary structure and identical post-translational modifications[27]. Although covalent differences have been sought, none has been detected. Despite this, the two molecules have quite different properties (see table 1.2). PrP^C is found on the surface of both normal and infected cells,

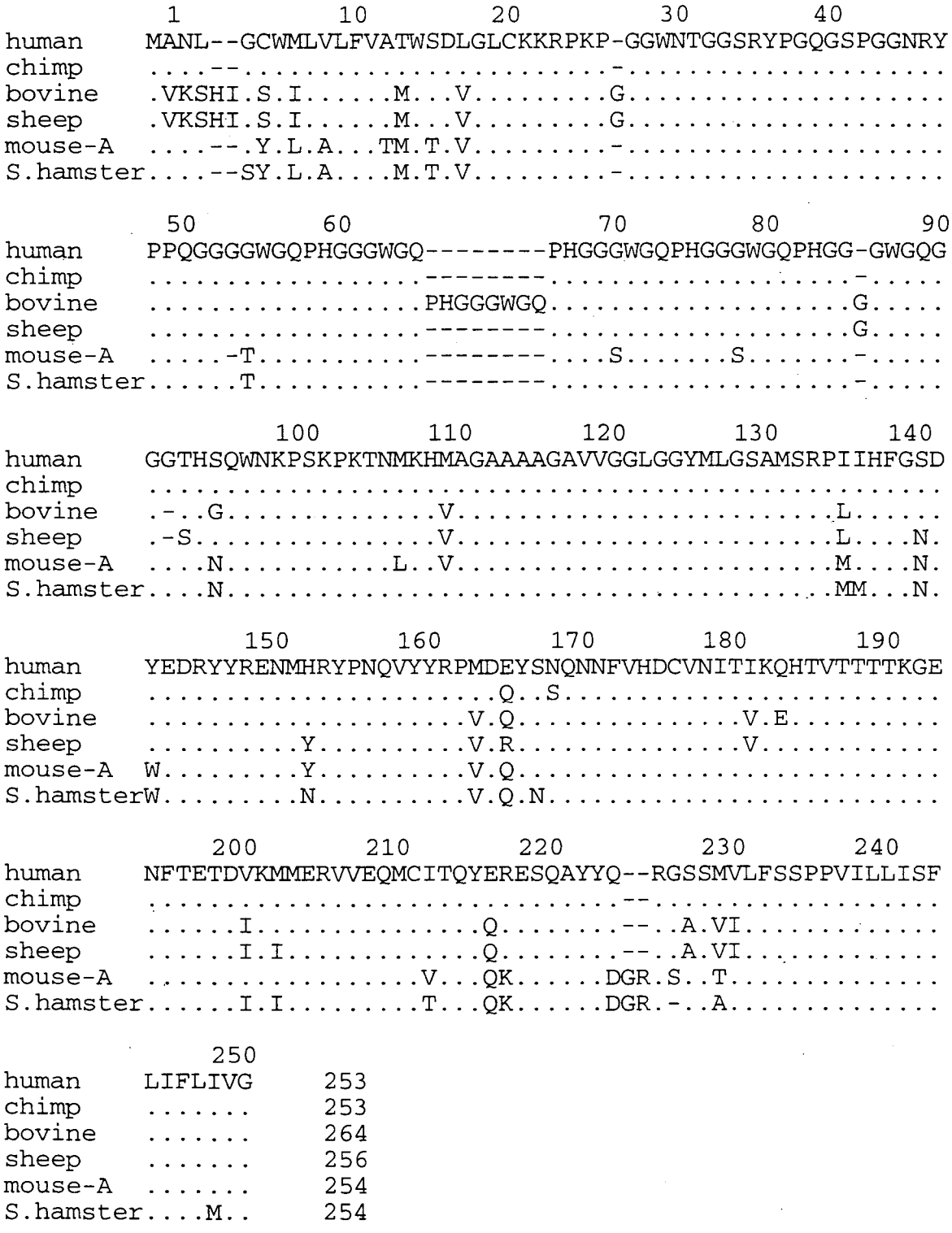

Figure 1.3: Sequence comparison of PrP from several species.

is synthesized and degraded rapidly[28], and is susceptible to protease digestion[18]. On the other hand, PrP^{Sc} is found in cytoplasmic vesicles of infected cells only, has a protease resistant core, PrP27-30, and is synthesized slowly and accumulates in diseased brain. PrP^{C} is not infectious while PrP^{Sc} is infectious.

The secondary structure composition of the two forms of PrP has been analyzed by Fourier-transform infrared spectroscopy (FTIR) and circular dichroism (CD). Using non-denaturing methods, both PrP^{C} and PrP^{Sc} were purified and the protease-resistant core of PrP^{Sc} was isolated. PrP^{C} was found to contain 42% α-helix and only 3% β-sheet[29], while PrP^{Sc} contained 30% α-helix and 43% β-sheet[29], and PrP27-30 contained either 21% α-helix and 54% β-sheet [29] or 17% α-helix, 47% β-sheet, and 31% turn[30]. This data suggests that a conformational change in PrP may be involved in prion diseases.

Table 1.2: Differences between PrP^{C} and PrP^{Sc}

PrP^{C}	PrP^{Sc}
non-infectious	infectious
found in normal and infected cells	found in infected cells
found on cell surface	found in cytoplasmic vesicles
susceptible to protease digestion	contains protease resistant core
synthesized and degraded rapidly	synthesized slowly and accumulates in the brains of infected animals
mostly α-helical	both α-helical and β-sheet

Eighteen mutations in the gene coding for PrP segregate with familial forms of prion diseases, thus explaining the genetic transmission of the diseases[24]. GSS has been found in families with the P102L mutation[31]. A 48

residue insert containing 6 octarepeats at residue 53 has been linked to CJD[32], as has the E200K substitution[33]. Mutations at residue 178 have been linked to both CJD[34,35] and FFI[36]. Other point mutations at residues 117[37], 198[38] and 217[39] also segregate with prion diseases.

1.5 Transgenic animals and the species barrier

Transgenic (Tg)animal studies have been helpful in understanding prion diseases and have supported the hypothesis that PrP is responsible for prion diseases, but have also generated results needing complex explanations. The first such study ablated the PrP gene from mice and showed that these PrP-null mice develop normally[25]. However, unlike normal mice, they could not be infected by intracranial injection of mouse PrP^{Sc}[40,41]. Tg mice carrying the P102L mutation linked to GSS in humans die from spontaneous CNS degeneration characterized by clinical signs indistinguishable from scrapie[42]. Brain extracts from two such Tg mice were serially passaged to normal mice and caused neurodegeneration[43]. Tg mice which produced shortened forms of PrP, including PrP27-30, were tested for susceptibility to infection. Results indicate that the full protein is necessary for susceptibility. Interestingly, although the protease resistant core of PrP^{Sc} consisting of residues 90-231 was capable of transmitting the disease, mice expressing a gene coding for the protein of this length were not susceptible to disease. This suggests that the octarepeat region is necessary for conversion of PrP^{C} into PrP^{Sc}.

Passage of prions from one species to another is a low probability process characterized by long incubation times. This has become known as the species barrier. Due to the species barrier, normal mice can only rarely be

infected by hamster prions and normal hamsters can only rarely be infected by mouse prions. When infection occurs, the plaques from the mouse infected with hamster prions contain only mouse PrP (i.e. host PrP), and its brain extracts can be used to infect other mice with shortened incubation times, but can not infect hamsters.

Tg mice carrying both the hamster PrP gene and the mouse PrP gene can be infected by either hamster or mouse prions. When injected with hamster prions, the plaques isolated from diseased brain contained only the hamster PrP, and the mice exhibited neuropathologic changes characteristic of hamsters. When these Tg mice were injected with mouse prions, the plaques contained only mouse PrP, and exhibited the changes characteristic of mice[44].

Tg mice expressing both human and mouse PrP were not susceptible to human prions. However if the mouse gene was disrupted and only the human gene was present, these mice became susceptible to human prions[45]. These results suggest that mouse PrP^{C} inhibited the conversion of human PrP^{C} to human PrP^{Sc}.

Chimeric PrP genes which cross mouse with hamster as well as mouse with human have been created and display a complex pattern of infection in which specific regions seem necessary for infection by prions from different species. For example, Tg(MHu2M) mice (mice containing the transgene which codes for residues 1-95 from mouse, 96-167 from humans, and 168-254 from mouse) were susceptible to human prions, in the presence or absence of the mouse PrP gene[45]. These results suggest that another host specific protein interacts with PrP and is necessary for conversion.

1.6 Prion Strains

There is evidence for distinct "strains" of prions having specific incubation times, distributions of vacuolar lesions, and patterns of PrP^{Sc} accumulation[46-48]. The mechanism by which the infectious protein carries strain information remains in question, although recent evidence suggests that the size of the protease resistant core varies among different strains[49]. This suggests that different conformations of PrP^{Sc} exist and cause slightly different diseases.

1.7 Structure of PrP^{C}

Until recently, recombinant PrP^{C} was not available, and thus no high-resolution structural studies of the full length protein could be carried out. In its place, extensive structure prediction was used to predict regions of significance. By comparing 11 mammalian and one avian PrP sequence, four regions of PrP were predicted to be helical: 109-122 (H1), 129-140 (H2), 178-191(H3), and 202-218 (H4)[50]. When peptides corresponding to these sequences were synthesized, only H2 was soluble in water, and the remaining three formed intermolecular β-sheets. Predicted structures based on this and other information were published for both PrP^{C}[51] and PrP^{Sc}[52].

H1 is thought to be important in conversion of PrP^{C} to PrP^{Sc} for several reasons: 1) it is very highly conserved across all species[23]; 2) it displays both α-helical and β-sheet characteristics[50,53], as the two forms of the protein do, and can induce β-sheet in other peptides[54]; 3) a patient with an amber mutation at residue 145 died from a prion disease[55]; 4) PrP27-30, containing residues 90-231, is infectious[18]; 5) it is in a region identified in PrP plaques (residues 58-150)[56]; 6) it is in a region in which sequence variations have the

greatest impact on transmission between species (residues 90-130)[24]; and 7) it is in a region shown to be toxic to neurons (residues 106-126)[57].

A method for over-expression and purification of recombinant PrP in *E. coli* was developed recently in at least two laboratories [58,59] and this has allowed for NMR structural studies of the soluble form of a truncated form (residues 121-231) of the protein[59] (see figure 1.4). The construct was derived from the mouse sequence, folded reversibly (ΔG_{fold} = -22 kJ/mol), and was soluble to 1 mM between pH 4 and pH 8.5. The structure differed significantly from the predicted structure, although the model's helices H3 and H4 and their relative orientation were predicted correctly.

The solution NMR structure contained three α-helices, residues 144 to 154, 179 to 193, and 200 to 217, (which will be called helix 1 - 3, as opposed to H1 - H4) and a short β-sheet formed by two β-strands, residues 128 to 131 and 161 to 164. As the protein was recombinantly expressed in *E. coli*, it was not glycosylated, but the disulfide bond was in place. A loop between residues 167 and 176 gave no NOESY cross-peaks, and was therefore assumed to be flexible. Highly conserved residues formed the hydrophobic core of the protein (which included several sidechains from helices 2 and 3, one sidechain from helix 1 and one from the β-sheet, as well as several loop sidechains). Several hydrophobic residues were found on the surface of the protein near the β-sheet and the loop preceding the first helix. The surface exhibited an uneven charge distribution; the face pointing towards the reader in figure 4 is highly positively charged while the opposite face is highly negatively charged. Six sites of mutation causing inherited diseases are contained in the construct, and all are in or directly adjacent to secondary structural elements. Three of these are found in the hydrophobic core and mutations at these sites may

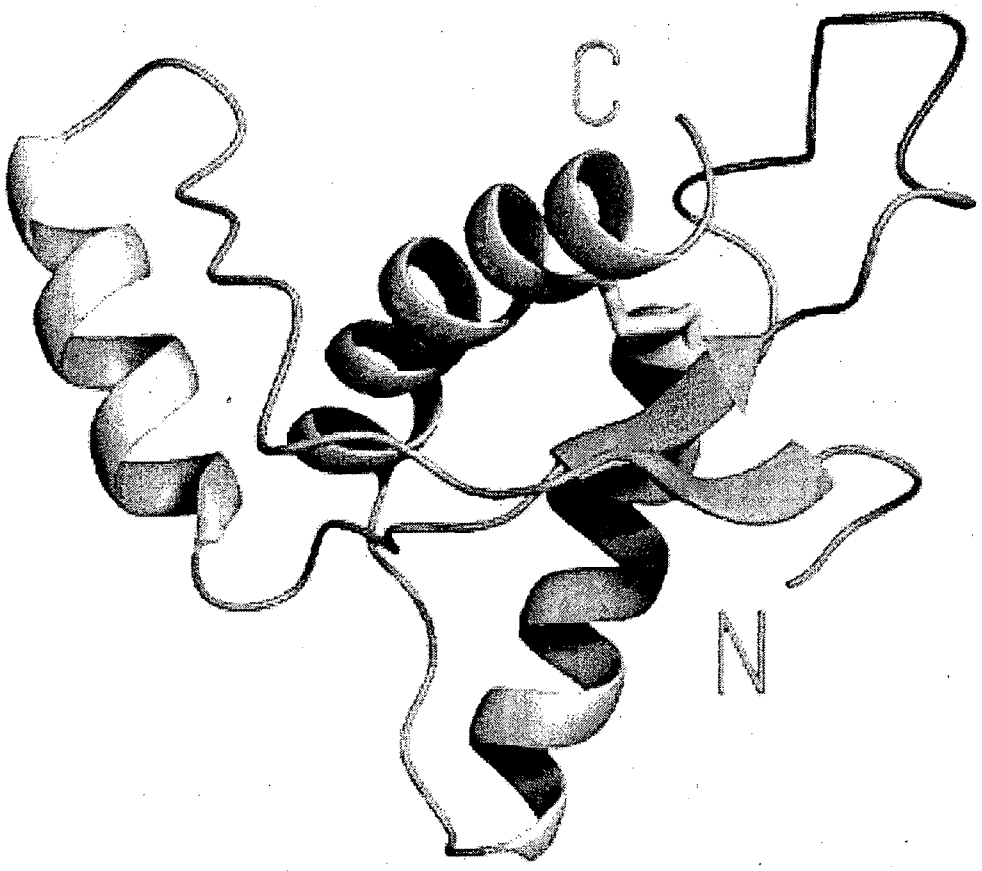

Figure 1.4: A ribbon diagram of the solution structure of PrP^C, residues 121-231. The structure contains three α-helices (residues 144-154, 179-193, and 200-217), two β-strands (residues 128-131 and 161-164) and a disulfide bond between cysteines 179 and 214. The loop from residues 167 to 176 gave no NOE's and was therefore believed to be flexible. (Reproduced with permission from Martin Billeter.)

destabilized the folded protein. The remaining three occur at the protein surface and mutations at these sites may effect protein-protein interactions.

1.8 The Conformational Change Hypotheses

Many general questions regarding prion diseases can not yet be answered and these questions must be resolved before the prion hypothesis is universally accepted and understood. Among these questions are: How does infectious protein enter the body? How does the infectious protein, once in the body, move across the blood/brain barrier and into the brain? What is the function of PrP^C? Are the diseases caused by a loss of function due to the conversion of PrP^C to a non-functional form? Are the diseases caused some new function of PrP^{Sc}? Or are the diseases due to the accumulation of PrP^{Sc} in the brain? How is the species barrier crossed and what are the risks of infection? Are there any similarities between prion diseases and other amyloid diseases, such as Alzheimer's Disease? Is there a way to prevent infection or to prevent neuronal degeneration once infection has occurred? By what mechanism is PrP^C converted to PrP^{Sc}?

The data presented above have led to several hypotheses regarding this last question. The model put forth by Prusiner, Cohen and co-workers is shown in figure 1.5. PrP^C transforms into an activated state PrP^{C*}, which is capable of interacting with PrP^{Sc}. The size and composition of the complex is not known, and no direct evidence supports its existence. Protein X then binds the complex and allows the conversion of PrP^{C*} to PrP^{Sc}. Thus, the cycle continues. This model accounts for several important features of prions. Prion infectivity multiplies exponentially, as would the number of infectious PrP^{Sc} molecules in the model. The model describes a post-

translational, non-covalent modification of PrP^C to form PrP^{Sc}, and this is supported by data. PrP^{C*} could be formed when PrP^C enters a lysozomal compartment, and could explain the accumulation of PrP^{Sc} inside the cell rather than on its surface. The species barrier could be explained by the model, as PrP^{C*} and PrP^{Sc} from different species may not interact, and protein X may be species specific. The model explains inherited prion diseases, since mutations in PrP may help form PrP^{Sc} by destabilizing either PrP^C or PrP^{C*}. Spontaneous diseases are explained by allowing PrP^C to stochastically convert to PrP^{C*} and PrP^{Sc}. Strains are explained by allowing for several forms of PrP^{Sc} with different conformations, each of which causes conversion to its own form and yields different symptoms.

Griffith first put forth a different mechanism of PrP^{Sc} formation, which was expanded on by Gajdusek and more recently by Lansbury, Caughey and co-workers[49,60] (see figure 1.6). In this model, PrP^C exists in its soluble form, but under certain cellular conditions, it can be in equilibrium with an unfolded form, PrP^U or an insoluble conformation. In the absence of PrP^{Sc}, the concentration of these alternate forms would be too low for nucleus formation and polymerization. However, in the presence of a PrP^{Sc} nucleus or seed, the insoluble conformer of PrP can be stabilized by interactions with PrP^{Sc}, leading to growth of the polymer. Alternatively, the PrP^{Sc} polymer could catalyze the conversion of PrP^C. This model explains the existence of strains by allowing for differently arranged PrP^{Sc} polymers and explains the inherited diseases as Prusiner's model does. In this model, spontaneous diseases may occur when a nucleus forms in the absence of a seed, a stochastic event. PrP^C may convert in lysosomes, accounting for the location of PrP^{Sc} in the cell. Plaques are often associated with disease, and diffraction data

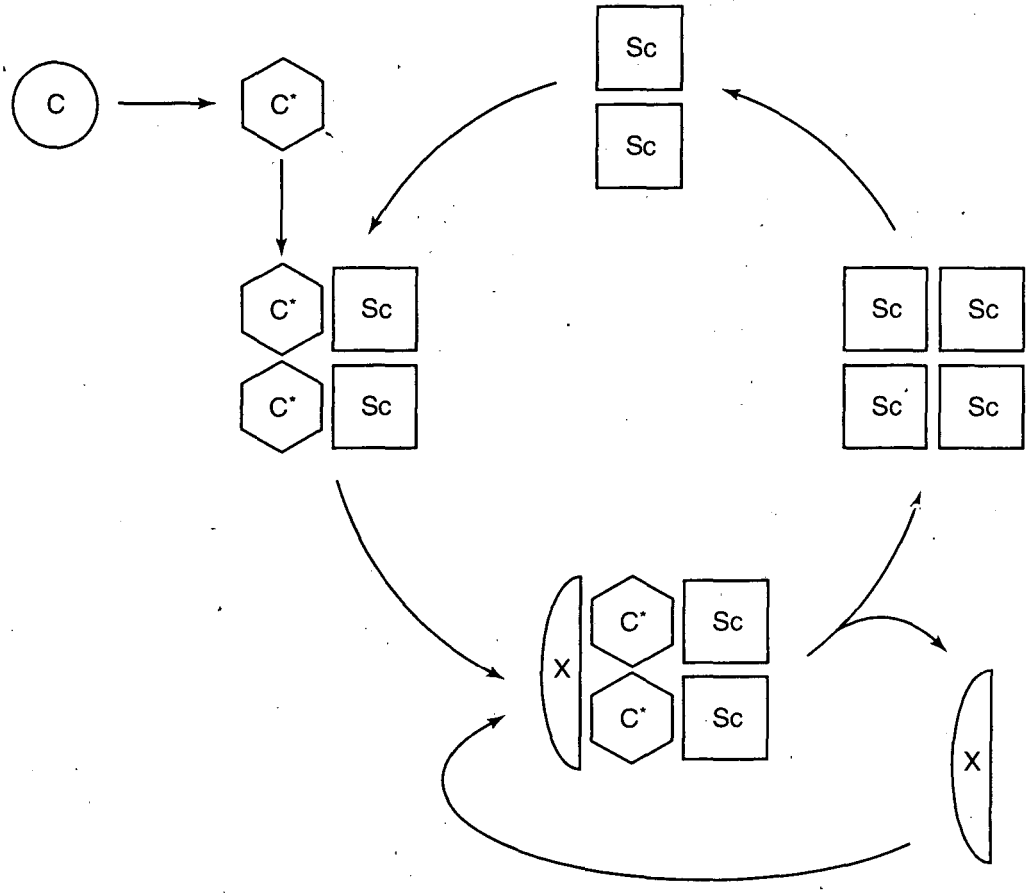

Figure 1.5: A current model for conversion of PrP^{C} into PrP^{Sc}. PrP^{C} transforms into an intermediate state PrP^{C*}, which can be bound by a multimeric form of PrP^{Sc}, shown here as a dimer. Protein X then binds the PrP^{C*}/PrP^{Sc} complex and PrP^{C*} is converted to PrP^{Sc}.

suggests that plaques are crystalline fibrils, giving some support to this hypothesis. However, some evidence exists suggesting that plaques are not necessary for disease[61].

Further evidence supporting and clarifying these models is necessary before these hypotheses can be universally accepted. The identity and role of protein X is an active research area. In 1994, a protease-resistant form of PrP was created *in vitro* starting from a partially denatured form of PrP^{C} using an excess of PrP^{Sc}[62]. Unfortunately, it was not possible to determine if the protease-resistant PrP formed was infectious, or if it was PrP^{Sc}. Such *in vitro* conversion of PrP^{C} to infectious PrP^{Sc} would lay to rest all doubts about the protein-only hypothesis.

1.9 The Role of Stuctural Biology in Understanding Prions

Knowledge of the structure of infectious PrP^{Sc} is vital for understanding prions. With a structure of PrP^{Sc}, it may become possible to understand how PrP molecules interact, how conversion of PrP^{C} to PrP^{Sc} occurs, which parts of PrP are necessary for conversion, how protein X interacts with PrP, what causes the species barrier, and what causes strains. It also becomes possible to design molecules that prevent conversion to PrP^{Sc} or prevent its harmful effects once it is made.

Unfortunately, few physical techniques are able to give atomic resolution information about a molecule that is not soluble and whose relevant state is non-crystalline. Because PrP^{Sc} is not soluble and because in its native state (i.e. in amyloid plaques) no three dimensional long-range order exists (although fibers appear ordered uniaxially), the two main tools for protein structure elucidation, x-ray crystallography and solution NMR,

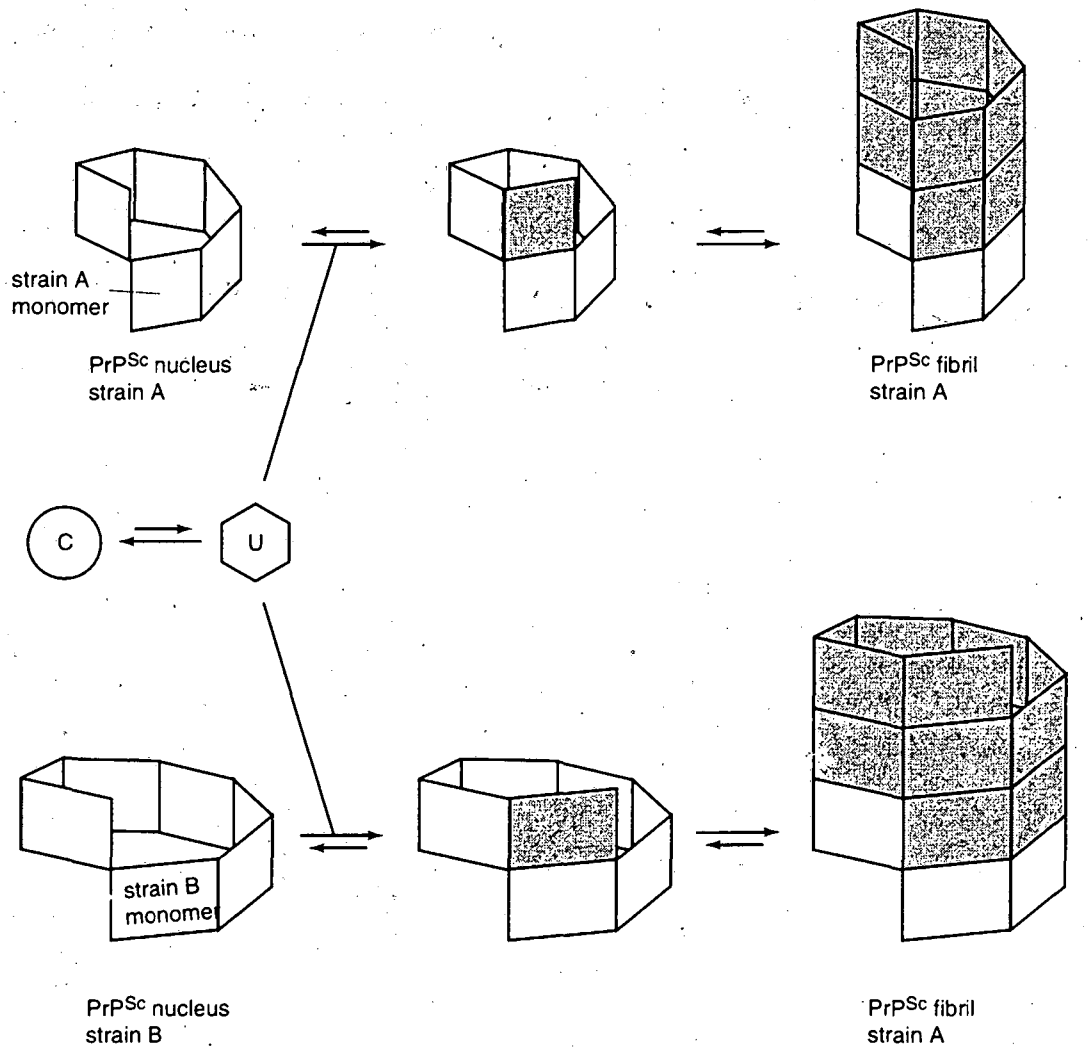

Figure 1.6: A current model for conversion of PrP^{C} into PrP^{Sc}. PrP^{C} unfolds partially before it is converted to PrP^{Sc} by a previously formed seed crystal of PrP^{Sc}. Strains exist due to different crystal forms of PrP^{Sc}. Each differently sized rectangle represents a monomer of a particular strain. The partially unfolded intermediate, U, attaches to the seed nucleus and eventually a fibril is formed.

can not be used. Thus, it becomes necessary to develop new techniques for studying PrP^{Sc}. Solid-State NMR (SSNMR) has the capability of gaining the information necessary for structure determination, but further technique development is necessary before this capability is realized. In chapter 2 of this introduction, SSNMR as a tool for protein structure determination is discussed in detail. In the rest of this thesis, new SSNMR techniques that I have developed are discussed, as are their application to peptides derived from prions.

References

(1) Gordon, W. S. *Vet. Rec.* **1946**, *58*, 516.
(2) Carr, K. *Nature* **1996**, *380*, 273-274.
(3) Hsiao, K.; Prusiner, S. B. *Neurology* **1990**, *40*, 1820-1827.
(4) Gajdusek, D. C.; Gibbs, D. J.; Alpers, M. *Nature* **1966**, *209*, 794.
(5) Masters, C. L.; Gadjusek, D. C.; Gibbs, C. J. *Brain* **1981**, *104*, 559-588.
(6) Fradkin, J. E.; Schonberger, L. B.; Mills, J. L.; Gunn, W. J.; Piper, J. M.; Wysowski, D. K.; Thomson, R.; Durako, S.; Brown, P. *J. Am. Med. Assoc.* **1991**, *265*, 880-884.
(7) Prusiner, S. B. *Science* **1982**, *216*, 136-144.
(8) M'Fadyean *J. Comp. Pathol.* **1918**, *31*, 102.
(9) Cho, H. J. *Nature* **1976**, *262*, 411.
(10) Gibbons, R. A.; Hunter, G. D. *Nature* **1967**, *215*, 1041.
(11) Diener, T. O. *Nature* **1972**, *235*, 218.
(12) Gajdusek, D. C. *Science* **1977**, *197*, 943.
(13) Latarjet, R.; Muel, B.; Haig, D. A.; Clarke, M. C.; Alper, T. *Nature* **1970**, *227*, 1341.
(14) Siakotos, A. N.; Raveed, D.; Longa, G. *J. Gen. Virol.* **1979**, *43*, 417.
(15) Marsh, R. F.; Malone, T. G.; Semancik, J. S. *Nature* **1978**, *275*, 146.
(16) Griffith, J. S. *Nature* **1967**, *215*, 1043.
(17) McKinley, M. P.; Bolton, D. C.; Prusiner, S. B. *Cell* **1983**, *35*, 57-62.
(18) Oesch, B.; Westaway, D.; Walchli, M.; McKinley, M. P.; Kent, S. B. H.; Aebersold, R.; Barry, R. A.; Tempst, P.; Teplow, D. B.; Hood, L. E.; Prusiner, S. B.; Weissmann, C. *Cell* **1985**, *40*, 735-746.
(19) Hope, J.; Morton, L. J.; Farquhar, C. F.; Multhaup, G.; Beyreuther, K.; Kimberlin, R. H. *EMBO J* **1986**, *5*, 2591-2597.
(20) Turk, E.; Teplow, D. B.; Hood, L. E.; Prusiner, S. B. *European Journal of Biochemistry* **1988**, *176*, 21-30.
(21) Stahl, N.; Borchelt, D. R.; Hsiao, L.; Prusiner, S. B. *Cell* **1987**, *51*, 229-240.
(22) Endo, T.; Groth, D.; Prusiner, S. B.; Kobata, A. *Biochemistry* **1989**, *28*, 8380-8388.
(23) Gabriel, J.-M.; al, e. *Proc. Natl. Acad. Sci. USA* **1992**, *89*, 9097.
(24) Schatzl, H. M.; DaCosta, M.; Taylor, L.; Cohen, F. E.; Prusiner, S. B. *J. Mol. Bio.* **1995**, *245*, 362-374.
(25) Bueler, H.; Fisher, M.; Lang, Y.; Bluethmann, H.; Lipp, H.-P.; DeArmond, S. J.; Prusiner, S. B.; Aguet, M.; Weissmann, C. *Nature* **1992**, *356*, 577-582.
(26) Collinge, J.; Whittington, M. A.; Sidle, K. C. L.; Smith, C. J.; Palmer, M. S.; Clarke, A. R.; Jeffreys, J. G. R. *Nature* **1994**, *370*, 295-297.
(27) Stahl, N.; Baldwin, M. A.; Teplow, D. B.; Hood, L.; Gibson, B. W.; Burlingame, A. L.; Prusiner, S. B. *Biochemistry* **1993**, *32*, 1991-2002.
(28) Borchelt, D. R.; Scott, M.; Taraboulos, A.; Stahl, N.; Prusiner, S. B. *J. Cell Biol.* **1990**, *110*, 743-752.

(29) Pan, K.-M.; Baldwin, M.; Nguyen, J.; Gasset, M.; Serban, A.; Groth, D.; Mehlhorn, I.; Huang, Z.; Fletterick, R. J.; Cohen, F. E.; Prusiner, S. B. *Proc. Natl. Acad. Sci. USA* **1993**, *90*, 10962-10966.
(30) Caughey, B. W.; Dong, A.; Bhat, K. S.; Ernst, D.; Hayes, S. F.; Caughey, W. S. *Biochemistry* **1991**, *30*, 7672-80.
(31) Hsiao, K.; Baker, H. F.; Crow, T. J.; Poulter, M.; Owen, F.; Terwilliger, J. D.; Westaway, D.; Ott, J.; Prusiner, S. B. *Nature* **1989**, *338*, 342-345.
(32) Poulter, M.; Baker, H. F.; Frith, C. D.; Leach, M.; Lofthouse, R.; Ridley, R. M.; Shah, T.; Owen, F.; Collinge, J.; Brown, G.; Hardy, J.; Mullan, M. J.; Harding, A. E.; Bennet, C.; Doshi, R.; Crow, T. J. *Brain* **1992**, *115*, 675-685.
(33) Goldfarb, L. G.; Mitrova, E.; Brown, P.; Toh, B. H.; Gajdusek, D. C. *Lancet* **1990**, *336*, 514-515.
(34) Goldfarb, L. G.; Haltia, M.; Brown, P.; Nieto, A.; Kovanen, J.; McCombie, W. R.; Trapp, S.; Gajdusek, D. C. *Lancet* **1991**, *337*, 425.
(35) Fink, J. K.; Warren, J. T.; Drury, I.; Murman, D.; Peacock, B. A. *Neurology* **1991**, *41*, 1647-1650.
(36) Medori, R.; Tritschler, H.-J.; LeBlanc, A.; Villare, F.; Manetto, V.; Chen, H. Y.; Xue, R.; Leal, S.; Montagna, P.; Cortelli, P.; Tinuper, P.; Avoni, P.; Mochi, M.; Baruzzi, A.; Hauw, J. J.; Ott, J.; Lugaresi, E.; Autilio-Gambetti, L.; Gambetti, P. *N. Engl. J. Med.* **1992**, *326*, 444-449.
(37) Doh-ura, K.; Tateishi, J.; Sasaki, H.; Kitamoto, T.; Sakaki, Y. *Biochem. Biophys Res. Commun.* **1989**, *163*, 974-979.
(38) Ghetti, B.; Tagliavini, F.; Masters, C. L.; Beyreuther, K.; Giaccone, G.; Verga, L.; Farlo, M. R.; Conneally, P. M.; Dlouhy, S. R.; Azzarelli, B.; Bugiani, O. *Neurology* **1989**, *39*, 1453-1461.
(39) Ikeda, S.; Yanagisawa, N.; Allsop, D.; Glenner, G. G. In *Amyloid and Amyloidosis*; J. B. Natvig, O. Forre, G. Husby, A. Husebekk, B. Skogen, K. Sletten and P. Westermark, Ed.; Kluwer Academic Publishers: Dordrecht, 1991; pp 737-740.
(40) Prusiner, S. B.; Groth, D.; Serban, A.; Koehler, R.; Foster, D.; Torchia, M.; Burton, D.; Yang, S. L.; DeArmond, S. J. *Proc. Natl. Acad. Sci. U.S.A.* **1993**, *90*, 10608-10612.
(41) Bueler, H.; Aguzzi, A.; Sailer, A.; Greiner, R. A.; Auenried, P.; Aguet, M.; Weismann, C. *Cell* **1993**, *73*, 1339-1347.
(42) Hsiao, K. K.; Scott, M.; Foster, D.; Groth, D. F.; DeArmond, S. J.; Prusiner, S. B. *Science* **1990**, *250*, 1587-1590.
(43) Prusiner, S. B. *Biochemisry* **1992**, *31*, 12277-12288.
(44) Prusiner, S. B.; Scott, M.; Foster, D.; Pan, K.-M.; Groth, D.; Mirenda, C.; Torchia, M.; Yang, S.-L.; Serban, D.; Carlson, G. A.; Hoppe, P. C.; Westaway, D.; DeArmond, S. J. *Cell* **1990**, *63*, 673-686.
(45) Telling, G. C.; Scott, M.; Mastrianni, J.; Gabizon, R.; Torchia, M.; Cohen, F. E.; DeArmond, S. J.; Prusiner, S. B. *Cell* **1995**, *63*, 79-90.
(46) Dickinson, A. G.; Meikle, V. M. H.; Fraser, H. *J. Comp. Pathol.* **1968**, *78*, 293-299.

(47) Bruce, M. E.; McBride, P. A.; Farquhar, C. F. *Neurosci. Lett.* **1989**, *102*, 1-6.
(48) DeArmond, S. J.; Yang, S.-L.; Lee, A.; Bowler, R.; Taraboulos, A.; Groth, D.; Prusiner, S. B. *Proc. Natl. Acad. Sci. USA* **1993**, *90*, 6449-6453.
(49) Bessen, R. A.; Kocisko, D. A.; Raymond, G. J.; Nandan, S.; Lansbury, P. T.; Caughey, B. *Nature* **1995**, *375*, 698-700.
(50) Gasset, M.; Baldwin, M. A.; Lloyd, D.; Gabriel, J.-M.; Holtzman, D. M.; Cohen, F.; Gletterick, R.; Prussiner, S. B. *Proc. Natl. Acad. Sci. USA* **1992**, *89*, 10940-10944.
(51) Huang, Z.; Gabriel, J.-M.; Baldwin, M. A.; Fletterick, R. J.; Prusiner, S. B.; Cohen, F. E. *Proc. Natl. Acad. Sci. USA* **1994**, *91*, 7139-7143.
(52) Huang, Z.; Prusiner, S. B.; Cohen, F. E. *Folding & Design* **1996**, *1*, 13-19.
(53) Zhang, H.; Kaneko, K.; Nguyen, J. T.; Livshits, T. L.; Baldwin, M. A.; Cohen, F. E.; James, T. L.; Prusiner, S. B. *J. Mol. Bio.* **1995**, *250*, 514-526.
(54) Nguyen, J.; Baldwin, M. A.; Cohen, F. E.; Prusiner, S. B. *Biochemistry* **1995**, *34*, 4186-4192.
(55) Kitamoto, T.; Iizuka, R.; Tateishi, J. *Biochem. Biophys. Res. Commun.* **1993**, *192*, 525-531.
(56) Tagliavini, F.; Prelli, F.; Ghisto, J.; Bugiani, O.; Serban, D.; Prusiner, S. B.; Farlow, M. R.; Ghetti, B.; Frangione, B. *EMBO J.* **1991**, *10*, 513-519.
(57) Brown, D. R.; Schmidt, B.; Kretzschmar, H. A. *Nature* **1996**, *380*, 345-347.
(58) Mehlhorn, I.; Groth, D.; Stockel, J.; Moffat, B.; Reilly, D.; Yansura, D.; Willett, S.; Baldwin, M.; Fletterick, R.; Cohen, F. E.; Vandlen, R.; Henner, D.; Prusiner, S. B. *Biochemistry* **1996**, *35*, 5528-5537.
(59) Riek, R.; Hornemann, S.; Wider, G.; Billeter, M.; Glockshuber, R.; Wuthrich, K. *Nature* **1996**, *382*, 180-182.
(60) Lansbury Jr., P. T.; Caughey, B. *Chemistry & Biology* **1995**, *2*, 1-5.
(61) Lasmezas, C. I.; Deslys, J. P.; Roabin, O.; Jaegly, A.; Beringue, V.; Peyrin, J. M.; Fournier, J. G.; Hauw, J. J.; Rossier, J.; Dormont, D. *Nature* **1997**, *275*, 402-405.
(62) Kocisko, D. A.; Come, J. H.; Priola, S. A.; Chesebro, B.; Raymond, G. J.; Lansbury, P. T.; Caughey, B. *Nature* **1994**, *370*, 471-474.

Chapter 2

Solid-State Nuclear Magnetic Resonance in Structural Biology

X-ray crystallography and solution NMR have developed into the most important tools for both protein and nucleic acid high-resolution structure determination. Unfortunately, both these tools also have limitations. X-ray diffraction can be applied only to those systems that can be crystallized, and whose conformation of interest is unaffected by the process of crystallization. Solution-state NMR studies are limited to small systems (~30 kDa or less) that are highly soluble (~1 mM). Thus, certain classes of proteins have for the most part evaded high-resolution structural studies.

As described in chapter 1, the plaques of amyloidogenic proteins are insoluble aggregates containing no long-range three-dimensional order. Thus, they are not amenable to either X-ray diffraction or solution NMR. Because of these limitations, there is need for another physical technique for high-resolution structure determination - one that can be applied to large, insoluble and non-crystalline systems. Recently, solid-state NMR (SSNMR) has started making progress towards meeting this demand. Although the ability to solve a high-resolution structure of an interesting biological system is still beyond its reach, over the past several years many tools have been developed to measure distances and dihedral angles. This introduction is meant to review these techniques and discuss current limitations.

2.1 Comparison of SSNMR with solution NMR structural techniques

Since the mid-1980's solution NMR has been used for protein and nucleic acid high-resolution structure determination, but the methods it employs are not applicable in SSNMR. An analysis of why this is true is helpful in understanding the tools SSNMR needs to develop in order to be able to solve structures at high resolution.

To solve a structure by solution NMR, a two step process similar to the following must be employed[1-3]. First, one carries out experiments that help assign all resonances. These experiments, like COSY[4,5] and TOCSY[6,7], give information on through-bond connections by using J-couplings between bonded nuclei to transfer magnetization and establish correlations. For small proteins whose spectra are sufficiently dispersed, two-dimensional experiments, in which proton resonances are correlated and detected, are sufficient. Because proton linewidths are on the order of 0.01 ppm, and protons resonate in approximately a 10 ppm range, many resonances can be distinguished easily and proteins containing on the order of 100 residues or less can be analyzed this way. In addition, the long T_2 relaxation times make it possible to let magnetization remain in the x-y plane for extended periods of time, allowing good magnetization exchange. For larger systems or systems with significant spectral overlap, it is necessary to use three-dimensional experiments and to assign the ^{15}N and ^{13}C resonances as well, and these techniques are now well established[3].

The second step in solving a structure is to acquire through-space distance information, through NOESY[8] experiments, and dihedral angle measurements, with J-coupling data[9-13]. The NOE uses dipolar couplings between nuclei of interest to transfer magnetization through a cross-

relaxation process, and thus the intensity of the NOE is inversely proportional to the internuclear distance to the sixth power. Once assignments have been done, NOESY cross-peak intensities are measured and distances extracted. J-couplings have been empirically correlated to dihedral angles, so measurements of J-couplings and use of the Karplus curve give bounds on dihedral angles. These distances and angles are used to calculate structures.

In SSNMR the process described above is not possible due to the nature of molecules in the solid state. All the differences between the two techniques stem from one very basic difference: in solids there is little motion because molecules are tightly packed, while in solution molecules are not tightly packed and therefore can tumble rapidly. The implications of this difference are shown in table 2.1.

In a static solid sample, the anisotropic interactions, i.e. those that depend on the orientation of the molecule with respect to the magnetic field, are important, while in solution they are averaged to zero. Specifically, the dipolar coupling and the chemical-shift anisotropy are present, and therefore, for systems other than single crystals, resonance lines are broad. This is a source of difficulty in SSNMR.

Because of the tight packing, distances between molecules are small and protons from one molecule are extensively dipolar coupled to protons from both the same molecule and neighboring molecules. This leads to very short T_2 relaxation times and excessive broadening, which changes the proton from being a detectable, resolvable, high-sensitivity nucleus to being a nucleus that must be decoupled to gain information about the system of interest. Proton spectra of non-crystalline samples, both static and under

Table 2.1: A comparison of Solution NMR and Solid-State NMR

Solution NMR	Solid-State NMR
solute molecules far apart on average, so intermolecular proton-proton distances long	molecules tightly packed, so intermolecular proton-proton distances short
anisotropic interactions (dipolar and chemical shift) averaged by fast molecular tumbling; information is lost but resonances are sharp	anisotropic interactions not averaged naturally; in static samples lines are broad, but no information is lost. magic-angle spinning necessary to obtain sharp resonances, leading to a loss of information.
protons detected; high sensitivity	due to dipolar couplings and CSA, protons excessively broadened, can not be observed, must be decoupled; lower sensitivity
favorable relaxation times: proton T_1 ~ 3 s proton T_2 ~ 2 s	unfavorable relaxation times: carbon T_1 ~ 30 s carbon T_2 ~ 10 ms
observed linewidths narrow (~ 0.1 ppm for proton)	observed linewidths broad (~ 1 ppm for carbon with MAS)
COSY type experiments used to assign resonances	T_2 relaxation times too short for COSY experiments
all internuclear distances can be measured in single NOESY experiment	distances must be measured pairwise; many specifically labeled samples and many experiments necessary
measurement of J-couplings gives dihedral angles via Karplus curve	J-couplings difficult to measure, other techniques must be used to measure dihedral angles
uniform labeling advantageous	selective labeling necessary

currently obtainable magic-angle-spinning (MAS) conditions[14-16], with few exceptions (i.e. unless a rare spin is used as a filter and homonuclear decoupling is used), are broad, featureless and uninformative. Whereas in solution NMR, most experiments start with magnetization on protons and

detect protons, in SSNMR protons can only be used as a source of magnetization (through cross-polarization[17]) for the enhancement of the signals of rare nuclei. The same is true for any abundant spin: excessive broadening due to dipolar coupling and CSA leads to severe spectral overlap. Thus, uniform ^{13}C and/or ^{15}N labeling is not useful either. It is a paradox that due to the higher amount of information present, the overall information content of spectra of abundant spins is reduced.

The samples used for solid-state NMR experiments must be carefully selected. A peptide can be isotopically labeled at several positions, but the resonances of these selected labels can not overlap. If they do, a technique like a double-quantum filter must be used to observe only the resonances due to the label of interest. Generally, it is best to use either chemically synthesized peptides, with specific labels introduced, or recombinant peptides, in which all residues of a given type, i.e. all alanines, are labeled. As will be discussed in the next sections, under MAS conditions, dipolar couplings and CSA tensors are ideally fully averaged, narrowing the lines.

However, even when ^{13}C or ^{15}N isotopes are used in conjunction with MAS, broad lines are observed in comparison to solution NMR. As will be discussed, this is due to incomplete averaging of dipolar couplings (both homonuclear and heteronuclear), incomplete averaging of the CSA, and/or inhomogeneity in the solid sample . For example all α-carbons (C_α) in a protein resonate within a 15 ppm range, and observed linewidths are on the order of 1 ppm under favorable conditions. Thus, only a small number of resonances may be labeled simultaneously.

Additional complications exist in solids, making solution techniques useless. The techniques used for assignments rely on J-couplings and thus

leave magnetization in the x-y plane for extended periods of time. Although some recent high-speed spinning results have been shown that COSY-type crosspeaks are observable, generally in solids T_2 relaxation times are too short to allow this; all magnetization relaxes before it transferred to coupled nuclei. Thus, COSY-type techniques are not generally useful in solids. The NOE relies on fluctuations in the dipolar Hamiltonian whose spectral density matches the frequency of the zero-quantum transitions (the difference between the two Larmor frequencies). The random tumbling of molecules in solution and internal motion in proteins provides these fluctuations. In solids, there is little motion, so these fluctuations do not occur and the main mechanism by which one gets NOE enhancement is not available. Lastly, broad lines in solids prevent measurement of J-couplings, thus no information on dihedral angles can be gained in this manner. Typical solid linewidths are on the order of 1 ppm, while J-couplings of interest are an order of magnitude smaller.

Thus, in solids, useful information can only be gained from rare spins, there is no general method available for assigning resonances, no general distance measurement technique, and no simple torsion angle measurement technique. However, a variety of techniques have been developed to measure specific distances and dihedral angles. The rest of this introduction deals with these techniques and their applications.

2.2 Introduction to Solid State NMR interactions and experiments

Static solid-state spectra inherently contain information on the dipolar couplings between nuclei and about the chemical-shift anisotropy and, thus, linewidths are broad. In order to be able to observe more than one resonance

in a chemical-shift region, one needs to average the CSA to its isotropic value. In doing so the dipolar coupling is also averaged to zero, leading to a loss of information.

2.2.1 The dipolar coupling

A spin 1/2 nucleus behaves as a small magnet and therefore generates a local magnetic field. This magnetic field can affect neighboring nuclei, in a manner similar to two interacting bar magnets. This through-space interaction between nuclei is called a dipolar interaction.

The dipolar coupling can be represented by a second rank tensor whose Hamiltonian can be written mathematically as:

$$\hat{\mathbf{H}}_{dd} = \frac{\mu_0 \gamma_1 \gamma_2}{4\pi}\left(\frac{h}{2\pi}\right)^2 \hat{I}_1 \bullet \hat{\hat{D}} \bullet \hat{I}_2.$$

This can be expanded using the definition of $\hat{\hat{D}}$, the dipolar tensor, to give:

$$\hat{\mathbf{H}}_{dd} = \frac{\mu_0 \gamma_1 \gamma_2}{4\pi r^3}\left(\frac{h}{2\pi}\right)^2 \left[3(\hat{I}_1 \bullet \hat{r}/r)(\hat{I}_2 \bullet \hat{r}/r) - \hat{I}_1 \bullet \hat{I}_2\right]$$

or, again expanding the dot products[18]:

$$\hat{\mathbf{H}}_{dd} = \frac{\mu_0 \gamma_1 \gamma_2}{4\pi r^3}\left(\frac{h}{2\pi}\right)^2 [A + B + C + D + E + F]$$

$$A = -\hat{I}_{1z}\hat{I}_{2z}\left(3\cos^2\vartheta - 1\right)$$

$$B = \frac{1}{4}\left[\hat{I}_{1+}\hat{I}_{2-} + \hat{I}_{1-}\hat{I}_{2+}\right]\left(3\cos^2\vartheta - 1\right)$$

$$C = -\frac{3}{2}\left[\hat{I}_{1z}\hat{I}_{2+} + \hat{I}_{1+}\hat{I}_{2z}\right]\sin\vartheta\cos\vartheta e^{-i\phi}$$

$$D = -\frac{3}{2}\left[\hat{I}_{1z}\hat{I}_{2-} + \hat{I}_{1-}\hat{I}_{2z}\right]\sin\vartheta\cos\vartheta e^{i\phi}$$

$$E = -\frac{3}{4}\hat{I}_{1+}\hat{I}_{2+}\sin^2\vartheta e^{-2i\phi}$$

$$F = -\frac{3}{4}\hat{I}_{1-}\hat{I}_{2-}\sin^2\vartheta e^{2i\phi}$$

where μ_0 is the permeability constant, γ_1 and γ_2 are the gyromagnetic ratios of the two coupled spins, h is Planck's constant, r is the distance between the

two coupled spins, and ϑ and ϕ are two Euler angles that define the orientation of the internuclear vector with respect to the magnetic field (figure 2.1). $\hat{I}_{1z}$ and $\hat{I}_{2z}$ are the spin angular-momentum operators parallel to the static magnetic field ($\hat{B}_0$) for the two spins, while $\hat{I}_{1+}$, $\hat{I}_{2+}$, $\hat{I}_{1-}$, and $\hat{I}_{2-}$ are the raising and lowering operators for the two spins, defined as

$$\hat{I}_+ = \hat{I}_x + i\hat{I}_y \quad \text{and} \quad \hat{I}_- = \hat{I}_x - i\hat{I}_y ,$$

where $\hat{I}_x$ and $\hat{I}_y$ are the spin angular momentum operators perpendicular to the static magnetic field.

If the dipolar interaction is weak with respect to the static magnetic field, the dipolar Hamiltonian can be truncated. The truncated heteronuclear dipolar coupling can be represented by the equation above with only the A term, while the truncated homonuclear dipolar coupling can be represented with terms A and B. Term B is known as the flip-flop term. In most cases only these terms are considered.

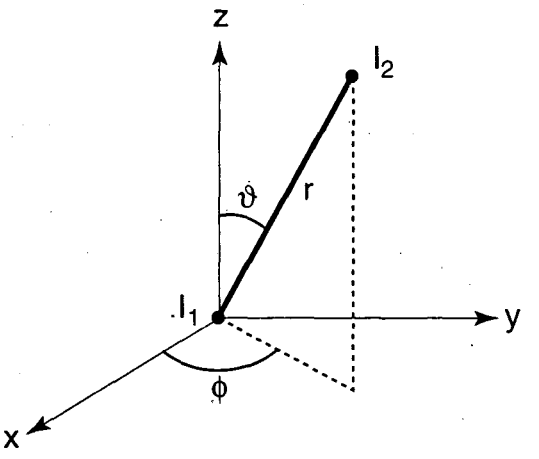

Figure 2.1: Definition of geometry for the dipole-dipole interaction of nuclei.

2.2.2 The chemical-shift anisotropy

A nucleus experiences shielding from the static magnetic field as a result of the electron cloud around that nucleus, an effect called the chemical shift. There is no *a priori* reason for this electron cloud to be isotropic. Different bonding arrangements distribute electrons differently around a nucleus. The anisotropic electron distribution, except in cases in which cubic symmetry is present, leads to an anisotropic shielding of the nucleus, and hence to chemical-shift anisotropy (CSA). For example, in a ^{13}C=O moeity, the electrons between the carbon and oxygen are pulled in the direction of the bond, leaving the sides perpendicular to the bond more susceptible to the B_0.

The CSA can also be represented by a second rank tensor whose Hamiltonian can be represented as follows:

$$\hat{\mathbf{H}}_{cs} = \gamma \frac{h}{2\pi} \hat{I} \bullet \hat{\hat{\sigma}} \bullet \hat{B}_0$$

where $\hat{\hat{\sigma}}$ represents the chemical-shift tensor. If the chemical shielding is weak with respect to the static magnetic field, the truncated expression for the chemical shielding becomes

$$\hat{\mathbf{H}}_{cs} = \gamma \frac{h}{2\pi} I_z \sigma_{zz} B_0$$

where

$$\sigma_{zz} = \sigma_{11} \sin^2 \vartheta \cos^2 \phi + \sigma_{22} \sin^2 \vartheta \sin^2 \phi + \sigma_{33} \cos^2 \vartheta \, .$$

σ_{11}, σ_{22}, and σ_{33} are the principal values of $\hat{\hat{\sigma}}$, and the angles ϑ and ϕ describe the orientation of $\hat{B}_0$ in the principal axis system (PAS), i.e the coordinate system in which the matrix representation of the tensor is diagonal. By introducing the isotropic shift as one-third the trace of the CSA tensor,

$$\sigma_{iso} = \frac{1}{3} Tr(\hat{\hat{\sigma}}) \, ,$$

and representing the new traceless principal values as

$$\sigma'_{11} = \sigma_{11} - \sigma_{iso}$$
$$\sigma'_{22} = \sigma_{22} - \sigma_{iso} \ ,$$
$$\sigma'_{33} = \sigma_{33} - \sigma_{iso}$$

(using $\sigma'_{22} = \sigma'_{11} + \sigma'_{22} - \sigma'_{11}$, $2\sigma'_{11} = -\sigma'_{33} - \sigma'_{22} + \sigma'_{11}$, and $(2\sin^2\phi - 1) = -\cos 2\phi$) the expression above for σ_{zz} can be rewritten as

$$\sigma_{zz} = \frac{1}{2}\left[\sigma'_{33}\left(3\cos^2\vartheta - 1\right) - \left(\sigma'_{22} - \sigma'_{11}\right)\sin^2\vartheta\cos 2\phi\right].$$

In a powdered sample, ϕ can take on any value and thus the last term of the expression above is averaged to zero, since the average over all angles of $\cos 2\phi$ is zero.

2.2.3 Magic-angle spinning

To obtain sharp lines in SSNMR and obtain "solution-like" spectra, MAS can be employed. Sample spinning simply involves rotating a sample around an axis at a given angle to B_0. By spinning at a certain angle with respect to B_0, the information lost due to spectral overlap can be regained.

MAS[14-16] averages the CSA and dipolar tensors, since the truncated forms of both have a $3\cos^2\vartheta - 1$ dependence. In the case of the dipolar interaction, ϑ represents the angle between the internuclear vector and the magnetic field, while in the case of the CSA, it represents the first Euler angle that rotates the PAS coordinate frame into the laboratory coordinate frame. In these cases, it can be shown[18] that

$$\left\langle 3\cos^2\vartheta - 1\right\rangle = \frac{1}{2}\left(3\cos^2\beta - 1\right)\left(3\cos^2\chi - 1\right)$$

where $\langle\ \rangle$ represents an average over time as the rotor spins, β represents the angle between the axis of rotation and $\hat{B}_0$, and χ represents the angle between the axis of rotation and internuclear vector or an axis of the PAS (figure 2.2). Clearly, β may be chosen such that $\left(3\cos^2\beta - 1\right) = 0$, thus making the average

of $\langle 3\cos^2\vartheta - 1\rangle$ zero. This angle, $\cos^{-1}(\sqrt{1/3})$ or 54.7°, is known as the magic angle. Both the dipolar and chemical-shift interactions are averaged to zero when a rotor is spun around an axis at this angle with respect to the magnetic field, narrowing the observed resonance lines.

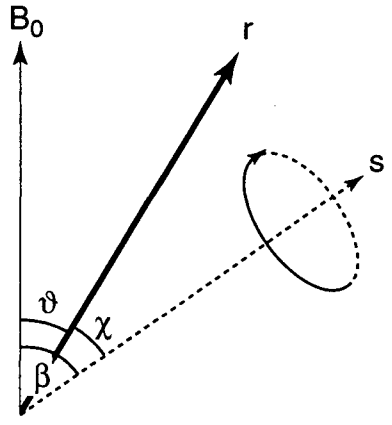

Figure 2.2: Geometry in a spinning experiment. The rotor rotates around the axis labeled s, at an angle β with respect to the static magnetic field, B_0. The internuclear vector, r, makes an angle ϑ with respect to B_0, and the angle χ is the angle between r and s.

Figure 2.3 shows static spectra that would result from a measurement of a dipolar coupling alone and several chemical-shift principal values alone. When a rotor is spun at the magic angle at speeds fast compared to an interaction frequency (i.e. the dipolar coupling expressed in Hertz or the chemical-shift anisotropy expressed in Hertz), the spectra simplify greatly, and only a single sharp resonance line is observed at the isotropic shift. However

when a rotor is spun at the magic angle at speeds slow compared to an interaction frequency, the spectra will split into spinning sidebands. The centerband is located at the isotropic shift and resonance lines will be spaced at multiples of the rotor frequency away from it. This is explained as follows. Because the chemical-shift Hamiltonian commutes with itself at different orientations of the rotor, the chemical shift is averaged out after each full rotor period[19]. As a result of this refocussing of the chemical shift, the time domain signal is periodic with a period of τ_r, the rotor period, and "rotational echoes" are observed. The frequency domain signal contains spectral intensity at $n2\pi/\tau_r$, spinning sidebands. This analysis holds for a isolated dipole-dipole pair with no chemical-shift interaction as well, because the Hamiltonian commutes with itself at all orientations of the rotor. However for more complicated situations, for example for two coupled spins with different chemical shifts, the situation is more complicated because the Hamiltonian does not commute with itself at all times. The "second averaging"[20] of the dipolar Hamiltonian (i.e. the effective truncation of the dipolar Hamiltonian in the presence of the stronger chemical-shift Hamiltonians) effectively allows the Hamiltonian to commute with itself and leads to the refocussing of the time domain signal and thus to spinning sidebands in the frequency domain. This is true as long as the rotor frequency is not equal to the difference in the isotropic shifts of the two spins, a situation known as rotational resonance, which will be dealt with later.

MAS can not be used to average the strong dipolar couplings found between abundant spins, such as protons. Decoupling by MAS requires spinning speeds much greater than the dipolar coupling. Since these couplings are on the order of 30 kHz and typical spinning speeds currently

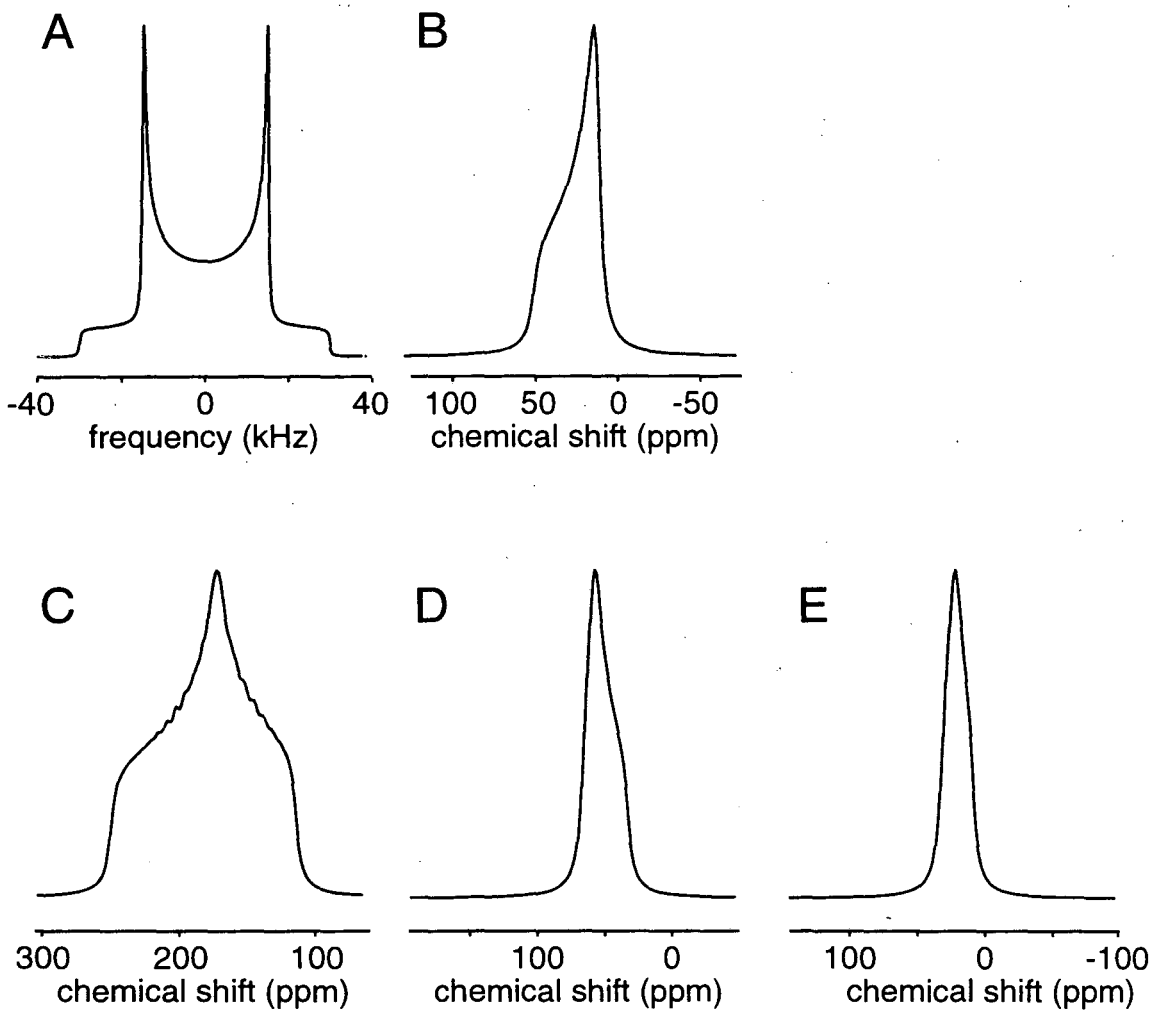

Figure 2.3: Simulations of static dipolar spectra and chemical-shift anisotropy spectra. (A) A dipolar coupling of 30 kHz, typical of the coupling between a ^{13}C and bonded ^{1}H. (B) An axially symmetric chemical-shift anisotropy, with σ_{11} = -12.5 ppm, σ_{22} = -12.5 ppm, σ_{33} = 25 ppm. (C) The CSA of the C=O in L-alanine, with σ_{11} = 243 ppm, σ_{22} =184 ppm, σ_{33} = 107 ppm. (D) The CSA of the C_α in L-alanine, with σ_{11} = 65 ppm, σ_{22} = 57 ppm, σ_{33} = 32 ppm. (E) The CSA of the CH_3 in L-alanine, assuming no rotation, with σ_{11} = 31 ppm, σ_{22} = 22 ppm, σ_{33} = 8 ppm. All spectra were the Fourier transforms of simulated free-induction decays which were exponentially broadened by 500 Hz.

attainable are only on the order of 15 kHz, it is not possible to average the couplings and MAS spectra of abundant spins are broadened by the presence of these couplings.

Thus, for dilute spins, fast MAS can be used to greatly simplify spectra, making them "solution-like". Slow spinning at the magic angle allows the retention of dipolar and CSA information while narrowing lines and increasing resolution. For abundant spins, other decoupling techniques must be used.

2.2.4 Cross polarization

Cross-polarization[17] is a method of enhancing X nuclei magnetization by transferring magnetization from ^{1}H nuclei, which have higher gyromagnetic ratios and relax faster. A 90° radio-frequency (rf) pulse (in the x-direction, for example) on protons moves proton magnetization to the x-y plane (in the -y-direction), and the protons are then spin-locked (i.e. continuously irradiated along the y-direction of the rotating frame). Simultaneous with the proton spin-lock, the X nuclei rf is switched on. The amplitude of the $\hat{B}_1$ fields created by the rf must be set such that

$$\gamma_H \hat{B}_1^H = \gamma_X \hat{B}_1^X ,$$

a condition known as the Hartmann-Hahn matching condition[21]. When the fields are matched in this way, the protons and X nuclei precess at the same rates in their respective rotating frames, and thus have matching energy levels. This allows transfer of magnetization between them, induced by the flip-flop term of the dipolar Hamiltonian.

Thermodynamics can be used to explain this magnetization transfer[17,18]. The Curie Law gives an expression for the equilibrium magnetization on protons in the laboratory frame:

$$M_0(H) = \frac{C_H B_0}{T_L},$$

where $M_0(H)$ is the magnetization on protons, T_L is the temperature of the lattice (with which the protons are at equilibrium), and

$$C_H = \frac{1}{4}\left(\frac{h}{2\pi}\right)^2 \frac{\gamma_H^2 N_H}{k}.$$

N_H represents the number of proton spins and k is Boltzmann's constant. This magnetization gives an energy of

$$E_0(H) = \frac{C_H (B_0)^2}{T_L},$$

since $E = M \times B$.

When the 90° rf pulse moves magnetization into the x-y plane and the spin-lock is applied, the system is no longer in equilibrium, but instead, $B_0 >> B_1^H$. The spin temperature in the rotating frame, T_S, can be found by solving

$$\frac{C_H B_0}{T_L} = \frac{C_H B_1^H}{T_S}.$$

At this point the protons are at a very low temperature, but the X nucleus has no magnetization in the rotating frame. Once magnetization starts being transferred, a new energy equilibrium is reached. The proton spin energy is $-\frac{C_H (B_1^H)^2}{T_S}$, and at equilibrium,

$$\frac{C_H (B_1^H)^2}{T_S} = \frac{C_H (B_1^H)^2 + C_X (B_1^X)^2}{T_S'}.$$

Since protons are abundant while X nuclei are rare, $C_H >> C_X$, so $T_S' \approx T_S$. Thus, the resulting magnetization on the X nuclei is

$$M(X) = \frac{C_X B_1^X}{T_S'} \approx \frac{C_X B_1^X}{T_S}.$$

Under the Hartmann-Hahn condition, $\gamma_H \hat{B}_1^H = \gamma_X \hat{B}_1^X$, and substituting for T_S,

$$M(X) = C_X \left(\frac{\gamma_H}{\gamma_X} \right) \frac{B_0}{T_L},$$

which is a factor of γ_H / γ_X greater than equilibrium magnetization for the X nucleus.

There are two main advantages of CP. First, because X nuclei have a lower γ than protons, there is an enhancement of magnetization on the order of γ_H / γ_X. The second advantage is due to the fact that X nuclei generally have much longer T_1 relaxation times than protons. Because magnetization starts on protons in CP, only protons must relax before starting the next experiment. Because ^{1}H T_1's are on the order of one second while carbon T_1's can be on the order of 30 seconds, a substantial time savings is gained. Thus, higher sensitivity experiments can be repeated more frequently when using CP.

2.2.5 Continuous wave proton decoupling

As was pointed out earlier, the presence of protons in solids leads to excessive broadening and therefore they must be decoupled. This is generally accomplished with continuous-wave (cw) decoupling, although new techniques have been developed recently that are more efficient[22].

Continuous proton irradiation serves to decouple the protons from the X nuclei. The heteronuclear dipolar couplings (^{1}H-X) are averaged to zero, and X nuclei can be observed without this interaction. The truncated heteronuclear dipolar coupling (term A in the expression for the dipolar coupling given above) can be inverted with a 180° rf pulse on either spin ($\hat{I}_z$

-> $-\hat{I}_z$, while $\hat{S}_z$, the X spin angular momentum, remains unchanged). Cw decoupling with constant phase functions by causing the magnetization (in the rotating frame) to precess around the axis of irradiation. For example, if the protons are irradiated with an applied rf field, $\hat{B}_1$, in the y-direction, the proton spins move from the +z direction through the x, -z, and -x directions back to +z. As the irradiation causes the proton magnetization to rotate, it averages the heteronuclear dipolar coupling to zero at the end of each cycle. The frequency with which magnetization rotates must be faster than frequency of the coupling it is averaging and, in addition, must also be faster than the proton-proton homonuclear couplings to effectively average the heteronuclear couplings to zero and narrow the resonance lines. Thus, high power irradiation is necessary.

2.2.6 The CPMAS experiment

The basic SSNMR experiment, which can be used as a building block for more complicated experiments or used by itself to gain useful information, is depicted in figure 2.4. The experiment is composed of the three components discussed above, cross-polarization (CP), MAS, and proton decoupling, and is known as CPMAS with proton decoupling, or just CPMAS, proton decoupling being assumed. While spinning at the magic angle, the larger magnetization of protons is transferred to the X nucleus (usually ^{13}C in this thesis) by cross polarization and then the protons are irradiated continuously while the magnetization, now on the X nuclei, is detected.

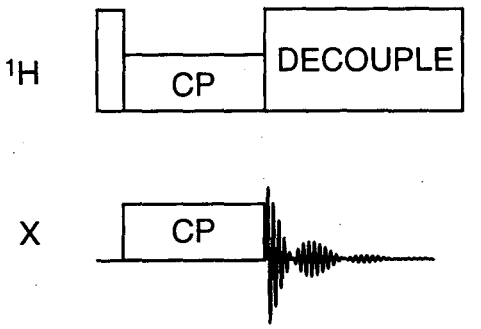

Figure 2.4: The cross-polarization experiment with ^1H decoupling. A 90° pulse brings ^1H magnetization into the x-y plane, where it is spin-locked. The X nuclei are spin-locked simultaneously, and if the Hartmann-Hahn matching condition, $\gamma_X \hat{B}_1^X = \gamma_H \hat{B}_1^H$, is met, cross-polarization takes place. High-power, continuous-wave proton decoupling is then switched on, and the X magnetization detected. This experiment, combined with magic-angle spinning, is the basic building block of most other SSNMR experiments, and is known as CPMAS.

2.3 Solid State NMR distance measurement techniques

Over the past ten years many techniques have been introduced that allow for a reintroduction of the dipolar coupling under MAS. In this section, those techniques that have been applied to biological systems will be reviewed. This is not meant to be a comprehensive review of all pulse sequences developed to measure dipolar couplings, but rather a review of those that have been applied to biomolecules.

Two main classes of dipolar recoupling techniques exist: those that drive magnetization exchange between coupled nuclei and those that dephase the dipolar coupling. Magnetization exchange between the nuclei can be driven by either rotor spinning (R^2) or radio-frequency pulses (RFDR). Both homonuclear and heteronuclear dephasing experiments have been devised. RF is used to dephase the dipolar coupling and prevent it from refocussing. Dephasing experiments that will be discussed are REDOR, TEDOR, DRAMA,

Table 2.2 A summary of distance-measurement techniques.

technique	interaction	advantages	limitations	applications	comments
R^2	homonuclear	selective; accurate; longitudinal mixing period	T_{2ZQ}, CSA orientations estimations necessary; inhomogeneity	refs. 28-33	$\Delta\omega_{iso}=n\omega_r$
RFDR	homonuclear	broadband; inhomogeneous lines not problematic; longitudinal mixing period	shift differences required; T_{2ZQ}, CSA orientations estimations necessary; weak couplings not observed	ref. 35	extension to mutliple spins possible, but not quantitative; one or two-dimensional
REDOR	heteronuclear	accurate; control experiment; π-pulse supercycles eliminate pulse imperfection issues	natural abundance problem; magnetization in transverse plane; non-selective; demanding in terms of hardware	refs. 46, 48-56, 58, 60	extension to mutliple spins possible, but not quantitative
TEDOR	heteronuclear	no natural abundance problem	double evolution required; no control experiment; magnetization in transverse plane; demanding in terms of hardware	refs. 47, 57	can be combined with REDOR
DRAMA	homonuclear	no isotropic shift difference required; no CSA tensor orientation dependence	broad CSA tensors and resonance offsets problematic; no $\pi/2$-pulse phase cycling; magnetization in transverse plane	refs. 59, 63	produces scaled powder patterns; one or two-dimensional
DRAWS	homonuclear	broad CSA tensors and resonant offsets not problematic; no CSA tensor orientation dependence	magnetization in transverse plane	ref. 65	

and DRAWS. Experiments and applications will be discussed, with emphasis on those that have been used extensively for distance measurements on biological systems. Table 2.2 summarizes the experiments that will be discussed.

2.3.1 Rotational Resonance (R^2)

When the spinning frequency under MAS is greater than the strength of a homonuclear coupling, the coupling is averaged to zero. Additionally, if isotropic chemical-shift difference, $\Delta\omega_{iso}$, between coupled spins is larger than the coupling strength, the flip-flop dipolar term can not contribute to energy exchange. An exception occurs when $\Delta\omega_{iso}$ is an integer multiple of the rotor frequency, ω_r, i.e. when

$$\Delta\omega_{iso} = n\omega_r,$$

a condition known as rotational resonance[23-25]. At this frequency, the rotor spinning energy matches the chemical-shift difference and the dipolar flip-flop term is reintroduced. For strongly coupled nuclei, a broadening and/or splitting of resonance lines can be observed. This phenomenon can be used to measure dipolar couplings when a non-equilibrium population is generated and the rate of magnetization exchange is monitored.

A simple pulse sequence for monitoring magnetization exchange between two spins I and S (a $^{13}C_\alpha$ and a $^{13}C{=}O$, for example) using R^2 is shown in figure 2.5. After cross-polarization, magnetization is returned to the z-direction. Then one spin, the I spin for example, is selectively inverted using either a long, weak rf pulse or a DANTE sequence[26]. This sets up the non-equilibrium population distribution. If the R^2 condition is met, magnetization exchange will occur during the subsequent variable mixing

period, τ. A $\pi/2$-pulse then returns magnetization to the x-y plane for detection. The rate of magnetization exchange can be determined the difference in signal intensities, $I_z - S_z$, as a function of τ. This rate can be compared with simulations and a distance can be derived. In the case of strong couplings, an oscillation in this difference magnetization is observed; the magnetization exchange will cause the populations to reverse, with the S spin inverting and the I spin returning towards its equilibrium direction. For weaker couplings, only a decay in this difference magnetization is observed. This is because of the dampening of the oscillations by relaxation.

The magnetization-exchange rate is a function of several parameters, all of which must be included to properly simulate the experiment and derive an accurate distance[23-25]. These parameters include the dipolar coupling

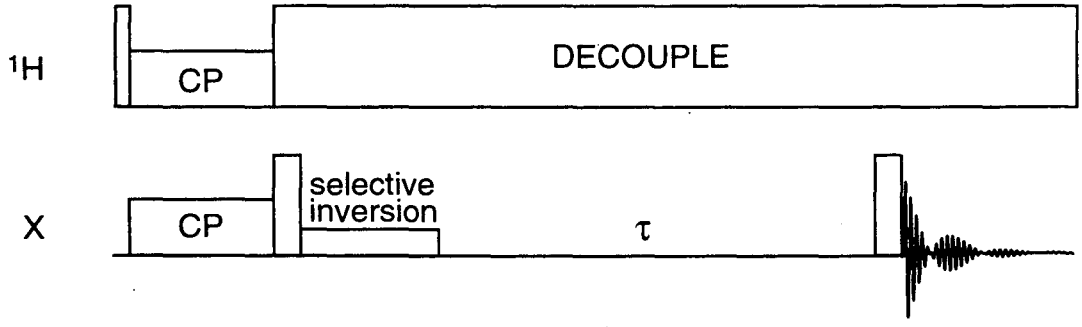

Figure 2.5: The rotational resonance (R^2) experiment. The entire experiment takes place under MAS, such that the difference in frequency at which the two spins of interest resonate is an integer multiple of the spinning speed. Protons are used for cross-polarization and are then decoupled for the remainder of the experiment. The X nuclei gain polarization from protons and are returned to the z-direction. One of the two spins is then selectively inverted, either by using a low power pulse or by using DANTE. The two spins evolve for a time τ, after which a $\pi/2$ pulse brings them back into the x-y plane for detection.

being measured, the chemical-shift tensor's principle values and relative orientation, the J-coupling between the nuclei of interest, the inhomogeneity of the observed resonances, and the zero-quantum relaxation time, T_2^{ZQ}. Some of these variables, for example the principle values of the CSA, are easily measured in other experiments. Others, like the relative orientations of the CSA tensors can be measured in rather difficult experiments, but are generally assumed based on studies of similar compounds. This assumption is generally not a source of large error since for low orders of R^2, i.e. n=1, magnetization exchange is not very sensitive to the relative orientations. For higher orders of R^2, this orientation dependence can be used to obtain dihedral angle information, as will be discussed below. It is not yet possible to measure the T_2^{ZQ}, and this number is typically estimated from the sum of the single-quantum T_2's[27]. The sources of zero-quantum relaxation are incomplete proton decoupling, molecular motion, and residual couplings to nearby nuclei.

The theory behind R^2 has been described in detail as a fictitious spin 1/2 system[25]. In this geometric description, the difference magnetization projects along the z-axis, while the Fourier components of the flip-flop term of the dipolar Hamiltonian project along the x-axis. The dipolar coupling term acts like an rf field and rotates the difference magnetization from +z to -y to -z to +y and back to +z. These oscillations, dampened by the T_2^{ZQ} relaxation, are observed.

Rotational resonance has been applied to several biomolecular systems. The original applications involved a study of the conformation of retinal bound to bacteriorhodopsin (bR), whose effective molecular weight in lipid is 85 kDa. Two conclusions were drawn. First, through introduction of two ^{13}C

labels into retinal, it was shown that the retinal is in the 6-s-*trans* configuration[28]. Second, by introduction of one ^{13}C label in retinal and one on the lysine sidechain that links it to bR, it was shown that the Schiff base linkage differs in two forms of dark-adapted bR[29]. In bR_{555} the bonding configuration was determined to be syn, while in bR_{568} it was determined to be anti. This information will help elucidate structural changes that bR undergoes during the photocycle and, therefore, how it functions as a proton pump.

Several studies of peptides within lipid bilayers have been carried out with R^2. First, it was shown that an 11-mer maintained its helical structure in a membrane environment[30]. Later, peptides corresponding to the transmembrane regions of glycophorin A in membranes were studied and the structure of the interface of the dimers was elucidated[31].

More recently, amyloid peptides have been under investigation. A model of a region of the β-Amyloid protein that is found in Alzheimer's disease plaques was generated based on distance constraints derived from R^2, confirming its antiparallel β-pleated sheet structure[32]. In a different study[33], a peptide derived from the human islet amyloid polypeptide (amylin) was studied. Six distances were measured and used to constrain backbone dihedral angles. Again, an antiparallel β-pleated sheet structure was observed. Additionally, intermolecular interactions gave information about the packing of the sheets to form fibrils.

The use of R^2 to determine dihedral angles by measurement of several key distances has been proposed[33]. Two distances limit the potential dihedral angles on a peptide backbone. The distance between $C_{\alpha,i}$ and C_{i+1}=O depends only on ϕ_{i+1}, if the peptide bond is assumed to be planar, while the distance

between C_i=O and $C_{\alpha,i+2}$ depends on ϕ_{i+1} and ψ_{i+1}. For symmetry reasons, it is impossible to limit solutions to one quadrant of Ramanchandran space. However, if these distances are measured accurately, the amount of Ramanchandran space available in each quadrant is greatly reduced. The use of these accurate distance constraints in combination with FTIR and measurements of isotropic chemical shifts, can be used to further limit Ramanchandran space by eliminating quadrants. However, the accuracy of R^2 may not be able to significantly reduce (ϕ,ψ) pairs. With an assumed accuracy of ±0.2 Å, a very favorable assumption, an accuracy of approximately ±20° in ϕ and ±40° in ψ can be achieved[33]. Although in this best case, (ϕ,ψ) solutions are limited, better NMR techniques that can be used to put tighter bounds on the torsion angles. If R^2 accuracy is lower, less accurate dihedral angle predictions would result.

2.3.2 Radio-Frequency Driven Dipolar Recoupling (RFDR)

RFDR[34] uses π-pulses during a longitudinal-mixing period, instead of using rotor spinning, to drive magnetization exchange among coupled spins. This is accomplished through the interference between the chemical-shift interactions and dipolar refocussing. The experiment can be performed in a one-dimensional or two-dimensional fashion. In the one-dimensional version, spectra are recorded as functions of the mixing time τ_m, as in R^2, and from the time dependence, a distance may be derived. The two-dimensional version gives cross-peaks for all spins that are coupled, although the intensities of the cross peaks are not necessarily quantitatively related to distances.

The two-dimensional RFDR pulse sequence is shown in figure 2.6. After CP, magnetization evolves during t_1 under proton decoupling. At the end of t_1, magnetization is returned to the z-direction and during the following mixing period, evolves under a single π-pulse per rotor period. The magnetization is then returned to the transverse plane for detection during t_2. It is important that the π-pulses used are not of an amplitude such that Hartmann-Hahn matching is achieved. If it is magnetization will be dissipated. π-pulses must also be phase cycled to compensate for pulse imperfections.

The Hamiltonian of interest during the mixing time includes terms for the chemical shift, the dipolar coupling, and the influence of the rf-pulses.

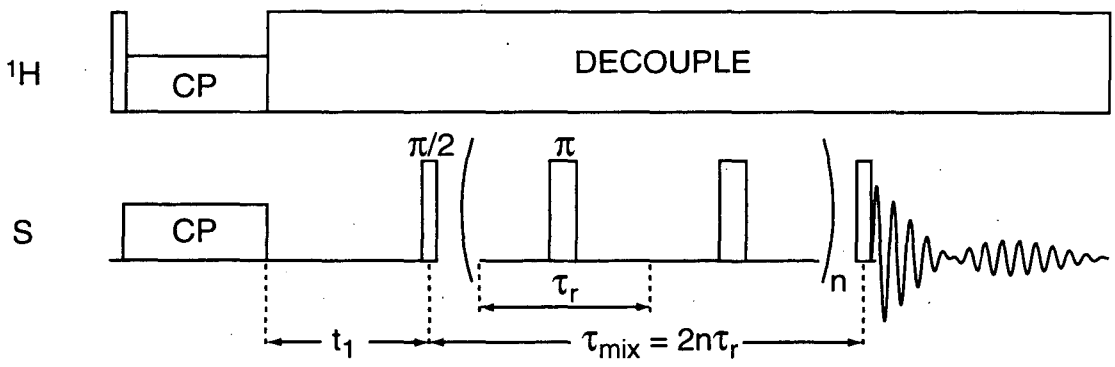

Figure 2.6: The radio-frequency driven dipolar recoupling (RFDR) 2D experiment. The entire experiment takes place under MAS. Protons are used for cross-polarization and then decoupled for the remainder of the experiment. The S spin gains polarization from protons, and evolves for a period t_1, after which it is returned to the z-direction. During the subsequent mixing period, which lasts an even multiple of rotor periods, one π-pulse is applied at the center of each rotor period. Before detection during t_2, a $\pi/2$-pulse returns magnetization to the transverse plane.

These interactions can be divided into those that commute with themselves at all times and those that do not. The term of interest does not commute with itself. It can be approximated using average Hamiltonian theory. Neglecting CSA, the zeroth order result for a two spin system is[34]

$$\hat{\mathbf{H}}_{dd}^{(0)} = -\frac{d}{2}[I_+S_- + I_-S_+]$$

where

$$d = \frac{2}{\pi}\sum_{m=1,2} d_{12,m}(\beta)\cos(m\alpha)\frac{\Delta\omega_{iso}/\omega_r}{m^2 - \left(\Delta\omega_{iso}/\omega_r\right)^2}(-1)^{m-1}\sin\left(\pi\Delta\omega_{iso}/\omega_r\right).$$

$d_{12,m}$ in this equation represents the flip-flop term prefactor (from term B of the dipolar coupling) and m is the index of the dipolar Fourier components. Thus the flip-flop term of the dipolar coupling is not averaged to zero by MAS when these π-pulses are performed on longitudinal magnetization. The rf drives magnetization transfer through this flip-flop term. Although this analysis was carried out for a spin pair, magnetization transfer also occurs for a multi-spin system.

Thus, RFDR can recover the dipolar coupling without relying on rotor speed. This is particularly useful for observing multiple spins at once and for inhomogenously broadened peaks in which not all crystallites can satisfy the rotational-resonance condition at once. However, as with R^2, magnetization exchange depends on the principle components of the chemical-shift tensor, the relative orientations of the chemical shift and dipolar tensors and the zero-quantum relaxation rate. In addition, spinning speed also determines the degree of magnetization transfer. Knowledge of all these parameters is necessary for precise distance determination.

Cross-peaks between {14-^{13}C}retinal and {ε-^{13}C,^{15}N}-Lys-bacteriorhodopsin (bR) have been observed using RFDR[35]. Although no

distances were calculated, such a technique could be useful in determining how retinal isomerization regulates proton transport in bR. In this study, two sets of cross-peaks were observed, one for each of the conformers of the retinal, i.e. cis and trans, and the intensities of these cross-peaks reflected the fact that in the cis-isomer the distance between the two labels is shorter. These experiments were done at -60°C.

2.3.3 Rotational-Echo Double-Resonance (REDOR) and Transferred-Echo Double-Resonance (TEDOR)

REDOR[36,37] is a simple extension of spin-echo double resonance[38,39] (SEDOR) which is a static experiment that uses π-pulses and spin-echoes to quantify heteronuclear couplings. The π-pulses prevent the refocussing of the dipolar interaction at the end of each echo. In a similar way, REDOR can be used to measure weak heteronuclear couplings through the use of rotor-synchronized π-pulses which prevent the refocussing of the dipolar interaction at the end of every MAS rotor cycle. In both cases, the π-pulses are used to dephase transverse magnetization by changing the sign of the dipolar interaction.

The pulse sequence for REDOR is shown in figure 2.7, for a heteronuclear I-S spin pair (^{15}N and ^{13}C, for example). After cross-polarization to the S spin, protons are decoupled for the remainder of the experiment. Two I spin π-pulses are inserted every rotor period and magnetization stays in the transverse plane. The second of these is synchronized with the end of every rotor period and switches the sign of the dipolar interaction so that dephasing during each period adds rather than canceling. The first π-pulse is inserted at a time less than or equal to half the

rotor period. It also reverses the sign of the dipolar interaction and, in doing so, prevents it from refocussing at the end of the rotor period. A phase is accumulated and therefore the echo intensity at the end of the rotor cycle is reduced. The π-pulse in the middle of the sequence on the S spin replaces the one on the I spin and refocusses the chemical shift. Signal is detected at the end of N dephasing cycles on the S spin. Phase cycling can be used to

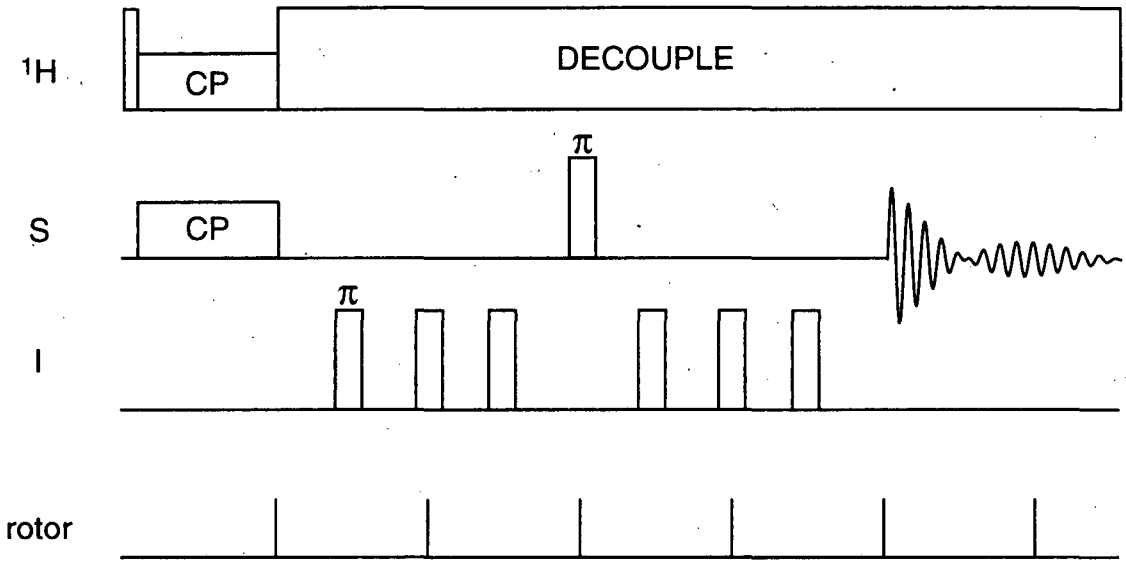

Figure 2.7: The rotational-echo double-resonance (REDOR) experiment. The entire experiment takes place under MAS. Protons are used for cross-polarization and then decoupled for the remainder of the experiment. The S spin gains polarization from protons, and a π pulse in the middle of the recoupling period, synchronized with the end of a complete rotor cycle, refocusses the chemical shift. Two π pulses are used every rotor period on the I spin channel, interupting the refocussing of the dipolar coupling between the I and S spins. The first of these occurs during first half of the rotor cycle, while the second is synchronous with the end of rotor cycles. Magnetization is detected on the S spins, again synchronized with a complete rotor cycle.

minimize the effects of pulse imperfections[40,41]. If the signal intensity, S, of this experiment is compared with the signal intensity of the same experiment without the I spin π-pulses, S_0, a dipolar coupling can be derived. Usually ΔS, (S_0 -S), is compared to S_0, and ΔS is a function of the number of dephasing cycles, N, the placement of the first π-pulse, and the dipolar coupling.

The dephasing in REDOR can be analyzed as follows[42]. The truncated Hamiltonian for the dipolar coupling between a heteronuclear spin pair (part A of the dipolar alphabet given above) can be rewritten under MAS as[15]:

$$\hat{\mathbf{H}}_{dd}(\mathbf{t}) = \omega_{dd}(t) I_z S_z$$

where

$$\omega_{dd}(\alpha,\beta,t) = \pm\frac{1}{2} D\left[\sin^2\beta\cos 2(\alpha+\omega_r t) - \sqrt{2}\sin 2\beta\cos(\alpha+\omega_r t)\right]$$

and D, the dipolar coupling constant, is given by

$$D = \frac{h}{2\pi}\frac{\gamma_I\gamma_S}{r_{IS}^3}$$

and α and β are the azimuthal and polar angles that relate the internuclear vector to the rotor frame. Using average Hamiltonian theory, the average dipolar frequency over a rotor period, τ_r, can be written as:

$$\overline{\omega}_{dd} = \frac{1}{\tau_r}\int_0^t \omega_{dd}(t')dt' \ .$$

This integral vanishes in the absence of I spin π-pulses, so full rotational echoes occur. However, with a single π-pulse at time t_p, this becomes

$$\overline{\omega}_{dd} = \frac{1}{\tau_r}\left[\int_0^{t_p}\omega_{dd}(t)dt - \int_{t_p}^{\tau_r}\omega_{dd}(t)dt\right].$$

For $t_p = \tau_r/2$, the average dipolar frequency is

$$\overline{\omega}_{dd} = 4\sqrt{2}D\sin\alpha\sin\beta\cos\beta \ .$$

This non-zero $\overline{\omega}_{dd}$ represents a phase acquired during each rotor cycle. The total phase accumulation, ΔΦ, for N dephasing cycles is

$$\Delta\Phi = \overline{\omega}_{dd} N\tau_r$$

and this leads to a dephasing of the rotational echo. The REDOR difference signal, $\Delta S/S$, is obtained by taking a full powder average:

$$\frac{\Delta S}{S} = 1 - \frac{1}{2\pi}\int_0^{2\pi}\int_0^{\pi/2} \cos(\Delta\Phi)\sin\beta d\beta d\alpha .$$

If the dipolar coupling is weak, $\Delta\Phi << 1$, the $\cos(\Delta\Phi)$ term can be expanded to give:

$$\frac{\Delta S}{S} = K(ND\tau_r)^2,$$

where K is a constant. Thus weak couplings can be observed by increasing the number of dephasing rotor periods.

There are several important considerations when using REDOR. The weaker the dipolar coupling, the more dephasing periods are necessary to measure it accurately. However, because magnetization is kept in the x-y plane, T_2 relaxation effectively limits the distances one can measure. Additionally, natural-abundance spins can contribute to REDOR dephasing, and interfere with measurements. An accurate measure of these natural-abundance contributions is possible, but difficult. Lastly, REDOR is non-selective. If more than one I spin is coupled to the S spin being detected, the total dipolar coupling, i.e. the sum of the individual couplings, is measured and information from the individual contributions of spins can not be obtained.

TEDOR[43,44] can be used to solve the problem with natural abundance described above. This experiment uses similar dephasing π-pulses, but filters signals so that only coupled nuclei are observed, like a double-quantum filter would. The pulse sequence is shown in figure 2.8, for a heteronuclear I-S spin pair. After cross-polarization to the I spin, protons are decoupled for the remainder of the experiment. As in REDOR, two S spin π-pulses are inserted

in each of N rotor periods and magnetization stays in the transverse plane. The magnetization built up is then transferred to the I spins with a pair of $\pi/2$-pulses at the end of a rotor period. Only I spins coupled to S spins will have magnetization transferred to them. If the phase of the I-spin $\pi/2$-pulse is reversed every other scan, background signals can be removed by subtracting the two scans. The sign of the transferred signal gets reversed by

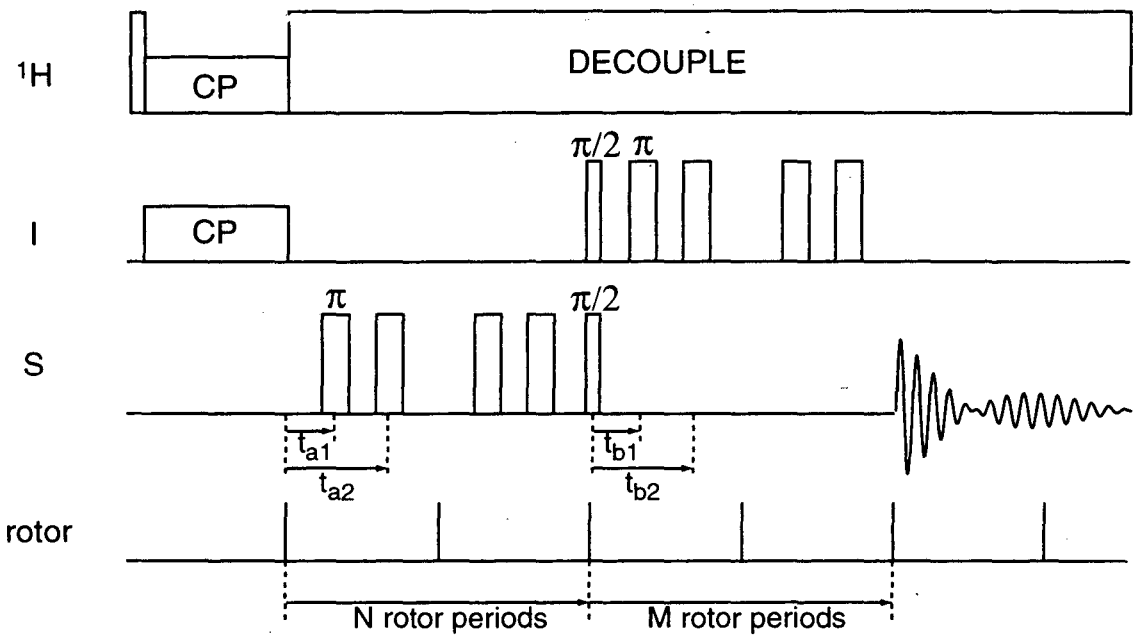

Figure 2.8: The transferred-echo double-resonance (TEDOR) experiment. The entire experiment takes place under MAS. Protons are used for cross-polarization and then decoupled for the remainder of the experiment. After gaining magnetization from protons, I spins evolve for N rotor periods under the influence of two π-pulses per rotor cycle on the S spin channel. Simultaneous $\pi/2$-pulses on the I and S spins transfer magnetization from I spins to S spins. This magnetization then evolves for M rotor period under the influence of two π-pulses per rotor cycle on the I spin channel, after which it is detected. The π-pulses are placed at times t_{x1} and t_{x2}, typically at $\tau_r/4$ and $3\tau_r/4$.

this phase change, while that of background signal remains unchanged. After this selection of magnetization, again, two π-pulses per rotor period are applied for M rotor periods, after which the S spin magnetization is detected.

The analysis of the TEDOR experiment[44,45] is similar to the one given for REDOR. If, as is normally done, the π-pulses are placed at 1/4 and 3/4 of the rotor period (times t_{a1} and t_{a2} in figure 2.8) the average dipolar frequency during the first half of the experiment is

$$\overline{\omega}_{dd} = 4\sqrt{2}D\cos\alpha\sin\beta\cos\beta$$

and the density matrix before the $\pi/2$ pulses is

$$\rho(t) = I_x\cos(\overline{\omega}_{dd}N\tau_r) + 2I_yS_z\sin(\overline{\omega}_{dd}N\tau_r)\ .$$

In REDOR, the first term is observed, while in TEDOR, the synchronous $\pi/2$-pulses convert the second term to magnetization that evolves to become observable on the S spin:

$$2I_yS_z\sin(\overline{\omega}_{dd}N\tau_r)\xrightarrow{(\pi/2)_{I,S}}-I_zS_y\sin(\overline{\omega}_{dd}N\tau_r)\ .$$

With the application of I spin π-pulses, this evolves into,

$$\sin(\overline{\omega}_{dd}N\tau_r)\left[-2I_zS_y\cos(\overline{\omega}_{dd}M\tau_r) + S_x\sin(\overline{\omega}_{dd}M\tau_r)\right]$$

of which the second term is observable. Again, a powder average is taken and the final observable S spin magnetization is

$$S = \frac{\pi}{2}\int_0^{2\pi}\int_0^{\pi/2}\sin(\overline{\omega}_{dd}N\tau_r)\sin(\overline{\omega}_{dd}M\tau_r)\sin\beta d\beta d\alpha\ .$$

Thus, the final observed magnetization is a function of the dipolar coupling, the number of rotor periods, N and M, and the length of the rotor period. No "control" experiment can be used to find S_0 in this case, because dephasing is used to select the magnetization that is observed. The time dependence of the TEDOR signal is, instead, compared with computer simulations to derive distances.

Although TEDOR eliminates the background signal problems, it still has two drawbacks, like those in REDOR. The weaker the dipolar coupling, the more dephasing periods, both N and M, are necessary to measure it accurately. TEDOR typically needs twice as many periods of dephasing to see the same coupling as REDOR. However, magnetization is kept in the x-y plane and T_2 relaxation can greatly limit the observable couplings. Secondly TEDOR is non-selective; all coupled spins are observed at once.

Combinations of TEDOR and REDOR have also been carried out. TEDOR is used in the first part of these sequences to produce selective magnetization and quantitation of a different coupling is then carried out through REDOR. For example, a molecule might be designed with three labels in it: a ^{31}P, a ^{13}C, and a ^{15}N. After cross polarization is carried out from ^{1}H to ^{31}P, TEDOR might be used to transfer magnetization to a strongly coupled ^{13}C nucleus. Because the molecule can be designed so that there is only one such ^{31}P-^{13}C pair, this transfer is selective and eliminates all other ^{13}C signals. This ^{13}C magnetization can then be observed after REDOR-type ^{15}N dephasing pulses are applied measuring the ^{15}N-^{13}C distance.

REDOR and TEDOR have been applied to many systems and many spin pairs with various maximum distances observable. These spin pairs (and maximum distances) include ^{13}C-^{15}N (5 Å), ^{13}C-^{31}P (8 Å), ^{13}C-^{19}F (10 Å), ^{19}F-^{31}P (16 Å). Initial studies using the techniques were on the antibiotic emerimicin and used ^{13}C-^{15}N REDOR[46] and ^{19}F-^{13}C REDOR/TEDOR[47] to measure an 8Å distance and show that the nine residue peptide adopts an α–helical structure.

The ternary complex formed by 5-enolpyruvylshikimate-3-phosphate synthase (EPSPS) with its ligand shikimate-3-phosphate (S3P) and a herbicide inhibitor N-(phosphonomethyl) glycine (Glp) has been studied extensively. The 46 kDa EPSPS is necessary for the synthesis of aromatic amino acids in plants and micro-organisms and this synthesis is inhibited by the commercially available Glp. Although a crystal structure of EPSPS without ligands is available, no crystals of complex have been suitable for diffraction. Many REDOR and TEDOR studies have been carried out to show that: 1) S3P is in close proximity to Glp[48]; 2) Glp is completely extended when bound to EPSPS[48]; 3) sidechains of three lysines, four arginines, and one histidine are in proximity to the binding site[49]; and 4) a cleft region closes on binding of S3P and Glp[50]. Molecular dynamics modeling in combination with these distance restraints give insight into the ligand geometry, showing that Glp does not bind to the complex in a similar fashion to the natural substrate PEP, thus making it unlikely that it behaves as a transition-state analog[51].

In addition, REDOR and TEDOR have been used on the following systems: the tripeptide melanostatin[52], a neurohormone; rat cellular retinol binding protein II[53]; the tridecapeptide α-factor[54], a yeast pheromone; a glutamine-binding protein[55]; an inhibitor bound to thermolysin[56]; a complex of ribulose-1,5-bisphosphate carboxylase/oxygenase[57]; a magainin analog in synthetic bilayers[58]; elongation factor Tu bound to magnesium guanosine diphosphate[59]; and the intact, membrane-bound serine receptor[60], a bacterial chemotaxis receptor.

2.3.4 Dipolar Recovery at the Magic Angle (DRAMA)

DRAMA[61] is essentially a homonuclear version of REDOR, but spectra it produces are scaled powder patterns. Magnetization is generated by cross-polarization and then evolves under a series of $\pi/2$ and π-pulses which prevent the dipolar coupling from averaging to zero at the end of a rotor cycle. The pulse sequence is shown in figure 2.9. Two X-channel $\pi/2$-pulses of opposite phase, separated by a time τ, are used to return magnetization to the z-direction for part of each rotor period. Maximum dephasing is accomplished when the condition $\omega_r\tau = \pi$ is met, so that τ becomes $\tau_r/2$. In the middle of every pair of rotor cycles, a π-pulse is used to refocus chemical

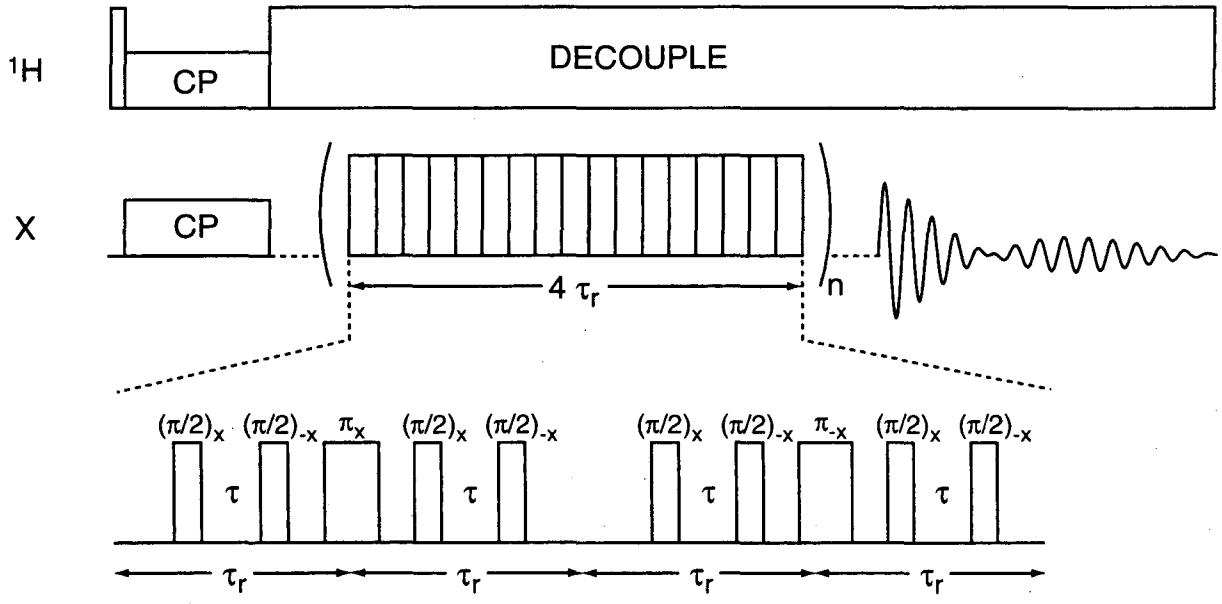

Figure 2.9: Dipolar recovery at the magic angle (DRAMA). The entire experiment takes place under MAS. Protons are used for cross-polarization and then decoupled for the remainder of the experiment. The X nuclei gain polarization from protons, and evolve under the application of two $\pi/2$-pulses per rotor cycle, separated by a period τ, and a π-pulse at the end of the first and third of every four rotor cycle period. This dephasing period goes on for n periods of 4 rotor cycles each, after which magnetization is detected.

shift and reduce effects of resonance offsets.

The full analysis of DRAMA has been carried out[61]. The Hamiltonian of interest is switched between evolution along the z-direction and evolution along the y-direction. Average Hamiltonian theory was used to show that the dipolar coupling is scaled down by $\sqrt{2}/\pi$ compared to the dipolar coupling that would be observed for a static sample.

Simulations of spectra obtained with the DRAMA pulse sequence show that the dipolar lineshapes observed are unaffected by resonance offsets up to $(3\tau_r)^{-1}$ and CSA widths of up to $(2\tau_r)^{-1}$. However, this limits the use of DRAMA to spin pairs with small chemical-shift differences and small anisotropies. Improved DRAMA sequences have been introduced to reduce these effects[62]. In addition, the use of $\pi/2$-pulses limits the phase cycling that can occur, and therefore the pulse sequence can cause loss of intensity due to pulse imperfections. The last disadvantage of DRAMA is that it, like REDOR, leaves magnetization in the transverse plane for extended times so T_2 relaxation limits the distances able to be measured.

DRAMA has been used to measure distances in two biologically relevant samples. ^{31}P-^{31}P DRAMA was used to measure a 7.4 Å distance in a twelve residue peptide[63]. The distance was between phosphine-sulfide substituted sidechains. The EPSPS ternary complex (see REDOR applications) was also studied using ^{31}P-^{31}P DRAMA[51]. The distance between phosphates in the ligand, S3P, and the inhibitor, Glp, was found to be approximately 8.5Å, showing the two bind near one another in the complex.

2.3.5 Dipolar Recoupling with a Windowless Sequence (DRAWS)

DRAWS[64] is a modified version of DRAMA that attempts to reduce the effects of undesirable interactions. It is a transverse experiment meant to detect a wide range of distances under MAS, even if the spins have large chemical-shift anisotropies, large differences in isotropic shift, and without dependence on the orientations of the CSA tensors. Magnetization is monitored as a function of the dipolar mixing time, and these curves are fit to simulations.

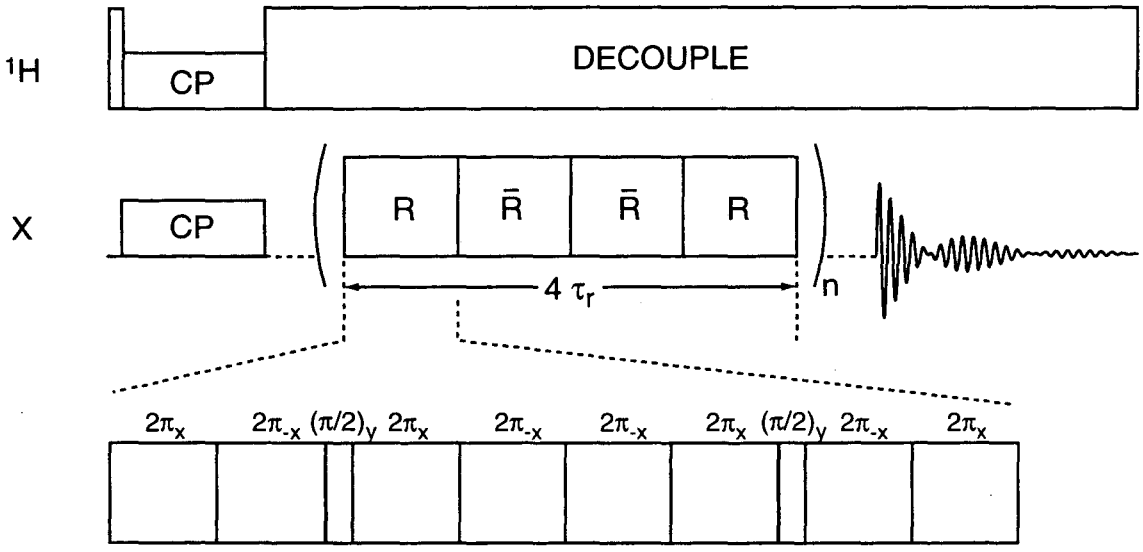

Figure 2.10: Dipolar recoupling with a windoless sequence (DRAWS). The entire experiment takes place under MAS. Protons are used for cross-polarization and then decoupled for the remainder of the experiment. The X nuclei gain polarization from protons, and evolve under the application of two π/2-pulses per rotor cycle, separated by 2π pulses as shown. This dephasing period goes on for n periods of 4 rotor cycles each, after which magnetization is detected.

The pulse sequence used for DRAWS is shown in figure 2.10. After CP, a supercycle of four DRAWS sequences is performed under constant proton decoupling. Each DRAWS cycle is composed of two $\pi/2$-pulses at 1/4 and 3/4 of the rotor cycle, as in DRAMA, but these pulses are separated by 2π-pulses as shown.

The complete average Hamiltonian analysis of DRAWS has been presented[64]. It was shown that, while the dipolar interaction is recoupled, the isotropic and anistropic chemical-shift interactions are suppressed. However average Hamiltonian is insufficient for describing the DRAWS sequence and numerical simulations must be used[64]. Dipolar corrections enter at second order and residual chemical shift effects also enter at higher orders. A scaling factor of about 0.33 is determined from experiment.

The DNA dodecamer d(CGCGAATTCGCG), which contains the binding site for the EcoRI restriction enzyme, was studied using DRAWS[65]. A maximum distance of 4.8Å between two ^{13}C nuclei was reported and the distances measured agree well with those found by x-ray crystallography. It was also found that hydration levels in samples can cause large changes in the internuclear distances.

2.3.6 Conclusions

The techniques described above have been shown to be useful in answering specific questions about systems of interest, especially in cases where a combination of ligand and biomolecule can be labeled. Although the techniques are becoming more robust and more widely applicable, still no general technique like the NOESY experiment has been developed. Before a

complete high-resolution solid-state structure can be elucidated, more general techniques will be necessary.

These distance-measurement techniques will be most useful when used in combination with dihedral-angle measurement techniques described below. This will enable more than one piece of data to be obtained from each sample, and will allow secondary and tertiary structural restraints to be obtained. Such combinations of techniques seem to hold the greatest promise for making SSNMR into a high-resolution structural-determination technique.

2.4. SSNMR secondary structure determination: isotropic chemical shifts

Early NMR spectroscopists interested in structural determination of proteins in solution attempted to understand secondary and tertiary structure in terms of isotropic chemical shifts, both theoretically[66] and experimentally[67]. In the 1980's, these initial methods of understanding structure were replaced with those described in section 2.1, using correlation spectroscopy, NOE's and J-couplings. However, attempts to correlate isotropic shifts with secondary structure continued successfully, first in solids, then empirically in solution, and most recently, theoretically in solution. These successes will be the topic of this section.

2.4.1 Isotropic shifts observed in solids by CPMAS

In the early 1980's several SSNMR studies employed CPMAS to investigate isotropic chemical shifts in peptides. These included work on ^{13}C in glycine[68-70], L-alanine[69,71,72], L-valine[69], L-leucine[69,75] and proline[76] in polypeptides and were reviewed by Saito[77,78]. It was shown in many cases

Table 2.3: Isotropic ^{13}C chemical shifts of various amino acids in polypeptides in α-helical and β-sheet conformations. All values are in ppm.

Amino Acid in poly-peptide	C_α		C_β		C=O		ref.
	α-helix	β-sheet	α-helix	β-sheet	α-helix	β-sheet	
Ala	52.4	48.2	14.9	19.9	176.4	171.8	71
	52.3	48.7	14.8	20.0	176.2	171.6	72
	52.8	49.3	15.5	20.3	176.8	172.2	69
Asp(OBzl)[a]	53.4	49.2	33.8	38.1	174.9	169.8	73
	53.6		34.2		174.9		69
Glu(OBzl)[a]	56.4	51.2	25.6	29.0	175.6	171.0	74
	56.8	51.1	25.9	29.7	175.4	172.2	69
Gly		43.2				168.4	68,70
		44.3				169.2	69
					171.6	168.5	70
Ile	63.9	57.8	34.8	39.4	174.9	172.7	75
		57.1		33.1		171.0	69
Leu	55.7	50.5	39.5	43.3	175.7	170.5	75
	55.8	51.2	39.6	43.7	175.8	171.3	69
Lys(Z)[b]	57.6	51.4	6.2	29.3	175.7	170.4	69
Met	57.2	52.2	30.2	34.8	175.1	170.6	69
Phe	61.3	53.2	35.0	39.3	175.2	169.0	69
Val	65.5	58.4	28.7	32.4	174.9	171.8	75
		58.2		32.4		171.5	69

[a] Poly-L-asparagine and glutamine with benzyl side-chain protecting groups.
[b] Poly-L-lysine with benzyloxycarbonyl side-chain protecting groups.

Table 2.4: Isotropic ^{15}N chemical shifts of various amino acids in polypeptides in α-helical and β-sheet conformations. All values are in ppm and are taken from reference 79.

Amino Acid in polypeptide	^{15}N	
	α-helix	β-sheet
Ala	98.6	101.8
Asp	99.2	100.4
		100.4
Glu	97.6	99.5
	97.6	99.5
Leu	97.0	107.0

that various secondary structures, including α-helices , β-sheets, π-helices, 10_3-helices, and 3_1-helices, could be distinguished on the basis of their ^{13}C isotropic shifts. Tables 2.3 and 2.4 summarize the isotropic shifts found for various ^{13}C and ^{15}N nuclei in residues of peptides in α-helix and β-sheet conformations.

Several important observations should be noted. First, the isotropic shifts in solids appear to be independent of primary structure; neighboring residues do not influence the shift. Second, different ^{13}C nuclei in a residue, for example a $^{13}C_\alpha$ and a $^{13}C_\beta$, shift in different directions upon moving from α-helix to β-sheet. Third, shifts as large as 8 ppm have been observed, and so are easily distinguishable even with the broad lines in SSNMR. Lastly, for carbonyl residues, hydrogen bonding may play an important role in causing shifts. An increase in hydrogen-bond length was found to correlate with a upfield shift in both alanine[80] and glycine[81] experimentally, and in theoretical calculations[82]. Differences in hydrogen bonding in various secondary structures may account for observed $^{13}C{=}O$ shifts.

2.4.2 Isotropic shifts observed in solution

A wealth of solution isotropic shift information became available once structures began being solved in the late 1980's. As a result, empirical observations of statistical significance were made for $^{13}C_\alpha$[83,84], $^{13}C_\beta$[83], $^{13}C{=}O$[84], $^{1}H_\alpha$[84], ^{1}HN[84], $^{1}H_\beta$[84], and ^{15}N[84]. Deviations from random-coil chemical shifts[1,84] were calculated. For example, it was noted that $^{13}C_\alpha$ shifts downfield by an average of 3.09 ppm from random-coil when in a helical structure, while it shifts upfield by an average of -1.48 ppm in a β-sheet. Shifts in the

opposite direction are observed for $^1H_\alpha$ and ^1H_N, while no significant trends were observed for ^{15}N.

Although attempts to correlate shifts with specific dihedral angles were attempted, it was not possible to obtain specific values for either ϕ or ψ from these empirical studies[84]. Instead, a method was introduced which looked for trends in shifts and identified secondary structure through these trends[85,86]. The technique involves two stages. First, a chemical-shift index is assigned to all identifiable residues on the basis of their $^1H_\alpha$ or $^{13}C_\alpha$ shifts. In the case of the $^1H_\alpha$, shifts for residues are compared with random-coil shifts and if they differ significantly from them, the residues are given an index of "1" larger shifts or a value of "-1" for smaller ones. The second stage involves the graphical display of indices as a function of residue number. A group of four consecutive "1's" lead to the identification of that region as helical, while a string of three consecutive "-1's" identifies a sheet. These trends are approximate; accuracies are about 90-95%. The indices are used in conjunction with other data, like NOE's and hydrogen-exchange rates, to identify secondary structure, but can not be relied upon as the sole means of assigning structure.

2.4.3 Isotropic chemical-shift calculations

The prediction of ^{13}C chemical shifts has become possible recently through use of *ab initio* quantum-chemical methods[87]. The total chemical shielding, σ_t, was separated into three components:

$$\sigma_t = \sigma_s + \sigma_l + \sigma_m$$

where σ_s represents the short-range contributions such as bond lengths, bond angles and torsion angles, σ_l represents the long-range electrostatic

contributions, and σ_m represents the magnetic contributions. Fortuitously, it was found that basis functions are only necessary for the atoms very close to the ^{13}C of interest, and that approximations could be made to account for the σ_l and σ_m terms. In other words, a full calculation need only be carried out for atoms in a peptide fragment such as that shown for alanine in figure 2.11. σ_s contributes most to shielding. The variable components of σ_s in a protein are dependent upon the torsion angles, ϕ and ψ. The overall widths and ~5 ppm separations between the helical and sheet conformations found experimentally are reproduced in these calculations and the majority of the separations can be accounted for by changing only ϕ and ψ. Theoretical results for $^{13}C_\alpha$ and $^{13}C_\beta$ correlate well with experimental results and only slight improvements are obtained when specific hydrogen bonding and a protein's charge field are incorporated into calculations.

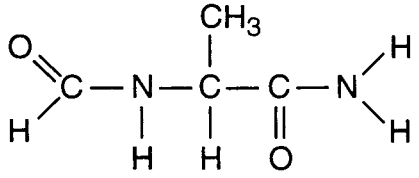

Figure 2.11: The alanine fragment used for *ab initio* chemical-shielding calculations.

Further studies[88,89] using gauge-including atomic orbital (GIAO) self-consistent field calculations were done on peptide fragments similar to that

used for alanine, shown in figure 2.11. Shieldings were found to be very sensitive to bond lengths and angles, however, observed experimental chemical-shift patterns could not be reconciled with the spread of bond lengths and angles in X-ray structures. In other words, a much larger spread in chemical-shift values would be expected if the variability in bond distances and angles found in X-ray structures were found in solution. Thus, bond distances and angles in alanine, for example, may be treated as fixed and information on all alanine residues in all proteins may be calculated from the same fragment. The chemical shift range observed is overwhelmingly dominated by changes in ϕ and ψ.

Chemical-shielding surfaces giving the shielding as a function of ϕ and ψ only were generated. Using these surfaces, one could predict chemical shieldings given the dihedral angles. More importantly, if isotropic shifts are known for several carbons, i.e. $^{13}C_\alpha$ and $^{13}C_\beta$, torsion angles could be uniquely predicted using the Z-surface method[90].

2.4.4 Isotropic shifts in structural refinement

Both the experimental and theoretical correlations of isotropic shifts with secondary structure have led to attempts to further refine solution structures[91-93]. Empirically or theoretically derived correlations between shifts and secondary structure are stored in tables, and experimental isotropic shifts are compared with values in these tables during structure refinement. If the torsion angles in the structure are consistent with the chemical shift found, no energy penalty is assessed, while if they are not consistent an energy penalty is calculated and applied. Although these additional refinement constraints have not yielded structures with lower RMSDs, they

have led to structures with fewer NOE violations. This is probably because this information is redundant with the information contained in J-couplings and dense NOE constraints. Additionally, these constraints may contribute to faster convergence in the early stages of structure calculations, when fewer NOE constraints are used.

2.5 SSNMR dihedral angle determination

Although the isotropic chemical shift can give general information on secondary structure, knowledge of exact dihedral angles can contribute to a better understanding of the high-resolution structure of a peptide. These angles can be determined indirectly by measuring several distances in a peptide[33], but techniques measuring these angles directly cost less and are more accurate. In the past several years, a variety of SSNMR techniques for directly measuring dihedral angles have been developed. All of these techniques employ a double or triple ^{13}C labeling scheme. The techniques being developed fall into three main categories. The first class correlates a CSA of a known or estimated orientation with either a dipolar coupling or another CSA via two-dimensional NMR, either static or spinning. The second class of techniques employs double-quantum coherences in two-dimensional experiments, also either static or under MAS. The last category uses the dependence of magnetization exchange in rotational-resonance experiments on the relative orientations of the CSA tensors. Experiments of each catagory will be discussed in detail, and a summary of these experiments is given in table 2.5.

2.5.1 Exchange spectroscopy

The initial experiments by Tycko and co-workers[94,95] used to measure torsion angles in polymers were simple extensions of two-dimensional exchange spectroscopy developed earlier[8,96]. These experiments involve measuring the correlations between NMR resonances detected in one time interval (t_1) with those detected in a second time interval (t_2). These two detection periods are separated by a mixing period, τ, during which magnetization is allowed to transfer from one nucleus to another via a dipolar mechanism (either spin-diffusion[97,98] or an active mechanism of transfer such as rotational resonance). Such experiments have been used previously to measure distances, chemical exchange, and dynamics in liquids[2] and structure and dynamics in solids[99].

Because the NMR frequencies measured in both t_1 and t_2 can depend on the orientation of an interaction in the molecular frame, dihedral-angle information is present in exchange experiments. The most useful interactions to monitor are the CSA and the dipolar coupling and several types of experiments have been developed to correlate these. The simplest experiments[95] correlate the CSA of one ^{13}C nucleus in t_1 with the CSA of a second ^{13}C nucleus in t_2, using a static sample and using spin-diffusion to transfer polarization (figure 2.12A). When the ^{13}C-^{13}C and ^{14}N-^{13}C dipolar couplings are small compared to the CSA, the primary interaction under which magnetization evolves is the ^{13}C chemical shift, since protons are decoupled. (If these dipolar couplings are not negligible, they must be accounted for.) The resulting 2-D spectra will have a ridges along the diagonal as well as off-diagonal ridges. The intensity along the diagonal will be at the resonance frequencies of each of the nuclei and is the result of

Table 2.5: A summary of dihedral angle measurement techniques.

technique	detection system	advantages	limitations	comments and references
CSA/CSA exchange spectroscopy	^{13}C -- ^{13}C	simple implementation; spin-diffusion mixing	natural abundance problematic; CSA orientation required; directly bonded spin pairs can not be used; most of detected signal not useful	static or under MAS; MAS experiment can use orietational weighting to further limit angles; two-dimensional spectra fit; ^{13}C-^{14}N coupling must be accounted for. Refs. 94,95.
CSA/dipole exchange spectroscopy	^{13}C-^{13}C -- ^{13}C	simple implementation; spin-diffusion mixing	natural abundance problematic; CSA tensor orientation required; static experiment; triple labeling required	two-dimensional spectra fit. Refs. 94,95.
RACO	^{1}H-$^{13}C_{\alpha}$ -- ^{13}C=O	MAS experiment; complex pulse sequence; magnetization transfer driven by modified R^2	natural abundance problematic; CS tensor orientation required;	two-dimensional spectra fit. Ref. 102.
SELFIDOQ	^{13}C -- ^{13}C	no natural abundance problem; directly bonded pairs may be used	loss of signal due to inefficient DQ creation and reconversion; static experiment; ^{13}C-^{14}N coupling present during t_1; CSA tensor orientation required; strongly coupled system required	two-dimensional spectra fit. Ref. 115.
modified SELFIDOQ	^{1}H-$^{13}C_{\alpha}$ -- ^{13}C=O	no natural abundance problem; no ^{13}C-^{14}N coupling	loss of signal due to inefficient DQ creation and reconversion; static experiment; CSA tensor orientation required; strongly coupled system required	two-dimensional spectra fit. Ref. 121.
2Q-HLF	^{1}H-^{13}C -- ^{13}C-^{1}H	MAS experiment; no natural abundance problem; ^{13}C-^{14}N coupling	loss of signal due to inefficient DQ creation and reconversion; complex sequence; strongly coupled system required	one-dimensional projection fit; similar experiment may be applied to peptide backbone. Ref. 122.
R^2	^{13}C-^{13}C	simple to use; MAS experiment	need broad chemical shift tensors; CSA tensor orientation required; T_{2ZQ} estimation required; strongly coupled system required	$\Delta\omega_{iso}=\omega_r$. Ref. 124.

magnetization that was detected on the same nucleus in both t_1 and t_2, i.e. magnetization that did not exchange during the period τ.

The off-diagonal intensity is due to magnetization that is detected on one nucleus during t_1 and a different nucleus during t_2, i.e. magnetization that has undergone exchange. It is the shape of these off-diagonal peaks that contains orientational information. If the relative orientations of the two nuclei in the molecular frame were random, i.e. if the molecule was unstructured in the region, the two nuclei would be uncorrelated and any cross-section parallel to either the ν_1 or ν_2 axis would have the same lineshape. This is due to the fact that for any orientation of the first nucleus measured in the first dimension, any orientation of the second nucleus would be possible and hence any part of the second nucleus' CSA could correlate. However, if the molecular structure is fixed, cross-sections of the off-diagonal peaks will have different lineshapes. The way to understand this is as follows. If the molecule is rigid, the orientation of the CSA of one nucleus is fixed with respect to the orientation of the CSA of a second nucleus in that molecule. The resonance frequency for each CSA is determined by the orientation of the molecule with respect to B_0, and each individual molecule in a static sample will have a single resonance frequency for each of its two labeled nuclei. Each orientation of the molecule with respect to B_0 contributes to the CSA lineshape of a spin at a particular frequency. If the resonant frequency of a nucleus is measured and then the magnetization of that nucleus is transferred to a second nucleus within a rigid molecule, the frequency of the second nucleus is determined by the orientation of the molecule. In a two-dimensional experiment, the frequency of one of those nuclei is measured in the first dimension and the frequency of the other

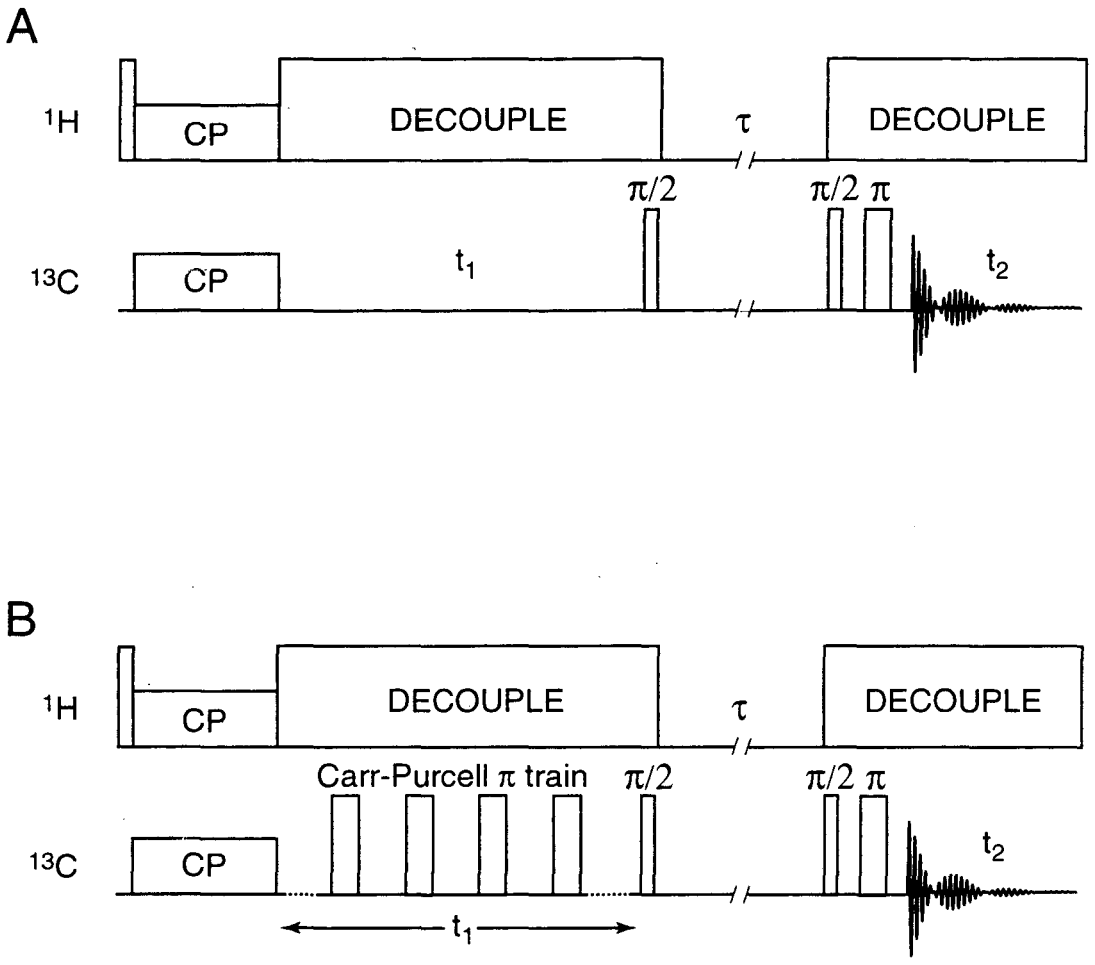

Figure 2.12: Exchange spectroscopy experiments for determining dihedral angles. (A) The CSA-CSA correlation. This experiment can be performed either static or under MAS. After cross-polarization, ^{13}C magnetization evolves for t_1 under proton decoupling. This magnetization is then returned to the z-direction. Through spin-diffusion, magnetization can transfer to other ^{13}C nuclei, and this process is expedited by turning off ^{1}H decoupling. ^{13}C magnetization is then returned to the x-y plane, where it is detected with an echo under proton decoupling. (B) The CSA-dipolar correlation. This experiment is similar to that in part A, except that, during the t_1 period, a Carr-Purcell pulse train is used to refocus chemical shift while allowing ^{13}C-^{13}C dipolar coupling to evolve.

nucleus in the second dimension. Each resonance (orientation) measured in t_1 will have only one possible resonance (orientation) in t_2. As a result of this, and because the relationship between the resonance frequencies of the two nuclei is not simple, a complex pattern forms.

If the principal values and the orientation of the CSA tensor in the molecular frame is known for each nucleus from previous experiments, then the relative orientation of the two CSA tensors can be calculated and spectra can be simulated for each possible relative orientation. These simulated spectra can be compared with experimental results, either by eye or by a fitting program, and, in this way, the relative orientation of the CSA tensors can be derived. Since the orientation of the individual CSA is known in the molecular frame, this relative orientation can be used to calculate the dihedral angle(s) between the nuclei.

Tycko and co-workers[95] first used this experiment on the polymers poly(methyl methacrylate) (PMMA) and poly(methyl acrylate) (PMA), isotopically enriched at the carbonyl carbon and the methoxy carbon. It was shown that the methyl ester side group has a planar conformation, with $\chi_1 \approx 0°$.

A similar technique[94,95] correlates a CSA tensor with a dipolar tensor (figure 2.12B). In this experiment, a pulse sequence is used during either t_1 or t_2 to eliminate the CSA interaction and evolve under a dipolar interaction. The CSA is measured in the other dimension. The dipolar interaction observed can either be homonuclear, in which case a Carr-Purcell pulse train[100] could be used to detect it, or heteronuclear, in which case a MREV-8 multiple-pulse sequence[101] or a RHEDS sequence[102], could be used. For example, in a triply ^{13}C labeled sample in which two of the ^{13}C nuclei are

directly bonded, the Carr-Purcell train can be used to refocus chemical shifts while the ^{13}C-^{13}C dipolar coupling between the spatially close nuclei evolves. This magnetization can then be transferred to the third nucleus whose CSA is measured. Thus, the bond direction between the directly bonded ^{13}C nuclei is correlated to the CSA of the third ^{13}C nucleus.

A similar argument as the one given above can be used to derive the torsion angles in this case. The orientation of a dipolar coupling is fixed in the molecular frame; it is parallel to the bond axis. If the molecule is rigid, then each orientation of the CSA with respect to B_0 will correlate with only one orientation of the dipolar coupling with respect to B_0. (The converse is not true, since the dipolar orientation is described by an axially symmetric tensor.) If the principal values and orientation of the CSA are known, then simulations can be carried out and compared with experiments to obtain dihedral angles.

These experiments were carried out by Tycko and co-workers on dimethyl succinate[94], giving data that is consistent with known crystal structure; on diammonium succinate[94], in which no crystal structure is known; and on poly(ethyl methyacrylate)[95] in which the data suggests that a planar side-chain conformation similar to that found for PMA and PMMA is predominant, but other conformations are present. Significant molecular dynamics are also observed.

The experiments described above can also be carried out under MAS[103]. In these cases, the intensities of the spinning sidebands contain the orientational information. Although simulations are slightly more complicated, it is possible to trace the evolution of the CSA tensors of nuclei and the dipolar tensor between a pair of nuclei in rigid molecules under rotor

spinning. The intensities of sidebands in these simulated spectra are again compared with experiment.

Tycko and co-workers have developed this method for peptides[103]. In samples with two ^{13}C=O on successive residues in a peptide, the CSA tensors of the two sites were correlated in a two-dimensional exchange experiment under MAS using spin-diffusion to transfer magnetization. It was shown that such experiments greatly limit the possible pairs of torsion angles in the tripeptide Alanine-Glycine-Glycine (AGG) in which the carbonyl-carbons of the alanine and the glycine were labeled.

To further limit the possible (ϕ, ψ) pairs, additional experiments were developed[104]. New pulse sequences were used to create an initial nuclear spin-polarization distribution different from the normal case in which the polarization is due to an isotropic molecular orientation. Simulations of these pulse sequences are relatively straight-forward, so sideband intensities are compared between simulations and experiments to obtain the structural information. These orientationally-weighted 2D MAS spectra are more sensitive to molecular conformation and can be used in conjunction with the previously described experiment to obtain additional constraints on the torsion angles in a single sample. These new experiments were also carried out on the doubly labeled AGG sample[104].

Ishii and co-workers developed an experiment which they call relayed anisotropy correlation (RACO) NMR[102] to measure the dipolar-CSA correlation under MAS (figure 2.13). In this experiment, the CSA of a C=O is measured during t_1, magnetization is transferred via a modified version of rotational resonance, and the dipolar tensor between a $^{13}C_\alpha$ and its attached proton is detected. CP is used to create magnetization on ^{13}C. Magnetization

is returned to the z-direction and a selective pulse is used to move $^{13}C{=}O$ magnetization to the x-y plane. Evolution under a 6π-pulse sequence[105] then allows CSA detection. Magnetization is returned to the z-direction for the exchange period. Polarization transfer is carried out by recoupling the $^{13}C{=}O$ - $^{13}C_\alpha$ dipolar coupling. If the sample were spinning at the rotational-resonance frequency, this transfer could be driven. But carrying out the entire experiment at the R^2 condition would lead to the presence of the couplings during times in which it is not desired. To allow R^2 magnetization transfer during the exchange period only, frequency-switched off-resonance irradiation[106] can be used to scale the isotropic frequency difference, $\Delta\omega_{iso}$. Thus, the rotor can be spun at a given frequency (not matching the rotational-resonance frequency), and $\Delta\omega_{iso}$ can be scaled to match the rotor frequency and reintroduce the dipolar coupling. This allows the dipolar interaction to be recoupled during the mixing period only. Once magnetization is transferred to the $^{13}C_\alpha$, a rotor-synchronous heteronuclear dipolar switching (RHEDS) pulse sequence[102] is used to observe the ^{13}C-^{1}H dipolar coupling. This sequence uses a windowless isotropic mixing sequence (WIM-12)[107] around a frequency-switched Lee-Goldberg (FSLG-2) sequence[108] to evolve under the coupling. The result of this experiment is a two-dimensional pattern similar to that obtained in the static experiment by Tycko and co-workers described above. As before, this pattern can be simulated and compared with experimental data to yield information about the dihedral angle ψ. The utility of this sequence was shown for 1,2-^{13}C labeled DL-alanine. Experimental results limited ψ to either $137° \pm 7°$ or $223° \pm 7°$, while the angle determined by neutron scattering was 135.5°.

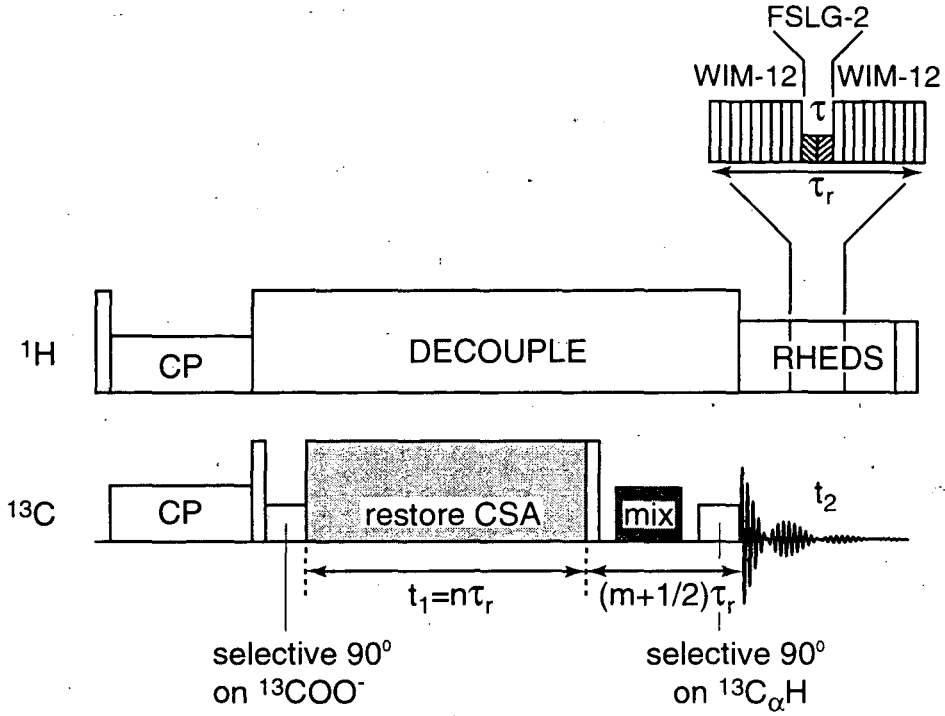

Figure 2.13: The relayed anisotropy correlation (RACO) experiment. This experiment is performed under MAS. After cross-polarization, ^{13}C magnetization is returned to the z-direction and a selective 90° pulse returns only the $^{13}COO^-$ magnetization to the x-y plane. A 6π-pulse sequence is used to restore the CSA on this $^{13}COO^-$ magnetization for t_1. During the subsequent mixing period, magnetization exchange between the $^{13}COO^-$ and the $^{13}C_\alpha H$ is driven by scaling their chemical-shift difference, with frequency-switched off-resonance irradiation, to match the rotational-resonance condition. A selective 90° pulse on the $^{13}C_\alpha H$ returns its magnetization to the transverse plane. The RHEDS sequence is used during detection so that only the $^{13}C_\alpha$-^{1}H dipolar coupling is observed. The entire experiment must be synchronized with rotor cycles, as shown.

One further improvement to the experiments described above would be the addition of another dimension so that correlations for multiple labels could be acquired simultaneously. Experiments incorporating an isotropic ^{13}C shift dimension with separated-local-field[109-112] (SLF) have recently been

described by Grant and co-workers[113] on a small molecule. Such techniques show promise for more complex systems with multiple labels.

The experiments described above have been shown to be of use in small molecules, polymers and peptides. They have several advantages over techniques that will be described below, as well as several disadvantages. For the most part, these correlation experiments are straight-forward and easy to implement. No complex pulse sequences or probes are necessary and high-speed MAS or high-powered radio-frequency pulses are not needed. Data analysis is also simple. Resolved powder patterns for the two spins being studied simplify analysis, but are not necessary[114]. Since spin-diffusion has been shown to be an effective way to transfer magnetization, systems with overlapping isotropic shifts, systems with small isotropic-shift differences, and systems with small homonuclear dipolar couplings can be studied. These techniques can also be applied to intermolecular interactions, so, for example, ligand binding may be studied. Although static experiments are not feasible in complex systems, the use of MAS enhances sensitivity sufficiently to make the experiments useful.

One disadvantage of these experiments is that all of them rely on knowledge of the chemical-shift tensor, particularly its orientation. The orientation of the CSA has been measured directly on a few model systems and is thought to be fairly constant for similar functional groups (i.e. in C=O, σ_{22} is parallel to the double bond axis). However, for most samples of interest, the tensor orientation would have to be assumed or measured independently. Furthermore, double or triple ^{13}C labels at neighboring residues are necessary for carrying out each measurement, and thus each measurement is costly. Directly bonded ^{13}C spin pairs are strongly dipolar

coupled and complicate analysis. Although one could use homonuclear decoupling to remove this, decoupling complicates the experiment and would be hard to carry out in practice, since it would have to be carried out simultaneously with proton decoupling and during detection. Another drawback is that a large percentage of the detected signal is not of use, since it lies on the diagonal and represents magnetization that has not exchanged. Lastly, natural-abundance ^{13}C can become a problem in large systems, and these experiments have no way of eliminating its contribution to spectra.

2.5.2 Double-quantum correlation experiments

The second class of experiments developed for measuring torsion angles correlates double-quantum evolution during t_1 with the CSA and ^{13}C-^{13}C dipolar couplings in t_2. Three different pulse sequences have been published to date, each a slight variation of the other. All of them use a sample in which two bonded nuclei are ^{13}C labeled. In the case of a peptide the two nuclei would be the C_α and the C=O, and the angle being measured is the angle between these spins, ψ.

The first such sequence published[115], SELFIDOQ, (figure 2.14A) is performed on a static sample. It uses a simple double-quantum excitation/reconversion sequence, based on the INADEQUATE sequence[116-119]. Magnetization evolves under this double-quantum coherence during t_1. During t_2, only heteronuclear decoupling is used, so evolution under the CSA and dipolar couplings occurs. The full product operator analysis has been worked out for the INADEQUATE sequence[120], and it shows that during t_1, magnetization evolves as $\cos(\omega_a + \omega_b)t_1$, where ω_a and ω_b are the chemical-shift frequencies of the two spins. When the full chemical-shift tensors are

used to calculate the frequencies, the relative orientation of the two CSA tensors must be accounted for (i.e. they must be rotated into a common frame) before the simple addition can be carried out. The rotation necessary for doing this can be chosen to be a function of the torsion angle between the directly bonded pair. Thus, $(\omega_a + \omega_b)$ contains all the information necessary to determine the relative orientations of the two CSA tensors and therefore the dihedral angle between them. However, additional information leading to more accurate dihedral angle estimations are obtained if the ridge pattern of the full two-dimensional spectra is compared with simulations, rather than using only this double-quantum dimension. Schmidt-Rohr first used SELFIDOQ on dilute (4%) double ^{13}C-labeled polyethelene mixed with unlabeled polyethelene, showing that it is in a *trans* conformation[115].

Schmidt-Rohr further developed this experiment for improved performance on peptides[121] (figure 2.14B). During the t_1 period in the experiment described above, magnetization evolved in the double-quantum state. In peptides, evolution during this period would be influenced by the ^{13}C-^{14}N coupling, which is comparable in strength to the CSA of the C_α carbon. This effect can be removed if, during t_1, one measures the $^{13}C_\alpha$-^{1}H dipolar coupling as it evolves in the double-quantum state, rather than measuring the CSA tensor sum. In the modified experiment, homonuclear decoupling is achieved via the MREV-8 homonuclear proton decoupling sequence with a 180° pulse in the center of the evolution period to refocus both chemical shifts and the undesired ^{13}C-^{14}N dipolar coupling. Thus, the double-quantum coherence is modulated only by the $^{13}C_\alpha$-^{1}H coupling, and is then reconverted to transverse magnetization on both the ^{13}C=O and $^{13}C_\alpha$ sites. This is detected as it evolves under the chemical shift and ^{13}C-^{13}C

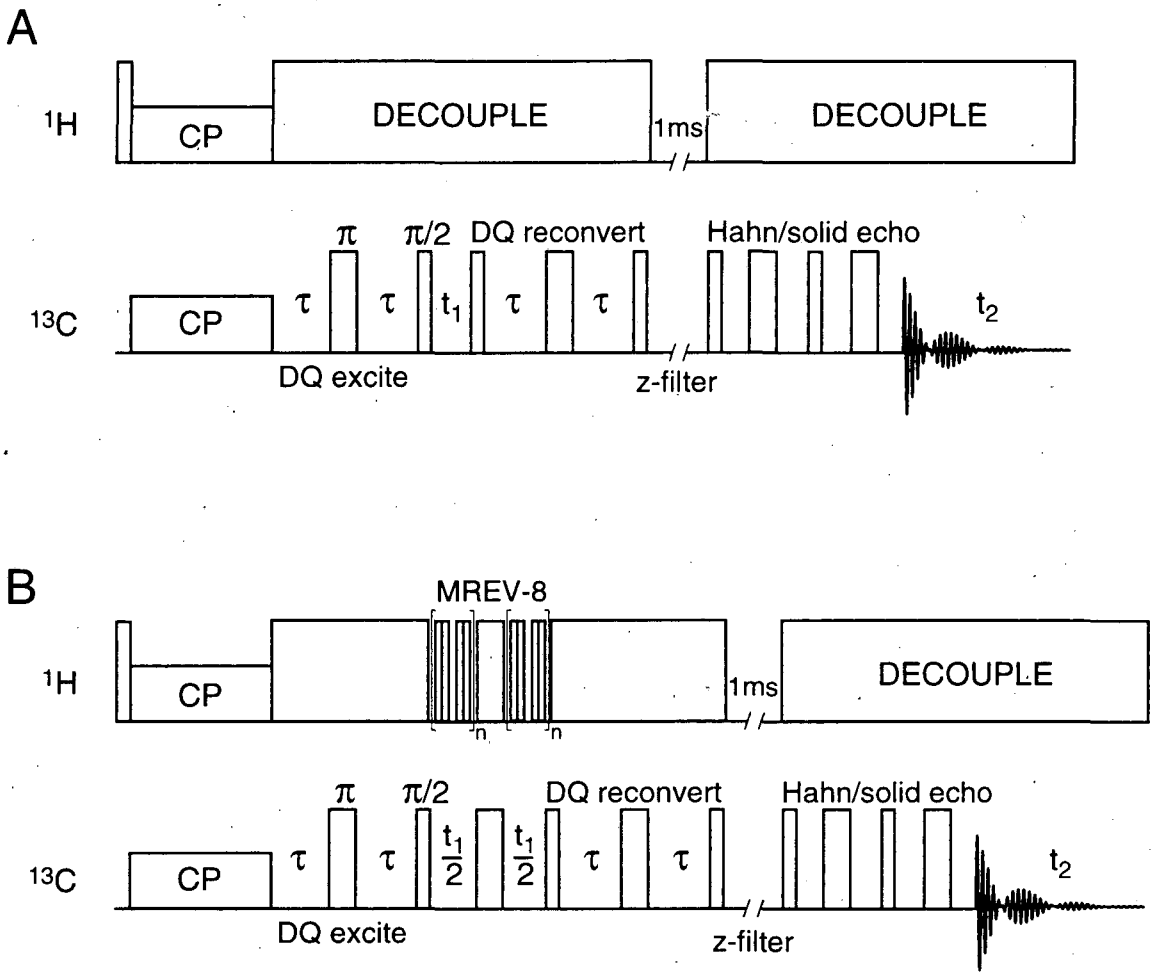

Figure 2.14: Static double-quantum experiments for determining dihedral angles. (A) The original SELFIDOQ sequence. After cross-polarization, double-quantum coherence is generated with the INADEQUATE sequence. During t_1, this coherence evolves as the sum of the two chemical-shift tensors. After reconversion, again with INADAQUATE, a z-filter is used for quadrature, and the ^{13}C magnetization is detected with a combined Hahn and solid echo sequence. During t_2, the magnetization evolves under both the CSA and dipolar operators. (B) The modified SELFIDOQ sequence. The sequence is the same as in part A, except that during t_1, MREV-8 multiple-pulse homonuclear decoupling is used instead of heteronuclear decoupling. This allows the double-quantum coherence to be modulated by the ^{13}C-^{1}H dipolar coupling only.

dipolar operators. Again, simulations are performed and compared with experimental results to obtain the ψ torsion angle.

The utility of this modified SELFIDOQ experiment was shown on doubly ^{13}C labeled L-leucine[121]. Very good agreement was seen between the experimental results and simulations based on the values of ψ from the crystal structure, and spectra for other values of ψ were markedly different.

Levitt and co-workers introduced an MAS version of this last experiment, which they call 2Q-HLF[122], shown in figure 2.15. In the experiments described, measurements are carried out on samples containing a H-C-C-H moiety, and the torsion angle describing the angle between the two C-H groups is obtained. The C7 multiple-pulse sequence[123] for generating double-quantum coherence under MAS is used. This coherence evolves for a fixed period, τ_r (one rotor cycle). The evolution period is divided into two parts. During the variable t_1, the two heteronuclear ^{13}C-^{1}H couplings modulate the double-quantum coherence because an MREV-8 multiple-pulse sequence is applied to protons. This evolution depends on the relative orientation of the two couplings. During the second part of the evolution period (τ_r-t_1) high-power proton decoupling is applied, so the dipolar couplings are suppressed. The homonuclear ^{13}C-^{13}C couplings and the CSA operator are still present during this entire period. These have no effect on the final evolution because the double-quantum coherence is not affected by the homonuclear dipolar coupling and, since the evolution period is one complete rotor cycle, the CSA is averaged to zero. If the carrier frequency is set so that the sum chemical shift is zero, evolution only occurs under the heteronuclear dipolar operator. This magnetization is reconverted by a second C7 sequence and detected. The projection of the final 2-D experiment

onto the double-quantum axis is compared with simulated spectra to derive the torsion angle.

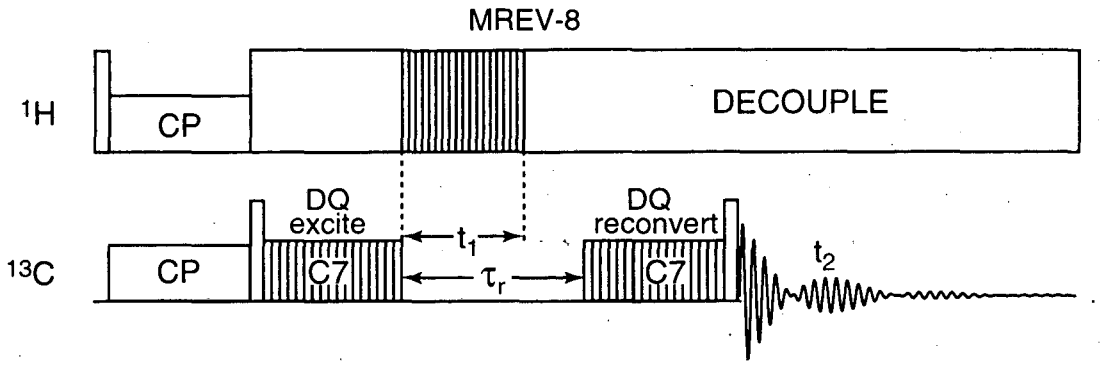

Figure 2.15: A double-quantum MAS experiment for determining dihedral angles. After cross-polarization, the C7 pulse sequence is used to excite the double-quantum coherence. During t_1, this coherence evolves under the MREV-8 sequence, allowing it to be modulated by the ^{13}C-^1H dipolar couplings. At the end of one complete rotor cycle, the coherence is reconverted and detected under heteronuclear ^1H decoupling. The projection of this 2-D experiment onto the double-quantum axis is analysed.

The 2Q-HLF experiment was used to study the torsion angles in ammonium hydrogen maleate and diammonium fumarate[122]. The first of these compounds was found to be in the *cis* conformation, while the second was found in the *trans* conformation. It is believed that this experiment can predict angles to within ±20° for torsion angles near the *cis* geometry and within ±10° near the *trans* geometry. The 2Q-HLF could now be used for measuring side-chain torsion angles, and it can be modified for use along the peptide backbone where the ^{13}C-^1H and ^{15}N-^1H couplings could be correlated.

The double-quantum experiments described in this section have some distinct advantages over exchange experiments. Natural-abundance ^{13}C magnetization is completely eliminated from these spectra, so large systems may be studied easily. All of the detected signal contributes to the data determining the angle of interest since no diagonal ridge pattern exists. Directly bonded nuclei can be used to study the torsion angle between them, thus allowing the labeling of a single residue rather than multiple residues, potentially lowering costs. The 2Q-HLF experiment, if applied to the backbone of a peptide, seems most promising, since it is an MAS experiment with increased sensitivity and because it does not rely on estimates of the orientation of the CSA.

However, these experiments are more difficult to carry out than the simple exchange experiments. The excitation of double-quantum coherences is inefficient and can require complex pulse sequences, as does homonuclear decoupling. Only strongly coupled systems may be studied, limiting the overall utility. For every pair of labels introduced, only one torsion angle can be determined, thus cost savings from the labeling of only a single residue are offset by the acquistion of more limited information.

2.5.3 Rotational resonance as a method of dihedral angle determination

Rotational resonance was described as a method for distance determination in section 2.3.1. In its description, it was pointed out that, for higher orders of the R^2 condition (for higher n in $n\omega_r=\Delta\omega_{iso}$), magnetization exchange is sensitive to the relative orientation of the CSA tensors of the nuclei, especially if the two spins have broad shift anisotropies. This can be explained as follows[124]. In R^2, the magnetization exchange is due to zero-

quantum transitions driven by rotor spinning. The zero-quantum spectra under MAS have intensities at the difference between the isotropic shifts and in sidebands at positions integer multiples of the rotor frequency away from this centerband. The intensities of these sidebands depend on the individual CSA tensor breadths, as well as on the relative orientation of the tensors. If the two are "parallel" in the sense that their most shielded axes lie in the same direction, sideband formation in the zero-quantum spectra would be weak, while if the most shielded axis for one is parallel with the least shielded axis of the other, sideband formation is strong. The strengths of these sidebands determine the rate of magnetization exchange for higher orders of R^2, and thus the magnetization exchange curves are sensitive to the relative orientation of the CSA tensors.

McDermott and co-workers used this orientational dependence to measure torsion angles in $^{13}C_2$ glycolic acid and in $^{13}C_2$ phosphoglycolic acid bound to the enzyme triose phosphate isomerase (TIM)[124]. The carbons in these samples have large shift anisotropies. Rotational-resonance simulations were used to fit the exchange curves measured and obtain estimations of the angles. The angle measurements obtained for the glycolic acid agreed with those determined by crystallography. Prediction of angles to within 20°-30° is possible.

Although this experiment gives high signal-to-noise, McDermott and co-workers point out that because the $^{13}C_\alpha$ is narrow, R^2 would not be a good technique for measuring dihedral angles along a peptide backbone. In addition, R^2 would not work in cases where the two spins have small or no isotropic shift difference, or in cases where the dipolar coupling between the spins was weak, giving a featureless difference-magnetization decay. In

addition, as before, R^2 simulations require careful estimates of many parameters, some of which can not be derived from experiment.

2.5.4 Conclusions

Clearly, all the techniques developed so far for dihedral angle measurement are useful in many but not all situations and one must carefully choose a technique once the characteristics of the system of interest are known. MAS techniques offer better sensitivity and are thus likely to be used more often in future applications. The ease of these experiments is important; complicated pulse schemes tend to reduce the efficiency of magnetization transfer. The analysis of experimental data with ease and without excessive assumptions is also necessary.

These techniques will be most useful when used in combination with the distance measurement techniques and isotropic shift techniques described above. Samples could be isotopically labeled in such a way as to maximize the information content in each sample, potentially measuring some distances and some isotropic shifts as well as some dihedral angles in each sample. Distances could be used to define tertiary structure, while angle measurements and isotropic shifts would define local secondary structure. Such combinations of techniques seem to hold the greatest promise for SSNMR as a high-resolution structural determination technique.

References

(1) Wüthrich, K. *NMR of Proteins and Nucleic Acids*; Wiley: New York, 1986.
(2) Ernst, R. R.; Bodenhausen, G.; Wokaun, A. *Principles of Nuclear Magnetic Resonance in One and Two Dimensions*; Clarendon Press: Oxford, 1987.
(3) Cavanagh, J.; Fairbrother, W. J.; Palmer, A. G.; Skelton, N. J. *Protein NMR Spectroscopy: Principles and Practise*; Academic Press: San Diego, 1996.
(4) Jeener, J. In *Proc. Ampere International Summer School II*; Basko Polje, Ygoslavia, 1971.
(5) Aue, W. P.; Bartholdi, E.; Ernst, R. R. *J. Chem. Phys.* **1976**, *64*, 2229.
(6) Braunschweiler, L.; Ernst, R. R. *J. Magn. Reson.* **1983**, *53*, 521.
(7) Davis, D. G.; Bax, A. *J. Am. Chem. Soc.* **1985**, *107*, 2820.
(8) Jeener, J.; Meier, B. H.; Bachman, P.; Ernst, R. R. *J. Chem. Phys.* **1979**, *71*, 4546.
(9) Karplus, M. *J. Phys. Chem.* **1959**, *30*, 11-15.
(10) Bystrov, V. F. *Progr. Nucl. Magn. Reson.* **1976**, *10*, 41-82.
(11) Pardi, A.; Billeter, M.; Wüthrich, K. *J. Mol. Biol.* **1984**, *180*, 741-751.
(12) Wagner, G.; Braun, W.; Havel, T. F.; Schaumann, T.; Go, N.; Wüthrich, K. *J. Mol. Biol.* **1987**, *196*, 611-639.
(13) Montelione, G. T.; Emerson, S. D.; Lyons, B. A. *Biopolymers* **1992**, *32*, 327-334.
(14) Andrew, E. R.; Bradbury, A.; Eades, R. G. *Nature (London)* **1958**, *182*, 1659.
(15) Lowe, I. J. *Phys. Rev. Lett.* **1959**, *2*, 285.
(16) Schaefer, J.; Stejskal, E. O. *J. Am. Chem. Soc.* **1976**, *98*, 1031-1032.
(17) Pines, A.; Gibby, M. G.; Waugh, J. S. *J. Chem. Phys.* **1973**, *59*, 569.
(18) Harris, R. K. *Nuclear Magnetic Resonance Spectroscopy*; Longmann Scientific & Technical: New York, 1986.
(19) Maricq, M. M.; Waugh, J. S. *J. Chem. Phys.* **1979**, *70*, 3300.
(20) Haeberlen, U. *High Resolution NMR In Solids*; Academic Press: San Diego, 1976.
(21) Hartmann, S. R.; Hahn, E. L. *Phys. Rev.* **1962**, *128*, 2042.
(22) Bennet, A. E.; Rienstra, C. M.; Auger, M.; Lakshmi, K. V.; Griffin, R. G. *J. Chem. Phys.* **1995**, *103*, 6951-6958.
(23) Raleigh, D. P.; Levitt, M. H.; Griffin, R. G. *Chem. Phys. Lett.* **1988**, *146*, 71-6.
(24) Raleigh, D. P.; Creuzet, F.; Das Gupta, S. K.; Levitt, M. H.; Griffin, R. G. *J. Am. Chem. Soc.* **1989**, *111*, 4502-3.
(25) Levitt, M. H.; Raleigh, D. P.; Creuzet, R.; Griffin, R. G. *J. Chem. Phys.* **1990**, *92*, 6347-6364.
(26) Morris, G. A.; Freeman, R. *J. Magn. Reson.* **1978**, *29*, 433.
(27) Kubo, A.; McDowell, C. A. *J. Chem. Soc., Faraday Trans. 1* **1988**, *84*, 3713-3730.

(28) Creuzet, F.; McDermott, A.; Gebhard, R.; van der Hoef, K.; Spijker-Assink, B.; Herzfeld, J.; Lugtenburg, J.; Levitt, M. H.; Griffin, R. G. *Science* **1991**, *251*, 783-786.
(29) Thompson, L. K.; McDermott, A.; Raap, J.; van der Wielen, C. M.; Lugtenburg, J.; Herzfeld, J.; Griffin, R. G. *Biochemistry* **1992**, *31*, 7931.
(30) Peersen, O. B.; Yoshimura, S.; Hojo, H.; aimoto, S.; Smith, S. O. *J. Am. Chem. Soc.* **1992**, *114*, 4332-4335.
(31) Smith, S. O.; Jonas, R.; Braiman, M.; Bormann, B. J. *Biochemistry* **1994**, *33*, 6334-41.
(32) Lansbury Jr., P. T.; Costa, P. R.; Griffiths, J. M.; Simon, E. J.; Auger, M.; Halverson, K. J.; Kocisko, D. A.; Hendsch, Z. S.; Ashburn, T. T.; Spencer, R. G. S.; Tidor, B.; Griffin, R. G. *Nature Structural Biology* **1995**, *2*, 990-998.
(33) Griffiths, J. M.; Ashburn, T. T.; Auger, M.; Costa, P. R.; Griffin, R. G.; Lansbury Jr., P. T. *J. Am. Chem. Soc.* **1995**, *117*, 3539-3546.
(34) Bennet, A. E.; Ok, J. H.; Griffin, R. G.; Vega, S. *J. Chem. Phys.* **1992**, *96*, 8624-8627.
(35) Griffiths, J. M.; Lakshmi, K. V.; Bennet, A. E.; Raap, J.; Van Der Wielen, C. M.; Lugtenburg, J.; Herzfeld, J.; Griffin, R. G. *J. Am. Chem. Soc.* **1994**, *116*, 10178-10181.
(36) Guilion, T.; Schaefer, J. *J. Magn. Reson.* **1989**, *81*, 196-200.
(37) *Rotational-Echo Double-Resonance NMR*; Gullion, T.; Schaefer, J., Ed.; Academic Press: San Diego, 1989; Vol. 13, pp 57.
(38) Herzog, B.; Hahn, E. L. *Phys. Rev.* **1956**, *103*, 148.
(39) Wang, P.-K.; Slichter, C. P.; Sinfelt, J. H. *Phys. Rev. Lett.* **1984**, *53*, 82.
(40) Gullion, T.; Baker, D. B.; Conradi, M. S. *J. Magn. Reson.* **1990**, *89*, 479.
(41) Gullion, T.; Schaefer, J. *J. Magn. Reson.* **1991**, *92*, 439.
(42) Pan, Y.; Gullion, T.; Schaefer, J. *J. Magn. Reson.* **1990**, *90*, 330-340.
(43) Hing, A. W.; Vega, S.; Schaefer, J. *J. Magn. Reson.* **1992**, *96*, 205-209.
(44) Hing, A. W.; Vega, S.; Schaefer, J. *J. Magn. Reson.* **1993**, *A103*, 151-162.
(45) Griffiths, J. M.; Griffin, R. G. *Analytica Chimica Acta* **1993**, *283*, 1081-1101.
(46) Marshall, G. R.; Beusen, D. D.; Kociolek, K.; Redlinshi, A. S.; Leplawy, M. T.; Pan, Y.; Schaefer, J. *J. Am. Chem. Soc.* **1990**, *112*, 963.
(47) Holl, S. M.; Marshall, G. R.; Beusen, D. D.; Kociolek, K.; Redlinski, A. S.; Leplawy, M. T.; McKay, R. A.; Vega, S.; Schaefer, J. *J. Am. Chem. Soc.* **1992**, *114*, 4830.
(48) Christensen, A. M.; Schaefer, J. *Biochemistry* **1993**, *32*, 2868-2873.
(49) McDowell, L. M.; Schmidt, A.; Cohen, E. R.; Studelska, D. R.; Schaefer, J. *J. Mol. Biol.* **1996**, *256*, 160-171.
(50) Studelska, D. R.; Klug, C. A.; Beusen, D. D.; McDowell, L. M.; Schaefer, J. *J. Am. Chem. Soc.* **1996**, *118*, 5476-5477.
(51) McDowell, L. M.; Klug, C. A.; Beusen, D. D.; Schaefer, J. *Biochemistry* **1996**, *35*, 5395-5403.
(52) Garbow, J. R.; McWherter, C. A. *J. Am. Chem. Soc.* **1993**, *115*, 238-244.

(53) McDowell, L. M.; Holl, S. M.; Qian, S.; Li, E.; Schaefer, J. *Biochemistry* **1993**, *32*, 4560-4563.
(54) Garbow, J. R.; Breslav, M.; Antohi, O.; Naider, F. *Biochemistry* **1994**, *33*, 10094-10099.
(55) Hing, A. W.; Tjandra, N.; Cottam, P. F.; Schaefer, J.; Ho, C. *Biochemistry* **1994**, *33*, 8651-8661.
(56) Beusen, D. D.; McDowell, L. M.; Slomczynska, U.; Schaefer, J. *J. Med. Chem.* **1995**, *38*, 2742-2747.
(57) Mueller, D. D.; Schmidt, A.; Pappan, K. L.; McKay, R. A.; Schaefer, J. *Biochemistry* **1995**, *34*, 5597-5603.
(58) Hirsh, D. J.; Hammer, J.; Maloy, W. L.; Blazyk, J.; Schaefer, J. *Biochemistry* **1996**, *35*, 12733-12741.
(59) McDowell, L. M.; Barkan, D.; Wilson, G. E.; Schaefer, J. *Solid State Nuclear Magnetic Resonance* **1996**, *7*, 203-210.
(60) Wang, J.; Balazs, Y. S.; Thompson, L. K. *Biochemistry* **1997**, *36*, 1699-1703.
(61) Tycko, R.; Dabbagh, G. *Chem. Phys. Lett.* **1990**, *173*, 461-465.
(62) Tycko, R.; Smith, S. O. *J. Chem. Phys.* **1993**, *98*, 932.
(63) Klug, C. A.; Studelska, D. R.; Chen, G.; Gilbertson, S. R.; Schaefer, J. *Solid State Nuclear Magnetic Resonance* **1996**, *7*, 173-176.
(64) Gregory, D. M.; Mitchell, D. J.; Stringer, J. A.; Kiihne, S.; Shiels, J. C.; Callahan, J.; Mehta, M. A.; Drobny, G. P. *Chem. Phys. Lett.* **1995**, *246*, 654-663.
(65) Mehta, M. A.; Gregory, D. M.; Kiihne, S.; Mitchell, D. J.; Hatcher, M. E.; Shiels, J. C.; Drobny, G. P. *Solid State Nuclear Magnetic Resonance* **1996**, *7*, 211-228.
(66) Sternlicht, H.; Wilson, D. *Biochemistry* **1967**, *6*, 2881-2892.
(67) Markley, J. L.; Meadows, D. H.; Jardetzky, O. *J. Mol. Biol.* **1967**, *27*, 25-35.
(68) Saito, H.; Iwanaga, Y.; Tabeta, R.; Narita, M.; Asakura, T. *Chem. Lett.* **1983**, 427.
(69) Kircheldorf, H. R.; Müller, D. *Macromolecules* **1983**, *16*, 615.
(70) Ando, S.; Yamonobe, T.; Ando, I.; Shoji, A.; Ozaki, T.; Tabeta, R.; Saito, H. *J. Am. Chem. Soc.* **1985**, *107*, 7648.
(71) Saito, H.; Tabeta, R.; Shojoi, A.; Ozaki, T. *Macromolecules* **1983**, *16*, 1050-1057.
(72) Kircheldorf, H. R.; Mutter, M.; Frazer, F.; Müller, D.; Forster, D. *Biopolymers* **1983**, *22*, 1357.
(73) Saito, H.; Tabeta, R.; Ando, I.; Ozaki, T.; Shoji, A. *Chem. Lett.* **1983**, 1437.
(74) Shoji, A.; Ozaki, R.; Saito, H.; Tabeta, R.; Ando, I. *Macromolecules* **1984**, *17*, 1472.
(75) Taki, T.; Yamashita, S.; Satoh, M.; Shibata, A.; Yamashita, T.; Tabeta, R.; Saito, H. *Chem. Lett.* **1981**, 1803.
(76) Saito, H.; Tabeta, R.; Shoji, A.; Ozaki, T.; Ando, I.; Miyata, T. *Biopolymers* **1984**, *23*, 2279-2297.
(77) Saito, H. *Magn. Reson. in Chemistry* **1986**, *24*, 835-852.
(78) Saito, H.; Ando, I. *Annu. Rep. NMR Spectrosc.* **1989**, *21*, 209-290.

(79) Shoji, A.; Ozaki, T.; Fujito, T.; Deguchi, K.; Ando, I. *Macromolecules* **1987**, *20*, 2441-2445.
(80) Asakawa, N.; Kuroki, S.; Kurosu, H.; Ando, I.; Shoji, A.; Ozaki, T. *J. Am. Chem. Soc.* **1992**, *114*, 3261-3265.
(81) Ando, S.; Ando, I.; Shoji, A.; Ozaki, T. *J. Am. Chem. Soc.* **1988**, *110*, 3380-3386.
(82) de Dios, A. C.; Oldfield, E. *J. Am. Chem. Soc.* **1994**, *116*, 11485-11488.
(83) Spera, S.; Bax, A. *J. Am. Chem. Soc.* **1991**, *113*, 5490-5492.
(84) Wishart, D. S.; Sykes, B. D.; Richards, F. M. *J. Mol. Biol.* **1991**, *222*, 311-333.
(85) Wishart, D. S.; Sykes, B. D.; Richards, F. M. *Biochemistry* **1992**, *31*, 1647-1651.
(86) Wishart, D. S.; Sykes, B. D. *J. Biomolecular NMR* **1994**, *4*, 171-180.
(87) de Dios, A. C.; Pearson, J. G.; Oldfield, E. *Science* **1993**, *260*, 1491-1496.
(88) de Dios, A. C.; Pearson, J. G.; Oldfield, E. *J. Am. Chem. Soc.* **1993**, *115*, 9768-9773.
(89) de Dios, A. C.; Oldfield, E. *J. Am. Chem. Soc.* **1994**, *116*, 5307-5314.
(90) Le, H.; Pearson, J. G.; de Dios, A. C.; Oldfield, E. *J. Am. Chem. Soc.* **1995**, *117*, 3800-3807.
(91) Kuszewski, J.; Qin, J.; Gronenborn, A. M.; Clore, G. M. *J. Magn. Reson. B* **1995**, *106*, 92-96.
(92) Pearson, J. G.; Wang, J. F.; Markley, J. L.; Le, H.; Oldfield, E. *J. Am. Chem. Soc.* **1995**, *117*, 8823-8829.
(93) Lüginbuhl, P.; Szyperski, T.; Wüthrich, K. *J. Mag. Res. B* **1995**, *109*, 229-233.
(94) Weliky, D. P.; Dabbagh, G.; Tycko, R. *J. Magn. Reson.* **1993**, *A104*, 10-16.
(95) Dabbagh, G.; Weliky, D. P.; Tycko, R. *Macromolecules* **1994**, *27*, 6183-6191.
(96) Henrichs, P. M.; Linder, M. *J. Magn. Reson.* **1985**, *58*, 458.
(97) Suter, D.; Ernst, R. R. *Phys. Rev.* **1986**, *B25*, 6038.
(98) Tycko, R.; Dabbagh, G. *Isr. J. Chem.* **1992**, *32*, 179.
(99) Schmidt-Rohr, K.; Speiss, H. W. *Multidimensional Solid-State NMR and Polymers*; Academic Press: London, 1994.
(100) Carr, H. Y.; Purcell, E. M. *Phys. Rev.* **1954**, *94*, 630.
(101) Rhim, W.-K.; Elleman, D. D.; Vaughan, R. W. *J. Chem. Phys.* **1973**, *59*, 3740.
(102) Ishii, Y.; Terao, T.; Kainosho, M. *Chem. Phys. Lett.* **1996**, *256*, 133-140.
(103) Weliky, D. P.; Tycko, R. *J. Am. Chem. Soc.* **1996**, *118*, 8487-8.
(104) Tycko, R.; Weliky, D. P.; Berger, A. E. *J. Chem. Phys.* **1996**, *105*, 7915-7930.
(105) Tycko, R.; Dabbagh, G.; Mirau, P. A. *J. Magn. Reson.* **1989**, *85*, 3816.
(106) Takegoshi, K.; Nomura, K.; Terao, T. *Chem. Phys. Lett.* **1995**, *232*, 424.
(107) Caravatti, P.; Braunschweiler, L.; Ernst, R. R. *Chem. Phys. Lett.* **1983**, *100*, 305.
(108) Bielecki, A.; Kolbert, A. C.; Levitt, M. H. *Chem. Phys. Lett.* **1989**, *155*, 341.

(109) Hester, R. K.; Ackerman, J. L.; Neff, B. L.; Waugh, J. S. *Phys. Rev. Lett.* **1976**, *36*, 1081.
(110) Stoll, M. E.; Vega, A. J.; Vaughan, R. W. *J. Chem. Phys.* **1976**, *65*,
(111) Rybaczewski, E. F.; Neff, B. L.; Waugh, J. S.; Sherfinski, J. S. *J. Chem. Phys.* **1977**, *67*, 1231.
(112) Linder, M.; Hohener, A.; Ernst, R. R. *J. Chem. Phys.* **1980**, *73*, 4959.
(113) Hu, J. Z.; Alderman, D. W.; Pugmire, R. J.; Grant, D. M. *J. Magn. Reson.* **1997**, *126*, 120-126.
(114) Tycko, R.; Dabbagh, G. *J. Am. Chem. Soc.* **1991**, *113*, 3592.
(115) Schmidt-Rohr, K. *Macromolecules* **1996**,
(116) Bax, A.; Freeman, R.; Kempsell, S. P. **1980**, *102*, 4849.
(117) Bax, A.; Freeman, R. *J. Magn. Reson.* **1980**, *41*, 507.
(118) Bax, A.; Freeman, R.; Frankiell, T.; Levitt, M. H. *J. Magn. Reson.* **1981**, *43*, 478.
(119) Mareci, T. H.; Freeman, R. *J. Magn. Reson.* **1982**, *48*, 158.
(120) Nakai, T.; McDowell, C. A. *Mol. Phys.* **1993**, *79*, 965.
(121) Schmidt-Rohr, K. *J. Am. Chem. Soc.* **1996**, *118*, 7601-3.
(122) Feng, X.; Lee, Y. K.; Sandstrom, D.; Eden, M.; Maisel, H.; Sebald, A.; Levitt, M. H. *Chem. Phys. Lett.* **1996**, *257*, 314-320.
(123) Lee, Y. K.; Kurur, N. D.; Helmle, M.; Johannessen, O. G.; Nielsen, N. C.; Levitt, M. *Chem. Phys. Lett.* **1995**, *242*, 304.
(124) Tomita, Y.; O'Conner, E. J.; McDermott, A. *J. Am. Chem. Soc.* **1994**, *116*, 8766-8771.

SECTION II:

SSNMR TECHNIQUE DEVELOPMENT

Chapter 3

Application of Rotational Resonance to Inhomogeneously Broadened Systems

3.1 Introduction

As described in the introduction, the reintroduction of dipolar couplings into solid-state nuclear magnetic resonance (NMR) magic-angle spinning (MAS) spectra has become an important method for the measurement of distances in polycrystalline solids. Homonuclear and heteronuclear dipolar couplings can be reintroduced through pulse sequences or, for homonuclear spin pairs, by matching the spinning speed to the difference of the isotropic chemical shifts, a particularly useful technique known as rotational-resonance magnetization-exchange[1,2]. To date, rotational resonance has produced reliable results in systems where the measured distances are known *a priori*, and error estimates have been derived by comparison with the known distances. The general utility of this technique is dependent on the ability to determine the zero-quantum relaxation times and to account for the effects of inhomogeneously broadened single-quantum transitions. Since the magnetization transfer caused by rotational resonance not only depends on the distance between spins but also on the rotational-resonance condition and the zero-quantum relaxation, it is important to take account of the impact of each parameter and to develop an approach for estimating errors.

In this chapter[3], a modified simulation program, including inhomogeneous broadening is described and used to fit the rotational-

resonance exchange curves, giving well defined errors of the distance (r_{cc}), the transverse zero-quantum relaxation time (T_{2ZQ}), and the inhomogeneous linewidth ($\Delta\nu_{1/2}$; full width at half height). For short distances, $r_{cc} \leq 3.5$Å, magnetization exchange curves show resolved oscillations and the correlation between parameters is low, allowing simultaneous optimization of all three parameters. For long distances, however, no resolved oscillations are observed in the magnetization exchange, and the parameters are highly correlated. In these cases, the use of the optimized values of T_{2ZQ} and $\Delta\nu_{1/2}$, obtained from a short distance measurement under similar conditions, to fit only r_{cc} is proposed.

3.2 Theory and Simulations

The theory of rotational-resonance experiments has been extensively discussed previously[2]. The relevant part of the homonuclear coupled two-spin system can be described as a fictitious spin-1/2 using Bloch-type equations in a reduced three by three Liouville space[4]. In this work T_{2ZQ} relaxation was included in the simulations; T_1 relaxation was assumed to be much longer and was therefore neglected. The simulation of the time-dependent Liouvillian was implemented using Floquet theory[5-7] using the NMR simulation environment GAMMA[8]. Powder averages were performed using the method of Cheng et al.[9] to obtain an optimal coverage of the sphere. Inhomogeneous broadening of the single-quantum transitions was introduced into the simulations by stepping the chemical-shift difference from the rotational-resonance condition with weightings appropriate to a Lorentzian lineshape[10]. The chemical-shielding tensor values were fixed at values taken from the literature[11], while the orientation of the three

principle axes with respect to the dipolar coupling was fixed at a random orientation. The J-coupling value was assumed to be 0 Hz. It has been shown that when the spinning speed equals the chemical-shift difference (i.e. the n=1 rotational-resonance condition), magnetization exchange is relatively insensitive to the chemical-shielding tensor values and its orientation[12,13].

The simulation program was integrated into a nonlinear least-square optimization routine, which allowed us to simultaneously optimize r_{cc}, T_{2ZQ} and $\Delta\nu_{1/2}$, or any subset of these parameters[13-15]. Statistical errors and cross-correlation coefficients, as well as error potentials and surfaces were calculated. For the optimizations, typical parameters were 18 time points, 200 different powder orientations, and a Floquet space truncated to a dimension of seven. Inhomogeneity was included by stepping the chemical-shift difference through ten values, up through three linewidths. The correlation between the chemical shift inhomogeneity of the two lines was determined by fitting this linewidth. If the chemical shifts of the two lines were completely correlated, the linewidth obtained would be zero, while if the two lines were completely uncorrelated, the resulting linewidth would equal the observed linewidth, i.e. the correlation of the chemical shift inhomogeneity of the two lines is reflected in the ratio of the observed linewidth and fit linewidth. A three-parameter optimization on an SGI Indigo^2 with a MIPS R4000 processor typically took several hours. For a one-parameter optimization of r_{cc}, optimization time was thirty minutes on the same computer.

3.3 Experimental Procedures

A home-built spectrometer operating at a ^1H Larmor frequency of 301.2 MHz and a Chemagnetics (Fort Collins, CO) 4-mm double resonance high-speed spinning probe were used for all experiments. Spinning speeds were controlled to ±10 Hz with long-term stability, using a home-built spinning-speed controller using a phase-locked loop. CP contact time was 2.5 ms, the ^1H decoupling field strength was 100 kHz, and recycle delays were 5 seconds.

All experiments were carried out on three doubly-labeled fourteen residue peptides, with the sequence MKHMAGAAAAGAVV[16]. The first sample (sample I) was ^{13}C labeled at the carbonyl of glycine-6 and C_α of alanine-7, with a distance of r_{cc} = 2.4 Å. The second sample (sample II) was labeled at the carbonyl of alanine-5 and C_α of alanine-7, providing an r_{cc} between 4.5 Å and 5.4 Å, depending on the conformation of the peptide. Sample II was diluted to 10% in natural abundance background to reduce intermolecular effects, which are insignificant for sample I. Sample III, used for hole burning experiments, was ^{13}C labeled at the carbonyl of alanine-7 and C_α of glycine-6, with an r_{cc} between 4.4 Å and 4.7 Å.

The pulse sequence used for rotational-resonance magnetization exchange is shown in figure 3.1. After cross polarization from protons to carbon, the carbon magnetization was stored along the z-axis and proton decoupling was turned on for the duration of the experiment. A variable delay (δ-τ_m) was inserted before the selective inversion to keep the total experiment time constant[15]. This led to the same power dissipation due to proton decoupling in all experiments, independent of τ_m, eliminating differential radio-frequency heating effects as a source of error in measurements. The on-resonance carbon magnetization was inverted with

either a weak cw-pulse or a DANTE sequence[17] and after a variable length mixing time, τ_m, a carbon read pulse returned the magnetization to the x-y plane for detection. During the entire experiment, the sample was spun at the magic angle at a frequency that was equal to the isotropic chemical shift difference between the ^{13}C labeled peaks.

Data were acquired as follows. At least 256 scans were acquired at the beginning of each experiment and discarded in order to allow the spectrometer and probe to stabilize. A cycle of data collection consisted of 32 or 64 scans acquired for each of the eighteen mixing times τ_m, with the time points in random order. These cycles were repeated many times. For each

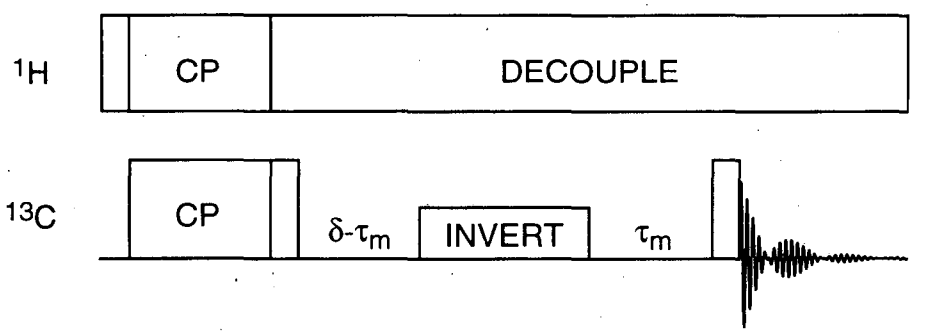

Figure 3.1: The pulse sequence used for rotational-resonance experiments. After cross-polarization the magnetization is stored in the z direction and the on-resonance component is inverted by a weak rf-pulse or a DANTE sequence. A variable length delay (δ-τ_m) is inserted before the inversion to keep the total experiment time constant, independent of τ_m. After the delay τ_m magnetization is returned to the x-y plane for detection. During the experiment, the sample is spun at the magic angle with the frequency set to the difference of the isotropic chemical shifts of the two lines. High-power proton decoupling is applied after cross polarization for the duration of the experiment.

experiment, the spectral regions occupied by the ^{13}C labels and a region occupied by natural-abundance resonances, resolved from the labeled peaks, were integrated separately. These integrals were used to calculate the experimental mean and standard deviation of the spectral amplitudes for the full data set.

The integral of the natural-abundance peak was monitored to ensure that all intensity changes are due to magnetization exchange rather than experimental artifact[18]. The natural-abundance peak was also used to estimate the natural-abundance contribution to each of the ^{13}C labeled peaks, since in general the natural-abundance isochromats do not undergo magnetization exchange at the same rate as the isotopically labeled nuclear pair. The natural-abundance contribution was subtracted from the integral of the labeled peak before statistical analysis and calculation of the difference magnetization. This subtraction was carried out using the integrals of identical spectral regions in both labeled and natural-abundance samples with spectra normalized in spectral regions resolved from resonances due to isotopic labels.

In order to determine if inhomogeneity values determined by fits were realistic, hole-burning experiments (figure 3.2) were carried out on sample III, spinning at the magic angle at a frequency matching the n=1 rotational-resonance condition for the chemical-shift difference between peak maxima. A separate frequency synthesizer was used to generate very low-power rf ($\gamma B_1/(2\pi) \approx 30$ Hz) that could be coupled into the probe. Two experiments were performed. After cross polarization, magnetization was stored along the

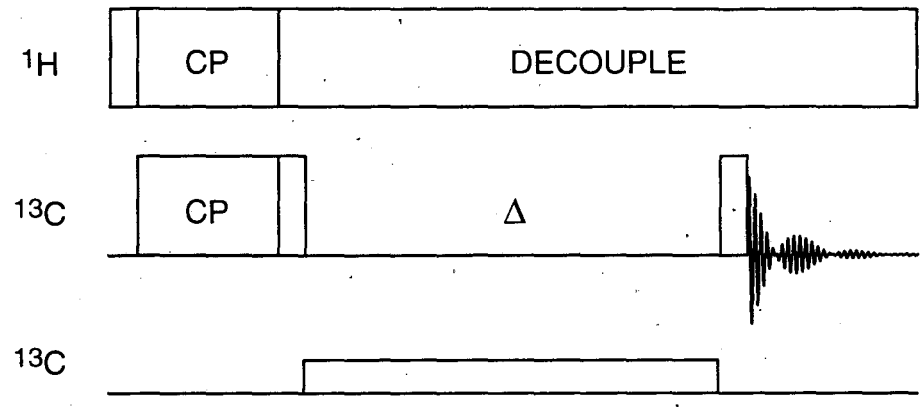

Figure 3.2: The pulse sequence used for hole-burning experiments. After cross-polarization, the magnetization is stored along the z direction and a weak rf-field is irradiated at the carbonyl frequency for Δ = 80 ms. The magnetization is then returned to the x-y plane for detection. During the experiment, the sample is spun at the magic angle with the frequency set to the difference of the isotropic chemical shifts of the two lines. High-power proton decoupling is applied after cross polarization for the duration of the experiment.

z-axis, and, in the first experiment, the low-power rf was turned on for 80 ms, with its frequency set to the center of the carbonyl resonance frequency. In the control experiment, the low-power rf was not used. In both cases, a read pulse was then applied, and the signal detected. In the hole-burning experiment, the long, weak rf pulse saturated a line within the carbonyl resonance whose linewidth was determined by the T_2 of the line. Because the rotational-resonance condition was met, this saturation was transferred to the spins of the C_α peak that were coupled to the spins being saturated. By subtracting the hole-burning experiment from the control, the shapes of the burned and transferred holes were obtained. If the lines were completely correlated, the

linewidth of the transferred hole would be determined by the T_2 of the C_α resonance, but if the lines were completely uncorrelated (randomly correlated), the linewidth of the transferred hole would be the product of the inhomogeneous linewidth and the linewidth of the rotational-resonance condition. If the lines were partially correlated, the linewidth would fall between these two values.

3.4 Evaluation of Data and Discussion

Fits of the inhomogeneous linewidth always resulted in values greater than zero but less than the observed linewidth, indicating partial, but not complete, correlation of the chemical-shift inhomogeneity of the two lines. The importance of including the inhomogeneous linebroadening into the simulations is clearly demonstrated in figure 3.3a. The best fit for a short distance (sample I) without inclusion of the inhomogeneous broadening ($\Delta\nu_{1/2}$ = 0 Hz, dashed line) fits the measured data very poorly, while inclusion of the inhomogeneity (solid line) improves the fit from χ^2 = 3052 to χ^2 = 49. The fitted parameters also differ considerably. For the two-parameter fit, we obtain r_{cc} = 2.229 ± 0.009 Å and T_{2ZQ} = 0.89 ±0.03 ms, while for the three-parameter fit, we obtain r_{cc} = 2.370 ± 0.046 Å, T_{2ZQ} = 9.54 ±0.41 ms, and $\Delta\nu_{1/2}$ = 77 ± 3 Hz. For the short distance, the parameters were largely uncorrelated, ($\rho(\Delta\nu_{1/2}, r_{cc}) = 0.4$, $\rho(\Delta\nu_{1/2}, T_{2ZQ}) = 0.6$, and $\rho(T_{2ZQ}, r_{cc}) = 0.5$). This can also be seen from the plot of the χ^2 error surfaces as a function of the three parameters (figure 3.4a). In the case of completely uncorrelated parameters, one would expect a circle in these plots[19]. The surfaces observed are only slightly elliptical. Therefore, the simultaneous optimization of all three parameters gives meaningful results.

For a long distance (sample II) the three-parameter fit yields no meaningful results due to the high correlation ($\rho(\Delta\nu_{1/2}, r_{cc}) = 0.99$, $\rho(\Delta\nu_{1/2}, T_{2ZQ}) = 0.82$, and $\rho(T_{2ZQ}, r_{cc}) = 0.88$) of the parameters, so simultaneous optimization of all three parameters is not possible. The high correlation of the parameters is clearly demonstrated in the χ^2 error surfaces (figure 3.4b) as a function of the three variable parameters showing error surfaces that are strongly distorted ellipses. Although inhomogeneity is present in the system, a good two-parameter fit (assuming no inhomogeneity) of rotational-resonance data for a long distance is possible (figure 3.3b, dashed line), due to the high correlation of parameters ($\rho(T_{2ZQ}, r_{cc}) = 1.00$). However such fits give unrealistic values and large error margins for fitted parameters: $r_{cc} = 4.558 \pm 1.35$ Å, $T_{2ZQ} = 0.53 \pm 0.97$ ms and $\chi^2 = 8.3$. In order to overcome this problem we propose to use the optimized values for $\Delta\nu_{1/2}$ and T_{2ZQ} obtained from the fit of the short distance in a one-parameter fit of r_{cc}. The transferability of these parameters should be a valid assumption if the samples are prepared under similar conditions, and have similar homogeneous and inhomogeneous linewidths. The one-parameter fit (using $T_{2ZQ} = 9.54$ ms and $\Delta\nu_{1/2} = 77$ Hz obtained from peptide I) results in a distance of $r_{cc} = 5.399 \pm 0.064$ Å (figure 3.3b, solid line). The χ^2 of this one-parameter fit is 7.7 compared to a χ^2 of 6.7 for the three parameter fit.

Presumably the best solution to the correlated parameter problem would be to measure T_{2ZQ} and $\Delta\nu_{1/2}$ independently. The zero-quantum relaxation time is difficult to measure and, so far, approximations have been used to calculate the T_{2ZQ} based on the T_2's of the two involved spins[20]. The correlation between inhomogeneous lines $\Delta\nu_{1/2}$ is also difficult to measure and will be discussed in more detail.

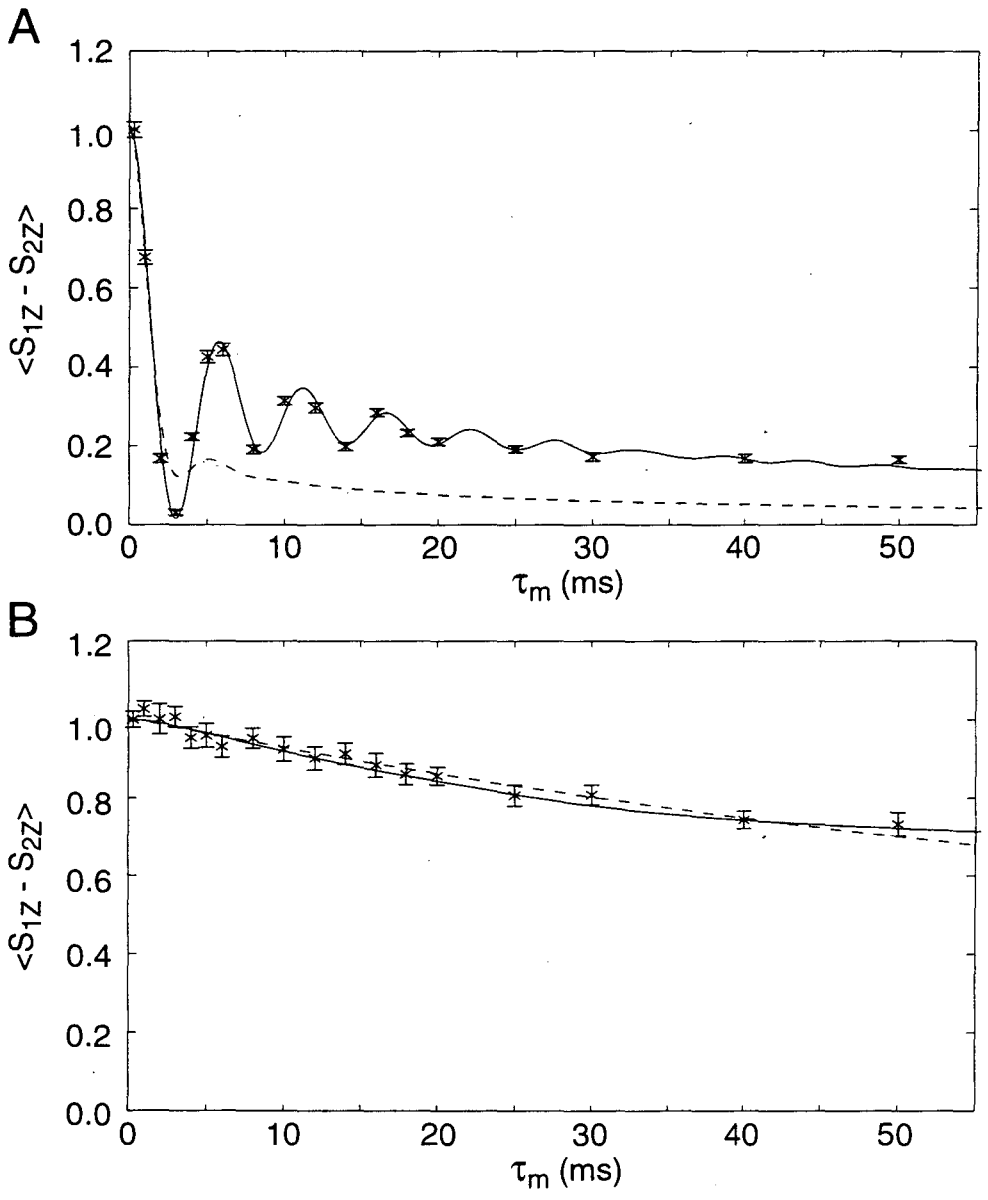

Figure 3.3: Experimental and simulated rotational-resonance magnetization-exchange curves for a) a short distance ($r_{cc} \approx 2.4$ Å, sample I) and b) a long distance ($r_{cc} \approx 4.5$ Å, sample II). The measurement for the short distance (a) shows well resolved oscillations. The best two-parameter fit (dashed line) with $\Delta\nu_{1/2} = 0$ Hz does not agree at all with the experimental data, while the three-parameter fit (solid line) agrees very well with the measured points. The measurement for the long distance (b) shows only a multiexponential decay but no oscillations. In this case both the two-parameter fit of the distance r_{cc} and the T_{2ZQ} (dashed line, $\Delta\nu_{1/2} = 0$) and the one-parameter fit of r_{cc} (solid line, $\Delta\nu_{1/2}$ and T_{2ZQ} set to optimized values from the short distance fit) give good agreement with the experimental data, but the two-parameter fit gives unrealistic values of the fit parameters.

For short distances, errors are determined by the three-parameter fit, and we report errors as two standard deviations, giving an r_{cc} for sample I between 2.28 Å and 2.46 Å, bracketing the true value of 2.40 Å. Error bounds for the longer distance measurements are calculated by putting bounds on the zero-quantum relaxation time and the inhomogeneity. To obtain a lower bound for the distance consistent with an experimental data set, a one-parameter fit of the distance was run setting T_{2ZQ} equal to the shortest estimated value and using the largest reasonable degree of inhomogeneous broadening. The upper bound for the distance came from a one-parameter fit of the distance, using the longest reasonable T_{2ZQ} value and the smallest reasonable amount of inhomogeneous broadening. The maximum T_{2ZQ} was taken to be 1.5 times the fit T_{2ZQ}, while the minimum was estimated from the single-quantum T_2's[20]. The maximum inhomogeneity was taken to be the linewidth of the broader of the two peaks, while its minimum was taken to be 0 Hz. This leads to an r_{cc} for sample II between 4.94 Å and 7.18 Å.

The inhomogeneous linewidth derived from fits of short distances indicate that the C=O and C_α lines are partially correlated. Hole-burning experimental results (figure 3.5) confirm these results. The hole burned by the low-power rf has a linewidth of 63 Hz, which is nearly the measured homogenous linewidth of the carbonyl (44 Hz ± 6) found from a CPMG experiment[21,22]. The linewidth of the transferred hole (95 Hz) is somewhat larger than the real homogenous linewidth of the C_α (48 Hz ± 6), but is smaller than the full inhomogeneous linewidth (151 Hz). This result clearly demonstrates that some inhomogeneity exists in the chemical-shift difference, but also suggests that the shift difference is at least partially correlated. This experimental result is consistent with results obtained

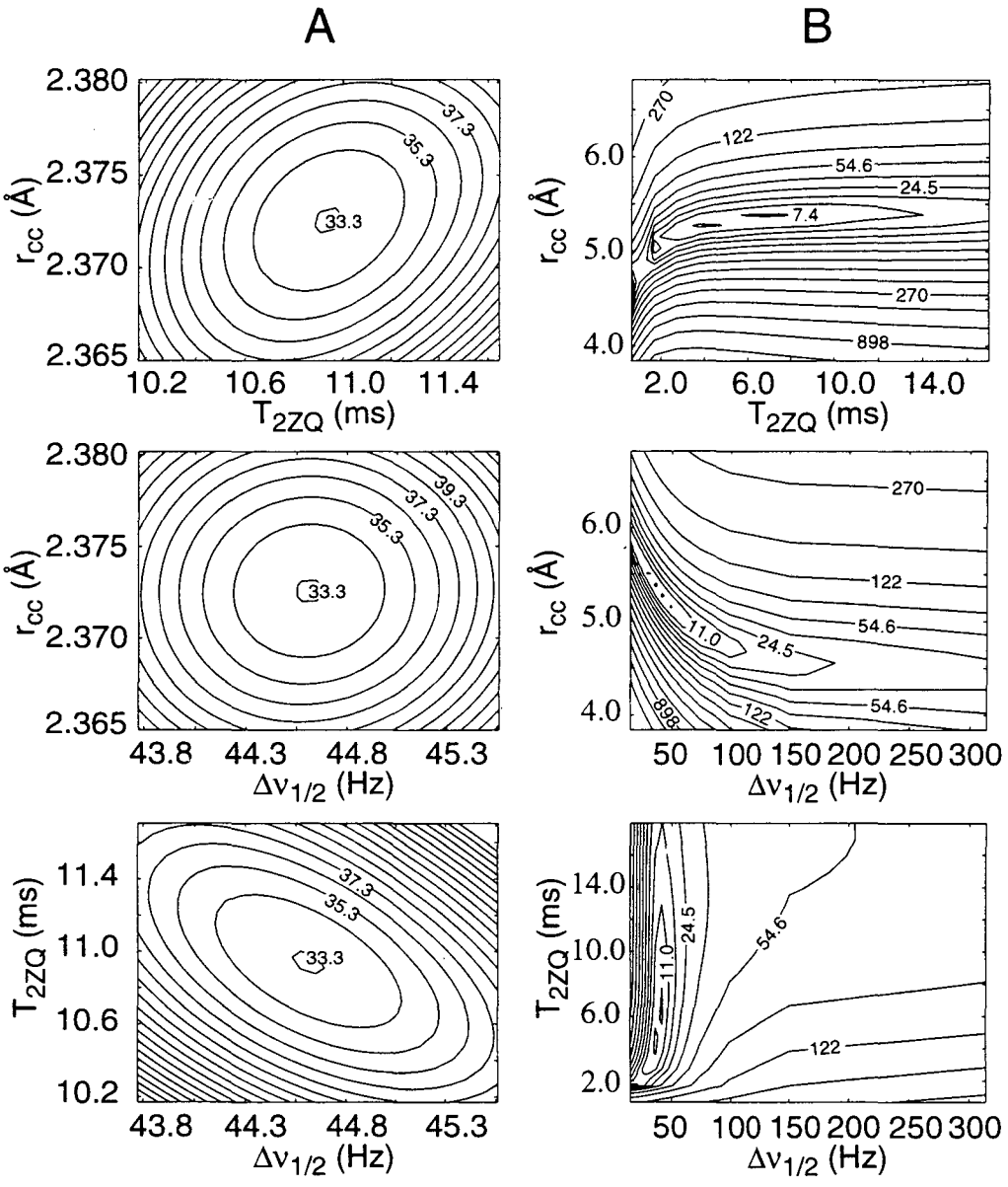

Figure 3.4: Two-dimensional error surfaces showing χ^2 as a function of the three different fit parameters r_{cc}, $\Delta\nu_{1/2}$, and T_{2ZQ} for a short distance (a) and a long distance (b). For the short distance, all three correlation coefficients are small ($\rho(\Delta\nu_{1/2},r_{cc}) = 0.4$, $\rho(\Delta\nu_{1/2}, T_{2ZQ}) = 0.6$, and $\rho(T_{2ZQ}, r_{cc}) = 0.5$), resulting in largely undistorted error ellipses. The long distance shows high correlations ($\rho(\Delta\nu_{1/2},r_{cc}) = 0.99$, $\rho(\Delta\nu_{1/2}, T_{2ZQ}) = 0.82$, and $\rho(T_{2ZQ},r_{cc}) = 0.88$) resulting in highly distorted error ellipses in the error surface plots.

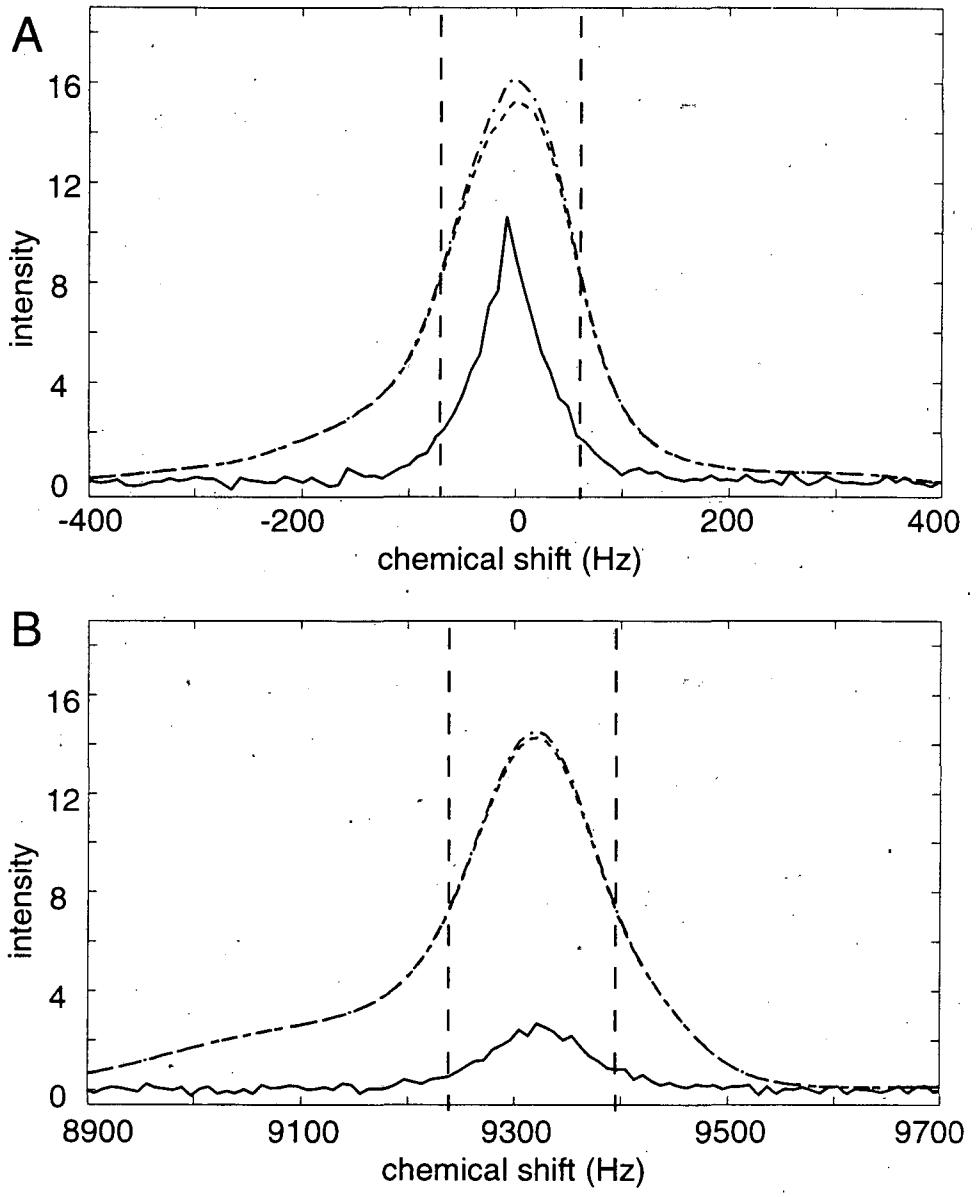

Figure 3.5: Experimental results of holeburning experiments for sample III. The hole-burned spectrum (- -), taken with the low-power ^{13}C rf during the delay Δ, is subtracted from the control spectrum (— . —), taken without the low-power rf. Vertical dashed lines indicate the half height of the control spectrum. Ten times the difference spectrum (—) shows the shape of the hole burned and of the hole transferred. a) An expansion of the carbonyl region. The difference spectra shows the shape of the hole burned by the low-power rf. Its linewidth is 63 Hz, which is approximately the width of the homogenous line (44 Hz $\pm$ 6). b) An expansion of the C_α region. The difference spectrum shows the hole transferred by rotational resonance. Its width is 95 Hz, which is between the linewidth of the homogeneous line (48 Hz $\pm$ 6) and the linewidth of the inhomogeneous line (151 Hz).

through parameter fitting, and supports our position that inhomogeneity should be included in the simulations and that our method of simulating inhomogeneity is acceptable.

3.5 Conclusions

A protocol for using rotational-resonance magnetization exchange to determine distances in inhomogeneously broadened systems has been described. Short distance measurements were used to determine the zero-quantum relaxation time and the degree of correlation of chemical-shift inhomogeneity in the sample through three-parameter fits, and these parameters were then used as constants in one-parameter fits for the longer distances. Errors were calculated by putting bounds on our estimates of these two parameters and doing one-parameter fits of the distance to obtain maximum and minimum possible distances. The incorporation of fitting procedures with explicit protocols for obtaining numerical error bounds is useful for the study of internuclear distances and structures by rotational-resonance magnetization-exchange techniques.

References:
(1) Raleigh, D. P.; Levitt, M. H.; Griffin, R. G. *Chem. Phys. Lett.* **1988**, *146*, 71-6.
(2) Levitt, M. H.; Raleigh, D. P.; Creuzet, R.; Griffin, R. G. *J. Chem. Phys.* **1990**, *92*, 6347-6364.
(3) Heller, J.; Larsen, R.; Ernst, M.; Kolbert, A. C.; Baldwin, M.; Prusiner, S. B.; Wemmer, D. E.; Pines, A. *Chem. Phys. Lett.* **1996**, *251*, 223-229.
(4) Ernst, R. R.; Bodenhausen, G.; Wokaun, A. *Principles of Nuclear Magnetic Resonance in One and Two Dimensions*; Clarendon Press: Oxford, 1987.
(5) Shirley, J. H. *Phys. Rev. B* **1965**, *138*, 979.
(6) Vega, S. *J. Chem. Phys.* **1992**, *96*, 2655-2680.
(7) Levante, T. O.; Baldus, M.; Meier, B. H.; Ernst, R. R. *Mol. Phys.* **1995**, *86*, 1195.
(8) Smith, S. A.; Levante, T. O.; Meier, B. H.; Ernst, R. R. *J. Magn. Reson.* **1994**, *A106*, 75-105.
(9) Cheng, V. B.; Suzukawa, H. H.; Wolfsberg, M. *J. Chem. Phys.* **1973**, *59*, 3992-3999.
(10) Griffiths, J. M.; Ashburn, T. T.; Auger, M.; Costa, P. R.; Griffin, R. G.; Lansbury Jr., P. T. *J. Am. Chem. Soc.* **1995**, *117*, 3539-3546.
(11) Duncan, T. M. *A Compilation of Chemical Shift Anisotropies*; The Farragut Press: Chicago, 1990.
(12) Raleigh, D. P.; Creuzet, F.; Das Gupta, S. K.; Levitt, M. H.; Griffin, R. G. *J. Am. Chem. Soc.* **1989**, *111*, 4502-3.
(13) Thompson, L. K.; McDermott, A.; Raap, J.; van der Wielen, C. M.; Lugtenburg, J.; Herzfeld, J.; Griffin, R. G. *Biochemistry* **1992**, *31*, 7931.
(14) Creuzet, F.; Raleigh, D. P.; Levitt, M. H.; Griffin, R. G. *J. Am. Chem. Soc.* in press.
(15) Tomita, Y.; O'Connor, E. J.; McDermott, A. *J. Am. Chem. Soc.* **1994**, *116*, 8766-8771.
(16) Prusiner, S. B. *Biochemisry* **1992**, *31*, 12277-12288.
(17) Morris, G. A.; Freeman, R. *J. Magn. Reson.* **1978**, *29*, 433.
(18) Peerson, O.; Groesbeek, M.; Aimoto, S.; Smith, S. O. *J. Am. Chem. Soc.* **1995**, *117*, 7228-7237.
(19) Clifford, A. A. *Multivariate Error Analysis*; Applied Science Publishers LTD: London, 1973.
(20) Kubo, A.; McDowell, C. A. *J. Chem. Soc., Faraday Trans. 1* **1988**, *84*, 3713-3730.
(21) Carr, H. Y.; Purcell, E. M. *Phys. Rev.* **1954**, *94*, 630.
(22) Meiboom, S.; Gill, D. *Rev. Sci. Instrum.* **1958**, *29*, 688.

Chapter 4

Determination of dihedral angles in peptides through experimental and theoretical studies of alpha-carbon chemical shielding tensors

4.1 Introduction

As was pointed out in the introduction, structural studies of peptides and proteins that aggregate, such as those responsible for Alzheimer's disease[1] and prion diseases[2], of membrane proteins such as bacteriorhodopsin[3] and glycophorin A[4], and of large systems which do not fall into the fast-tumbling regime[5,6] have been carried out via SSNMR. Many SSNMR techniques have been developed recently to measure both distances[7-10] and dihedral angles[11-15] in solids. However, most of these methods require a doubly labeled sample per distance or angle being measured. The information content per sample is thus low, making SSNMR expensive.

One possible means for augmenting the information from SSNMR is to use *ab initio* chemical-shielding computations to gain insight into the backbone structure of a protein. In such methods, the chemical shielding is calculated as a function of the backbone (and potentially the side-chain) torsion angles. Correlations between isotropic chemical shifts and secondary structure in proteins were discussed in the introduction and have been observed in both liquids[16,17] and solids[2,18,19] and have been reproduced in theoretical calculations[20,21]. Such correlations allow the determination of chemical-shift/shielding surfaces[16,22-24] as a function of the dihedral angles. Coupling these calculations with experimental chemical-shift data has

permitted both the further refinement of solution structures[25-27], as well as probability-based predictions of dihedral angles[28].

In this chapter[29], a technique for the determination of backbone dihedral angles in solid-state peptides and proteins which exploits the additional information contained in the chemical-shift anisotropy through the measurement of the chemical-shift tensor and comparison with theoretical calculations via the Z-surface method[28] is introduced. Whereas previously two or three experimental isotropic chemical shifts would be needed to determine a unique phi/psi (ϕ/ψ) pair[28], this can now be achieved in solids by using just the three components of the chemical-shift anisotropy (CSA) of a single alpha-carbon (C_α). This technique is experimentally simple: using a 1-D cross-polarization magic-angle-spinning[30,31] spectrum at spinning speeds slow compared to the CSA (slow CPMAS), one can derive the CSA for a singly ^{13}C labeled sample. If a 2-D CPMAS experiment[32-41] is used to resolve any overlap in the many spinning sidebands, this method should also be applicable to samples with multiple ^{13}C labels.

The $^{13}C_\alpha$ CSA of the central alanine in three crystal forms of the tripeptides glycyl-L-alanyl-L-valine[42] (G*AV) and L-alanyl-L-alanyl-L-alanine[43,44] (A*AA and A*AA-hemihydrate) by slow CPMAS experiments have been measured. The measured values correlate well with those calculated by *ab initio* methods using ϕ and ψ angles around the central alanine C_α taken from the known crystal structures. Using the correlation for the A*AA and A*AA-hemihydrate peptides and the measured CSA of G*AV, ϕ/ψ space probability surfaces (Z-surfaces) are calculated for the alanine C_α in G*AV. The highest calculated probability is within ±12° in both ϕ and ψ of the values determined in the x-ray crystal structure. Although in this work only

the correlation for alanine residues and for backbone dihedral angles is determined, the method is general and can be extended to other amino acids and possibly to side-chain dihedral angles with the addition of more tensor restraints.

4.2 Experimental

4.2.1 Fmoc-^{13}C amino acids

$^{13}C_\alpha$-labeled alanine (Cambridge Isotope Laboratories, Andover, MA) was Fmoc-protected in a manner similar to one previously described[45]. To 3.75 mmol of alanine dissolved in H_2O (60 mL), 0.945 g (11.25 mmol) of sodium bicarbonate ($NaHCO_3$) was added. After dissolving 1.265 g (3.75 mmol) of N-(9-fluorenylmethoxycarbonyloxy) succinimide (Fmoc-O-Suc) in acetone (60 mL), the mixtures were combined. The cloudy mixture became clear after stirring for 24 hours, at which point the acetone was removed by rotary evaporation. Citric acid (1M) was used to precipitate Fmoc-$^{13}C_\alpha$-alanine from the aqueous solution. Ethyl acetate (EtOAc) (150 mL) was added to redissolve the precipitate. The mixture was transferred to a separatory funnel and the layers were separated. The aqueous layer was washed with EtOAc (100 mL). The combined organic layers were then washed with H_2O (2 x 100 mL) and saturated NaCl (2 x 100 mL). The organic layers were dried over magnesium sulfate and the solvent was removed by rotary evaporation. The product was used for solid-phase peptide synthesis without further purification.

4.2.2 Tripeptides

G*AV and A*AA were synthesized using N-Fmoc protected amino acids on an Applied Biosystems 431A peptide synthesizer. The peptides were cleaved from the resin and deprotected by stirring for 3 hours in a 95% (v/v) trifluoroacetic acid (TFA)/H_2O solution. The mixture was filtered to remove resin. TFA was removed by rotary evaporation, followed by lyophilization. The cleaved A*AA was then redissolved in H_2O and purified by reversed-phase HPLC on a Vydac C-18 column. Purity and identity of all samples were checked by electrospray-ionization mass spectrometry (Hewlett-Packard 5989A).

4.2.3 Crystallization

Peptides were crystallized following the protocols described previously, with slight modifications made in order to crystallize larger quantities. In all cases, small crystal clusters were obtained, large single crystals are not necessary in this approach. G*AV[42] was dissolved in a minimal volume of warm H_2O and the solution was placed in a Petri dish. The dish was then placed into a sealed container over a reservoir of methanol. Due to vapor diffusion, small crystals formed quickly and crystallization was complete within a day. A*AA was crystallized in two crystal forms[43,44]. The first, A*AA-hemihydrate (needles), was formed by dissolving the tripeptide in a solution of 20% *N,N'*-dimethylformamide (DMF)/H_2O and placing the solution in a glass Petri dish. The solvent was allowed to evaporate slowly. The second crystal form of A*AA (plates) was formed by a similar procedure, except that the concentration of DMF was 60%.

The dihedral angles around the central alanine for the peptides as determined by the crystal structures were: G*AV: ϕ = -68.7°, ψ = -38.1°; A*AA

molecule A: ϕ = -143.4°, ψ = 160.2° and A*AA molecule B: ϕ = -164.1°, ψ = -149.0°; A*AA-hemihydrate molecule A: ϕ = -145.7°, ψ = 145.5° and A*AA-hemihydrate molecule B: ϕ = -156.2°, ψ = 149.9°.

4.2.4 Solid State NMR

All ^{13}C NMR spectra were obtained at 7.07 Tesla (corresponding to a ^{13}C Larmor frequency of 75.74 MHz) on a home-built spectrometer based on a Tecmag (Houston, Texas) pulse programmer. A Chemagnetics (Fort Collins, CO) 4-mm double-resonance MAS probe was used for all experiments. Spinning speeds were controlled to ±1 Hz using a home-built spinning-speed controller. CP contact time was 2.5 ms, the ^{1}H decoupling field strength was 108 kHz, and the recycle delay was 1.5 seconds. For each crystal form studied, slow CPMAS experiments at three spinning speeds were carried out.

The experimental data was fit by integrating a simulation program into a non-linear least-square optimization routine. Four-parameters, the isotropic shift, δ_{11}, δ_{22}, and the linewidths, were simultaneously fit. The simulation using Floquet theory[46-48] was written in the NMR simulation environment GAMMA[49]. Powder averages were perfomed using the method of Cheng et al.[50] to obtain an optimal coverage of the sphere. The presence of the directly attached ^{14}N introduced both a dipolar and a quadrupolar contribution to the sideband pattern. The quadrupolar interaction has been previously determined to be negligible [51-54] (less than 20 Hz at 75 MHz) and was therefore not included. However, the ^{14}N-^{13}C dipolar coupling is comparible in magnitude to, but smaller than, the $^{13}C_\alpha$ CSA. This interaction has been analysed in detail for the carbonyl carbon[14], and can be extended to the C_α by using an additional rotation to bring the CSA into the

dipolar frame. Following Tycko[14], a "local-field tensor", $\bar{\bar{\delta}}^*(m)$, can be defined, such that $\bar{\bar{\delta}}^*(m) = \bar{\bar{\delta}} + \bar{\bar{D}}(m)$ where $\bar{\bar{D}}(m)$ is the dipolar correction to $\bar{\bar{\delta}}$, the chemical shift tensor. Thus, $\bar{\bar{\delta}}$ is brought into the dipolar frame by rotating around two Euler angles, α and β, where α represents a rotation around δ_{33} and β represents a subsequent rotation around δ_{22}. Adding $\bar{\bar{D}}(m)$ and diaganolizing the resultant tensor, the effective CSA for each of the three ^{14}N spin states can be calculated. The observed MAS spectrum is the superposition of the sub-spectra due to these three local field tensors. MAS sub-spectra were calculated for each of the ^{14}N spin states using the orientation of the CSA with respect to the ^{14}N-^{13}C bond determined in our theoretical calculations for GA*V, (α = -47.3°, β = 71.9°) and a dipolar coupling of 712.7 Hz, corresponding to a ^{14}N-^{13}C bond distance of 1.45 Å. The experimental data was fit to the sum of the resulting sub-spectra, and errors were calculated. An average of the CSA values derived from each of the three experiments was taken and used to compare with theoretically calculated values. Isotropic-shift values were measured relative to the carbonyl carbon of glycine at 176.04 ppm.

4.3 Computational

Shielding calculations were performed using the TEXAS-90 program[55] which utilizes the gauge-including-atomic-orbital (GIAO) method[56,57]. All calculations were done on an *N*-formyl-L-alanine amide fragment extensively minimized at the helical geometry. A "locally dense" basis set was employed consisting of 6-311++G(2d,2p) basis functions on the central residue and 6-31G basis functions on the formyl and amide groups. Computations were performed on IBM RISC/6000 workstations (Models 340, 350, and 360; IBM

Corporation, Austin, TX). The shielding surfaces were constructed by choosing 358 ϕ,ψ points in Ramachandran space, with a more dense placement of points in the allowed regions. Z-surfaces for the chemical-shift tensors were created using a Gaussian equation:

$$Z_{\delta_{nn}}(\phi,\psi) = \exp[-(\delta_{nn}^{ecs} - \delta_{nn}(\phi,\psi))^2 / \omega^2]$$

where δ_{nn}^{ecs} is the experimental chemical-shift tensor, $\delta_{nn}(\phi,\psi)$ is the chemical-shift tensor surface, and ω is the root-mean-square deviation for the theory/experiment correlation. All surfaces were approximated using a Matlab (The Mathworks, Boston, MA) "best fit" function.

4.4 Results and Discussion

The CPMAS spectra of crystalline $^{13}C_\alpha$-labeled A*AA-hemihydrate at spinning speeds of 821 Hz, 928 Hz, 1024 Hz and 10 kHz are shown in figure 4.1. Similar data were collected for crystalline $^{13}C_\alpha$-labeled G*AV and for the other A*AA crystal form (data not shown). Although two molecules with slightly different conformations exist in the unit cells of both forms of A*AA, the resolution of our experiments was not high enough to differentiate between them, and only one line was observed. Isotropic shifts were determined for each tripeptide using the fast spinning spectrum referenced to the carbonyl carbon of glycine at 176.04 ppm. For each slow spinning spectrum, non-linear least-square fits were used to determine the chemical-shift tensor (figure 4.1) and error estimates. The average value of the three measurements was used. These were (in ppm): A*AA: $\delta_{11} = 70.2 \pm 0.2$, $\delta_{22} =$

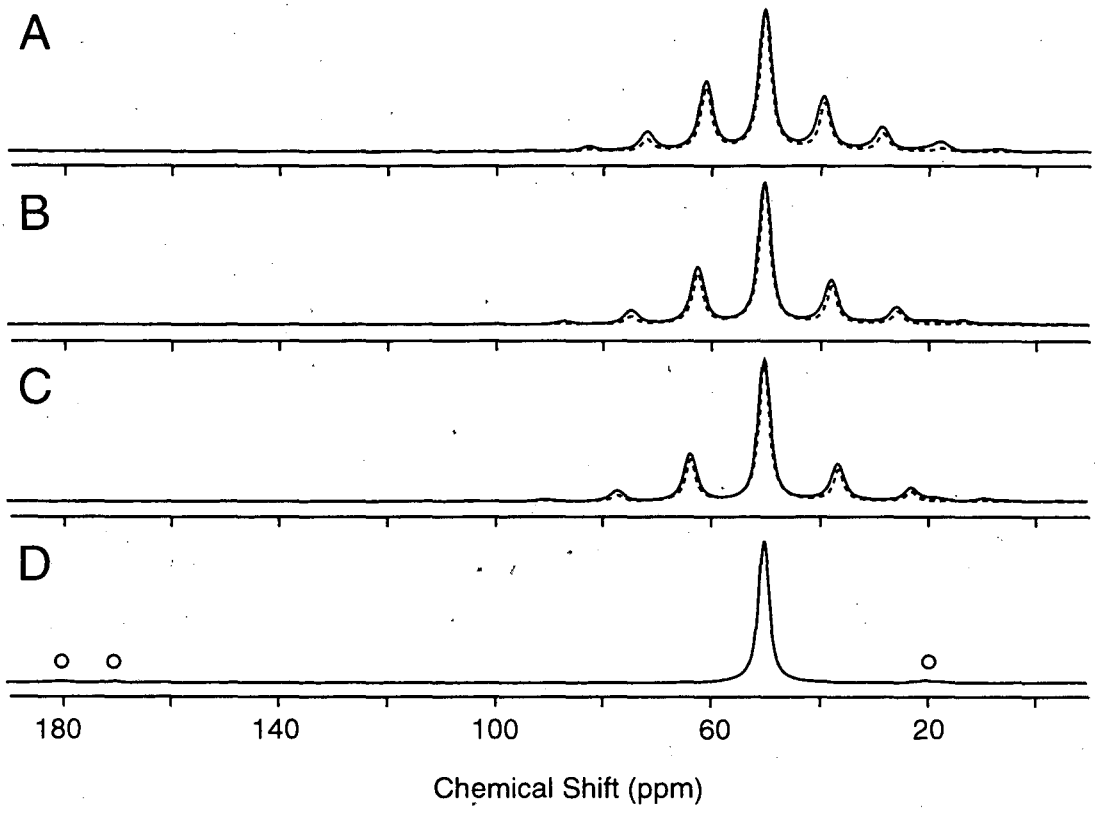

Figure 4.1: CPMAS spectra for crystalline $^{13}C_{\alpha}$-labeled A*AA-hemihydrate (solid lines) and their best fits (dashed lines). For all experiments, the CP contact time was 2.5 ms, the decoupling field strength was 108 kHz, and the recycle delay was 1.5 s. A. 40,960 scans were acquired, spinning at 821 Hz. B. 24,576 scans were acquired, spinning at 928 Hz. C. 28,672 scans were acquired, spinning at 1024 Hz. D. 2,048 scans were acquired, spinning at 10 kHz. This spectrum was not fit, since it contains little information about the CSA. Open circles show natural abundance ^{13}C sites. All chemical shifts are referenced to ^{13}C=O glycine at 176.04 ppm.

54.9 ± 0.2, δ_{33} = 23.6 ± 0.4; A*AA-hemihydrate: δ_{11} = 71.0 ± 1.2, δ_{22} = 55.8 ± 1.6, δ_{33} = 24.0 ± 2.8; G*AV: δ_{11} = 76.9 ± 0.04, δ_{22} = 55.4 ± 0.05, δ_{33} = 25.5 ± 0.09.

In figure 4.2, we show the computed alanine chemical-shielding surfaces for σ_{11} (A), σ_{22} (B), and σ_{33} (C). Using these surfaces and backbone dihedral angles from the x-ray studies, theoretical chemical-shielding values for each of the tripeptides were calculated and compared with the experimental values found above (figure 4.3). Two correlations were calculated, one for the three tripeptides G*AV, A*AA, and A*AA-hemihydrate and one for only A*AA and A*AA-hemihydrate. Although the slopes of the best fit lines (-0.67 for G*AV, A*AA, and A*AA-hemihydrate, and -0.66 for A*AA and A*AA-hemihydrate) are not unity, correlation coefficients of R=0.99 and R=0.98 and rmsd values of ω=2.15 and ω=2.58 ppm were observed. The low rmsd values demonstrate that the backbone dihedral angles are the main determinants of the tensor components of the C_α chemical shift. To determine if the correlation is unique, i.e. to determine if the tensor components alone are sufficient to predict ϕ and ψ, the Z-surface method[28] was used.

For a given observable, such as a component of the CSA tensor, it is possible to define a surface in ϕ/ψ space which gives the Bayesian probability that the observed value corresponds to a particular ϕ/ψ pair. In the case of a Z-surface, this probability is defined by the Gaussian function given above. As one can see from the Z-surface in figure 4.4A, a single parameter, i.e. the C_α isotropic shift, is insufficient to determine uniquely two independent variables (such as two backbone angles), but three parameters are usually sufficient. This was demonstrated in solution studies in which the isotropic shifts of the C_α, C_β, and H_α were measured and used to calculate Z-surfaces

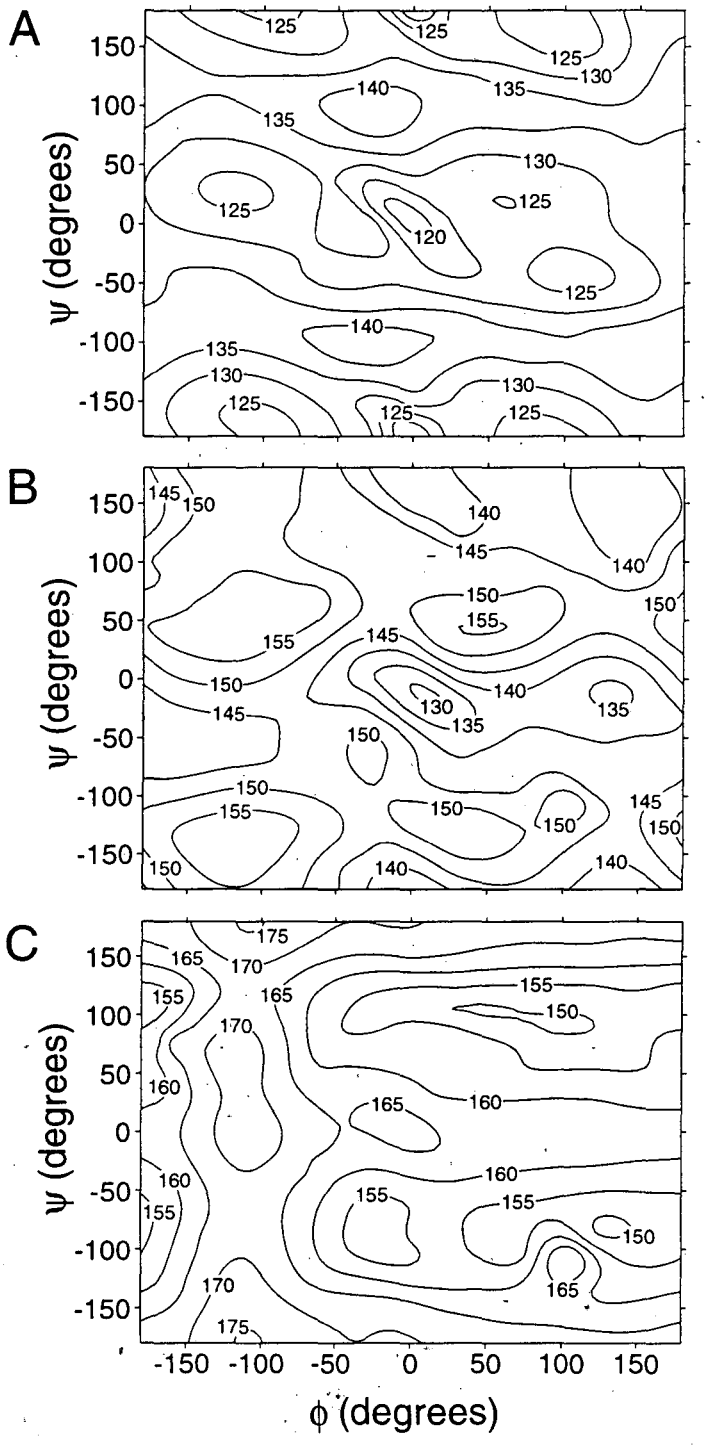

Figure 4.2: Alanine Ramachandran shielding surfaces for C_α sites in N-formyl-L-alanine amide. A. σ_{11}; B. σ_{22}; C. σ_{33}. Surfaces were approximated using 358 points spread over ϕ/ψ space with a more dense placement of points in allowed regions.

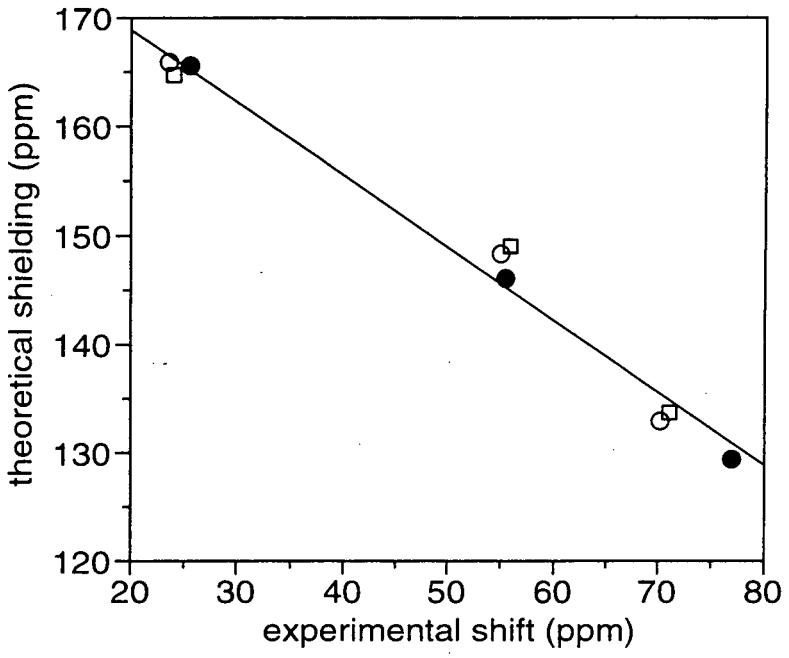

Figure 4.3: Theoretical $^{13}C_{\alpha}$ chemical-shift tensor elements for G*AV (filled circles), A*AA (open circles) and A*AA-hemihydrate (open squares) calculated using the GIAO method and dihedral angles taken from the crystal structures versus the experimentally measured tensors (slope = -0.67, y-intercept = 182.17, R = 0.99, and rmsd = 2.15 ppm). For G*AV, the experimentally determined values (in ppm) were δ_{11} = 76.9 ± 0.04 , δ_{22} = 55.4 ± 0.05 , δ_{33} = 25.5 ± 0.09, and the calculated values were σ_{11} = 129.45, σ_{22} = 146.18, and σ_{33} = 164.46. For A*AA, the experimentally determined values were δ_{11} = 70.2 ± 0.2 , δ_{22} = 54.9 ± 0.2 , δ_{33} = 23.6 ± 0.4, and the calculated values were σ_{11} = 132.93, σ_{22} = 148.20, and σ_{33} = 165.92. For A*AA-hemihydrate, the experimentally determined values were δ_{11} = 71.0 ± 1.2 , δ_{22} = 55.8 ± 1.6 , δ_{33} = 24.0 ± 2.8 , and the calculated values were σ_{11} = 133.75, σ_{22} = 148.95, and σ_{33} = 164.65.

for the backbone angles, and the intersection of these three Z-surfaces narrowed the solution to a single ϕ/ψ pair[28].

In solids, additional experiments to determine the C_β and H_α isotropic shifts are not needed, since the three components of the chemical-shift anisotropy, δ_{11}, δ_{22}, and δ_{33}, provide the necessary three independent parameters. Because the isotropic-shift value is contained in δ_{11}, δ_{22}, and δ_{33}, even small errors in its measurement would be amplified in a product of those three Z-surfaces. Three alternative parameters, the isotropic shift, the width of the CSA (δ_{33}-δ_{11}) and the breadth of the CSA (δ_{22}-δ_{11}) were used to eliminate the propagation of error. The ^1Z width, breadth, and isotropic surfaces for G*AV are shown in figure 4.4 along with the ^3Z surface which represents the product of the three ^1Z surfaces. When the correlation based only on A*AA and A*AA-hemihydrate data is used to scale the calculated tensor surfaces, three high-probability solutions are predicted (Figures 4D-E) for G*AV. The highest probability solution (Gaussian probability, P = 0.91) is ϕ = -79.9° and ψ = -47.8°, which is close to the values determined by x-ray crystallography (ϕ = -68.7° and ψ = -38.1°). Of the other two high probability solutions, one (P = 0.84) is in an allowed region (ϕ = -55.8°, ψ = -18.8°), while the other (P = 0.82) is sterically unallowed (ϕ = -59.5°, ψ = 10.1°).

Although there are two possible solutions in the allowed regions of Ramachandran space, we expect that the accuracy of predictions will increase as more data points are used to calculate the correlation of theory and experiment, and as experiments are carried out at higher field where the ratio of the CSA to the dipolar coupling is larger. However, several factors could lead to a decrease in accuracy. In general the effects of motion on the CSA must be accounted for, although these effects could be ignored in our study

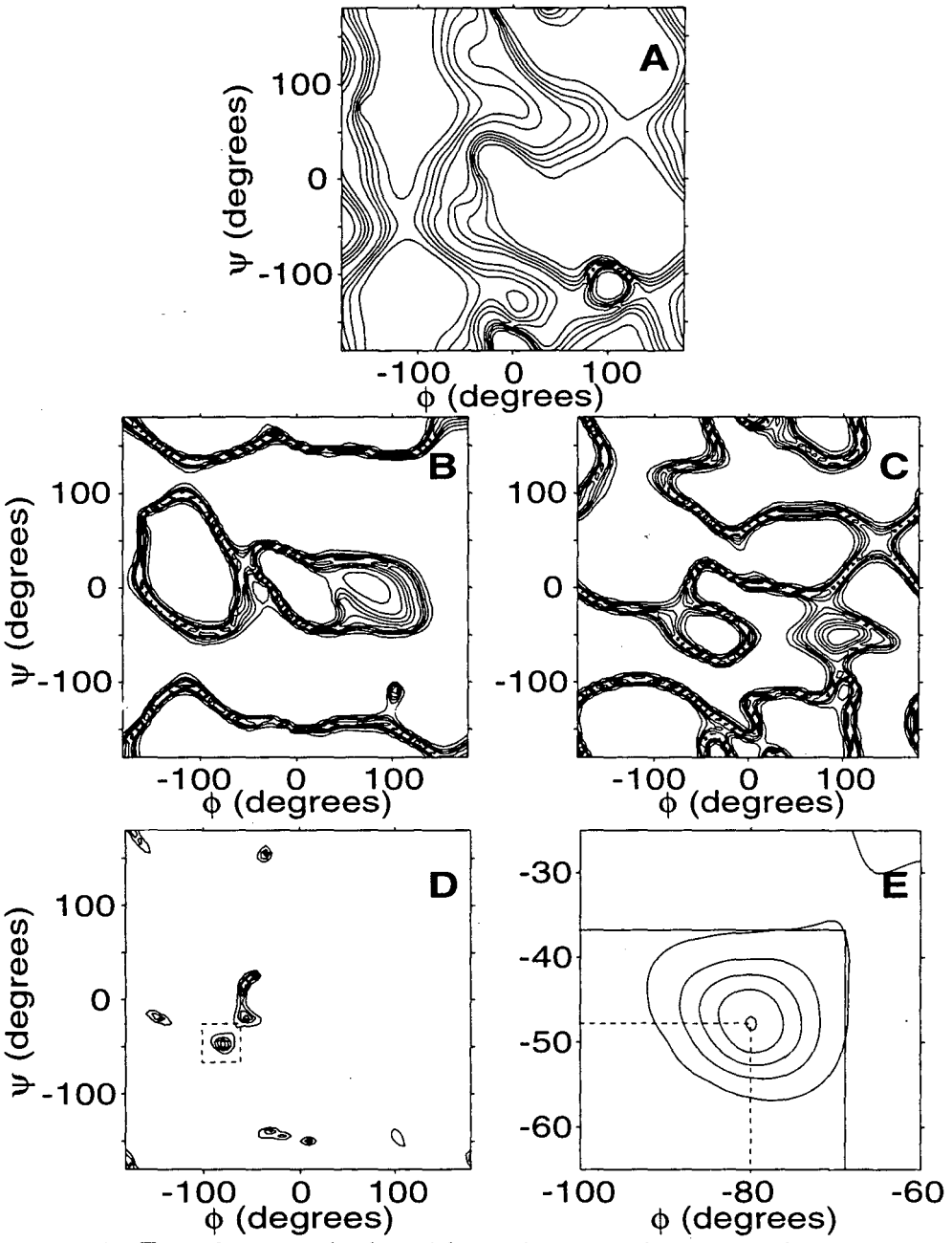

Figure 4.4: Z-surfaces calculated from the experimentally determined chemical-shift anisotropy for the C_α alanine in G*AV and theoretical chemical-shielding surfaces scaled by the correlation determined using A*AA and A*AA-hemihydrate. A. ^{1}Z-surface for the isotropic shift. B. ^{1}Z-surface for the width of the CSA (δ_{33} - δ_{11}). C. ^{1}Z-surface for the breadth of the CSA (δ_{22} - δ_{11}). D. ^{3}Z-surface showing the intersection of the surfaces from A, B, and C. The boxed region contains the area of highest probability and is expanded in E. The dihedral angles as determined by measurement of the CSA tensor are ϕ = -79.9°, ψ = -47.8° (dashed lines), while those determined in the crystal structure are ϕ = -68.7°, ψ = -38.1° (solid lines). In all cases, contours are plotted at 10%, 30%, 50%, 70%, and 90% of the maximum intensity.

since crystaline peptides were used. Deuterium relaxation studies might be used to determine the effects of motion when necessary, however this might introduce larger uncertainties. Lower signal-to-noise or overlapping spectra would also lead to a decrease in the accuracy of dihedral angle predictions. Our results demonstrate that the three tensor components are sufficient to greatly narrow the possible ϕ/ψ angles and to allow accurate predictions in the general case.

4.5 Conclusions

A simple method for the determination of dihedral angles in peptides and proteins in the solid state has been described. The chemical-shift tensors of the central $^{13}C_\alpha$ in three crystalline tripeptides have been measured by slow CPMAS, and have correlated the measured values with shieldings calculated by *ab initio* methods. This correlation was then used to calculate ϕ/ψ Z-surfaces for the three components of the CSA, and the intersection of the three surfaces predicted ϕ/ψ pairs. For G*AV, three high probability ϕ/ψ pairs were predicted. The highest probability pair lies within ±12° of the ϕ/ψ pair determined in the crystal structure. The results demonstrate that the tensor components of a single site are sufficient to greatly narrow the possible dihedral angles and, in the best case, to accurately predict them. Furthermore, the inclusion of Z-surfaces for C_β chemical-shift tensors, as well as Z-surfaces which predict the orientation of the CSA, should provide additional constraints on the backbone dihedral angles, thereby increasing the predictive power of the CSA/Z surface method. The Z-surface approach used with C_β

and C_γ CSA tensors might also provide constraints on side-chain torsion angles.

References:
(1) Lansbury, P. T. J.; Costa, P. R.; Griffiths, J. M.; Simon, E. J.; Auger, M.; Halverson, K. J.; Kocisko, D. A.; Hendsch, Z. S.; Ashburn, T. T.; Spencer, R. G. S.; Tidor, B.; Griffin, R. G. *Nature Structural Biology* **1995**, *2*, 990-998.
(2) Heller, J.; Kolbert, A. C.; Larsen, R.; Ernst, M.; Bekker, T.; Baldwin, M.; Prusiner, S. B.; Pines, A.; Wemmer, D. E. *Protein Science* **1996**, *5*, 1655-1661.
(3) Creuzet, F.; McDermott, A.; Gebhard, R.; van der Hoef, K.; Spijker-Assink, B.; Herzfeld, J.; Lugtenburg, J.; Levitt, M. H.; Griffin, R. G. *Science* **1991**, *251*, 783-786.
(4) Smith, S. O.; Jonas, R.; Braiman, M.; Bormann, B. J. *Biochemistry* **1994**, *33*, 6334-6341.
(5) Christensen, A. M.; Shaefer, J. *Biochemistry* **1993**, *32*, 2868-2873.
(6) Williams, J. C.; McDermott, A. E. *Biochemistry* **1995**, *34*, 8309-8319.
(7) Raleigh, D. P.; Levitt, M. H.; Griffin, R. G. *Chem. Phys. Lett.* **1988**, *146*, 71-76.
(8) Gullion, T.; Schaefer, J. *J. Magn. Reson.* **1989**, *81*, 196-200.
(9) Tycko, R.; Dabbagh, G. *Chem. Phys. Lett.* **1990**, *173*, 461-465.
(10) Ishii, Y.; Terao, T. *J. Magn. Res., Series A* **1995**, *115*, 116-118.
(11) Tomita, Y.; O'Connor, E. J.; McDermott, A. *J. Am. Chem. Soc.* **1994**, *116*, 8766-8771.
(12) Schmidt-Rohr, K. *Macromolecules* **1996**, *29*, 3975-3981.
(13) Feng, X.; Lee, Y. K.; Sandstrom, D.; Eden, M.; Maisel, H.; Sebald, A.; Levitt, M. H. *Chem. Phys. Lett.* **1996**, *257*, 314-320.
(14) Tycko, R.; Weliky, D. P.; Berger, A. E. *J. Chem. Phys.* **1996**, *105*, 7915-7930.
(15) Mehta, M.; Bower, P.; Gregory, D.; Zebroski, H.; Drobny, G. In *Experimental NMR Conference*; Asilomar, CA, 1996.
(16) Spera, S.; Bax, A. *J. Am. Chem. Soc.* **1991**, *113*, 5490-5492.
(17) Wishart, D. S.; Sykes, B. D. *J. Biomolecular NMR* **1994**, *4*, 171-180.
(18) Saito, H. *Magn. Reson. in Chemistry* **1986**, *24*, 835-852.
(19) Saito, H.; Ando, I. *Annu. Rep. NMR Spectrosc.* **1989**, *21*, 209-290.
(20) de Dios, A. C.; Pearson, J. G.; Oldfield, E. *Science* **1993**, *260*, 1491-1496.
(21) Laws, D. D.; de Dios, A. C.; Oldfield, E. *J. Biomol. NMR* **1993**, *3*, 607-612.
(22) de Dios, A. C.; Oldfield, E. *J. Am. Chem. Soc.* **1994**, *116*, 5307-5314.
(23) Laws, D. D.; Le, H.; de Dios, A. C.; Havlin, R. H.; Oldfield, E. *J. Am. Chem. Soc.* **1995**, *117*, 9542-9546.
(24) Asakawa, N.; Hiromichi, K.; Ando, I. *J. Mol. Structure* **1994**, *323*, 279-285.
(25) Kuszewski, J.; Qin, J.; Gronenborn, A. M.; Clore, G. M. *J. Magn. Reson. B* **1995**, *106*, 92-96.
(26) Pearson, J. G.; Wang, J. F.; Markley, J. L.; Le, H.; Oldfield, E. *J. Am. Chem. Soc.* **1995**, *117*, 8823-8829.
(27) Luginbühl, P.; Szyperski, T.; Wüthrich, K. *J. Mag. Res. B* **1995**, *109*, 229-233.
(28) Le, H.; Pearson, J. G.; de Dios, A. C.; Oldfield, E. *J. Am. Chem. Soc.* **1995**, *117*, 3800-3807.

(29) Heller, J.; Laws, D. D.; Tomasseli, M.; King, D. S.; Pines, A.; Wemmer, D. E.; Havlin, R. H.; Oldfield, E. *J. Am. Chem. Soc.* **1997**, *in press*,
(30) Pines, A.; Gibby, M. G.; Waugh, J. S. *J. Chem. Phys.* **1973**, *59*, 569-590.
(31) Schaefer, J.; Stejskal, E. O. *J. Am. Chem. Soc.* **1976**, *98*, 1031-1032.
(32) Bax, A.; Szeverenyi, N. M.; Maciel, G. E. *J. Magn. Reson.* **1983**, *52*, 147-152.
(33) Gan, Z. *J. Am. Chem. Soc.* **1992**, *114*, 8307.
(34) Hu, J. Z.; Alderman, D. W.; Chaohui, Y.; Pugmire, R. J.; Grant, D. M. *J. Magn. Reson. A* **1993**, *105*, 82-87.
(35) Lipmaa, E.; Alla, M.; Turherm, T. In *Proceedings of the XIXth Congress Ampere*; Heidelberg, 1976; pp 241.
(36) Yarim-Agaev, Y.; Tutunjian, P. N.; Waugh, J. S. *J. Magn. Reson.* **1982**, *47*, 51-60.
(37) Bax, A.; Szeverenyi, N. M.; Maciel, G. E. *J. Magn. Reson.* **1983**, *51*, 400-408.
(38) Tycko, R.; Dabbagh, G.; Mirau, P. A. *J. Magn. Reson.* **1989**, *85*, 265-274.
(39) Bax, A.; Szeverenyi, N. M.; Maciel, G. E. *J. Magn. Reson.* **1983**, *55*, 494-497.
(40) Nakai, T.; Ashida, J.; Terao, T. *J. Chem. Phys.* **1988**, *88*, 6049-6058.
(41) Frydman, L.; Chingas, G. C.; Lee, Y. K.; Grandinetti, P. J.; Eastman, M. A.; Barrall, G. A.; Pines, A. *J. Chem. Phys.* **1992**, *97*, 4800-4808.
(42) Chaturvedi, S.; Kuantee, G.; Parthasarathy, R. *Biopolymers* **1991**, *31*, 397-407.
(43) Fawcett, J. K.; Camerman, N.; Camerman, A. *Acta Crystallogr. B* **1975**, *31*, 658-665.
(44) Hempel, A.; Camerman, N.; Camerman, A. *Biopolymers* **1991**, *31*, 187-192.
(45) Ten Kortenaar, P. B. W.; Van Dijk, B. G.; Peeters, J. M.; Raaben, B. J.; Adam, P. J. H. M.; Tesser, G. I. *Int. J. Peptide Protein Res.* **1986**, *27*, 398-400.
(46) Shirley, J. H. *Phys. Rev. B* **1965**, *138*, 979.
(47) Vega, S. *J. Chem. Phys.* **1992**, *96*, 2655-2680.
(48) Levante, T. O.; Baldus, M.; Meier, B. H.; Ernst, R. R. *Mol. Phys.* **1995**, *86*, 1195-1212.
(49) Smith, S. A.; Levante, T. O.; Meier, B. H.; Ernst, R. R. *J. Magn. Reson.* **1994**, *A106*, 75-105.
(50) Cheng, V. B.; Suzukawa, H. H.; Wolfsberg, M. *J. Chem. Phys.* **1973**, *59*, 3992-3999.
(51) Hexem, J. G.; Frey, M. H.; Opella, S. J. *J. Am. Chem. Soc.* **1981**, *103*, 224.
(52) Zumbulyadis, N.; Henrichs, P. M.; Young, R. H. *J. Chem. Phys.* **1981**, *75*, 1603.
(53) Naito, A.; Ganapathy, S.; McDowell, C. A. *J. Chem. Phys.* **1981**, *74*, 5393.
(54) Naito, A.; Ganapathy, S.; McDowell, C. A. *J. Magn. Reson.* **1982**, *48*, 367.
(55) Wolinski, K.; Hinton, J. F.; Pulay, P. *J. Am. Chem. Soc.* **1990**, *112*, 8251-8260.
(56) London, F. *J. Phys. Radium* **1937**, *8*, 397-409.
(57) Ditchfield, R. *J. Chem. Phys.* **1972**, *56*, 5688-5691.

Chapter 5

Electron-nuclear distances in solids

5.1 Introduction

Although the dipolar recoupling techniques discussed in previous chapters are typically capable of measuring ^{13}C-^{13}C distances of up to about 7Å, the longest distances that have been measured were carried out using ^{31}P-^{19}F REDOR. Long distance constraints of this kind could play important roles in biomolecular structural studies, both in solids and solution. The use of such constraints could provide information on the overall fold of a biomolecule, either protein or nucleic acid, especially when used in combination with shorter distance measurements and dihedral angle measurements. These constraints might also be helpful in determining changes in conformation such as structural changes in membrane receptor proteins upon ligand binding, prion protein refolding due to infectivity, and DNA bending upon protein binding. For these reasons, it would be useful to have other robust distance measurement techniques available capable of measuring distances in the 10 - 30 Å range.

Because the gyromagnetic ratio of an electron is 673 times greater than that of a proton, the dipolar couplings between an electron and a nucleus are on the order of 673 times stronger than those between a proton and a nucleus. Such strong couplings should be easily detectable since they would lead to relaxation effects equivalent to proton-nuclear at approximately 9 (the cube root of 673) times the distance. Thus, it might be possible to measure quantitatively distances between a nucleus and a localized unpaired electron

spin, such as one found on a nitroxide free-radical. In a protein, a nitroxide spin-label could be introduced on a cysteine residue and the distance between it and any resolved and assigned ^{13}C resonances might be measured through relaxation studies.

Nitroxide labels have been successfully employed as structural probes in solution. In one type of experiment[1-7], the unpaired electron's coupling to proximal protons was monitored through linewidth studies. T_2 relaxation times of the protons decreased, leading to an increase in linewidths. Distances were estimated qualitatively using the $1/r^6$ dependence of the linewidths, where r is the distance between the free electron and the nucleus. Other studies[8,9] used soluble free-radicals to probe which protons were on the surface of a protein and which were buried. The dissolved spin-label could collide with the protein surface, causing those protons on the surface to relax quickly, leaving only buried protons observable. Recently, another study[10] monitored conformational changes in a protein using the interaction of a free-radical and a ^{13}C nucleus. Distances were estimated qualitatively by measuring linewidths.

In solids, the experiments described above must be modified. Because molecules in a solid are tightly packed, a free-radical will be coupled not only to the nuclei on the same molecule, but also to nuclei on neighboring molecules. For this reason, the spin-labels must be diluted so that only intramolecular couplings are observed. Additionally, the relaxation times of free-radicals in the solid state are different from those in solution and are more important in the absence of molecular tumbling. The relaxation properties of the nuclei will depend on those of the electron, which are not known at high field in the solid state. For these reasons some calibration

experiments must be performed in order to make a quantitative distance measurement. By understanding the changes in the relaxation properties of nuclei a known distance away from a paramagnetic center, it may be possible to quantitatively measure unknown distances.

To obtain the contribution of the paramagnetic center to relaxation of the nucleus, the relaxation properties of two samples must be measured. This is because in a paramagnetic sample, there is still a significant diamagnetic contribution to relaxation. The total relaxation times in a paramagnetic sample are functions of both the relaxation times in a diamagnetic sample, T_1^{dia} and T_2^{dia}, and the paramagnetic contributions, T_1^{para} and T_2^{para}:

$$\frac{1}{T_1^{total}} = \frac{1}{T_1^{dia}} + \frac{1}{T_1^{para}}$$

and

$$\frac{1}{T_2^{total}} = \frac{1}{T_2^{dia}} + \frac{1}{T_2^{para}}.$$

To solve these equations for the paramagnetic contributions, both the total relaxation times and the relaxation times in a diamagnetic sample must be measured separately.

The investigation of these spin-label - nuclear interactions is a three step process. First, test molecules must be synthesized. These molecules must contain a ^{13}C nucleus at a known distance from a nitroxide spin-label in a rigid molecule. Several variations of this molecule must be made: one with a ^{13}C and a nitroxide, one with natural-abundance carbon and a nitroxide-analog (this nitroxide-analog does not contain a free-radical), and one with a ^{13}C-nitroxide-analog pair. The second molecule, the "unlabeled" one, is used to dilute the first so that only intramolecular interactions exist. The last molecule is used to measure the relaxation properties of the nuclei in the absence of the spin-label. The nitroxide-analog contains no localized free

electron and must be similar enough to the nitroxide label used so that the two molecules mix and do not separate into phases. Two such sets of molecules have been synthesized. The first is a derivative of para-aminobenzoic acid that contains a methyl group that can be ^{13}C labeled and a TEMPO free-radical. In this case the distance between the localized electron and the ^{13}C methyl is approximately 12 Å. The second set is based on the GCN4 coiled-coil. A mutation, methionine 2 replaced by a cysteine, was introduced so that a TEMPO spin-label could be easily attached, and four nuclei along the backbone were ^{13}C labeled. These nuclei were V9 C=O, L19 C_α, A24 C_β, and G31 C_α, and the distances to the localized electron were approximately 14.4 Å, 28.7 Å, 34.5 Å, and 46 Å, respectively. (Distances are approximate because the nitroxide spin-label used is not rigidly bound to the peptide. Distances may vary by approximately 2.5 Å[11].) The crystal structure of GCN4 is known[12] and the molecule is a fairly rigid, long cylinder.

The second step in these experiments is to locate the resonance lines due to the ^{13}C introduced in the presence of the nitroxide spin-label. This can be done with the CPMAS experiment[13,14] that has been described previously in this thesis, or it can be done using a simple one-pulse sequence under MAS. This simpler sequence just involves a $\pi/2$ pulse on ^{13}C and detection under proton decoupling. As pointed out in chapter 2, this experiment has two disadvantages: long recycle delays must be used to account for the longer ^{13}C relaxation times and the experiment is less sensitive that CPMAS. However, this experiment may be useful if the presence of the electron affects the protons from which magnetization is being transferred. Using the molecules described above, no spectral intensity could be assigned to the introduced ^{13}C using either of these pulse sequences.

The last step experimentally would be to measure the relaxation properties of the nuclei by observing the behavior of the identified resonance lines under various pulse sequences. A CPMG[15,16] experiment could be used to measure T_2, while a simple inversion-recovery experiment could measure T_1. Because the resonance lines due to the ^{13}C could not be found in our model system, these experiments could not be carried out.

This chapter describes the synthesis of the model compounds described above and the SSNMR experiments performed on them. This is followed by a discussion of the results and possible future experiments that might be performed to overcome the problems.

5.2 Synthesis ^{13}C-spin-labeled molecules

General: Unless otherwise noted, reagents and solvents were obtained from commercial suppliers and were used without further purification. Immediately before use, tetrahydofuran (THF) was distilled under N_2 from Na/benzophenone, methylene chloride (CH_2Cl_2) was distilled from CaH_2 and N,N-Diisopropylethylamine (DIEA) was distilled from KOH. Unless otherwise specified, extracts were dried over $MgSO_4$ and filtered through a fine glass frit. Concentration *in vacuo* refers to removing volatile solvents under aspirator vacuum using a Buchi rotary evaporator, followed by further evacuation with a mechanical two-stage pump. Mass Spectrometry was performed by D.S. King, Molecular and Cell Biology Department, University of California, Berkeley.

5.2.1 Benzoic Acid Derivative:

BOC-4-amino benzoic acid (1):

To 2.50 g (18.3 mmol) of 4-aminobenzoic acid dissolved in H_2O was added 3.80 g (45.6 mmol) of sodium bicarbonate ($NaHCO_3$). While the reaction mixture was stirring on ice, 12.0 g (54.75 mmol) of di-*tert*-butyl dicarbonate was added.. An additional 1.40 g (18.3 mmol) of $NaHCO_3$ was added after one hour. After 80 hours, the reaction mixture was brought to pH 3.5 using 1 N HCl, causing the product to precipitate. The product was redissolved in 100 mL of ethyl acetate (EtOAc). The mixture was transferred to a separatory funnel and the layers were separated. The aqueous layer was washed with EtOAc (2 x 100 mL). The combined organic layers were then washed with deionized water (2 x 100 mL) and saturated NaCl solution (2 x 100 mL), dried and solvent was removed *in vacuo* to yield 3.04 g (70.2 %). An NMR spectrum was taken for analysis.

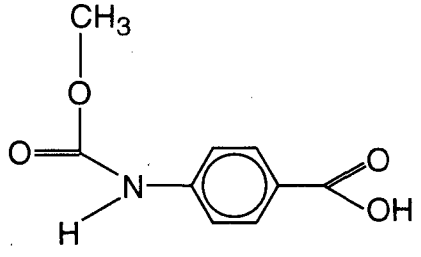

(1)

Methyl,BOC-4-aminobenzoic acid (2):

In a flame-dried round-bottom flask, 0.5 g (2.1 mmol) of **1** was dissolved in 8.0 mL of THF. Methyl iodide (1.05 mL, 17 mmol) was then added and the mixture placed on ice. A flame-dried 3-necked flask was charged with 0.144 g (6.0 mmol) NaH (40% oil dispersion). The NaH was

washed three times with hexanes, the supernatant being decanted each time. The reaction vessel was placed on ice and the THF mixture was added. The mixture was placed under a blanket of N_2 and stirred. The product (**2**) precipitated after several hours. The precipitate was redissolved in 10 ml of EtOAc and 10 ml of H_2O and brought to pH 3 with 3 N HCl. The mixture was transferred to a separatory funnel and the layers were separated. The aqueous layer was washed with EtOAc (4 x 25 mL). The combined organic layer was then washed deionized water (25 mL) , 1 M sodium thiosulfate (2 x 25 mL), deionized water (25 mL), saturated NaCl solution (25 mL). The organic layer was dried and the solvent was removed *in vacuo* yielding 0.44 g (83.4%). An NMR spectrum of the product (**2**) was taken.

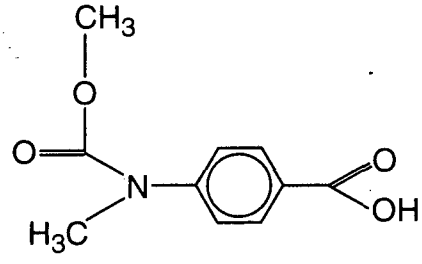

(2)

Tetramethyl piperdine methyl,BOC-benzoic acid (3):

To 0.34 g (1.35 mmol) of **2**, dissolved in 20 mL of CH_2Cl_2, 0.259 g (1.35 mmol) of 1,2-Dichloroethane (EDC) and 0.182 g (1.35 mmol) of 1-Hydroxybenzotriazole hydrate (HoBt) were added and the mixture was stirred under N_2 for one hour. To the reaction flask, 0.211 mL (1.23 mmol) of 4-Amino-2,2,6,6-tetramethylpiperdine and 0.43 mL (2.46 mmol) of DIEA were

added. The reaction mixture was stirred under a N_2 blanket for 24 hours. The mixture was diluted to 40 mL with CH_2Cl_2, washed 1 N HCl (2 x 50 mL), H_2O (50 mL), saturated $NaHCO_3$ solution (50 mL), H_2O (50 mL), and saturated NaCl solution (50 mL). The solution was dried and concentrated *in vacuo*. The final product **3** was crystallized from 60% Ethyl acetate/ 40% Hexanes. An NMR spectrum was taken and the molecular weight was measured via mass spectrometry.

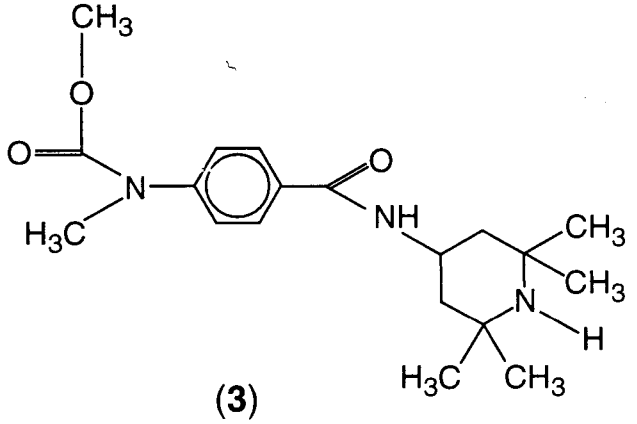

(3)

To synthesize the ^{13}C labeled, spin-labeled equivalent, **4**, the same procedure was used, except ^{13}C methyl iodide was used and 4-amino-TEMPO was substituted for the 4-Amino-2,2,6,6-tetramethylpiperdine. Mass spectrometry was used to check molecular weights and NMR spectra were taken.

Three NMR samples were prepared. The first, which will be called "NA/Pip" consisted of 175 mg of **3**; the second, "1% ^{13}C/TEMPO", consisted of 2 mg of product **4** with 198 mg of product **3**; the third, "5% ^{13}C/TEMPO", consisted of 5 mg of product **4** with 95 mg of product **3**. These samples were

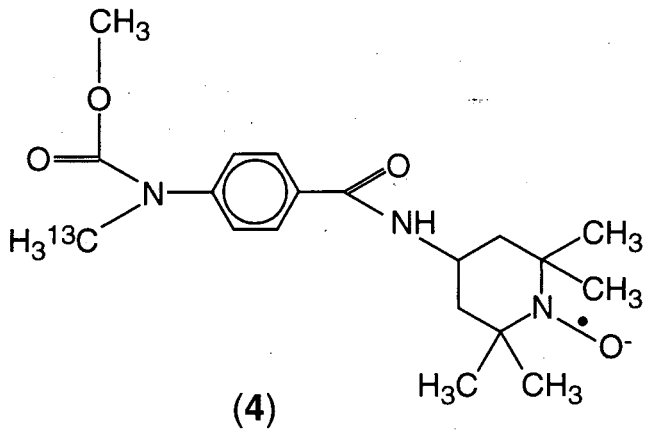

(4)

dissolved in a mixture of MeOH/EtOAc and solvent was removed *in vacuo.* Samples were then lyophilized from benzene. To check that the **4** dispersed in **3**, EPR spectra of the solid samples were taken and compared with an EPR spectrum of a solid sample of **4**. The dilute samples showed a significantly narrower EPR spectra, since broadening due to electron-electron interactions is minimized after dilution.

5.2.2 GCN4-TEMPO Synthesis

GCN4 with an M2C mutation, aceylated at the N-terminus, was synthesized using N-Fmoc protected amino acids on a Applied Biosystems peptide synthesizer. Two syntheses were carried out, one with all natural abundance carbon, and the second with ^{13}C enriched amino acids at four sites: V9 C=O, L19 C_α, A24 C_β, and G31 C_α. The peptides were cleaved by stirring them in a cleavage cocktail containing 82.5% (by volume) TFA, 5% phenol, 5% thioanisole, 5% H_2O, and 2.5% ethanedithiol for 3 hours[17]. The mixture was filtered and TFA was removed *in vacuo.* The remaining filtrate was forcefully injected into cold *tert*-butyl methyl ether causing the peptide to

precipitate. The mixture was centrifuged, the supernatant decanted, and the pellet was dispersed into fresh cold ether. This procedure was carried out six times, and the final pellet was air dried overnight. The cleaved peptide was then redissolved in H_2O and purified by reverse-phase HPLC on a Waters PrepLC C-18 column. Purity was checked by electrospray ionization mass spectrometry.

Fmoc-^{13}C amino acids:

^{13}C-labeled amino acids (Cambridge Isotope Laboratories, Andover, MA) were Fmoc protected using the following procedure. To 3.75 mmol of each amino acid, dissolved in ddH_2O (60 mL), 0.945 g (11.25 mmol) of $NaHCO_3$ was added. After dissolving 1.265 g (3.75 mmol) of N-(9-fluorenylmethoxycarbonyloxy) succinimide (Fmoc-O-Suc) in acetone (60 mL), the mixtures were combined. The Fmoc-O-Suc partially precipitates, but redissolves slowly. The reaction mixtures were left stirring for 24 hours at which point the acetone was removed *in vacuo*. Citric Acid (1M) was used to precipitate the Fmoc-amino acids from the H_2O. EtOAc (150 mL) was added to redissolve the precipitate. The mixtures were transferred to separatory funnels and the layers were separated. The aqueous layers were washed with EtOAc (100 mL). The combined organic layers were then washed with H_2O (2 x 100 mL) and saturated NaCl solution (2 x 100 mL). The organic layers were dried and solvent removed *in vacuo*. NMR spectra showed the correct products were formed, and the Fmoc-amino acids were used for solid-state synthesis without further purification.

4-(2-bromoacetamido)-4-amino-2,2,6,6-tetramethylpiperdine (5):

In order to increase the probability that the spin-labeled, ^{13}C GCN4 molecule would disperse in, and co-crystallize, with the natural-abundance carbon GCN4, a spin-label analog, 4-(2-iodoacetamido)-4-amino-2,2,6,6-tetramethylpiperdine (IAATMP, **6**), was synthesized. In CH_2Cl_2 (3 mL), 0.06 mL (0.6 mmol) of bromoacetyl bromide was added to 0.06 mL (0.3 mmol) of 4-amino-2,2,6,6-tetramethylpiperdine. The mixture was placed on ice, and **5** immediately precipitated. An attempt was made to attach **5** to the cysteine in GCN4, but the reaction proceeded too slowly and a GCN4 dimer, as observed by mass spectrometry, formed instead. Thus, **5** was dissolved in N,N-Dimethylformamide (DMF) and then several equivalents of NaI were added. The reaction was refluxed at 70 °C for 8 hours. Solvent was removed *in vacuo* and residual DMF was pumped off under high vacuum overnight[18,19]. The product **6** crystallized when dissolved in H_2O and its molecular weight was checked by mass spectrometry.

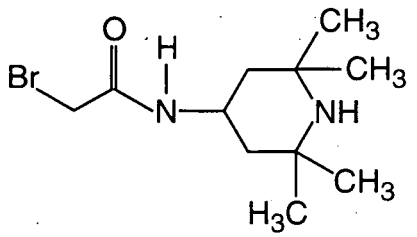

(5)

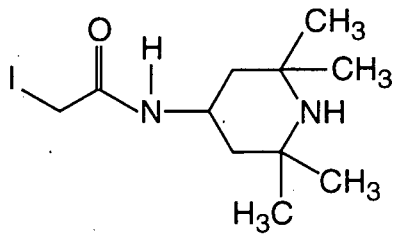

(6)

The IAATMP and the 4-(2-iodoacetamido)-TEMPO were reacted with cys2 on GCN4 by adding 5 equivalents of the small molecule for each equivalent of peptide and stirring for two hours in 50% AcN/ 50% phosphate buffer (25 mM, pH 7.2). Two products were seen; one was the desired labeled

peptide, either GCN4-AATMP (GCN4 with the attached acetamido-4-amino-2,2,6,6-tetramethylpiperdine) or GCN4-TEMPO, and the other was GCN4 dimer (as determined by mass spectrometry). These two products were easily separable by HPLC. Circular dichroism showed that the GCN4-IAATMP molecule was highly helical in 25 mM phosphate buffer (pH 7.2).

Several NMR samples were made: $^{13}C_4$-GCN4-AATMP, 1% $^{13}C_4$-GCN4-TEMPO in GCN4-AATMP, 2% $^{13}C_4$-GCN4-TEMPO in GCN4-AATMP, 2% NA-GCN4-TEMPO in GCN4-AATMP, and NA-GCN4-AATMP. These samples were lyophilized from 10 mM phosphate buffer (pH 7.2) after allowing them to equilibrate overnight. Attempts to crystallize these samples under conditions similar to GCN4 without the spin-label[12] were unsuccessful.

5.3 Solid State NMR Results

All ^{13}C NMR spectra were obtained at 7.07 Tesla (corresponding to a ^{13}C Larmor frequency of 75.74 MHz) on a home-built spectrometer based on a Tecmag (Houston, Texas) pulse programmer. A Chemagnetics (Fort Collins, CO) 4-mm double resonance MAS probe was used for all experiments.

5.3.1 Benzoic Acid Derivatives

Several SSNMR experiments were performed on four samples: 34 mg of NA/Pip, 44 mg of 1% ^{13}C/TEMPO, approx. 30 mg of 5% ^{13}C/TEMPO, and 22 mg of 100% ^{13}C/TEMPO. CPMAS spectra were recorded spinning at 10 kHz, using 50 kHz proton decoupling and a 2.5 ms CP contact time. Although it was expected that the 1% ^{13}C/TEMPO and the 5% ^{13}C/TEMPO samples would have either an additional resonance peak or additional intensity at an existing

resonance, no significant differences between spectra recorded for the NA/Pip, 1% ^{13}C/TEMPO and the 5% ^{13}C/TEMPO were seen (see figure 5.1). Once normalized, these spectra could be subtracted and no significant intensity was observed in these difference spectra. However, signal-to-noise ratios were different from those expected. For example, the signal-to-noise, after 4096 scans, for 34 mg of NA/Pip was 44-to-1, while for 44 mg of 1% ^{13}C/TEMPO, after the same number of scans, the signal-to-noise was only 20-to-1. CPMAS experiments with different CP mixing times (from 25 μs to 2.5 ms) and one-pulse experiments recorded with echoes using the same decoupling field strengths were also unsuccessful at detecting differences (data not shown).

CPMAS spectra of the 100% ^{13}C/TEMPO sample show one peak (figure 5.1). Relaxation experiments on this sample indicate that T_1 is approximately 26 ms and T_2 is approximately 1.6 ms.

5.3.2 GCN4 Derivatives

Similar experiments as those described above were carried out on the following samples: 100% $^{13}C_4$-GCN4-AATMP, 1% $^{13}C_4$-GCN4-TEMPO in GCN4-AATMP, 2% $^{13}C_4$-GCN4-TEMPO in GCN4-AATMP, 2% NA-GCN4-TEMPO in GCN4-AATMP and NA-GCN4-AATMP. CPMAS spectra were recorded for all the samples and compared. Four strong resonance lines were observed for the 100% $^{13}C_4$-GCN4-IAATMP sample, as expected (figure 5.2). However, none of the other spectra showed significant differences (figure 5.2). In other words, the signal that should have resulted from the isotope enrichment were not detectable in the presence of the spin-label. Again, CPMAS experiments with different CP mixing times (from 50 μs to 2.5 ms)

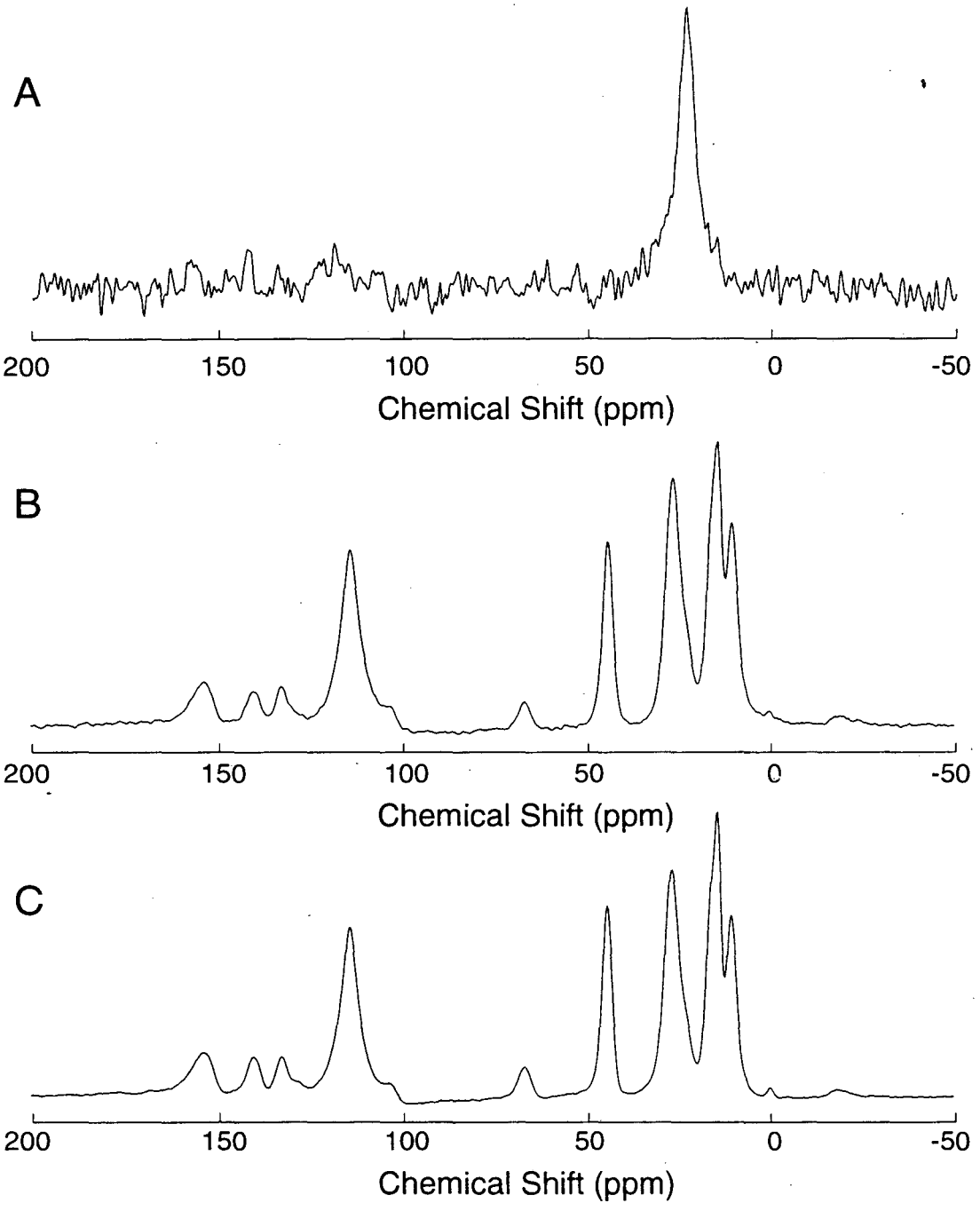

Figure 5.1: CPMAS spectra of para-aminobenzoic acid derivatives samples. A) 4096 scans of 22 mg of 100% ^{13}C/TEMPO, spinning at 10 kHz. B) 32,000 scans of 44 mg of 1% ^{13}C/TEMPO spinning at 10 kHz. C) 32,000 scans of 34 mg of NA/Pip spinning at 10 kHz. The chemical shift axis reference is approximate.

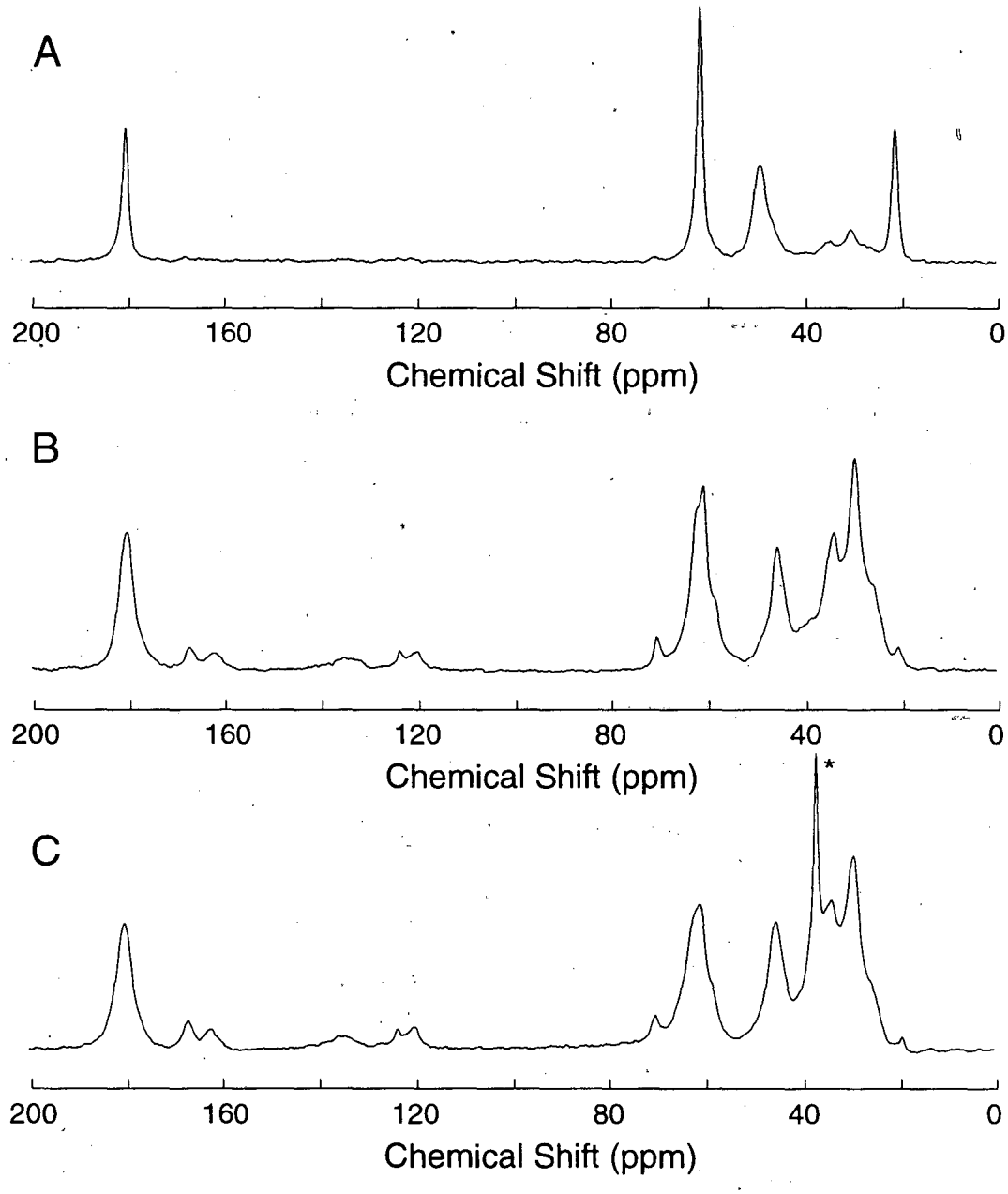

Figure 5.2: CPMAS spectra of GCN4 samples. A) 2048 scans of 100% $^{13}C_4$-GCN4-AATMP, spinning at 10 kHz. B) 53248 scans of 1% $^{13}C_4$-GCN4-TEMPO, spinning at 10 kHz. The peak marked with an asterisk is an impurity. C) 53248 scans of NA-GCN4-AATMP, spinning at 10 kHz. All chemical shifts are referenced to the C=O of glycine at 176.04 ppm.

and one-pulse experiments recorded with echoes were also unsuccessful at detecting differences (data not shown).

5.4 Discussion and future work

The failure to observe magnetization due to the ^{13}C enrichment in the presence of the spin-label for either system using SSNMR is puzzling. Because of the large distances, little shift in the ^{13}C resonance frequency is expected; the Fermi-contact terms should be negligible. Thus, one would expect to see enhancement of existing resonance lines due to the isotopic enrichment. None was observed. Several explanations of this are possible, but all seem unlikely. First, it is possible that the presence of the electron shortens the relaxation times so much that the peaks are broadened out and are unobservable. Although it might be suspected that this is the case for the para-aminobenzoic acid derivative, this explanation is improbable because it seems unlikely that the free-radical is having an effect at distances as large as the 46 Å found in the GCN4 sample. Second, it may be possible that the presence of the electron is interfering with CP. This is a possibility because the coupling to the ^{13}C is approximately four times weaker than the coupling to the surrounding ^{1}H nuclei. This is supported by the lower signal-to-noise found in the 1% ^{13}C/TEMPO para-aminobenzoic acid derivative sample, despite the fact that there was more sample in the rotor. However, one-pulse experiments which do not use CP would then be able to detect the enrichment. This was not the case. Additionally, the experiments done with short CP times would probably show differences due to the enrichment, which, again, was not the case. Another explanation maybe be that the dilute samples only have a small percentage of the ^{13}C label, a percentage equivalent

to the natural-abundance contribution, differences are hard to detect and difference spectroscopy should be avoided. If this were the case, higher signal-to-noise spectra might be able to detect the enrichment. No extra magnetization was detected even when higher signal-to-noise ratios were achieved.

To resolve some of the issues raised above, experiments might be done using a nucleus other than ^{13}C. A good choice for an alternative nucleus is ^{2}H. Its gyromagnetic ratio is close to that of ^{13}C so distance ranges that might be measured will not be effected significantly. The advantage of using ^{2}H is that there is virtually no natural-abundance problem. Instead of having to measure differences in magnetization by subtracting spectra of natural-abundance samples from spectra of enriched samples, only the ^{2}H enriched samples would be necessary. Thus, if any magnetization was detected in the sample with the ^{2}H and the nitroxide spin-label, that magnetization would be influenced by the presence of the spin-label. Additionally, low temperature experiments might be useful, since at low temperatures, electron relaxation times might be much longer. These experiments are now underway.

References:

(1) Wien, R. W.; Morrisett, J. D.; McConnell, H. M. *Biochemistry* **1972**, *11*, 3703-3716.
(2) Dwek, R. A.; Knott, J. C. A.; Marsh, D.; McLaughlin, A. C.; Press, E. M.; Price, N. C.; White, A. I. *Eur. J. Biochem.* **1975**, *53*, 25-39.
(3) Schmidt, P. G.; Kuntz, I. D. *Biochemistry* **1984**, *23*, 4261-4266.
(4) Moonen, C. T. W.; Scheek, R. M.; Boelens, R.; Muller, R. *Eur. J. Biochem.* **1984**, *141*, 323-330.
(5) Anglister, J.; Frey, T.; McConnell, H. M. *Biochemistry* **1984**, *23*, 5372-5375.
(6) Kosen, P. A.; Scheek, R. M.; Naderi, H.; Basus, V. J.; Manogaran, S.; Schmidt, P. G.; Oppenheimer, N. J.; Kuntz, I. D. *Biochemistry* **1986**, *25*, 2356-2364.
(7) DeJong, E. A. M.; Claesen, C. A. A.; Eaemen, C. J. M.; Harmsen, B. J. M.; Konings, R. N. H.; Tesser, G. I.; Hilbers, C. W. *J. Magn. Reson.* **1988**, *80*, 197-213.
(8) Petros, A. M.; Muller, L.; Kopple, K. D. *Biochemistry* **1990**, *29*, 10041-10048.
(9) Espositos, G.; Molinari, H.; Motta, A.; Niccolai, N. ; Espositos, G.; Molinari, H.; Motta, A.; Niccolai, N., Ed.: Cagliari, Italy, 1989, pp 11.
(10) Kleereloper, Q.; Howarth, J. W.; Guo, X.; Solaro, R. J.; Rosevear, P. R. *Biochemistry* **1995**, *34*, 13343-13352.
(11) Rabenstein, M.D.; Shin, Y.K. *Proc. Natl. Acad. Sci. USA* **1995**, 92, 8239-8243.
(12) O'Shea, E. K.; Klemm, J. D.; Kim, P. S.; Alber, T. *Science* **1991**, *254*, 539-544.
(13) Pines, A.; Gibby, M. G.; Waugh, J. S. *J. Chem. Phys.* **1973**, *59*, 569.
(14) Schaefer, J.; Stejskal, E. O. *J. Am. Chem. Soc.* **1976**, *98*, 1031-1032.
(15) Carr, H. Y.; Purcell, E. M. *Phys. Rev.* **1954**, *94*, 630.
(16) Meiboom, S.; Gill, D. *Rev. Sci. Instrum.* **1958**, *29*, 688.
(17) King, D. S.; Fields, C. G.; Fields, G. B. *Int. J. Peptide Protein Research* **1990**, *36*, 255-266.
(18) Finkelstien, N. *Chemische Berichte* **1920**, *43*, 1528.
(19) Sartori, M. F. *Chem. Rev.* **1951**, *48*, 237.

SECTION III:

APPLICATION OF SSNMR TO PRION PEPTIDES

Chapter 6

Solid-State NMR Studies of the Prion Protein H1 Fragment

6.1 Introduction

As pointed out in Chapter 1, secondary structure analysis of PrP^C based on sequence homology and molecular modeling predicted that it contains four α-helices, designated H1 to H4. Biological data suggest that it is the first two of these helices that convert to β-sheet in PrP^{Sc} [1,2]. When peptides corresponding to these four regions were synthesized, three of them were found to have very low solubility in H_2O, and FTIR, CD and electron microscopy showed that they formed β-sheets and polymerized into fibrils [3,4]. However, CD and solution NMR studies in organic solvents, such as hexafluoroisopropanol (HFIP), or detergents, such as sodium dodecyl sulfate (SDS), have shown that H1 and H2, as well as peptides corresponding to longer segments of PrP containing these regions, can form α-helices[5]. Thus, these synthetic peptides seem to be able to model some aspects of the conformational pluralism which is exhibited by PrP.

As yet the scrapie isoform of PrP has proven intractable to high resolution spectroscopic or crystallographic study. PrP^{Sc} is particularly problematic as it is insoluble and forms aggregates lacking long-range order[6]. Solid-state NMR is one of the few techniques able to answer specific structural questions about peptides or proteins in immobile states, such as aggregated peptides and membrane proteins, through the use of chemical-shift information and specific distance measurements. In this chapter[7], the use of solid-state NMR to gain structural information about an aggregated form of

the first of the predicted structural regions, H1 (residues 109-122 of the Syrian hamster PrP sequence), is described.

It has already been pointed out that ^{13}C chemical shifts are highly correlated with peptide secondary structure in the solid state[8,9]. Cross-polarization/magic-angle spinning (CPMAS) techniques[10,11] have been employed to determine chemical shifts of specifically ^{13}C labeled H1 peptides, and this information has been used to gain insight into the overall secondary structure of these peptides. ^{13}C CPMAS spectra can yield isotropic chemical shifts with relatively high accuracy. These chemical shifts predominately reflect the local conformations of the peptides and are largely independent of the identity of neighboring residues. Conformations of α_R-helix, α_L-helix, ω-helix, 3_{10} helix and β-sheet can be distinguished on the basis of chemical shift, given high enough resolution. Chemical shifts of amino-acid carbons in the solid state in a β-sheet conformation differ by as much as 8 ppm from those in an α-helix[8]. Similarly strong correlations have been seen in solution[12,13], and reproduced in recent theoretical work[14]. By using CPMAS to determine isotropic shifts, meaningful information about secondary structure of aggregated proteins can be gained.

Internuclear distance-measurement techniques with doubly ^{13}C labeled peptides have also been used to determine specific distances. Types of secondary structure can be distinguished and structural details discovered best through the measurement of a large number of distances. Strong homonuclear dipolar couplings in solids prevent the use of solution-state proton NMR experiments, such as NOESY[15] and TOCSY[16,17]. Thus, alternative techniques must be employed to determine distances in solids, and recently many such techniques have been discussed already. Rotational-

resonance (R^2) magnetization exchange[18,19] is a homonuclear distance-measurement technique that has been applied to several biological systems[20,21], including one amyloid system[22]. For carbon labels, the technique can be used to measure distances of up to about 7Å, with no R^2 effects indicating that the distance between a pair of ^{13}C labels is greater than about 7Å.

6.2 Materials and Methods

6.2.1 Sample Preparation

The labeled PrP peptides, with amidated C-termini, were synthesized using N-Fmoc protected amino acids on a Millipore (Bedford, MA) Model 9050 Plus PepSynthesizer. ^{13}C-labeled Fmoc-amino acids were purchased either from Cambridge Isotope Laboratories (Woburn, MA), or Isotec (Miamisburg, OH). The peptides were purified by reverse-phase HPLC and then lyophilized, dissolved in dilute HCl, and re-lyophilized to remove residual TFA. The purity and incorporation of ^{13}C labels was confirmed by mass spectrometry. For CPMAS chemical-shift measurements, singly ^{13}C labeled samples were then redisolved in 50% acetonitrile (AcN)/50% H_2O or 100% hexafluoroisopropanol (HFIP) and lyophilized into a powder.

In order to obtain narrower NMR spectral lines for rotational-resonance experiments, doubly ^{13}C labeled samples were dissolved in excess H_2O, partially dried by blowing air over them and then allowed to equilibrate in an atmosphere of 78% humidity over a saturated solution of ammonium chloride at 25°C. Linewidths obtained from this method were narrower than those from lyophilized samples, reflecting a structurally more homogenous sample. Intermolecular effects in distance measurements were minimized by

diluting labeled samples approximately 1:9 in unlabeled H1, except for the two samples with short (i.e. $r_{cc} \leq 2.5$Å) distances in which intermolecular contributions were negligible.

6.2.2 Data Acquisition

All experiments were performed on a home-built spectrometer operating at a ^{1}H Larmor frequency of 301.2 MHz. For the CPMAS experiments used to measure chemical shifts, a home-built double-resonance probe was used. The ^{1}H decoupling field strength was 62 kHz, the CP contact time was 2 ms, and the recycle delay was set to 2 s. A Chemagnetics (Fort Collins, CO) 4 mm double-resonance high-speed spinning probe was used for rotational-resonance experiments. Spinning speeds were controlled using a home-built spinning-speed controller using a phase-locked loop as the central element in the control circuit. Spinning speeds could be controlled to within ±10 Hz with long-term stability. CP contact time was 2.5 ms and the ^{1}H decoupling field strength was 100 kHz.

For rotational-resonance magnetization-exchange experiments, total experiment times were kept constant by introducing a variable delay while ^{13}C magnetization was stored along the z-axis before inversion[23]. This lead to the same average power dissipation due to proton decoupling in all experiments, thus eliminating radio-frequency heating effects as a possible source of error in the measurements. By observing natural-abundance peaks throughout the experiment, it was confirmed that all changes in signal intensity were due to magnetization exchange. Two hundred and fifty six scans were acquired and discarded at the start of each series of experiments to allow for spectrometer and probe stabilization. The n=1 rotational-resonance

condition was used for all experiments[19]. Recycle delays were 5.0 seconds. Weak pulses or DANTE sequences[24] were used to invert the carbonyl resonance. To account for spectrometer drift and to determine experimental precision, the following protocol was utilized. Thirty-two or sixty-four scans were collected for each slice, and eighteen magnetization exchange time points were sampled in random order[25]. This eighteen time point experiment was cycled through repeatedly, and experiments for each time point were averaged and statistically analysed to determine mean values and standard deviations of the experimental data. Natural-abundance contributions to the two lines were calculated by comparing natural-abundance peaks in the methyl region of the spectra with the same peaks in the spectrum of unlabeled H1, and using this scaling factor to calculate the amount of natural-abundance ^{13}C under the labeled peaks[25]. Since these contributions do not undergo magnetization exchange, they were subtracted out before the difference magnetization was calculated. This difference magnetization as a function of rotational-resonance time was used in the R^2 fitting procedure described below.

6.2.3 Line fitting

In CPMAS experiments to determine chemical shifts, samples lyophilized from HFIP gave spectra with two partially resolved resonances. One of these lines appeared at the chemical shift of the AcN/H_2O form, and was interpreted to be due to incomplete conversion to the HFIP form. For these spectra, chemical shifts and linewidths were obtained by fitting lines using two Lorentzians with FELIX (Biosym, La Jolla, CA). The fit values of chemical shifts were then used in data analysis.

6.2.4 Rotational-resonance simulations

Rotational-resonance magnetization-exchange simulations, including corrections for inhomogeneous broadening, and χ^2 minimizations using model data generated using Floquet theory [26-28], were written using the simulation environment GAMMA[29] and were discussed elsewhere[30]. Three-parameter fits were performed on samples of known, short distances ($i_{C=O}$ to $i+1_{C\alpha}$) to obtain values for the zero-quantum relaxation times (T_{2ZQ}) and for the correlation between inhomogenous linewidths. Using these values, one-parameter minimizations were performed to obtain distances for all other samples. The values for the chemical-shift anisotropies and orientations were held fixed for all simulations. The assumed assignment of the relative orientation of the chemical-shift principal axes should introduce only a small additional error in the distance measurements since the n=1 rotational-resonance condition is not very sensitive to these parameters[31,32].

The errors of the optimized distances were calculated as follows. For shorter distances, errors were taken to be two standard deviations as determined by the three-parameter fit. For longer distances, in order to obtain a lower bound for the distance consistent with an experimental data set, a one-parameter fit of the distance was run setting T_{2ZQ} equal to the shortest estimated value and using the largest possible degree of inhomogeneous broadening. The upper bound for the distance came from a one-parameter fit of the distance, using the longest possible T_{2ZQ} value and the smallest possible amount of inhomogeneous broadening. The maximum T_{2ZQ} was taken to be 1.5 times the fit T_{2ZQ}, while its minimum was calculated using the method of Kubo and McDowell[33], i.e.

$$\frac{1}{T_{2ZQ}} = \frac{1}{T_2^{(a)}} + \frac{1}{T_2^{(b)}}$$

where a and b are the two spins involved, and the T_2 values were obtained from rotor-synchronized CPMG experiments taken with the MAS frequency away from the rotational-resonance condition. The maximum inhomogeneity was taken to be the linewidth of the broader of the two peaks, while its minimum was taken to be 0 Hz.

6.3 Results and Discussion

6.3.1 Chemical Shifts

The isotropic shifts of carbonyl ^{13}C labels throughout the H1 fragment were measured after lyophilization both from AcN/H_2O and from HFIP. Chemical-shift changes on the order of 3 ppm were observed for ^{13}C resonances when the solvent was changed, although samples lyophilized from HFIP showed an additional minor component retaining the chemical shift of the form lyophilized from AcN/H_2O. Figure 6.1 shows the CPMAS spectra for a sample of a mixture of alanine 115 ^{13}C=O, $^{13}C_\alpha$, and $^{13}CH_3$ labeled H1 peptides lyophilized from AcN/H_2O (A) and from HFIP (B). Since conversion of the sample to the HFIP form was only approximately 70%, and the two peaks were not completely resolved, we fit each HFIP spectral line with two Lorentzians to obtain accurate chemical shifts. Our data indicate that H1 can exist in at least two different conformations in the solid state, depending on the solvent from which the sample is lyophilized. We define the secondary-structure index, X_{SS}, in a similar way to Wishart and Sykes, [13], as a measure of the degree to which a ^{13}C's chemical shift agrees with literature values for either α-helix or β-sheet:

$$X_{SS} = 2 * \frac{\delta_{expt} - \overline{\delta}_{lit}}{\Delta\delta_{lit}}$$

where δ_{expt} is the experimentally determined chemical shift, $\overline{\delta}_{lit}$ is the average of the literature values of the chemical shifts for a particular residue in an α–helix and in a β-sheet[8] (when more than one literature value for a residue in a particular conformation exists, an average of these values is taken before the $\overline{\delta}_{lit}$ is calculated), and $\Delta\delta_{lit} = \overline{\delta}_{\beta} - \overline{\delta}_{\alpha}$, is the difference of shifts for a particular residue in an α–helix and in β-sheet. X_{SS} is +1 when the chemical shift is in perfect agreement with literature values for a sheet conformation, while it is -1 when it is in perfect agreement with published values for the α-helix conformation. Trends in the secondary-structure index are indicative of types of secondary structure, even in the presence of some outliers. When lyophilized from AcN/H_2O, carbonyl (figure 6.2), C_α, and C_β chemical shifts throughout the peptide agree reasonably well with literature values for β-sheet. Glycine 119 carbonyl shows two resolved resonances, indicating that more than one conformation is present in our polycrystalline sample. The chemical shift of one of these resonances is consistent with the β-sheet conformation, while the other is likely to be some sort of turn, because its chemical shift is similar to the chemical shifts for helical forms. Carbonyl secondary structure indices for the AcN/H_2O form, from residue 112 to 122 are: 0.5, 0.4, 1.2, 0.7, 0.8, 0.6, 0.5, 0.9 (-1.8), 0.6, 0.1, -1.4. The chemical shifts of the major component of samples prepared from HFIP show secondary structure indices indicative of α-helical conformation. Indices of the minor components remain indicative of β-sheet, although low signal-to-noise and errors in fitting make the precision of these calculations lower. The indices for the HFIP form's major (minor) peak for the carbonyl carbons of residues

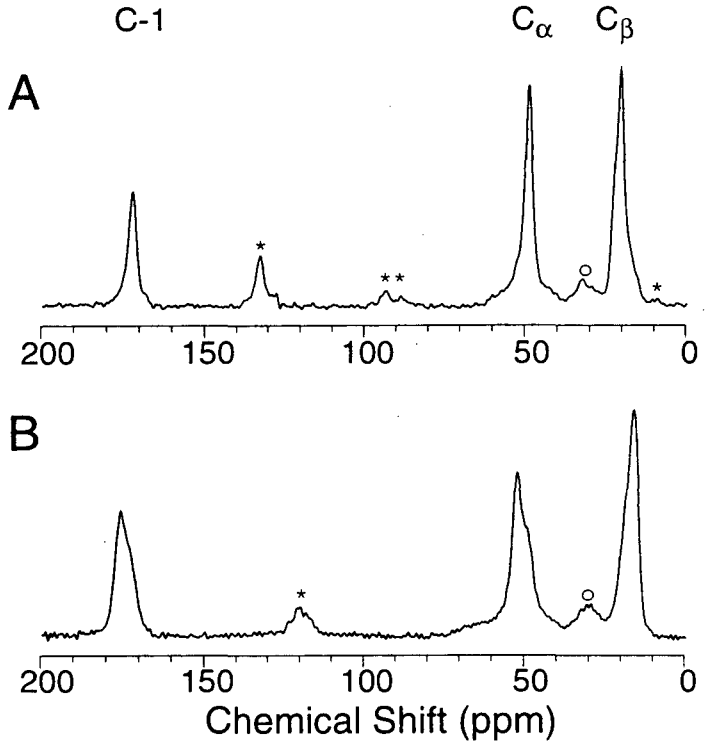

Figure 6.1: A) CPMAS spectrum of a mixture of alanine 115 $^{13}C{=}O$, $^{13}C_\alpha$, and $^{13}CH_3$ labeled H1 peptides lyophilized from 50% AcN/50% H2O. Sixty-four scans were acquired with a CP contact time of 2.0 ms, and a recycle delay of 1.5 s. The spinning speed was approximately 3.0 kHz. Peaks marked with a '*' are spinning sidebands and those marked with an 'o' are due to natural-abundance background ^{13}C. All chemical shifts are referenced to $^{13}C{=}O$ glycine at 176.04 ppm. B) CPMAS spectrum of the same peptides lyophilized from HFIP. The same experimental parameters as in a) were used. Dotted lines indicate the positions of the lines when lyophilized from 50% AcN/50% H2O.

112 to 120 are: -0.4 (0.7), -0.9 (0.1), -1.3, -0.7 (0.7), -0.9 (0.4), -1.0 (0.1), -0.3 (0.4), -2.2 (0.3), -0.1 (0.4). No minor peak was observed for glycine 114.

Samples lyophilized from HFIP were found to be water sensitive. Chemical shifts for these samples were observed to change after exposure to

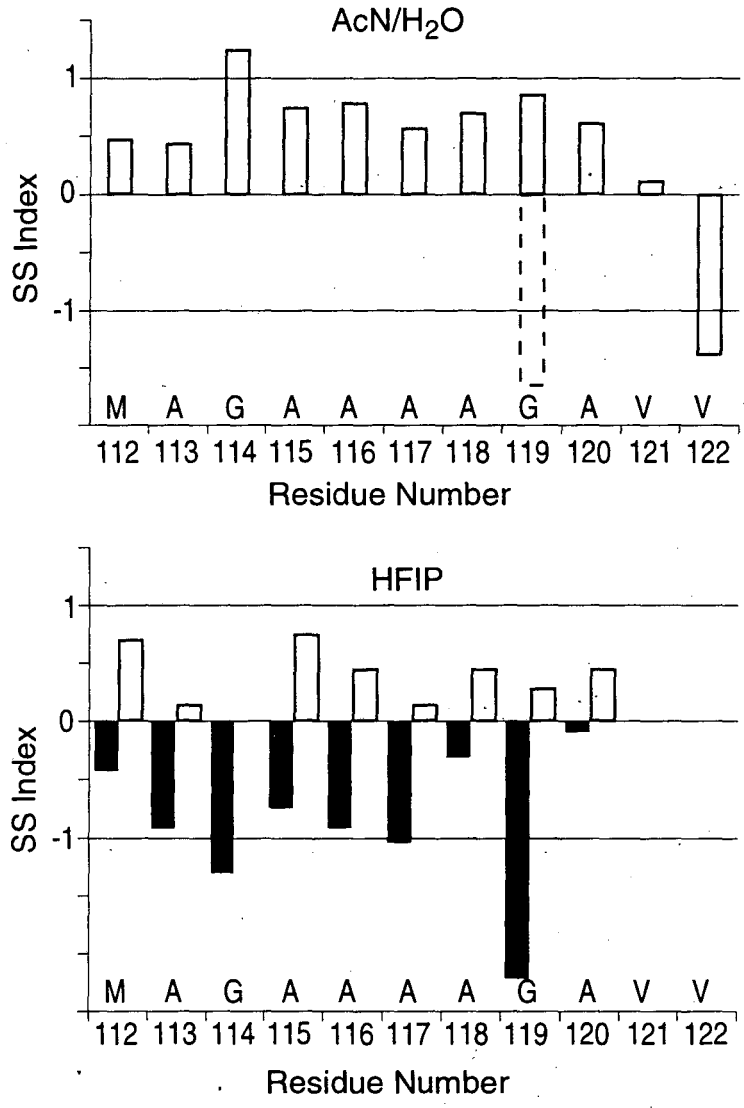

Figure 6.2: Carbonyl secondary-structure index values for the central residues of the H1 peptide obtained from CPMAS spectra of singly-labeled peptides. A value of +1 (-1) indicates perfect agreement with published chemical shifts of that residue type in a β-sheet (α-helix) conformation. Chemical shifts for the HFIP form were obtained by line fitting spectra and the filled bars indicate the secondary-structure index value for the main peak (>70%), while the white bars indicate the secondary-structure index value for the minor peak. Published carbonyl chemical-shift data in ppm are as follows: alanine (β-sheet): 171.8, 171.6 and 172.2; alanine (α-helix): 176.4, 176.2 and 176.8; glycine (β-sheet): 168.5, 168.4, and168.5; glycine (α-helix): 171.7, 171.4, 172.0, and 172.1; methionine (β-sheet): 170.6; methionine (α-helix): 175.1; valine (β-sheet): 171.5 and 171.8; valine (α-helix): 174.9. Larger errors are expected in the HFIP data due to the need to fit two unresolved peaks to acquire chemical shifts.

water vapor. Figure 6.3A is the spectrum of the mixture of alanine 115 labeled peptides lyophilized from HFIP. The shifts of the 3 lines are in good agreement with the helical conformation, with X_{SS} = -0.7, -1.0, and -0.7 for the $^{13}C{=}O$, $^{13}C_\alpha$, and $^{13}CH_3$ lines, respectively. When the samples were exposed to an environment of 30% humidity (H_2O vapor over a saturated solution of $CaSO_4$ at 25°C), for 30 minutes, partial conversion to the sheet-like conformation was observed, as illustrated in figure 6.3B. Figure 6.3C illustrates the spectrum after exposing the sample to 100% humidity for 2 hours. The lines then occur at a chemical shift indicative of a pure β–sheet conformation, with X_{SS} = 0.7, 0.6, and 1.36 for the $^{13}C{=}O$, $^{13}C_\alpha$, and $^{13}CH_3$ lines, respectively. We interpret this to mean that the helical form obtained from HFIP is only meta-stable in the solid state, and when water is present, a sheet form is preferred.

6.3.2 Rotational Resonance

A total of seven C=O - C_α distances were measured in H1 (table 6.1) and compared with distances expected from idealized α–helix and β-sheet conformations. From these idealized models and the experimental and fitting precision, it appears that although rotational resonance can be used to measure i to i+1 and i to i+2 distances, the precision is insufficient to distinguish between types of secondary structure. Thus, i to i+3 distances are better indicators of types of secondary structure.

The issue discussed in chapter 3, sample inhomogeneity, becomes important in these measurements[30]. Because the samples showed significant

Table 6.1: Measured and theoretical distances for the seven doubly labeled H1 peptides.

C=O label	C_α label	best fit distance (Å)	minimum distance (Å)	maximum distance (Å)	α-helical distance[a] (Å)	β-sheet distance[a] (Å)
115	116	2.4	2.3	2.5	2.4	2.4
115	117	5.8	5.4	7.8	4.5	5.4
115	118	5.8	5.6	7.8	4.5	8.8
114	115	2.4	2.3	2.5	2.4	2.4
113	115	5.4	4.9	7.2	4.5	5.4
114	117	6.6	6.3	8.5	4.5	8.8
113	116	6.0	5.6	7.7	4.5	8.8

[a]Distances derived from idealized α-helical and β-strand conformations.

inhomogenous broadening (as determined by spin-echo experiments) and the rotational-resonance condition is fairly narrow, the rotational-resonance condition may not be satisified simultaneously by all isochromats of the lines. Thus, they cannot undergo efficient magnetization exchange, and the measured distances appear systematically longer than the "true" distance. As discussed in chapter 3, such off rotational-resonance effects due to incomplete correlation between inhomogenous lines can be accounted for in simulations[30]. Thus accurate distances can be obtained.

For short distances, we fit the distance, the T_{2ZQ} and the inhomogeneous linewidth simultaneously. Since, in the case of short distances, the three parameters are not highly correlated (cross-correlation

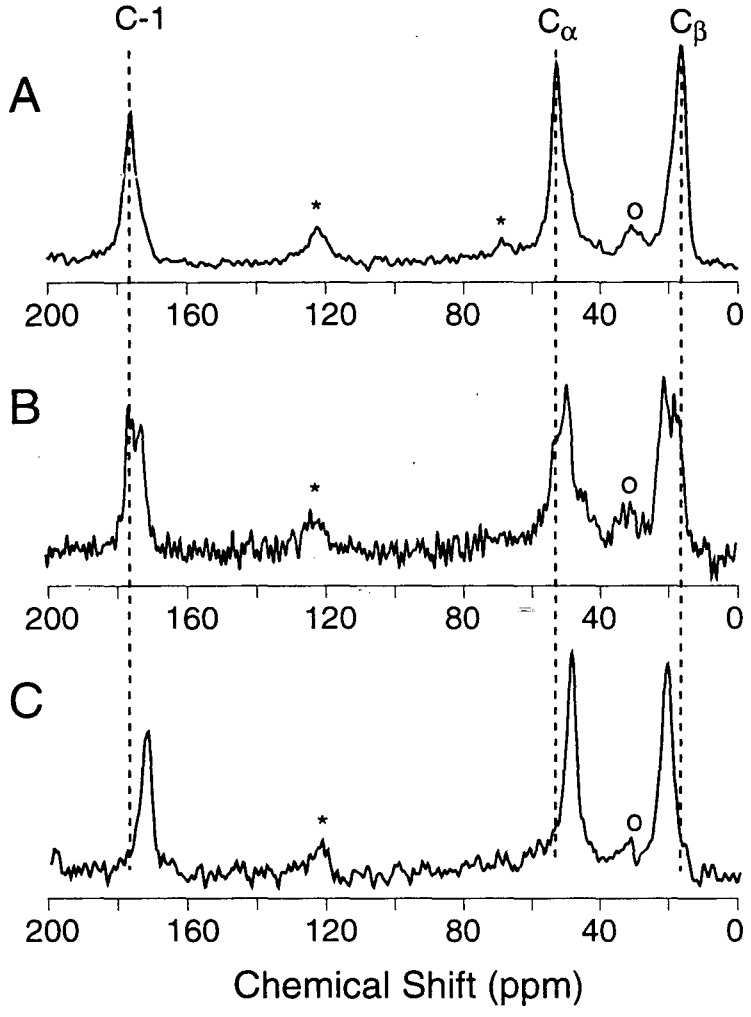

Figure 6.3: CPMAS spectra of a mixture of alanine 115 $^{13}C{=}O$, $^{13}C_\alpha$, and $^{13}CH_3$ H1 peptides a) lyophilized from HFIP; b) after exposure to air at 30% humidity (H2O vapor over a saturated solution of CaSO4 at 25°C) for 30 minutes; c) after 2 hour exposure to air at 100% humidity. Experimental parameters are as in figure 1, except the number of scans were 1024 for A, 2384 for B, and 512 for C, and less sample was used. Peaks marked with a '*' are spinning sidebands and those marked with an 'o' are due to natural-abundance background ^{13}C. The dotted lines indicate the positions of the shifts when lyophilized from HFIP.

coefficients of $\rho < 0.6$), the distance, T_{2ZQ} and inhomogeneous linewidth can simultaneously be obtained for these samples. We assume these parameters are transferable between samples. Figure 6.4A shows the data and fit for a measurement of the distance from glycine 114 C=O to alanine 115 C_α. The best fit gave a distance of 2.37 Å, which is within experimental error of the correct distance of approximately 2.42 Å. The value of the zero-quantum relaxation time, 9.5 ms, was longer than expected from the T_2 values [33] of the individual lines (5.0 ± 0.4 ms for the carbonyl and 6.7 ± 0.7 ms for the C_α). The inhomogeneous linewidth obtained, 76.3 Hz (full width at half height), indicates some correlation between the C=O and C_α peak, but not complete correlation. This agrees well with the results of experiments designed to measure this correlation[30]. In the case of longer distances the three parameters are highly correlated (cross-correlation coefficients of $\rho \sim 0.9$). Thus, the results of a simultaneous fit to all three parameters are not meaningful. The values of the T_{2ZQ} and the inhomogeneity obtained in the fits of i to i+1 peptides were therefore used as fixed constants for fits of the distance for the other peptides. Figures 6.4B and 6.4C, show the data and simulations for peptides labeled at the C=O of alanine 115 and the C_α of alanine 117, and the same carbonyl and the C_α of alanine 118. Distances measured and estimated errors are listed in table 1.

The rotational-resonance data are consistent with an extended conformation for H1. Distances expected for a β-sheet conformation are slightly longer than the three i to i+3 distance distances measured, but could be consistent with a bent β-sheet model. More distance measurements and greater accuracy would allow the solution of the structure of the H1 peptide to higher resolution.

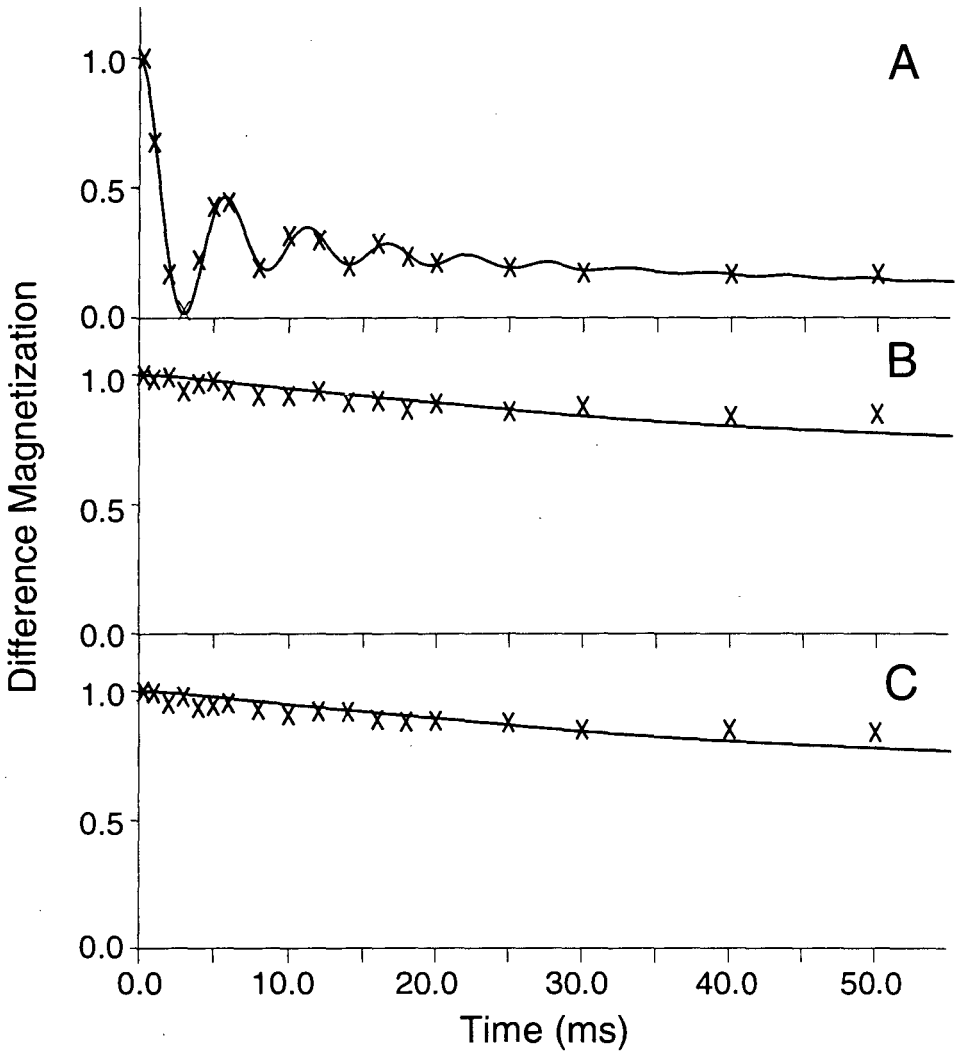

Figure 6.4: Experimental rotational-resonance magnetization-exchange curves and best fits for doubly ^{13}C labeled H1 peptides. A) For a peptide labeled at the C=O of glycine 114 and the C_α of alanine 115, values of the three-parameters fit were: distance = 2.37 Å; T_{2ZQ} = 9.5 ms; inhomogenous linewidth $\Delta\nu_{1/2}$ = 152.6 Hz (full width at half height). Correlation coeficients were all less than 0.6. Thirty-two scans for each of the eighteen experimental time points were collected sixteen times. B) For a peptide labeled at C=O of alanine 115 and the Ca of alanine 117, values of the T_{2ZQ} and the inhomogeneous linewidth were fixed at values obtained in (A), and the distance was fit to 5.78 Å. Sixty-four scans for each of the eighteen experimental time points were collected eleven times. C) For a peptide labeled at C=O of alanine 115 and the Ca of alanine 118, values of the T_{2ZQ} and the inhomogeneous linewidth were fixed at values obtained in (A), and the distance was fit to 5.81 Å. Sixty-four scans for each of the eighteen experimental time points were collected seven times. Error bars indicating experimental precision (not shown) are smaller than the symbols.

6.4 Conclusions

From our distance measurements and chemical-shift data, it appears that H1 forms an extended, primarily β-sheet-like conformation when lyophilized from AcN/H_2O or dried from pure H_2O. When lyophilized from HFIP, incomplete conversion to the second conformation and overlapping residues make distance measurement more difficult. However, the chemical-shift data from the HFIP form are consistent with the presence of an α-helix. This α-helical conformation appears to be only metastable, and reverts to an extended conformation when exposed to water. The observed conversion is consistent with earlier FTIR data for the peptides[3]. Additionally, this study defines the specific residues involved in secondary structure, and, interestingly, shows that the same sequence of residues is involved in the α-helical or β-sheet conformation. Structural predictions for the protein from molecular modeling[2], and the hypothesis that the infectivity of PrP is the result of a conformational change in H1 and surrounding regions of the protein[34], are also consistent with the present study. Clearly, caution is required when comparing results from this isolated peptide to the corresponding region of the entire PrP molecule.

It may also be of interest to note that these results are similar to those of a solid state NMR study of a portion of the Aβ peptide found in amyloid deposits in the brains of patients of Alzheimer's Disease. Data on the Aβ peptide residues 34-42 suggested a β-sheet or bent β-sheet conformation around a Gly-Gly bond[22].

References:

(1) Huang, Z.; Gabriel, J.-M.; Baldwin, M. A.; Fletterick, R. J.; Prusiner, S. B.; Cohen, F. E. *Proc. Natl. Acad. Sci. USA* **1994**, *91*, 7139-7143.
(2) Huang, Z.; Prusiner, S. B.; Cohen, F. E. *Folding & Design* **1996**, *1*, 13-19.
(3) Gasset, M.; Baldwin, M. A.; Lloyd, D.; Gabriel, J.-M.; Holtzman, D. M.; Cohen, F.; Gletterick, R.; Prussiner, S. B. *Proc. Natl. Acad. Sci. USA* **1992**, *89*, 10940-10944.
(4) Nguyen, J.; Baldwin, M. A.; Cohen, F. E.; Prusiner, S. B. *Biochemistry* **1995**, *34*, 4186-4192.
(5) Zhang, H.; Kaneko, K.; Nguyen, J. T.; Livshits, T. L.; Baldwin, M. A.; Cohen, F. E.; James, T. L.; Prusiner, S. B. *J. Mol. Bio.* **1995**, *250*, 514-526.
(6) Nguyen, J. T.; Inouye, H.; Baldwin, M.; Fletterick, R. J.; Cohen, F. E.; Prusiner, S. B.; Kirschner, D. A. *J. Mol. Biol.* **1995**, *252*, 412-422.
(7) Heller, J.; Kolbert, A. C.; Larsen, R.; Ernst, M.; Bekker, T.; Baldwin, M.; Prusiner, S. B.; Pines, A.; Wemmer, D. E. *Protein Science* **1996**, *5*, 1655-1661.
(8) Saito, H. *Magn. Reson. in Chemistry* **1986**, *24*, 835-852.
(9) Kricheldorf, H. R.; Muller, D. *Macromolecules* **1983**, *16*, 615-623.
(10) Pines, A.; Gibby, M. G.; Waugh, J. S. *J. Chem. Phys.* **1973**, *59*, 569.
(11) Schaefer, J.; Stejskal, E. O. *J. Am. Chem. Soc.* **1976**, *98*, 1031-1032.
(12) Spera, S.; Bax, A. *J. Am. Chem. Soc.* **1991**, *113*, 5490-5492.
(13) Wishart, D. S.; Sykes, B. D. *J. Biomolecular NMR* **1994**, *4*, 171-180.
(14) de Dios, A. C.; Pearson, J. G.; Oldfield, E. *Science* **1993**, *260*, 1491-6.
(15) Jeener, J.; Meier, B. H.; Bachman, P.; Ernst, R. R. *J. Chem. Phys.* **1979**, *71*, 4546.
(16) Braunschweiler, B. L.; Ernst, R. R. *J. Magn. Resn.* **1983**, *53*, 521.
(17) Davis, D. G.; Bax, A. *J. Am. Chem. Soc.* **1985**, *107*, 2820.
(18) Raleigh, D. P.; Levitt, M. H.; Griffin, R. G. *Chem. Phys. Lett.* **1988**, *146*, 71-6.
(19) Levitt, M. H.; Raleigh, D. P.; Creuzet, R.; Griffin, R. G. *J. Chem. Phys.* **1990**, *92*, 6347-6364.
(20) Creuzet, F.; McDermott, A.; Gebhard, R.; van der Hoef, K.; Spijker-Assink, B.; Herzfeld, J.; Lugtenburg, J.; Levitt, M. H.; Griffin, R. G. *Science* **1991**, *251*, 783-786.
(21) Smith, S. O.; Jonas, R.; Braiman, M.; Bormann, B. J. *Biochemistry* **1994**, *33*, 6334-41.
(22) Lansbury Jr., P. T.; Costa, P. R.; Griffiths, J. M.; Simon, E. J.; Auger, M.; Halverson, K. J.; Kocisko, D. A.; Hendsch, Z. S.; Ashburn, T. T.; Spencer, R. G. S.; Tidor, B.; Griffin, R. G. *Nature Structural Biology* **1995**, *2*, 990-998.
(23) Tomita, Y.; O'Connor, E. J.; McDermott, A. *J. Am. Chem. Soc.* **1994**, *116*, 8766-8771.
(24) Morris, G. A.; Freeman, R. *J. Magn. Reson.* **1978**, *29*, 433.
(25) Peerson, O.; Groesbeek, M.; Aimoto, S.; Smith, S. O. *J. Am. Chem. Soc.* **1995**, *117*, 7228-7237.
(26) Shirley, J. H. *Phys. Rev. B* **1965**, *138*, 979.
(27) Vega, S. *J. Chem. Phys.* **1992**, *96*, 2655-2680.

(28) Levante, T. O.; Baldus, M.; Meier, B. H.; Ernst, R. R. *Mol. Phys.* **1995**, *86*, 1195-1212.
(29) Smith, S. A.; Levante, T. O.; Meier, B. H.; Ernst, R. R. *J. Magn. Reson.* **1994**, *A106*, 75-105.
(30) Heller, J.; Larsen, R.; Ernst, M.; Kolber, A. C.; Baldwin, M.; Prusiner, S. B.; Wemmer, D. E.; Pines, A. *Chem. Phys. Lett.* **1996**, *251*, 223-229.
(31) Raleigh, D. P.; Creuzet, F.; Das Gupta, S. K.; Levitt, M. H.; Griffin, R. G. *J. Am. Chem. Soc.* **1989**, *111*, 4502-3.
(32) Thompson, L. K.; McDermott, A.; Raap, J.; van der Wielen, C. M.; Lugtenburg, J.; Herzfeld, J.; Griffin, R. G. *Biochemistry* **1992**, *31*, 7931.
(33) Kubo, A.; McDowell, C. A. *J. Chem. Soc., Faraday Trans. 1* **1988**, *84*, 3713-3730.
(34) Cohen, F. E.; Pan, K. M.; Huang, Z.; Baldwin, M.; Fletterick, R. J.; Prusiner, S. B. *Science* **1994**, *264*.

Chapter 7

Application of the CSA/Z surface method to the prion protein H1 fragment

7.1 Introduction

Dihedral angle measurements used in conjunction with distance measurements can define the structure of proteins. In solution, backbone torsion angles are measured using J-couplings and the Karplus curve[1-5]. These angles are then used as constraints when calculating structures. In solids, isotropic shifts have been correlated with secondary structure[6] and, recently, direct measurements of dihedral angles[7-14] have been made possible (see section 2.4). However, isotropic-shift values can only roughly categorize secondary structure and the direct dihedral angle measurement techniques have not yet been applied to biological systems of interest. Solid-state rotational-resonance distance measurements[15,16] have been used to define torsion angles to elucidate the structure of peptides derived from pancreatic amyloid[17]. This method, however, requires several assumptions and can only be used if measured distances are accurate. Results show that if distances are measured to ±0.2 Å, ϕ and ψ are only restrained to within ±20° and ±40°, respectively.

A simple method for determining dihedral angles, the CSA/Z surface method[18], was described in chapter 4. This method uses slow spinning speed cross-polarization magic-angle-spinning[19,20] (slow CPMAS) to measure the principle values of the chemical-shift anisotropy (CSA) tensor, and compares these values with theoretically derived chemical-shielding surfaces to derive backbone torsion angles. Angle measurements are accurate to approximately

±12° and should improve as more data points are used to correlate the theoretically derived chemical shifts with experimentally observed ones.

Distance measurements and isotropic shift measurements on the H1 fragment of the prion protein were described in chapter 6[21]. From the data, it appears as if H1 is mostly α-helical when lyophilized from hexafluoro-isopropanol (HFIP), while it is more β-sheet-like when lyophilized from acetonitrile (AcN)/H_2O. This conclusion is consistent with predicted structures for the region[22,23], and with the hypothesis that a conformational change in this region may play an important role in the formation of infectious prion protein and prion amyloids[24]. Models predict that the H1 region may be helical in normal form of the prion protein, PrP^C, while it probably forms intermolecular β-pleated sheets in the amyloid plaques. This chapter describes the use of the CSA/Z method on H1 samples lyophilized from AcN/H_2O to better understand the structure of the peptides.

7.2 Materials and Methods

7.2.1 Sample Preparation

Synthesis of samples was described in section 6.2.1. Four double ^{13}C samples were used: H1(115-^{13}C=O, 118-$^{13}C_\alpha$), H1(113-^{13}C=O, 115-$^{13}C_\alpha$), H1(114-^{13}C=O, 117-$^{13}C_\alpha$), and H1(113-^{13}C=O, 116-$^{13}C_\alpha$). These samples contain the four alanines in the center of the H1 peptide.

7.2.2 Data Acquisition and Processing

All experiments were performed on a home-built spectrometer operating at a ^1H Larmor frequency of 301.2 MHz. A Chemagnetics (Fort Collins, CO) 4 mm double-resonance high-speed spinning probe was used for

rotational-resonance experiments. Spinning speeds were controlled using a home-built spinning-speed controller using a phase-locked loop as the central element in the control circuit (see appendix 1). Spinning speeds could be controlled to within ±1 Hz for slow speeds, with long-term stability. CP contact time was 2.0 ms and the ^{1}H decoupling field strength was 100 kHz. Isotropic shifts were measured relative to the ^{13}C=O of glycine (176.04 ppm), using a fast CPMAS experiment.

Data was processed using Matlab (The Mathworks, Boston, MA) and then spectra were fit using the GAMMA[25] routines described in section 4.2.4[18] and in appendix B.

7.3 Results and Discussion

The CPMAS spectra of crystalline H1(114-^{13}C=O, 117-$^{13}C_{\alpha}$) at spinning speeds of 783 Hz, 858 Hz, and 952 Hz are shown in figure 7.1. Similar data were collected for the other H1 peptides (data not shown). For each spectrum, a non-linear least-square fits was used to determine the chemical-shift tensor for the $^{13}C_{\alpha}$ (figure 7.1) and error estimates. The average value of the measurements was used for most of the samples, although only one data set was acquired for H1(113-^{13}C=O, 116-$^{13}C_{\alpha}$) due to low signal-to-noise. The average chemical shifts were as follows (in ppm): 115-$^{13}C_{\alpha}$: $\delta_{11} = 68.0 \pm 0.8$, $\delta_{22} = 55.6 \pm 1.1$, $\delta_{33} = 23.7 \pm 1.9$; 116-$^{13}C_{\alpha}$: $\delta_{11} = 71.4 \pm 1.1$, $\delta_{22} = 55.6 \pm 1.3$, $\delta_{33} = 23.5 \pm 2.4$; 117-$^{13}C_{\alpha}$: $\delta_{11} = 69.0 \pm 1.0$, $\delta_{22} = 57.1 \pm 1.3$, $\delta_{33} = 25.0 \pm 2.3$; 118-$^{13}C_{\alpha}$: $\delta_{11} = 69.8 \pm 1.1$, $\delta_{22} = 54.3 \pm 1.3$, $\delta_{33} = 22.7 \pm 2.4$.

The correlation between theory and experiment calculated for the three crystalline tripeptides (G*AV, A*AA, and A*AA-hemihydrate) described in

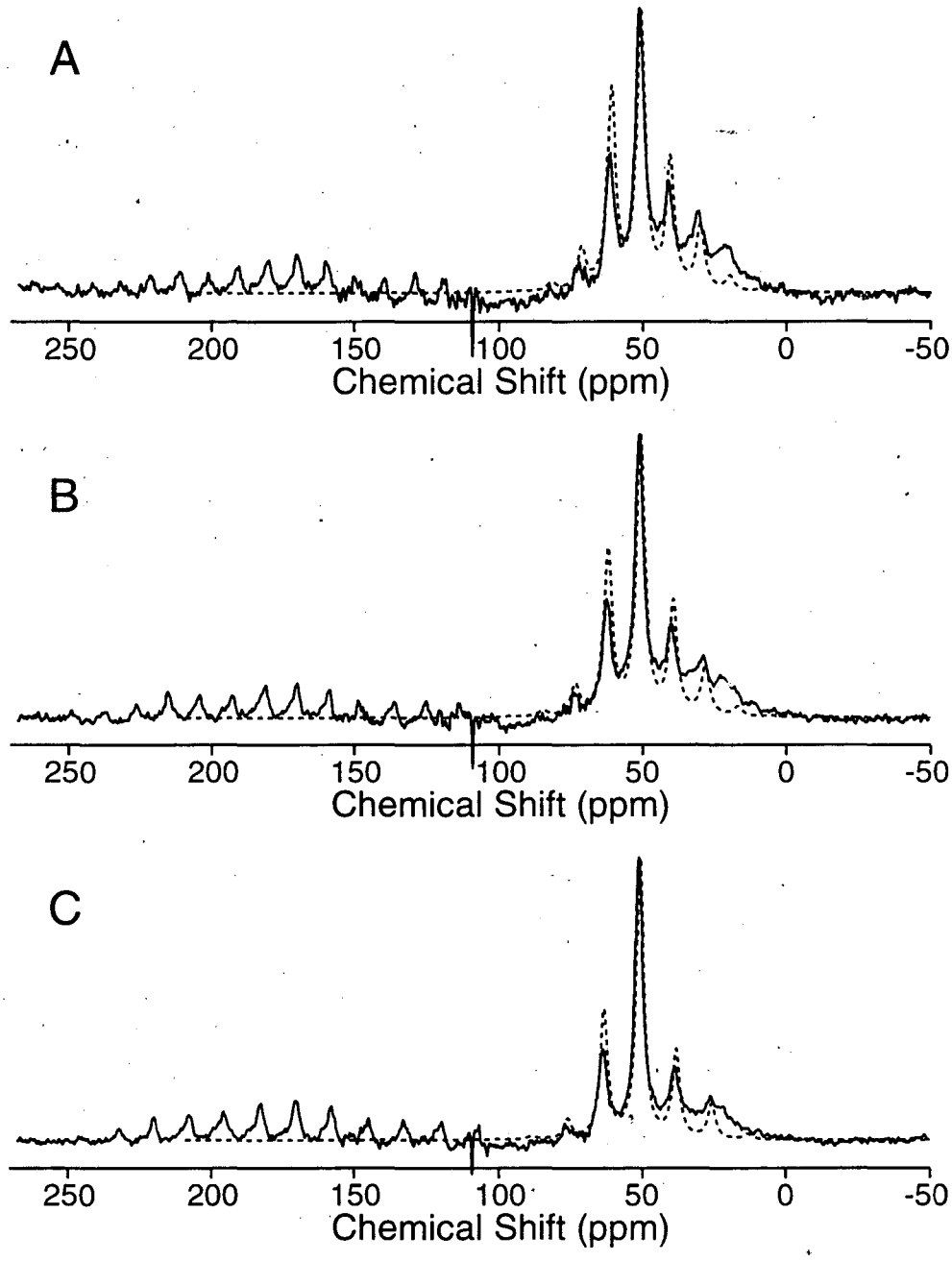

Figure 7.1: CPMAS spectra for crystalline H1(114-^{13}C=O 117-$^{13}C_{\alpha}$ (solid lines) and their best fits (dashed lines). For all experiments, the CP contact time was 2.0 ms, the decoupling field strength was 100 kHz, and the recycle delay was 1.5 s. 8192 scans were acquired for each spectrum. A. Spinning at 783 Hz. B. Spinning at 858 Hz. C. Spinning at 952 Hz. Signal due to 115 ^{13}C=O sites is centered at approximately 172.5 ppm. This signal and its spinning sidebands were not fit. All chemical shifts are referenced to ^{13}C=O glycine at 176.04 ppm.

chapter 4 was used. The slope of the best fit line was -0.67, the correlation coefficient was R=0.99 and the rmsd value was ω=2.15 ppm.

When this correlation was used to scale the calculated tensor surfaces and both ^1Z and ^3Z-surfaces were calculated (see chapter 4), several high probability solutions were predicted for each of the C_α sites (figure 7.2). The sets of possible solutions were similar in most cases. Only those solutions with Gaussian probabilities over 0.3 are reported, and the dihedral angles for those solutions are accurate to within ±2° due to the size of the steps used in calculating the ^1Z-surfaces. For 115-$^{13}C_\alpha$, highest probability solution (P=0.98) was ϕ = -92° and ψ = -68°. For 116-$^{13}C_\alpha$, solutions were: ϕ = -90° and ψ = -58° (P=0.99), ϕ = -140° and ψ = -30° (P=0.94), ϕ = -172° and ψ = 166° (P=0.82), ϕ = -26° and ψ = 154° (P=0.67), ϕ = -6° and ψ = –144° (P=0.64). For 117-$^{13}C_\alpha$, solutions were: ϕ = -144° and ψ = -36° (P=0.67), ϕ = -90° and ψ = -68° (P=0.54), ϕ = -172° and ψ = 156° (P=0.50). For 118-$^{13}C_\alpha$, solutions were: ϕ = -90° and ψ = -60° (P=0.82), ϕ = -142° and ψ = -30° (P=0.43), ϕ = -170° and ψ = 162° (P=0.35), ϕ = -4° and ψ = -144° (P=0.35). Total probabilities for each sample do not add to 1.0 because the probability is a measure of how well the chemical shifts predicted by the angles in question match the data, rather than being the probability that those angles are the correct solution as compared with all other angles.

In all cases, one high-probability solution (near ϕ = -90°, ψ = -65°) lies just outside of allowed Ramachandran space. Of the two other solutions found in most of these samples, one (ϕ = -140°, ψ = -40°) lies in a region in which helices are commonly located, while the other(ϕ = -170°, ψ = 160°) lies in a sheet region. Because many solutions appear, it is impossible to choose which is the "correct" one.

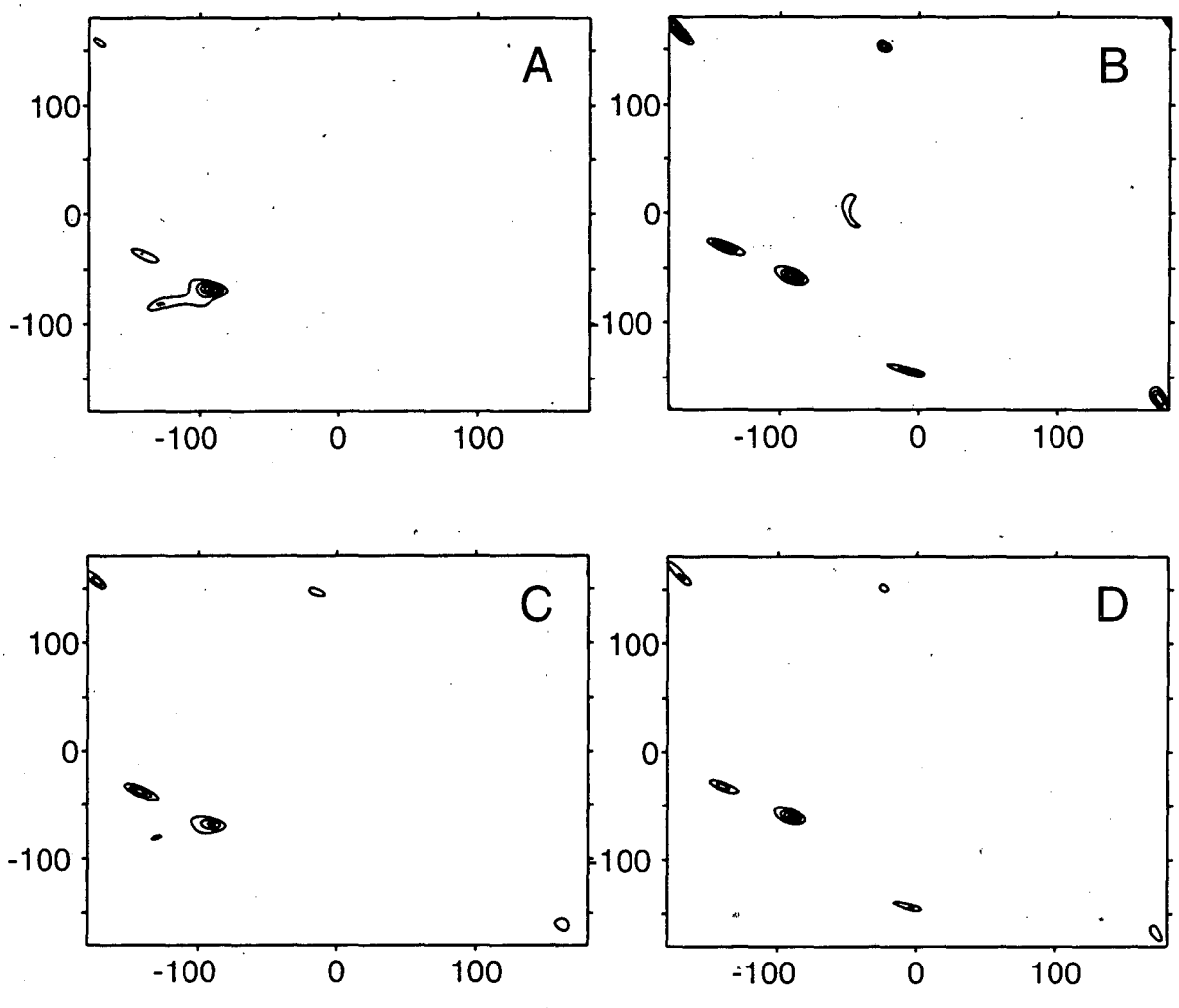

Figure 7.2: ^{3}Z-surfaces calculated from the experimentally determined chemical-shift anisotropies for C_α alanines in the H1 peptides and theoretical chemical-shielding surfaces scaled by the correlation determined in chapter 4 for three tripeptides. The ^{3}Z-surfaces are for A. 115-$^{13}C_\alpha$; B. 116-$^{13}C_\alpha$; C. 117-$^{13}C_\alpha$; D. 118-$^{13}C_\alpha$. Maximum probabilities and the angles associated with them are described in the text. In all cases, contours are plotted at 10%, 30%, 50%, 70%, and 90% of the maximum intensity.

The ^{3}Z-surfaces for the H1 peptides and the ^{3}Z-surface reported for the tripeptide G*AV in chapter 4 (figure 4.4) look similar, although the angles of highest probability are not exactly the same. A ^{3}Z-surface for a hypothetical β-sheet looks quite different[26] (data not shown?). It is interesting to understand why this is so and why such a variety of solutions are present. First, the differences in isotropic shifts between α-helix and β-sheet for alanine is only about 4 ppm. The observed rmsd for the correlation of theory and experiment derived from the tripeptide studies is 2.15 ppm and this value is used as the width of the Gaussian from which the ^{1}Z-surfaces are calculated. The measured isotropic shifts for the H1 peptides were in the region between those for helix and those for sheet and the width of the Gaussian was broad enough to include both the helical areas of the tensor surfaces and the sheet areas. The values of the breadth (δ_{22}-δ_{11}) were similar to those for a helix, while those for the width (δ_{33}-δ_{11}) were similar to those expected for a sheet. This lead to results with patterns in Ramachandran space that were similar to those expected for a helix, but are not narrowed enough to be definitive.

To get better Z-surfaces with narrower ranges of results, it is necessary to better define the correlation between theory and experiment. A lower rmsd would lead narrower Gaussians. This is only possible through the collection of more data points, a process that is underway. For other amino acids, such as valine, with larger differences of chemical shifts between secondary structures, the Z-surface method will be able to predict angles with more accuracy. This is due to the steepness of the tensor surfaces in the allowed regions of Ramachandran space.

The β-pleated sheets predicted by Pauling[27] for the silk fibril have dihedral angles of approximately $\phi = -139°$ and $\psi = 135°$. Griffiths and co-

workers[17] measured angles of $\phi = -100°$ and $\psi = 94°$ in pancreatic amyloid peptides. A model of the aggregates with exaggerated pleating was developed from these rotational-resonance studies. An "accordion-like" motion was used to account for this pleating , and the result was a more compact structure in which internuclear distances were shorter than those expected in the Pauling model.

Neither set of these dihedral angle values is observed for the H1 peptides. Solutions closer to Pauling's are present, but are more than 30° off in both ϕ and ψ. The interatomic distances observed for H1 using rotational resonance (discussed in chapter 6) are more consistent with the Griffiths model since distances were shorter than those expected for an extended β-sheet. Isotropic shifts of carbonyl carbons are consistent with β-sheet structure, but are not able to help differentiate between regions of sheet. Whether one of these sheet structures is present, or whether lyophilized H1 peptides contain multiple conformations leading to a range of distances and a range of dihedral angles is still an open question.

7.4 Conclusions

The CSA/Z surface method can be used to determine dihedral angles in peptides of unknown conformation. The H1 fragment of the prion protein was previously predicted to form β-pleated sheets and distances measured on H1 peptides were consistent with a highly pleated sheet. Isotropic shift measurements also agreed with this conclusion. In this study, it was shown that the dihedral angles around the central alanines in H1 peptides also may be consistent with this hypothesis. Angles for four peptides containing

different $^{13}C_\alpha$ sites in the central region of H1 were measured and a solution in the extended/β-sheet region of Ramachandran space exists, although other solutions near the α-helix region also exist. In all cases the solution with the highest Gaussian probability lay outside the conformationally allowed region of Ramachandran space. Other, two-dimensional techniques of measuring the CSA might be useful in this case, since they are more accurate and since they can be used to distinguish multiple conformations.

It is possible that the H1 peptide is unstructured. Rotational resonance distances measured could be an average of several distances and the measured CSA could be an average of several CSA tensors. Experiments that could distinguish between such average measurements and single distance or CSA measurements could be developed in the future to address this issue.

From the data in this chapter and in the previous chapter, there is a strong possibility that H1, when lyophilized from acetonitrile and water, takes on an extended, β-sheet-like conformation. However, other conformations can not be ruled out. This β-sheet-like structure is consistent with predictions for the behavior of H1 in the infectious form of the prion protein

References:
(1) Karplus, M. *J. Phys. Chem.* **1959**, *30*, 11-15.
(2) Bystrov, V. F. *Progr. Nucl. Magn. Reson.* **1976**, *10*, 41-82.
(3) Pardi, A.; Billeter, M.; Wüthrich, K. *J. Mol. Biol.* **1984**, *180*, 741-751.
(4) Wagner, G.; Braun, W.; Havel, T. F.; Schaumann, T.; Go, N.; Wüthrich, K. *J. Mol. Biol.* **1987**, *196*, 611-639.
(5) Montelione, G. T.; Emerson, S. D.; Lyons, B. A. *Biopolymers* **1992**, *32*, 327-334.
(6) Saito, H. *Magn. Reson. in Chemistry* **1986**, *24*, 835-852.
(7) Weliky, D. P.; Dabbagh, G.; Tycko, R. *J. Magn. Reson.* **1993**, *A104*, 10-16.
(8) Dabbagh, G.; Weliky, D. P.; Tycko, R. *Macromolecules* **1994**, *27*, 6183-6191.
(9) Tomita, Y.; O'Conner, E. J.; McDermott, A. *J. Am. Chem. Soc.* **1994**, *116*, 8766-8771.
(10) Feng, X.; Lee, Y. K.; Sandstrom, D.; Eden, M.; Maisel, H.; Sebald, A.; Levitt, M. H. *Chem. Phys. Lett.* **1996**, *257*, 314-320.
(11) Ishii, Y.; Terao, T.; Kainosho, M. *Chem. Phys. Lett.* **1996**, *256*, 133-140.
(12) Schmidt-Rohr, K. *Macromolecules* **1996**,
(13) Schmidt-Rohr, K. *J. Am. Chem. Soc.* **1996**, *118*, 7601-3.
(14) Tycko, R.; Weliky, D. P.; Berger, A. E. *J. Chem. Phys.* **1996**, *105*, 7915-7930.
(15) Raleigh, D. P.; Levitt, M. H.; Griffin, R. G. *Chem. Phys. Lett.* **1988**, *146*, 71-6.
(16) Levitt, M. H.; Raleigh, D. P.; Creuzet, R.; Griffin, R. G. *J. Chem. Phys.* **1990**, *92*, 6347-6364.
(17) Griffiths, J. M.; Ashburn, T. T.; Auger, M.; Costa, P. R.; Griffin, R. G.; Lansbury Jr., P. T. *J. Am. Chem. Soc.* **1995**, *117*, 3539-3546.
(18) Heller, J.; Laws, D. D.; Tomasseli, M.; King, D. S.; Pines, A.; Wemmer, D. E.; Havlin, R. H.; Oldfield, E. *J. Am. Chem. Soc.* **1997**, *in press*,
(19) Pines, A.; Gibby, M. G.; Waugh, J. S. *J. Chem. Phys.* **1973**, *59*, 569.
(20) Schaefer, J.; Stejskal, E. O. *J. Am. Chem. Soc.* **1976**, *98*, 1031-1032.
(21) Heller, J.; Kolbert, A. C.; Larsen, R.; Ernst, M.; Bekker, T.; Baldwin, M.; Prusiner, S. B.; Pines, A.; Wemmer, D. E. *Protein Science* **1996**, *5*, 1655-1661.
(22) Huang, Z.; Gabriel, J.-M.; Baldwin, M. A.; Fletterick, R. J.; Prusiner, S. B.; Cohen, F. E. *Proc. Natl. Acad. Sci. USA* **1994**, *91*, 7139-7143.
(23) Huang, Z.; Prusiner, S. B.; Cohen, F. E. *Folding & Design* **1996**, *1*, 13-19.
(24) Stahl, N.; Baldwin, M. A.; Teplow, D. B.; Hood, L.; Gibson, B. W.; Burlingame, A. L.; Prusiner, S. B. *Biochemistry* **1993**, *32*, 1991-2002.
(25) Smith, S. A.; Levante, T. O.; Meier, B. H.; Ernst, R. R. *J. Magn. Reson.* **1994**, *A106*, 75-105.
(26) Laws, D. D., personal communication.
(27) Salemme, F. R. *Prog. Biophys. Mol. Bio.* **1983**, *42*, 95.

APPENDIX A:

SPINNING SPEED CONTROLLER CIRCUIT DIAGRAM

Spinning Speed Controller Circuit Diagram

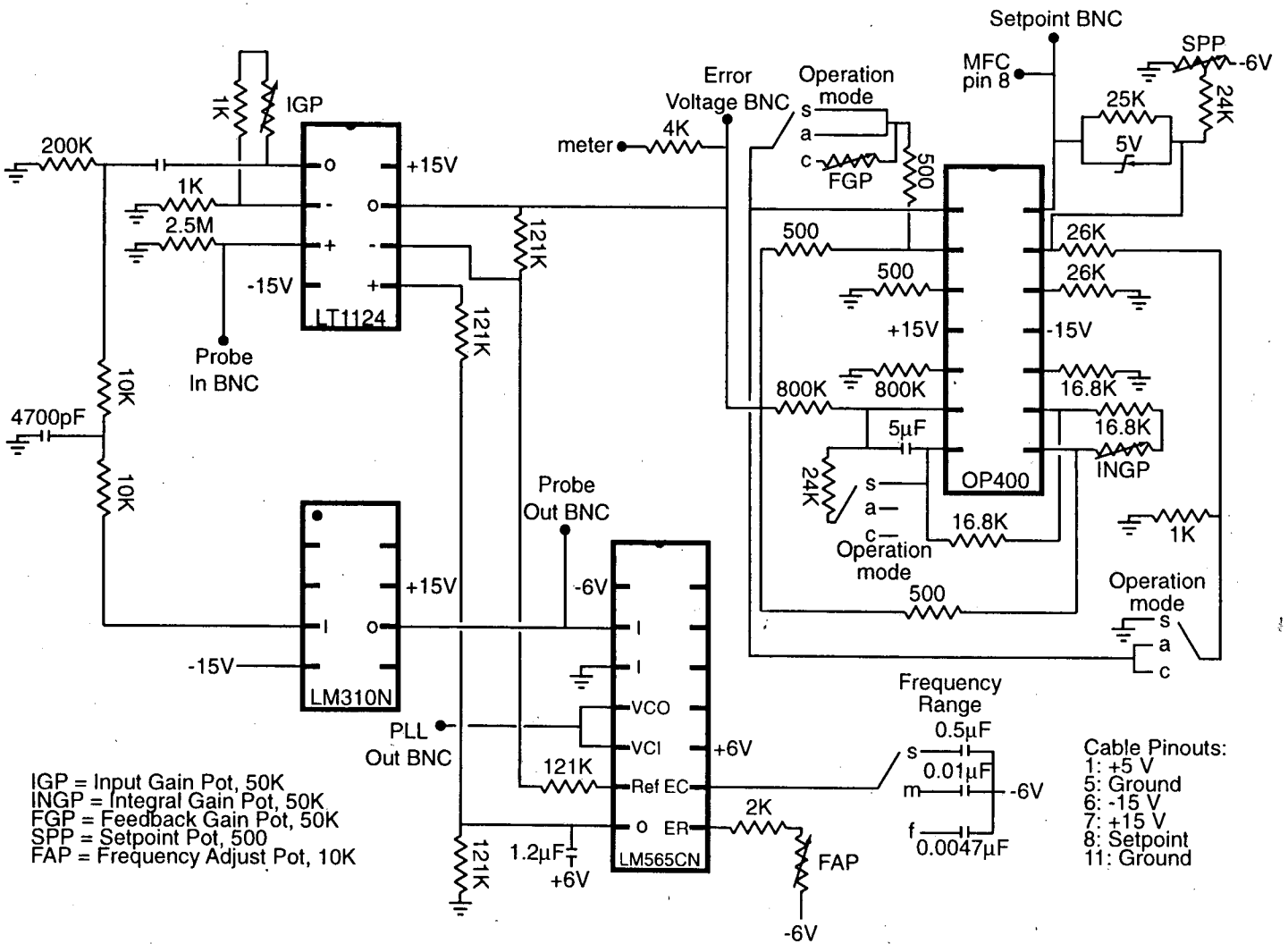

APPENDIX B:

PROGRAMS

The following pages contain the important programs for processing rotational-resonance data, fitting it, and simulting it, as well as programs for fitting and simulting a ^{13}C slow CPMAS spectra to get the CSA principle values in the presence of the ^{14}N coupling.

The first program is written in C and takes processed rotational-resonance spectra in text format, adds spectra which correspond to the same magnetization-exchange period, corrects them for natural abundance, find the variences and difference magnetizations, and outputs all of this into another text file. This data is then entered into the second program, written by Matthias Ernst in the GAMMA environment, with only minor additions by the author. This program uses Minuit to fit the rotational-resonance data. It fits the distance, the zero-quantum T_2, and the line-width inhomogeneity. The third program is simply a simulation of rotational-resonance magnetization which includes line-width inhomogeneity.

The second set of programs was written by Marco Tomaselli in the GAMMA environment. The first of these fits a CPMAS spectrum. It is meant to be used to analyze slow CPMAS spectra of C_α carbons on the backbone of a peptide with a close ^{14}N nucleus. The program fits the isotropic shift, the s11 and s22 values (it assumes a traceless tensor), and linewidths. The last program simply simulates these spectra.

```
#include <stdio.h>
#include <math.h>

/*
this program takes processed rr data
as a 2D array of text with sets of repeated
data and processes it further by correcting
for natural abundance, calculating variences,
calculating the differnce magnetization,
and outputing the data in text format.
*/

main()
{
#define MAXT1 2048
#define MAXRPT 100

float tmp, norm;
char infile[60], outfile[60];
int j, i, k, sw, sidebands, z, offset;
int pts, t1, rpts, center1, center2, width1, width2, spin;
float integral1[MAXT1], integral2[MAXT1], diffmag[MAXT1], stddev1[MAXT1],
stddev2[MAXT1];
float rptint1[MAXRPT][MAXT1], rptint2[MAXRPT][MAXT1], time[MAXT1];
float na1, na2, natabund1, natabund2, summag;
FILE *ifile, *ofile;

while(1)
    {
    printf("input file name:\n");
    scanf("%s",infile);
    if ((ifile = fopen(infile,"r"))==NULL)
        fprintf(stderr,"\nCan't open input file.\n");
    else
        break;
    }
while(1)
    {
    printf("output file name:\n");
    scanf("%s",outfile);
    if ((ofile = fopen(outfile,"w"))==NULL)
        fprintf(stderr,"\nCan't open output file.\n");
    else
        break;
    }

printf("number of points?\n");
scanf("%i",&pts);
printf("spectral width in Hz(+/- ?Hz)?\n");
scanf("%i",&sw);
printf("spinning speed in Hz?\n");
scanf("%i",&spin);
```

```
printf("number of sidebands to integrate?\n");
scanf("%i",&sidebands);
printf("number of t1 pts?\n");
scanf("%i",&t1);
printf("number of repeats?\n");
scanf("%i",&rpts);
printf("CO site center?\n");
scanf("%i",&center1);
printf("CO site width(+/- ? pts)?\n");
scanf("%i",&width1);
printf("Ca site center?\n");
scanf("%i",&center2);
printf("Ca site width?\n");
scanf("%i",&width2);
printf("natural abundance background for CO?\n");
scanf("%f",&na1);
printf("natural abundance background for Ca?\n");
scanf("%f",&na2);
printf("t1 values for ouput on separate lines?\n");
for(i=1;i<=t1;i++)
    scanf("%f",&time[i]);

/*initialize*/
for (i=1; i<=t1; i++)
    {
    integral1[i]=0;
    integral2[i]=0;
    diffmag[i]=0;
    stddev1[i]=0;
    stddev2[i]=0;
    for (j=1; j<=rpts;j++)
        {
        rptint1[j][i]=0;
        rptint2[j][i]=0;
        }
    }

summag=0;
/* read in input */
for (j=1; j<=rpts;j++)
    {
    printf("Starting repeat %i.....\n", j);
    for (i=1; i<=t1; i++)
        {
        for (k=1; k<=pts; k++)
            {
            /* read real input*/
            if (fscanf(ifile,"%f",&tmp) !=EOF )
                {
                /* integrate peaks */
                for (z=0; z<=sidebands; z++)
                    {
```

```
                    offset =(int)((float)((z*spin*pts)/(2*sw)) + .5);
                    if (k>=(center1-offset-width1) && k<=(center1-offset+width1))
                        {
                        integral1[i] = integral1[i] + tmp;
                        rptint1[j][i] = rptint1[j][i] + tmp;
                        }
                    if (z && k>=(center1+offset-width1) && k<=(center1+offset+width1))
                        {
                        integral1[i] = integral1[i] + tmp;
                        rptint1[j][i] = rptint1[j][i] + tmp;
                        }
                    }
                if (k>=(center2-width2) && k<=(center2+width2))
                    {
                    integral2[i] = integral2[i] + tmp;
                    rptint2[j][i] = rptint2[j][i] + tmp;
                    }
                }
            else
                {
                printf("EOF reached before complete. Check data sizes.\n");
                exit(1);
                }

            /*read imag input*/
            if (fscanf(ifile,"%f",&tmp) == EOF)
                {
                printf("EOF2 reached before complete. Check data sizes.\n");
                exit(1);
                }
            }
        }
    }
fclose(ifile);

natabund1=integral1[1]*na1/rpts;
natabund2=integral2[1]*na2/rpts;
printf("natabund1 %f\n", natabund1);
printf("natabund2 %f\n", natabund2);

/*calc variances*/
for (i=1; i<=t1; i++)
    {
    integral1[i]=integral1[i]/rpts - natabund1;
    integral2[i]=integral2[i]/rpts - natabund2;
    for (j=1; j<=rpts; j++)
     {
     rptint1[j][i]=rptint1[j][i] - natabund1;
     rptint2[j][i]=rptint2[j][i] - natabund2;
     }
    }
for (i=1; i<=t1; i++)
```

```
    summag = summag + integral1[i] + integral2[i];
summag = summag/(t1*2);
printf("summag %f\n", summag);
if (rpts !=1)
    {
    for (i=1; i<=t1; i++)
        {
        integral1[i]=integral1[i] - summag;
        integral2[i]=integral2[i] - summag;
        for (j=1; j<=rpts; j++)
         {
         rptint1[j][i]=rptint1[j][i] - summag;
         rptint2[j][i]=rptint2[j][i] - summag;
/*actually this is variences*/
         stddev1[i]=stddev1[i]+(rptint1[j][i]-integral1[i])*(rptint1[j][i]-integral1[i])/(rpts-1);
         stddev2[i]=stddev2[i]+(rptint2[j][i]-integral2[i])*(rptint2[j][i]-integral2[i])/(rpts-1);
         }
        }
    }

norm=0;
for (i=1; i<=t1; i++)
    {
    diffmag[i] = integral1[i] - integral2[i];
    if (fabs(diffmag[i]) > fabs(norm))
        norm = diffmag[i];
    }

/* output */
fprintf(ofile, "t1\tint1\tint2\tdiffmag\tstddev\n");
for (i=1; i<=t1;i++)
{
fprintf(ofile,"%f\t%f\t%f\t%f\t%f\n",time[i],integral1[i],integral2[i],diffmag[i]/norm,
(sqrt(stddev1[i] + stddev2[i])/norm)/sqrt(rpts));
}
for (i=1; i<=t1;i++)
{
for (j=1; j<=rpts; j++)
    fprintf(ofile,"%6.1f ",rptint1[j][i]);
fprintf(ofile,"\n");
for (j=1; j<=rpts; j++)
    fprintf(ofile,"%6.1f ",rptint2[j][i]);
fprintf(ofile,"\n");
}
fclose(ofile);
}
```

```
/*
rrsimfi_3_opt.cc

simulate rotational resonance as a fictious spin 1/2 system
floquet approach in liouville space
uses real reduced (3x3) liouville relaxation
basis in Liouville space is Ix Iy and Iz
dw must be a multiple of the rotorcycle, since scaling of
projection from Floquet to Liouville space is not implemented.

uses MINUIT for minimization

MAER 13.5.1995, modified by JH
*/

#include "gamma.h"
#include "floq_op.h"

void fcn(int*, double*, double*, double*, int*);
extern "C" int minuit_(void (*fcn) (int*, double*, double*, double*, int*), int*);

/* these are global variables to copy argc and argv into. Otherwise
  we can not access them from the subroutine since there is no simple
  way of passing them into fcn.
*/
int  ARGC;
char **ARGV;

main(int argc, char *argv[])

{  int x=0;

  ARGC = argc;
  ARGV = argv;
   (void) minuit_(&fcn, &x);
}

void fcn(int *npar, double *grad, double *chi2, double *param, int *iflag)

{ static int ncalls=0;
 static gen_op H[5], U, U1;
  static space_T Adip, Acsa1, Acsa2, Acsa1_R, Acsa2_R, Adip_R;
  static double D, delta_CSA1, etha_CSA1, iso_CSA1;
  static double J, delta_CSA2, etha_CSA2, iso_CSA2;
 static int i,j,k,m,Fnp,count,qu,N1;
 static String name;
 const double thetam=54.73561032;
 static double mas_freq, dist;
 static double dw,T2zq;
  static double alpha_D,beta_D,gamma_D;
  static double alpha_CSA1,beta_CSA1,gamma_CSA1;
  static double alpha_CSA2,beta_CSA2,gamma_CSA2;
```

```
 static double alpha,beta,gamma;
 complex temp;
 static complex twopi = complex(2.0*PI,0);
 static double time_m[30];
 static int time_s[30];
 static double data_m[30];
 static double error_m[30];
 static double data_s[30];
 static int debug = 0;
 static matrix help(3,3,0);
 static matrix zero(3,3,0);
//inhomo
 static int ninhms, step;
 static double T2i, T2, lwt[100], lint, inhmss;
//end inhomo

 int value1[] = {2, 50, 100, 144, 200, 300, 538, 1154};
 int value2[] = {1, 7, 27, 11, 29, 37, 55, 107};
 int value3[] = {1, 11, 41, 53, 79, 61, 229, 271};

 ++ncalls;
 dist = param[0]*1e-10;
 T2zq = param[1];
 T2  = param[2];

 D = 1e-7*6.72335079e7*6.72335079e7*1.05457266e-34/(2*PI*dist*dist*dist);


 help.put(-1.0,0,0);
 help.put(-1.0,1,1);
 help.put( 2.0,2,2);
 help = - (complex) D * help;
 Adip = A2(help);

 cout << "this is call number " << ncalls << " with d = " << dist << " m and D = " << D << "
Hz\n";
 cout << "T2zq = " << T2zq << "sec.   T2 =" << T2 <<" sec.  1/T2 =" << 1/T2 << " Hz\n";
 cout.flush();

 if(*iflag == 1)
 { /* initialize all stuff - this part is only done once */

  complex_setf(0, 0, 1, 10, 6);
  count = 1;
  query_parameter(ARGC,ARGV,count++,"Euler angle alpha          ? ", alpha_D);
  query_parameter(ARGC,ARGV,count++,"Euler angle beta           ? ", beta_D);
  query_parameter(ARGC,ARGV,count++,"Euler angle gamma          ? ", gamma_D);
  query_parameter(ARGC,ARGV,count++,"J-coupling constant        ? ", J);
  query_parameter(ARGC,ARGV,count++,"chemical shift 1 (iso CSA)  ? ", iso_CSA1);
  query_parameter(ARGC,ARGV,count++,"CSA tensor 1 (delta CSA)    ? ", delta_CSA1);
  query_parameter(ARGC,ARGV,count++,"CSA tensor 1 (etha CSA)     ? ", etha_CSA1);
  query_parameter(ARGC,ARGV,count++,"Euler angle alpha          ? ", alpha_CSA1);
```

```
  query_parameter(ARGC,ARGV,count++,"Euler angle beta          ? ", beta_CSA1);
  query_parameter(ARGC,ARGV,count++,"Euler angle gamma         ? ", gamma_CSA1);
  query_parameter(ARGC,ARGV,count++,"chemical shift 2 (iso CSA)  ? ", iso_CSA2);
  query_parameter(ARGC,ARGV,count++,"CSA tensor 2 (delta CSA)    ? ", delta_CSA2);
  query_parameter(ARGC,ARGV,count++,"CSA tensor 2 (etha CSA)     ? ", etha_CSA2);
  query_parameter(ARGC,ARGV,count++,"Euler angle alpha         ? ", alpha_CSA2);
  query_parameter(ARGC,ARGV,count++,"Euler angle beta          ? ", beta_CSA2);
  query_parameter(ARGC,ARGV,count++,"Euler angle gamma         ? ", gamma_CSA2);
  query_parameter(ARGC,ARGV,count++,"MAS Frequency             ? ", mas_freq);
  query_parameter(ARGC,ARGV,count++,"Powder Quality (cheng)      ? ", qu);
  query_parameter(ARGC,ARGV,count++,"Floquet dimension         ? ", N1);
  query_parameter(ARGC,ARGV,count++,"Number of Data Points      ? ", Fnp);
  query_parameter(ARGC,ARGV,count++,"Data Filename              ? ", name);
  query_parameter(ARGC,ARGV,count++,"Debugging flag            ? ", debug);
// inhomo
  query_parameter(ARGC,ARGV,count++,"Number of steps           ? ", ninhms);
// end inhomo

  dw = (1.0/mas_freq);

  cout << "Program version: " << __FILE__ << " compiled at " << __DATE__ ", "
     << __TIME__ << "\n\n";
  cout << "Parameters:\n";
  cout << "rotation angle thetam    : " << thetam << " Degree\n";
  cout << "distance between spins   : " << dist << " m (initial value)\n";
  cout << "dipolar coupling constant: " << D << " Hz\n";
  cout << "relativ orientation of D tensor: (" << alpha_D << "," <<
       beta_D << "," << gamma_D << ")\n";
  cout << "J-coupling constant      : " << J << " Hz\n";
  cout << "isotropic shift 1        : " << iso_CSA1 << " Hz\n";
  cout << "CSA tensor 1 (delta)     : " << delta_CSA1 << " Hz\n";
  cout << "CSA tensor 1 (etha)      : " << etha_CSA1 << " Hz\n";
  cout << "relativ orientation of CSA tensor: (" << alpha_CSA1 << "," <<
       beta_CSA1 << "," << gamma_CSA1 << ")\n";
  cout << "isotropic shift 2        : " << iso_CSA2 << " Hz\n";
  cout << "CSA tensor 2 (delta)     : " << delta_CSA2 << " Hz\n";
  cout << "CSA tensor 2 (etha)      : " << etha_CSA2 << " Hz\n";
  cout << "relativ orientation of CSA tensor: (" << alpha_CSA2 << "," <<
       beta_CSA2 << "," << gamma_CSA2 << ")\n";
  cout << "MAS frequency:           " << mas_freq << " Hz\n";
  cout << "Powder Quality Number:   " << qu << "\n";
  cout << "Floquet Dimension (MAS): " << N1 << "\n";
  cout << "Number of data points:   " << Fnp << " points\n";
  cout << "time increments (dw):    " << dw << " s\n";
  cout << "zero quantum T2:         " << T2zq << " s (initial value)\n";
  cout << "Output filename:         " << name << "\n";
// inhomo
  cout << "Inhomogeneous Linewidths: " << 1/T2 << " Hz (initial value)\n";
  cout << "Number of Inhomo Steps:   " << ninhms << "\n";
// end inhomo

 //setup for the space tensors
```

```
  help.put(-1.0/2.0*(1.0+etha_CSA1),0,0);
  help.put(-1.0/2.0*(1.0-etha_CSA1),1,1);
 help.put( 1.0,2,2);
 help = (complex) delta_CSA1 * help;
 Acsa1 = A2(help);
  Acsa1 = Acsa1.rotate(alpha_CSA1,beta_CSA1,gamma_CSA1);
  Acsa1 = Acsa1.rotate(-gamma_D,-beta_D,-alpha_D);

  help.put(-1.0/2.0*(1.0+etha_CSA2),0,0);
  help.put(-1.0/2.0*(1.0-etha_CSA2),1,1);
 help.put( 1.0,2,2);
 help = (complex) delta_CSA2 * help;
 Acsa2 = A2(help);
  Acsa2 = Acsa2.rotate(alpha_CSA2,beta_CSA2,gamma_CSA2);
  Acsa2 = Acsa2.rotate(-gamma_D,-beta_D,-alpha_D);

 if(*npar > 3)
 { cerr << "the number of parameters is not correct.\n";
   cerr << "there are " << (*npar) << " instead of 1 to 3 parameters.\n";
  cerr << "aborting ...\n\n";
  exit(1);
 }
 fstream fpin;
 fpin.open(name,ios::in);
  if(! fpin.is_open())
 { cerr << "can't open " << name << " for reading\n" ;
  cerr << "aborting ...\n\n";
  exit(1);
 }
  for(i=0;i<Fnp;++i)
 { fpin >> time_m[i];
   fpin >> data_m[i];
  fpin >> error_m[i];
   time_s[i] = int(time_m[i]/dw+0.5);
   if(time_s[i] == 0)
    time_s[i] = 1;
 }
 fpin.close();
 cout << "read " << Fnp << " datapoints:\n";
 for(i=0;i<Fnp;++i)
   cout << time_m[i] << " s\t\t" << data_m[i] << "\n";
 cout.flush();
}

if(*iflag == 2)
{ /* calculate first derivatives not implemented (yet ?)  */
}

if(*iflag == 3)
{ /* clean up if necessary not needed here */
}
```

```
 if(*iflag == 4)
 { /* this is the normal call, no special action needed */
 }

 if(*iflag > 4 || *iflag <= 0)
 { /* invalid number for *iflag */
   cerr << "Function FCN called with invalid *iflag = " << *iflag << "\n\n";
 }

 /* here we calculate the chi2 for the current parameter set */
 /* this is done for all values of *iflag                    */
//inhomo
 T2i = 1./T2;
 inhmss = 6*T2i/ninhms;              /* 3*2*t2i/ninhms for 3linewidths */
  lint = T2i*(atan((float)((ninhms-1)*inhmss+inhmss/2)*T2));
  lwt[0] = T2i*(atan((float)(inhmss/2)*T2))/lint;
 for (i=1;i<ninhms;i++)
    lwt[i]=T2i*(atan(((i+1)*inhmss-inhmss/2)*T2)-atan((i*inhmss-inhmss/2)*T2))/lint;
//end inhomo

  for(i=0;i<Fnp;++i)
   data_s[i] = 0;

//here starts the powder loop
//reference JCP 59 (8), 3992 (1973.

 for(count=1; count<value1[qu]; ++count)
 { beta  = 180.0 * count/value1[qu];
   alpha = 360.0 * ((value2[qu]*count) % value1[qu])/value1[qu];
   gamma = 360.0 * ((value3[qu]*count) % value1[qu])/value1[qu];
   if(debug>1)
   { cout << count << "\tbeta = " << beta << "\talpha = "
        << alpha << "\tgamma = " << gamma << "\n";
    cout.flush();
   }

//now we rotate the space tensor
    Adip_R  =  Adip.rotate(alpha,beta,gamma);
    Acsa1_R = Acsa1.rotate(alpha,beta,gamma);
    Acsa2_R = Acsa2.rotate(alpha,beta,gamma);

    for(i=0;i<5;++i)
    H[i] = gen_op(zero);

//now we can fill the hamiltonians for the different side diagonals

   for(j=-2;j<=2;++j)
   { temp = twopi*Adip_R.component(2,j)  * d2(j,0,thetam)*1/sqrt(6.0);
    H[j+2].put(+temp,1,2);
    H[j+2].put(-temp,2,1);
     temp = twopi*Acsa1_R.component(2,j) * d2(j,0,thetam)*1/sqrt(6.0) * 2.0 -
```

```
        twopi*Acsa2_R.component(2,j) * d2(j,0,thetam)*1/sqrt(6.0) * 2.0;
    H[j+2].put(+temp,0,1);
    H[j+2].put(-temp,1,0);
   }
   temp = H[2].get(1,2)+twopi*J;
   H[2].put(+temp,1,2);
   H[2].put(-temp,2,1);
    temp = H[2].get(0,1)+twopi*(iso_CSA1-iso_CSA2+inhmss);
   H[2].put(+temp,0,1);
   H[2].put(-temp,1,0);
  temp = complex(1/T2zq,0);
   H[2].put(temp,0,0);
   H[2].put(temp,1,1);
//inhomo
   for(step=0;step<ninhms;step++)
   { temp = H[2].get(0,1)-twopi*inhmss;
    H[2].put(+temp,0,1);
    H[2].put(-temp,1,0);
// end inhomo

//now we can set up the floquet hamiltonian and fill it with H[i]

     floq_op H_floq(N1,3,mas_freq);
     for(i=-2;i<=2;++i)
     { if(H[i+2].exists())
       { H_floq.put_sdiag(H[i+2],i);
      }
     }
      H_floq.add_omegai();
      floq_op U_floq = exp(H_floq*complex(-dw));
      U_floq.set_DBR();
     U = gen_op(zero);
      for(i=0;i<3;++i)
     { for(j=0;j<3;++j)
      { temp = 0;
        for(k=-N1;k<=N1;++k)
         temp += U_floq.get(k,0,i,j);
        U.put(temp,i,j);
      }
     }
      U.set_EBR();
     U = log(U);
     for(m=0;m<Fnp;++m)
     { U1 = exp(complex(time_s[m])*U); // this is U1 = U ^ time_s[m]
       U1.set_DBR();
//inhomo
       data_s[m] += Re(U1.get(2,2))*sin(beta/180*PI)*lwt[step];
    }
   }
//end inhomo
 } // end of powder loop
 if(debug>1)
```

```
{ cout << "measured and simulated values:\n";
  for(i=0;i<Fnp;++i)
    cout << time_m[i] << "\t" << data_m[i] << "\t" << data_s[i] << "\n";
}

*chi2 = 0;
 for(i=Fnp-1;i>=0;--i)
 { data_s[i] = data_s[i]/data_s[0];
   *chi2 += (data_m[i]-data_s[i])*(data_m[i]-data_s[i])/(error_m[i]*error_m[i]);
 }
 if(debug)
 { cout << "measured and simulated values:\n";
   for(i=0;i<Fnp;++i)
     cout << time_m[i] << "\t" << data_m[i] << "\t" << data_s[i] << "\n";
 }
 cout << "chi2 for this iteration " << *chi2 << "\n\n";
 cout.flush();
}
```

```
/*
rrsimfi_3.cc

simulate rotational resonance as a fictious spin 1/2 system
floquet approach in liouville space
uses real reduced (3x3) liouville relaxation
basis in Liouville space is Ix Iy and Iz
dw must be a multiple of the rotorcycle, since scaling of
projection from Floquet to Liouville space is not implemented.

MAER 13.5.1995, modified by JH
*/

#include "gamma.h"
#include "floq_op.h"

main(int argc, char *argv[])

{
 gen_op H[5], U, U1;
 space_T Adip, Acsa1, Acsa2, Acsa1_R, Acsa2_R, Adip_R;
 double D, delta_CSA1, etha_CSA1, iso_CSA1;
 double J, delta_CSA2, etha_CSA2, iso_CSA2;
 int i,j,k,m,Fnp,count,qu,N1;
 String name;
 const double thetam=54.73561032;
 double mas_freq, dist;
 double dw,T2zq;
 double alpha_D,beta_D,gamma_D;
 double alpha_CSA1,beta_CSA1,gamma_CSA1;
 double alpha_CSA2,beta_CSA2,gamma_CSA2;
 double alpha,beta,gamma;
 complex temp, scale;
 complex twopi = complex(2.0*PI,0);
 matrix zero(3,3,0);

//inhomo
 int ninhms, inhmss, inhmlw, step;
 double T2i, T2, lwt[100], lint;
//end inhomo

 int value1[] = {2, 50, 100, 144, 200, 300, 538, 1154};
 int value2[] = {1, 7, 27, 11, 29, 37, 55, 107};
 int value3[] = {1, 11, 41, 53, 79, 61, 229, 271};

 complex_setf(0, 0, 1, 10, 6);
 count = 1;
 query_parameter(argc,argv,count++,"Distance between spins (A)  ? ", dist);
 query_parameter(argc,argv,count++,"Euler angle alpha          ? ", alpha_D);
 query_parameter(argc,argv,count++,"Euler angle beta           ? ", beta_D);
 query_parameter(argc,argv,count++,"Euler angle gamma          ? ", gamma_D);
 query_parameter(argc,argv,count++,"J-coupling constant        ? ", J);
```

```
 query_parameter(argc,argv,count++,"chemical shift 1 (iso CSA)  ? ", iso_CSA1);
 query_parameter(argc,argv,count++,"CSA tensor 1 (delta CSA)    ? ", delta_CSA1);
 query_parameter(argc,argv,count++,"CSA tensor 1 (etha CSA)     ? ", etha_CSA1);
 query_parameter(argc,argv,count++,"Euler angle alpha           ? ", alpha_CSA1);
 query_parameter(argc,argv,count++,"Euler angle beta            ? ", beta_CSA1);
 query_parameter(argc,argv,count++,"Euler angle gamma           ? ", gamma_CSA1);
 query_parameter(argc,argv,count++,"chemical shift 2 (iso CSA)  ? ", iso_CSA2);
 query_parameter(argc,argv,count++,"CSA tensor 2 (delta CSA)    ? ", delta_CSA2);
 query_parameter(argc,argv,count++,"CSA tensor 2 (etha CSA)     ? ", etha_CSA2);
 query_parameter(argc,argv,count++,"Euler angle alpha           ? ", alpha_CSA2);
 query_parameter(argc,argv,count++,"Euler angle beta            ? ", beta_CSA2);
 query_parameter(argc,argv,count++,"Euler angle gamma           ? ", gamma_CSA2);
 query_parameter(argc,argv,count++,"MAS Frequency               ? ", mas_freq);
 query_parameter(argc,argv,count++,"Powder Quality (cheng)      ? ", qu);
 query_parameter(argc,argv,count++,"Floquet dimension           ? ", N1);
 query_parameter(argc,argv,count++,"Number of Data Points       ? ", Fnp);
 query_parameter(argc,argv,count++,"Zero Quantum T2             ? ", T2zq);
 query_parameter(argc,argv,count++,"Output Filename             ? ", name);

// inhomo
 query_parameter(argc,argv,count++,"Inhomogeneous Linewidth     ? ", inhmlw);
 query_parameter(argc,argv,count++,"Inhomogeneous Step Size     ? ", inhmss);
 query_parameter(argc,argv,count++,"Number of steps             ? ", ninhms);

 T2i = inhmlw;
 T2 = 1./inhmlw;
 lint = T2i*(atan( (float)((ninhms-1)*inhmss + inhmss/2) * T2));

  lwt[0] = T2i*( atan((float)(inhmss-inhmss/2)*T2) )/lint;
//cout << "lwt:\t" << lwt[0] <<" for step number:\t0\n";
 for (i=1;i<ninhms;i++)
  { lwt[i]=T2i*(atan(((i+1)*inhmss-inhmss/2)*T2)-atan((i*inhmss-inhmss/2)*T2))/lint;
//  cout << "lwt:\t" << lwt[i] <<" for step number:\t" << i <<"\n";
 }

// end inhomo

 dw = (1.0/mas_freq);
 dist = dist*1e-10;
 D = 1e-7*6.72335079e7*6.72335079e7*1.05457266e-34/(2*PI*dist*dist*dist);

 cout << "\n\nSimulation of isotropic chemical shift by dipolar coupling\n";
 cout << "=============================================================\n\n";
 cout << "Program version: " << __FILE__ << " compiled at " << __DATE__ ", "
    << __TIME__ << "\n\n";
 cout << "Parameters:\n";
 cout << "rotation angle thetam    : " << thetam << " Degree\n";
 cout << "distance between spins   : " << dist << " m\n";
 cout << "dipolar coupling constant: " << D << " Hz\n";
 cout << "relativ orientation of D tensor: (" << alpha_D << "," <<
       beta_D << "," << gamma_D << ")\n";
 cout << "J-coupling constant      : " << J << " Hz\n";
```

```
 cout << "isotropic shift 1       : " << iso_CSA1 << " Hz\n";
 cout << "CSA tensor 1 (delta)    : " << delta_CSA1 << " Hz\n";
 cout << "CSA tensor 1 (etha)     : " << etha_CSA1 << " Hz\n";
 cout << "relativ orientation of CSA tensor: (" << alpha_CSA1 << "," <<
       beta_CSA1 << "," << gamma_CSA1 << ")\n";
 cout << "isotropic shift 2       : " << iso_CSA2 << " Hz\n";
 cout << "CSA tensor 2 (delta)    : " << delta_CSA2 << " Hz\n";
 cout << "CSA tensor 2 (etha)     : " << etha_CSA2 << " Hz\n";
 cout << "relativ orientation of CSA tensor: (" << alpha_CSA2 << "," <<
       beta_CSA2 << "," << gamma_CSA2 << ")\n";
 cout << "MAS frequency:          " << mas_freq << "Hz\n";
 cout << "Powder Quality Number:  " << qu << "\n";
 cout << "Floquet Dimension (MAS):  " << N1 << "\n";
 cout << "Number of data points:  " << Fnp << " points\n";
 cout << "time increments (dw):   " << dw << " s\n";
 cout << "zero quantum T2:        " << T2zq << " s\n";
 cout << "Output filename:        " << name << "\n";

// inhomo
 cout << "Inhomogeneous Linewidths:  " << inhmlw << " Hz\n";
 cout << "Inhomo Correction Stepsize:" << inhmss << " Hz\n";
 cout << "Number of Inhomo Steps:  " << ninhms << "\n";
// end inhomo

 block_1D data(Fnp);
 block_1D data_sum(Fnp);

//setup for the space tensors
  matrix help(3,3,0);

  help.put(-1.0,0,0);
  help.put(-1.0,1,1);
 help.put( 2.0,2,2);
 help = - (complex) D * help;
 Adip = A2(help);

  help.put(-1.0/2.0*(1.0+etha_CSA1),0,0);
  help.put(-1.0/2.0*(1.0-etha_CSA1),1,1);
 help.put( 1.0,2,2);
 help = (complex) delta_CSA1 * help;
 Acsa1 = A2(help);
  Acsa1 = Acsa1.rotate(alpha_CSA1,beta_CSA1,gamma_CSA1);
  Acsa1 = Acsa1.rotate(-gamma_D,-beta_D,-alpha_D);

  help.put(-1.0/2.0*(1.0+etha_CSA2),0,0);
  help.put(-1.0/2.0*(1.0-etha_CSA2),1,1);
 help.put( 1.0,2,2);
 help = (complex) delta_CSA2 * help;
 Acsa2 = A2(help);
  Acsa2 = Acsa2.rotate(alpha_CSA2,beta_CSA2,gamma_CSA2);
  Acsa2 = Acsa2.rotate(-gamma_D,-beta_D,-alpha_D);
```

```
 String name1 = name+".mat";
 String name2 = name;

//here starts the powder loop
//reference JCP 59 (8), 3992 (1973.

 for(count=1; count<value1[qu]; ++count)
 { beta  = 180.0 * count/value1[qu];
   alpha = 360.0 * ((value2[qu]*count) % value1[qu])/value1[qu];
   gamma = 360.0 * ((value3[qu]*count) % value1[qu])/value1[qu];
    cout << count << "\tbeta = " << beta << "\talpha = "
        << alpha << "\tgamma = " << gamma << "\n";
   cout.flush();

//now we rotate the space tensor
    Adip_R  =  Adip.rotate(alpha,beta,gamma);
    Acsa1_R = Acsa1.rotate(alpha,beta,gamma);
    Acsa2_R = Acsa2.rotate(alpha,beta,gamma);

    for(i=0;i<5;++i)
    H[i] = gen_op(zero);

//now we can fill the hamiltonians for the different side diagonals

   for(j=-2;j<=2;++j)
   { temp = twopi*Adip_R.component(2,j)  * d2(j,0,thetam)*1/sqrt(6.0);
    H[j+2].put(+temp,1,2);
    H[j+2].put(-temp,2,1);
     temp = twopi*Acsa1_R.component(2,j) * d2(j,0,thetam)*1/sqrt(6.0) * 2.0 -
          twopi*Acsa2_R.component(2,j) * d2(j,0,thetam)*1/sqrt(6.0) * 2.0;
    H[j+2].put(+temp,0,1);
    H[j+2].put(-temp,1,0);
  }
   temp = H[2].get(1,2)+twopi*J;
   H[2].put(+temp,1,2);
   H[2].put(-temp,2,1);
    temp = H[2].get(0,1)+twopi*(iso_CSA1-iso_CSA2+inhmss);
   H[2].put(+temp,0,1);
   H[2].put(-temp,1,0);
   temp = complex(1/T2zq,0);
   H[2].put(temp,0,0);
   H[2].put(temp,1,1);
//inhomo
   for(step=0;step<ninhms;step++)
   { temp = H[2].get(0,1)-twopi*inhmss;
    H[2].put(+temp,0,1);
    H[2].put(-temp,1,0);
// end inhomo

//now we can set up the floquet hamiltonian and fill it with H[i]

     floq_op H_floq(N1,3,mas_freq);
```

```
    for(i=-2;i<=2;++i)
    { if(H[i+2].exists())
      H_floq.put_sdiag(H[i+2],i);
    }
    H_floq.add_omegai();
    floq_op U_floq = exp(H_floq*complex(-dw));
    U_floq.set_DBR();
   U = gen_op(zero);
    for(i=0;i<3;++i)
   { for(j=0;j<3;++j)
    { temp = 0;
      for(k=-N1;k<=N1;++k)
       temp += U_floq.get(k,0,i,j);
      U.put(temp,i,j);
    }
   }
    delete [] U_floq;
    U.set_DBR();
   U1 = gen_op(zero);
   U1.put(complex(1),0,0);
   U1.put(complex(1),1,1);
   U1.put(complex(1),2,2);
   for(m=0;m<Fnp;++m)
   { data.put(U1.get(2,2), m);
    U1 = U*U1;
   }
    data_sum += data*sin(beta/180.0*PI)*lwt[step];
 } //end inhomo loop
} // end of powder loop
 scale = Re(data_sum(0));
 for(i=0;i<Fnp;++i)
   data_sum.put(data_sum(i)/scale,i);
 MATLAB(name1,name2,data_sum,1);
}
```

```
/*
rrsimfi_3.cc

simulate rotational resonance as a fictious spin 1/2 system
floquet approach in liouville space
uses real reduced (3x3) liouville relaxation
basis in Liouville space is Ix Iy and Iz
dw must be a multiple of the rotorcycle, since scaling of
projection from Floquet to Liouville space is not implemented.

MAER 13.5.1995, modified by JH
*/

#include "gamma.h"
#include "floq_op.h"

main(int argc, char *argv[])

{
 gen_op H[5], U, U1;
 space_T Adip, Acsa1, Acsa2, Acsa1_R, Acsa2_R, Adip_R;
 double D, delta_CSA1, etha_CSA1, iso_CSA1;
 double J, delta_CSA2, etha_CSA2, iso_CSA2;
 int i,j,k,m,Fnp,count,qu,N1;
 String name;
 const double thetam=54.73561032;
 double mas_freq, dist;
 double dw,T2zq;
 double alpha_D,beta_D,gamma_D;
 double alpha_CSA1,beta_CSA1,gamma_CSA1;
 double alpha_CSA2,beta_CSA2,gamma_CSA2;
 double alpha,beta,gamma;
 complex temp, scale;
 complex twopi = complex(2.0*PI,0);
 matrix zero(3,3,0);

//inhomo
 int ninhms, inhmss, inhmlw, step;
 double T2i, T2, lwt[100], lint;
//end inhomo

 int value1[] = {2, 50, 100, 144, 200, 300, 538, 1154};
 int value2[] = {1, 7, 27, 11, 29, 37, 55, 107};
 int value3[] = {1, 11, 41, 53, 79, 61, 229, 271};

 complex_setf(0, 0, 1, 10, 6);
 count = 1;
 query_parameter(argc,argv,count++,"Distance between spins (A)  ? ", dist);
 query_parameter(argc,argv,count++,"Euler angle alpha          ? ", alpha_D);
 query_parameter(argc,argv,count++,"Euler angle beta           ? ", beta_D);
 query_parameter(argc,argv,count++,"Euler angle gamma          ? ", gamma_D);
 query_parameter(argc,argv,count++,"J-coupling constant        ? ", J);
```

```
 query_parameter(argc,argv,count++,"chemical shift 1 (iso CSA)  ? ", iso_CSA1);
 query_parameter(argc,argv,count++,"CSA tensor 1 (delta CSA)    ? ", delta_CSA1);
 query_parameter(argc,argv,count++,"CSA tensor 1 (etha CSA)     ? ", etha_CSA1);
 query_parameter(argc,argv,count++,"Euler angle alpha           ? ", alpha_CSA1);
 query_parameter(argc,argv,count++,"Euler angle beta            ? ", beta_CSA1);
 query_parameter(argc,argv,count++,"Euler angle gamma           ? ", gamma_CSA1);
 query_parameter(argc,argv,count++,"chemical shift 2 (iso CSA)  ? ", iso_CSA2);
 query_parameter(argc,argv,count++,"CSA tensor 2 (delta CSA)    ? ", delta_CSA2);
 query_parameter(argc,argv,count++,"CSA tensor 2 (etha CSA)     ? ", etha_CSA2);
 query_parameter(argc,argv,count++,"Euler angle alpha           ? ", alpha_CSA2);
 query_parameter(argc,argv,count++,"Euler angle beta            ? ", beta_CSA2);
 query_parameter(argc,argv,count++,"Euler angle gamma           ? ", gamma_CSA2);
 query_parameter(argc,argv,count++,"MAS Frequency               ? ", mas_freq);
 query_parameter(argc,argv,count++,"Powder Quality (cheng)      ? ", qu);
 query_parameter(argc,argv,count++,"Floquet dimension           ? ", N1);
 query_parameter(argc,argv,count++,"Number of Data Points       ? ", Fnp);
 query_parameter(argc,argv,count++,"Zero Quantum T2             ? ", T2zq);
 query_parameter(argc,argv,count++,"Output Filename             ? ", name);

// inhomo
 query_parameter(argc,argv,count++,"Inhomogeneous Linewidth     ? ", inhmlw);
 query_parameter(argc,argv,count++,"Inhomogeneous Step Size     ? ", inhmss);
 query_parameter(argc,argv,count++,"Number of steps             ? ", ninhms);

 T2i = inhmlw;
 T2 = 1./inhmlw;
 lint = T2i*(atan( (float)((ninhms-1)*inhmss + inhmss/2) * T2));

 lwt[0] = T2i*( atan((float)(inhmss-inhmss/2)*T2) )/lint;
//cout << "lwt:\t" << lwt[0] <<" for step number:\t0\n";
 for (i=1;i<ninhms;i++)
  { lwt[i]=T2i*(atan(((i+1)*inhmss-inhmss/2)*T2)-atan((i*inhmss-inhmss/2)*T2))/lint;
//  cout << "lwt:\t" << lwt[i] <<" for step number:\t" << i <<"\n";
 }

// end inhomo

 dw = (1.0/mas_freq);
 dist = dist*1e-10;
 D = 1e-7*6.72335079e7*6.72335079e7*1.05457266e-34/(2*PI*dist*dist*dist);

 cout << "\n\nSimulation of isotropic chemical shift by dipolar coupling\n";
 cout << "=========================================================\n\n";
 cout << "Program version: " << __FILE__ << " compiled at " << __DATE__ ", "
    << __TIME__ << "\n\n";
 cout << "Parameters:\n";
 cout << "rotation angle thetam    : " << thetam << " Degree\n";
 cout << "distance between spins   : " << dist << " m\n";
 cout << "dipolar coupling constant: " << D << " Hz\n";
 cout << "relativ orientation of D tensor: (" << alpha_D << "," <<
       beta_D << "," << gamma_D << ")\n";
 cout << "J-coupling constant      : " << J << " Hz\n";
```

```
 cout << "isotropic shift 1       : " << iso_CSA1 << " Hz\n";
 cout << "CSA tensor 1 (delta)    : " << delta_CSA1 << " Hz\n";
 cout << "CSA tensor 1 (etha)     : " << etha_CSA1 << " Hz\n";
 cout << "relativ orientation of CSA tensor: (" << alpha_CSA1 << "," <<
       beta_CSA1 << "," << gamma_CSA1 << ")\n";
 cout << "isotropic shift 2       : " << iso_CSA2 << " Hz\n";
 cout << "CSA tensor 2 (delta)    : " << delta_CSA2 << " Hz\n";
 cout << "CSA tensor 2 (etha)     : " << etha_CSA2 << " Hz\n";
 cout << "relativ orientation of CSA tensor: (" << alpha_CSA2 << "," <<
       beta_CSA2 << "," << gamma_CSA2 << ")\n";
 cout << "MAS frequency:          " << mas_freq << "Hz\n";
 cout << "Powder Quality Number:  " << qu << "\n";
 cout << "Floquet Dimension (MAS): " << N1 << "\n";
 cout << "Number of data points:  " << Fnp << " points\n";
 cout << "time increments (dw):   " << dw << " s\n";
 cout << "zero quantum T2:        " << T2zq << " s\n";
 cout << "Output filename:        " << name << "\n";

// inhomo
 cout << "Inhomogeneous Linewidths: " << inhmlw << " Hz\n";
 cout << "Inhomo Correction Stepsize:" << inhmss << " Hz\n";
 cout << "Number of Inhomo Steps:  " << ninhms << "\n";
// end inhomo

 block_1D data(Fnp);
 block_1D data_sum(Fnp);

//setup for the space tensors
  matrix help(3,3,0);

  help.put(-1.0,0,0);
  help.put(-1.0,1,1);
 help.put( 2.0,2,2);
 help = - (complex) D * help;
 Adip = A2(help);

  help.put(-1.0/2.0*(1.0+etha_CSA1),0,0);
  help.put(-1.0/2.0*(1.0-etha_CSA1),1,1);
 help.put( 1.0,2,2);
 help = (complex) delta_CSA1 * help;
 Acsa1 = A2(help);
  Acsa1 = Acsa1.rotate(alpha_CSA1,beta_CSA1,gamma_CSA1);
  Acsa1 = Acsa1.rotate(-gamma_D,-beta_D,-alpha_D);

  help.put(-1.0/2.0*(1.0+etha_CSA2),0,0);
  help.put(-1.0/2.0*(1.0-etha_CSA2),1,1);
 help.put( 1.0,2,2);
 help = (complex) delta_CSA2 * help;
 Acsa2 = A2(help);
  Acsa2 = Acsa2.rotate(alpha_CSA2,beta_CSA2,gamma_CSA2);
  Acsa2 = Acsa2.rotate(-gamma_D,-beta_D,-alpha_D);
```

```
String name1 = name+".mat";
String name2 = name;

//here starts the powder loop
//reference JCP 59 (8), 3992 (1973.

for(count=1; count<value1[qu]; ++count)
{ beta  = 180.0 * count/value1[qu];
  alpha = 360.0 * ((value2[qu]*count) % value1[qu])/value1[qu];
  gamma = 360.0 * ((value3[qu]*count) % value1[qu])/value1[qu];
  cout << count << "\tbeta = " << beta << "\talpha = "
       << alpha << "\tgamma = " << gamma << "\n";
  cout.flush();

//now we rotate the space tensor
   Adip_R  =  Adip.rotate(alpha,beta,gamma);
   Acsa1_R = Acsa1.rotate(alpha,beta,gamma);
   Acsa2_R = Acsa2.rotate(alpha,beta,gamma);

   for(i=0;i<5;++i)
   H[i] = gen_op(zero);

//now we can fill the hamiltonians for the different side diagonals

  for(j=-2;j<=2;++j)
  { temp = twopi*Adip_R.component(2,j)  * d2(j,0,thetam)*1/sqrt(6.0);
    H[j+2].put(+temp,1,2);
    H[j+2].put(-temp,2,1);
    temp = twopi*Acsa1_R.component(2,j) * d2(j,0,thetam)*1/sqrt(6.0) * 2.0 -
         twopi*Acsa2_R.component(2,j) * d2(j,0,thetam)*1/sqrt(6.0) * 2.0;
    H[j+2].put(+temp,0,1);
    H[j+2].put(-temp,1,0);
  }
  temp = H[2].get(1,2)+twopi*J;
  H[2].put(+temp,1,2);
  H[2].put(-temp,2,1);
   temp = H[2].get(0,1)+twopi*(iso_CSA1-iso_CSA2+inhmss);
  H[2].put(+temp,0,1);
  H[2].put(-temp,1,0);
  temp = complex(1/T2zq,0);
  H[2].put(temp,0,0);
  H[2].put(temp,1,1);
//inhomo
  for(step=0;step<ninhms;step++)
  { temp = H[2].get(0,1)-twopi*inhmss;
    H[2].put(+temp,0,1);
    H[2].put(-temp,1,0);
// end inhomo

//now we can set up the floquet hamiltonian and fill it with H[i]

     floq_op H_floq(N1,3,mas_freq);
```

```
    for(i=-2;i<=2;++i)
    { if(H[i+2].exists())
      H_floq.put_sdiag(H[i+2],i);
    }
    H_floq.add_omegai();
    floq_op U_floq = exp(H_floq*complex(-dw));
    U_floq.set_DBR();
   U = gen_op(zero);
    for(i=0;i<3;++i)
   { for(j=0;j<3;++j)
    { temp = 0;
      for(k=-N1;k<=N1;++k)
       temp += U_floq.get(k,0,i,j);
      U.put(temp,i,j);
    }
   }
    delete [] U_floq;
    U.set_DBR();
   U1 = gen_op(zero);
    U1.put(complex(1),0,0);
    U1.put(complex(1),1,1);
    U1.put(complex(1),2,2);
    for(m=0;m<Fnp;++m)
    { data.put(U1.get(2,2), m);
     U1 = U*U1;
    }
     data_sum += data*sin(beta/180.0*PI)*lwt[step];
  } //end inhomo loop
 } // end of powder loop
 scale = Re(data_sum(0));
 for(i=0;i<Fnp;++i)
   data_sum.put(data_sum(i)/scale,i);
 MATLAB(name1,name2,data_sum,1);
}
```

```
//-------------------------------------------------------------*-c++-*-
//
//
// Simulate MAS-Experiment for a 2 Spin system with powder average.
// one 13C spin and one 14N spin
//
// 1) no quadrupol coupling is assumed for the 14N
// 2) no CSA is assumed for the 14N
//
// ------> both these effects can be incorporated as well
//
// written by Marco Tomaselli
//-----------------------------------------------------------------

#include "gamma.h"
#include "floq2_op.h"
#include "floq_op.h"
#include "nmr_floq_acq.h"


main (int argc, char *argv[])
{


 // constants for Poweder Average
 // Reference: Cheng73
 //   Vera B. Cheng, Henry H. Suzukawa Jr. and Max Wolfsberg
 //   Investigations of a nonrandom numerical method for multidimensional integration
 //   J.Chem.Phys 59 3992-9 (1973)

 int cheng1[] = {  2,   3,   5,   8,   13,
            21,  34,  55,  89,  144,
           233, 377, 616, 987, 1597,
          2584, 4181, 6765, 10946, 17711};
 int cheng2[] = {  1,   1,   2,   3,   5,
            8,  13,  21,  34,  55,
            89, 144, 233, 377, 616,
           987, 1597, 2584, 4181, 6765};


 int p=1;                          // Parameter count
 int cheng;                        // Index for cheng1 and cheng2
 String outFileName;               // Output filename
 int N;                      // Floquet dimension
 int NP;                           // Number of points in spectrum
 double omegar=0;                  // Rotation frequency
 double lamor=0;           // (For conversion of PPM to Hz)
 double minFreq, maxFreq;          // Spectral range for spectrum
 double sig11,sig22,sig33;    // three principal components
 double dip;               // dipolar coupling 13C-14N
 double alpha_c,beta_c,gamma_c;// relative tensor orientation
 double lw;                // exp broadening factor [Hz]
```

```
query_parameter (argc,argv,p++,"outname          = ", outFileName);
query_parameter (argc,argv,p++,"N              = ", N);
query_parameter (argc,argv,p++,"cheng number     = ", cheng);
query_parameter (argc,argv,p++,"omegar          = ", omegar);
query_parameter (argc,argv,p++,"Lamor frequency   = ", lamor);
query_parameter (argc,argv,p++,"sigma 11        = ", sig11);
query_parameter (argc,argv,p++,"sigma 22        = ", sig22);
query_parameter (argc,argv,p++,"sigma 33        = ", sig33);
query_parameter (argc,argv,p++,"dipol coupl. [Hz]  = ", dip);
query_parameter (argc,argv,p++,"alpha           = ", alpha_c);
query_parameter (argc,argv,p++,"beta            = ", beta_c);
query_parameter (argc,argv,p++,"gamma           = ", gamma_c);
query_parameter (argc,argv,p++,"exp broad.      = ", lw);
query_parameter (argc,argv,p++,"NP             = ", NP);
query_parameter (argc,argv,p++,"Minimal frequency  = ", minFreq);
query_parameter (argc,argv,p++,"Maximal frequency  = ", maxFreq);


// Open the Output file and write the Parameters into it

 ofstream os (outFileName+"."+dec(N)+".dat");

os << "# MAS Powder Simulation \n ";
os << "# Program Version: " << __FILE__ << " compiled at "
   << __DATE__ << " " << __TIME__ << "\n" ;
os << "# N             = " << N          << "\n";
os << "# cheng          = " << cheng      << "\n";
os << "# Steps in Powder   = " << cheng1[cheng] << "\n";
os << "# omegar         = " << omegar     << "\n";
os << "# Lamor frequency   = " << lamor      << "\n";
os << "# NP            = " << NP         << "\n";
os << "# Minimal frequency  = " << minFreq     << "\n";
os << "# Maximal frequency  = " << maxFreq     << "\n";
os << "# sig11          = " << sig11      << "\n";
os << "# sig22          = " << sig22      << "\n";
os << "# sig33          = " << sig33      << "\n";
os << "# dipol-coupl [Hz]  = " << dip        << "\n";
os << "# alpha          = " << alpha_c    << "\n";
os << "# beta           = " << beta_c     << "\n";
os << "# gamma          = " << gamma_c    << "\n";


spin_system AB (2);          //Set up a spin system

 AB.isotope(0,"13C");
 AB.isotope(1,"14N");

coord B (0,0,1);             //Set up the field vector

block_1D spect(NP),          // Spectrum of one orientation
```

```
    specsum(NP);                    // Spectrum of the powder


 spin_T TTS1 = T_CS2(AB,0,B);           // spin tensor Spin 1

                    // no CSA is assumed for 14N !!!!

 gen_op H1 = sqrt(1./6.)*(2*Iz(AB,0)*Iz(AB,1));     // heteronuclear dipol


// this preparation is done selectively on the carbon spin


 gen_op detect = Im(AB,0);       // detection operator I_
 gen_op sigma0 = Iz(AB,0);    // eqilibrium density matrix
 gen_op sigma1=Iypuls(AB,sigma0,0,90.);
                                 // Prepare density matrix after 90-y-puls

// set up the dipol-tensor

 matrix dc(3,3);
  dc.put_h(-dip/2.,0,0);dc.put_h(0.,0,1);dc.put_h(0.,0,2);
            dc.put_h(-dip/2.,1,1);dc.put_h(0.,1,2);
                      dc.put_h(dip,2,2);
 space_T DIP(A2(dc));


 // now define CSA tensors relative to the dipol tensor
 //set up CSA-Tensor for spin 0, this is the 13C tensor (in PPM convert to Hz)

 matrix s1(3,3);
  s1.put_h(sig11,0,0);s1.put_h(0.,0,1);s1.put_h(0.,0,2);
              s1.put_h(sig22,1,1);s1.put_h(0.,1,2);
                        s1.put_h(sig33,2,2);
 s1 *= lamor;
 space_T CS1(A2(s1));
 space_T CS1n = T_rot(CS1,alpha_c,beta_c,gamma_c);


 // define and initialise the density matrix in then Floquet space
 // Reference Tilo Levante, Floquet Theory, hand out 1992

 floq_op fsigma   ( N, AB.HS(), omegar);
 fsigma.put_block ( sigma1, 0, 0);



 gen_op H_0, H_1, H_2;                  // Fourier expansion of the Hamiltonian
                                 // H = e^(-2(i2PI)t) adj(H_2)
                                 //   + e^(-1(i2PI)t) adj(H_1)
                                 //   + adj(H_0)
                                 //   + e^( 1(i2PI)t) H_1
```

```
                                        //   + e^( 2(i2PI)t) H_2

H_0 = T_prod(CS1n,TTS1,0);
                                        // Time and orientation independent component
                                        // of the Hamiltonian


 // ----------------------powder loop  --------------------------

for (int b=1;b<cheng1[cheng];b++)
 {
    cout<<"b="<<b<<"of"<<cheng1[cheng]<<"\r";
  cout.flush();

  // calculate the orientation for the current step (formulas see Cheng73)
  // alpha = 360 * cheng1 * ((cheng2*b) mod cheng1)

  double beta  = 180./cheng1[cheng] * b;
  double alpha = 360./cheng1[cheng] * ((cheng2[cheng]*b)%cheng1[cheng]);

  // Rotate the space tensor for this orientation

   space_T CS1R=T_rot(CS1n,alpha,beta,0);
   space_T DIPR=T_rot(DIP,alpha,beta,0);

  // Calculate the space (and time) dependent parts of the Hamiltonian

  H_1=CS1R.component(2,1)*TTS1.component(2,0)+
    DIPR.component(2,1)*H1;
   H_1=(1/sqrt(3.))*H_1;


  H_2=CS1R.component(2,2)*TTS1.component(2,0)+
    DIPR.component(2,2)*H1;
   H_2=(1/sqrt(6.))*H_2;

  // define the Floquet Hamiltonian

   floq_op HAMFLOQ (N,AB.HS(),omegar); // Hamilton Floquet Matrix

   HAMFLOQ.put_sdiag(adjoint(H_2),-2); // set side diagonal # -2
   HAMFLOQ.put_sdiag(adjoint(H_1),-1); // set side diagonal # -1
  HAMFLOQ.put_sdiag(H_0,0);         // set main diagonal
   HAMFLOQ.put_sdiag(H_1,1);                  // set side diagonal # 1
   HAMFLOQ.put_sdiag(H_2,2);                  // set side diagonal # 1
  HAMFLOQ.add_omega();               // Add omegas on diagonal


  // Calculate the spectrum using the approach from
  // Tilo Levante, Floquet Theory, hand out 1992
```

```
    // assuming that the third axis for the powder average
    // is the same as the MAS spinning axis

    spec_maspowder(fsigma, detect, HAMFLOQ, minFreq, maxFreq, NP, spect);

    spect *= sin(beta*PI/180.);
   specsum += spect;
  }


 specsum  = IFFT(specsum);
 exponential_multiply(specsum,-lw);          // Apodization
 specsum  = FFT(specsum);

  for (int i=0;i<NP;i++)
   os<< minFreq+(maxFreq-minFreq)*i/NP << " " <<
     Re(specsum(i)) << " " << Im(specsum(i)) <<"\n";

 cout << "\n";
}
```

ERNEST ORLANDO LAWRENCE BERKELEY NATIONAL LABORATORY
ONE CYCLOTRON ROAD | BERKELEY, CALIFORNIA 94720

Prepared for the U.S. Department of Energy under Contract No. DE-AC03-76SF00098